

Electronic Supporting Information (ESI)

Novel design of dual-action Pt(IV) anticancer pro-drugs based on cisplatin and derivatives of the Tyrosine Kinase Inhibitors imatinib and nilotinib

Darren Fergal Beirne, Barbara Farkaš, Chiara Donati, Valentina Gandin, Isabel Rozas, Trinidad Velasco-Torrijos, Diego Montagner

Table of contents

Materials and Methods.....	2
Characterisation Data:	
¹ H/ ¹³ C NMR, COSY, HSQC, HMBC, IR, HRMS & LCMS of 2	2-5
¹ H/ ¹³ C NMR, COSY, HSQC, HMBC, IR, HRMS & LCMS of 3	6-9
¹ H/ ¹³ C NMR, COSY, HSQC, HMBC, IR, HRMS & LCMS of 4	9-12
¹ H/ ¹³ C NMR, COSY, HSQC, HMBC, IR, HRMS & LCMS of 5	13-16
¹ H/ ¹³ C NMR, COSY, HSQC, HMBC, IR, HRMS & LCMS of 6	16-19
¹ H/ ¹³ C/ ¹⁹⁵ Pt NMR, COSY, HSQC, HMBC, IR & HRMS of A	20-23
¹ H/ ¹³ C/ ¹⁹ F NMR, COSY, HSQC, HMBC, IR, HRMS & LCMS of 9	24-27
¹ H/ ¹³ C/ ¹⁹ F NMR, COSY, HSQC, HMBC, IR, HRMS & LCMS of 10	28-31
¹ H/ ¹³ C/ ¹⁹ F NMR, COSY, HSQC, HMBC, IR, HRMS & LCMS of 11	32-35
¹ H/ ¹³ C/ ¹⁹ F NMR, COSY, HSQC, HMBC, IR, HRMS & LCMS of 12	36-39
¹ H/ ¹³ C/ ¹⁹ F/ ¹⁹⁵ Pt NMR, COSY, HSQC, HMBC, IR & HRMS of B	40-44
Uv-Vis Stability of A & B	44
NMR Reduction Studies of A & B	45
Computational Details: DFT Optimisation & Docking Studies.....	46-52
Computational Details: Molecular Dynamics.....	53-61
Biological Details: Experiments with Cultured Human Cancer Cells.....	62
Biological Details: Cell Cultures.....	62
Biological Details: MTT Assay.....	62
Biological Details: Inhibition of PDGFR α and c-KIT Kinase Activity.....	62
References.....	62-63

Materials and Methods

All reagents, solvents and reactants were purchased from commercial sources (Sigma-Aldrich and Flourochem) and used without further purification unless specified. [Tetrakis-(triphenylphosphine) palladium(0)] was provided by Johnson Matthey through the JM PGM Award Scheme PGMAS54. *Elemental Analyses* (Carbon, Hydrogen and Nitrogen) were performed with a PerkinElmer 2400 series II analyser. *Infrared (IR)* spectrometry was conducted on a Perkin Elmer Spectrum 100 FT-IR. Attenuated Total Reflectance Fourier transform Infrared (ATR-FTIR) spectra were taken in the region 4000 cm^{-1} to 650 cm^{-1} , using 4 scans with a resolution of 4 cm^{-1} . *ESI Mass Spectra* were recorded with a Waters LCT Premier XE Spectrometer. Microwave assisted organic syntheses were conducted using a CEM Discover microwave synthesis reactor equipped with an Explorer 12 Hybrid Autosampler. *NMR analyses* were conducted with a Bruker Advance spectrometer at 500 MHz for ^1H , 126 MHz for ^{13}C , 107 MHz for ^{195}Pt and 470 MHz for ^{19}F nuclei. Samples were typically dissolved in $\text{DMSO-}d_6$ and CDCl_3 and added to 5-mm sample tubes. The probe temperature was maintained at 298 K, unless stated otherwise. The residual solvent peaks were used as an internal standard for ^1H and ^{13}C experiments. For ^{195}Pt , an external reference of Na_2PtCl_4 in D_2O (adjusted to $\delta = -1628$ ppm from Na_2PtCl_6) was used. Chemical shifts were recorded in parts per million (ppm), while the coupling constant (J) was recorded in Hz when applicable. *TLC* was conducted using TLC Silica gel 60 RP-2 (silanized) plates with a fluorescent indicator at 254 nm, bought from Sigma-Aldrich Ireland. Lyophilisation was conducted on a Labconco Freezone 1 Dry system. *LC-MS* was performed on an Agilent Technologies 1200 Series instrument consisting of a G1322A Quaternary pump and a G1314B UV detector (254 nm) coupled to an Advion Expression L Compact Mass spectrometer (ESI) operating in positive mode. *UV-Stability Studies*: complexes A and B were dissolved in a mixture of DMSO/PBS buffer (1/9) and the UV-VIS spectra were recorded at different interval using a Varian CARY 50 spectrophotometer with a wavelength range of 200-800 nm and a scan rate of 600 nm min^{-1} . *Reduction Studies*: complexes A and B were dissolved in 500 μL of $\text{DMSO-}d_6$ (18 mM solution) and 10 eq. of ascorbic acid were added. The reduction was followed by $^1\text{H-NMR}$ and $^{195}\text{Pt NMR}$. $^1\text{H NMR}$ spectra were recorded at $t = 0\text{h}$, 1h; 2h; 4h; 6h; 10h and 24h. $^{195}\text{Pt NMR}$ spectrum was recorded at $t = 24\text{h}$.

Compound 2

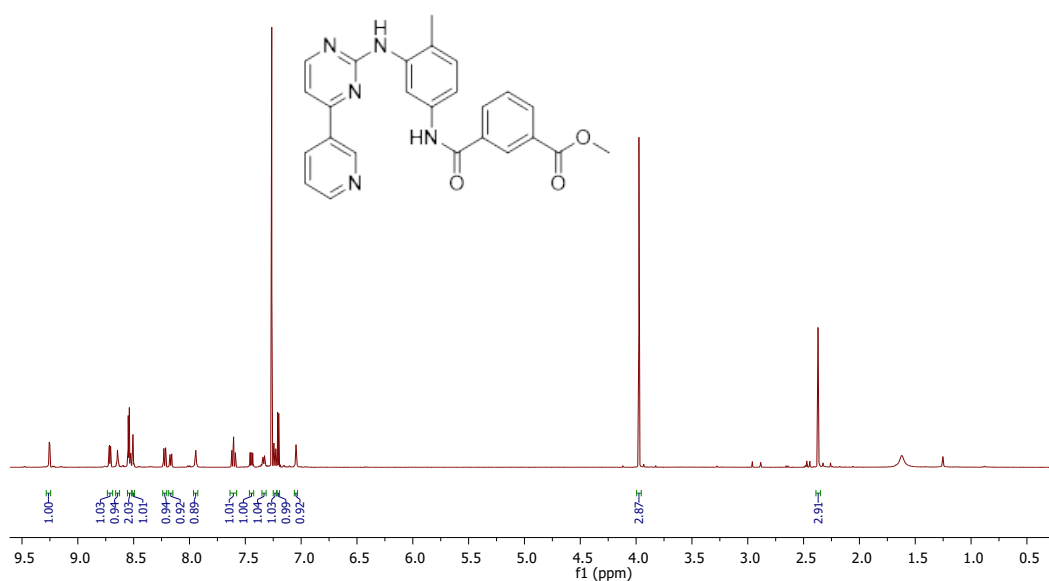


Fig. 1Sa. $^1\text{H NMR}$ of **2** in CDCl_3

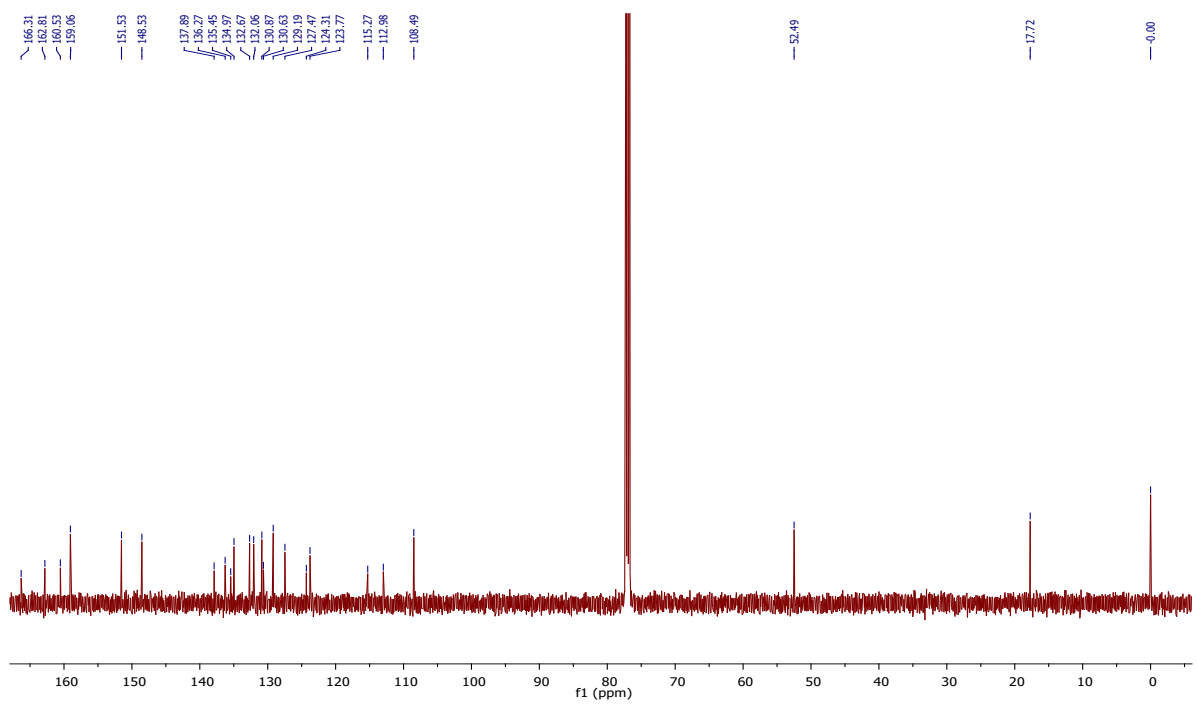


Fig. 1Sb. ^{13}C NMR of **2** in CDCl_3

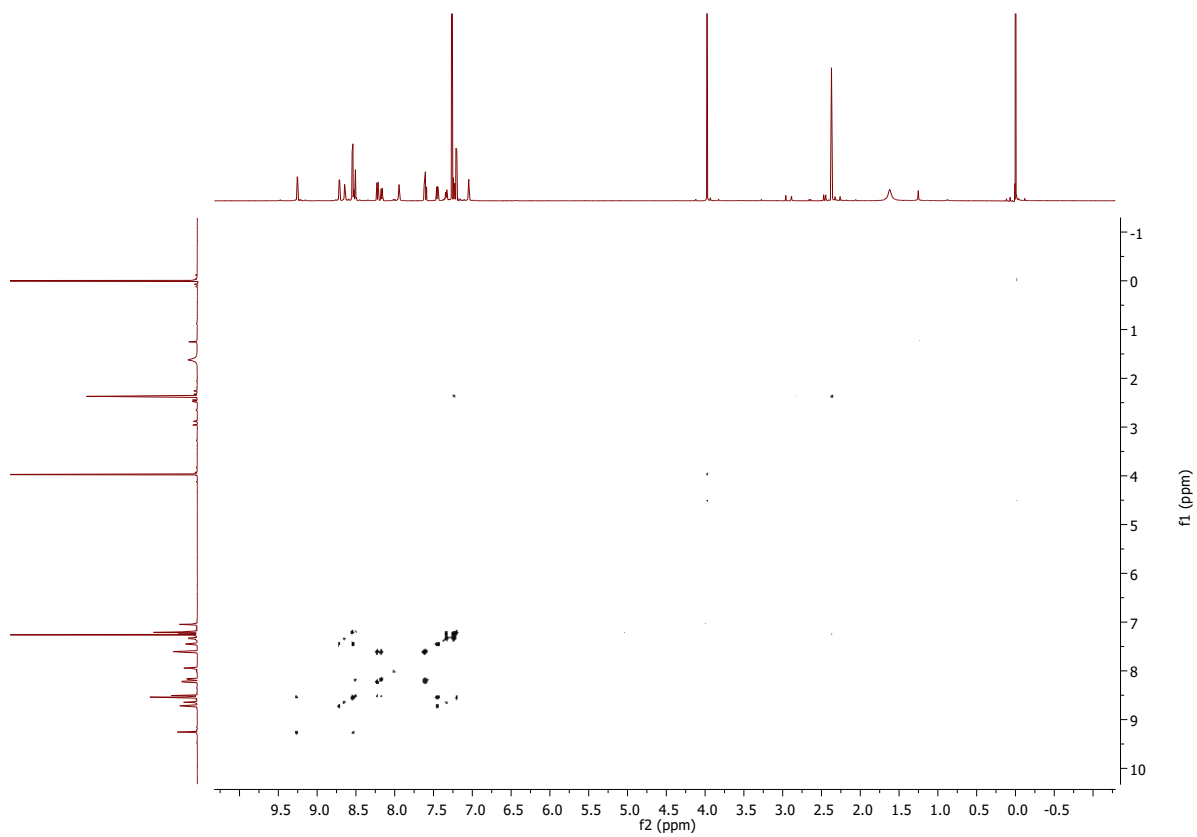


Fig. 1Sc. COSY of 2 in CDCl₃

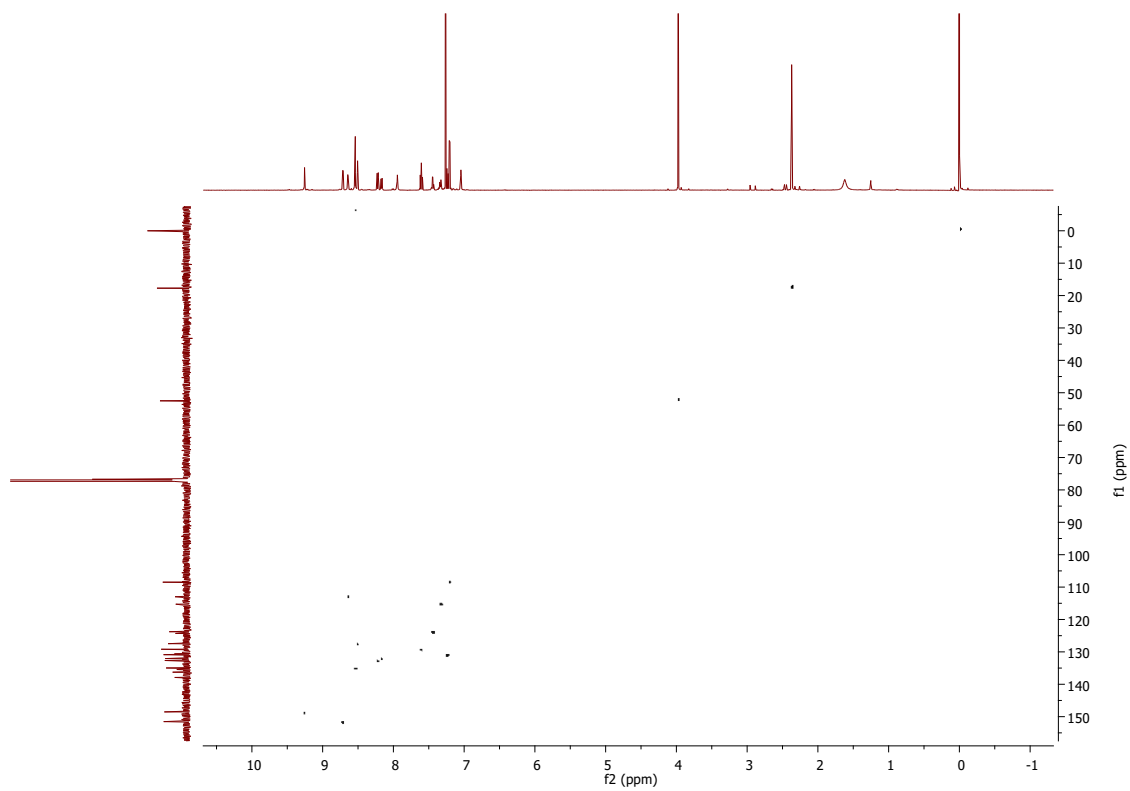


Fig. 1Sd. HSQC of 2 in CDCl₃

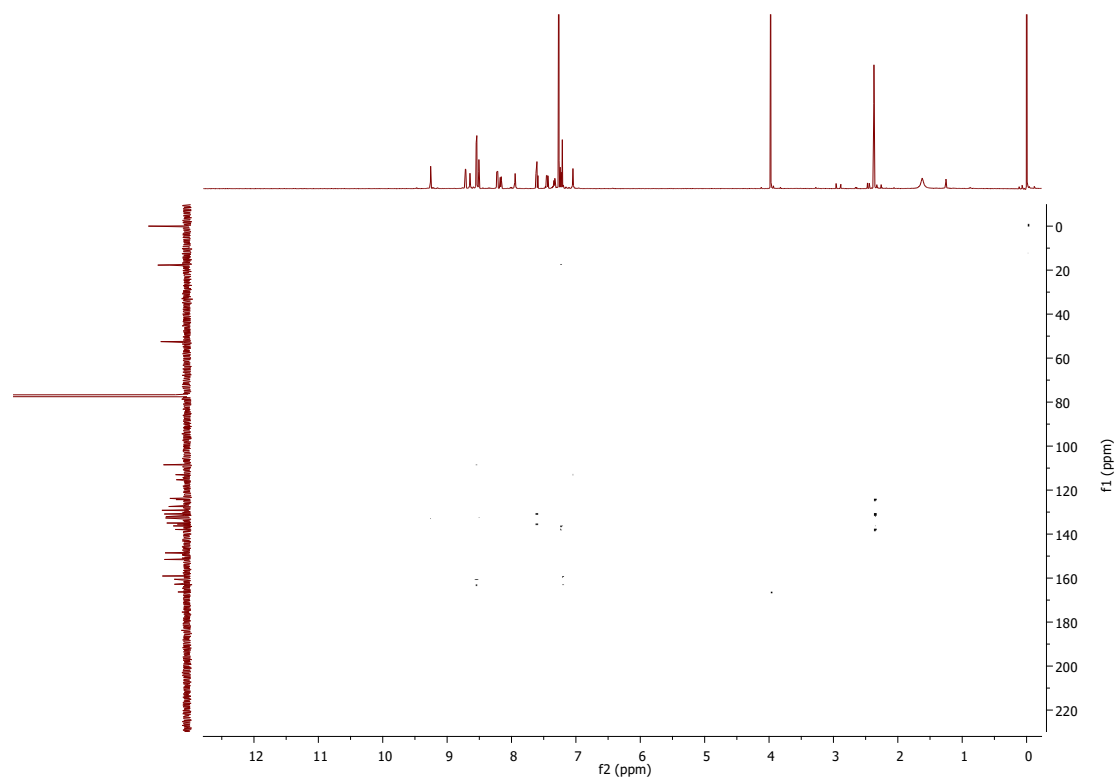


Fig. 1Se. HMBC of 2 in CDCl₃

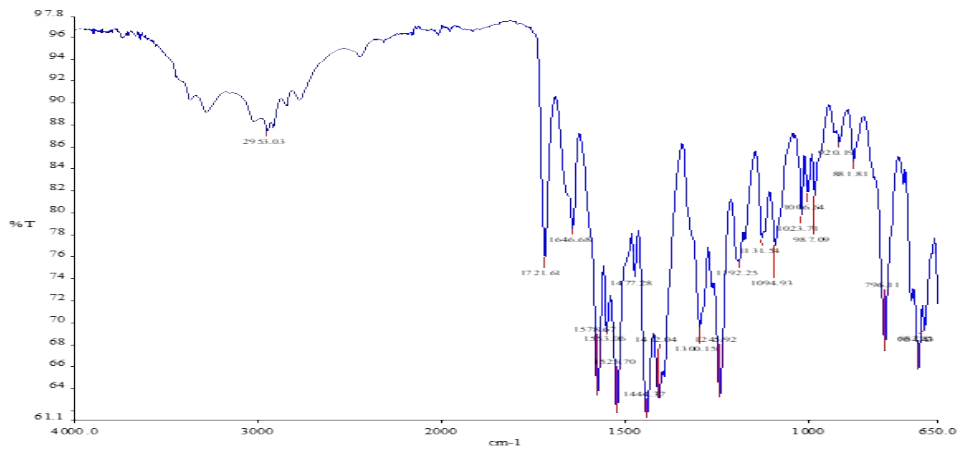


Fig. 1Sf. IR of 2

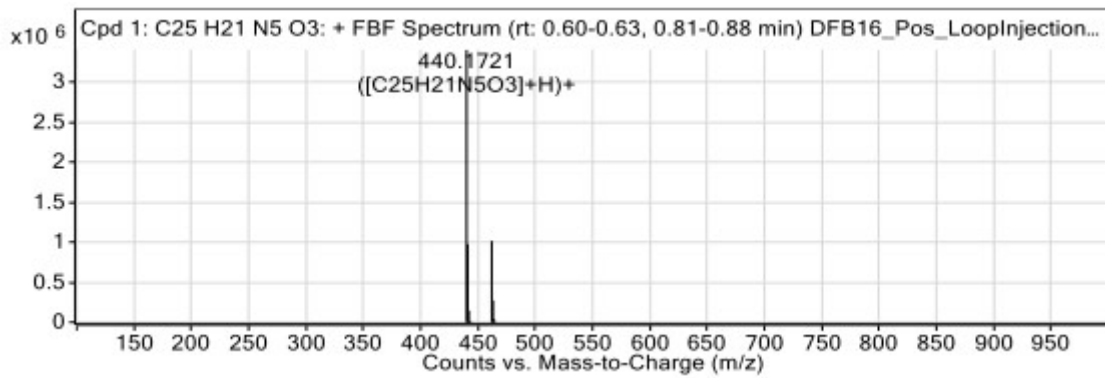


Fig. 1Sg. HRMS of 2

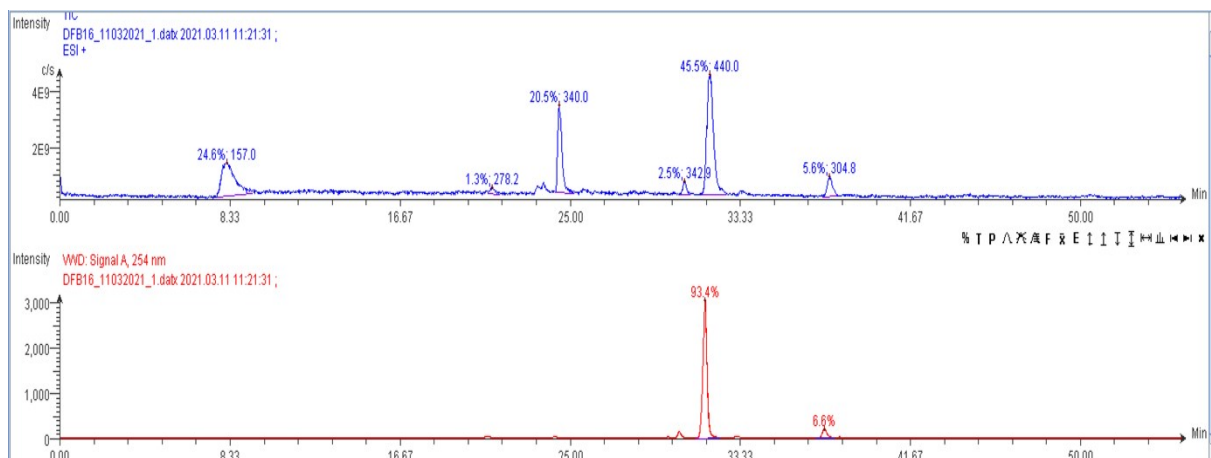


Fig. 1Sh. LCMS of 2

Compound 3

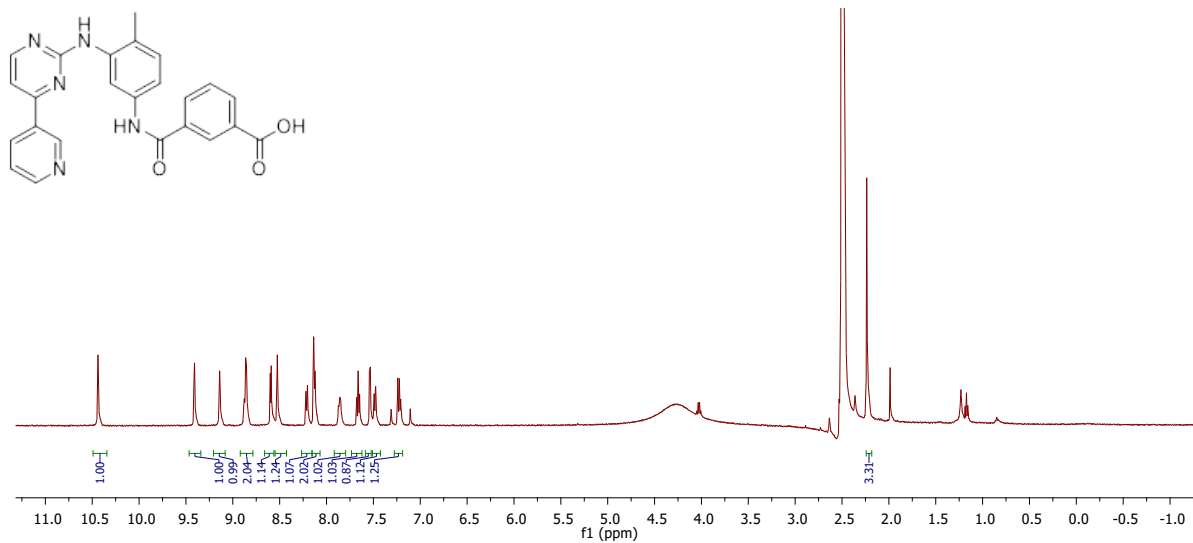


Fig. 2Sa. ¹H NMR of 3 in DMSO-d₆

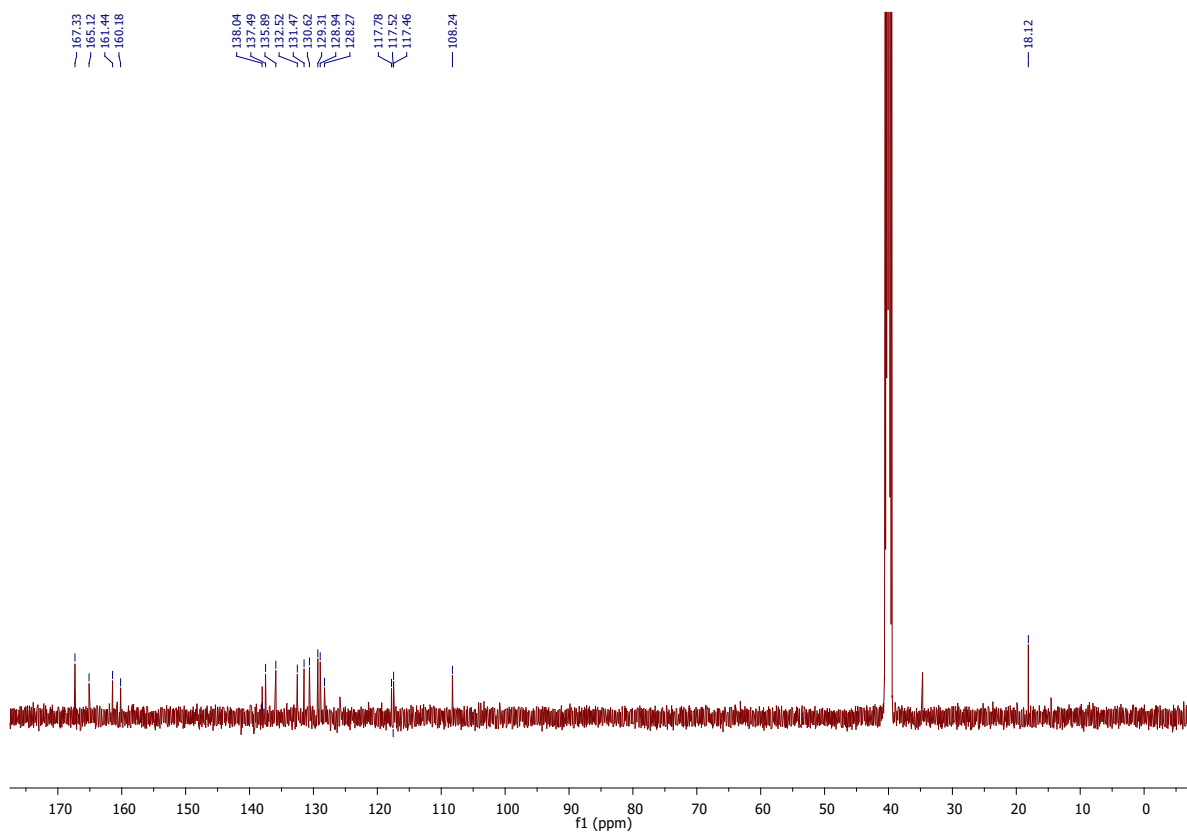


Fig. 2Sb. ¹³C NMR of 3 in DMSO-d₆

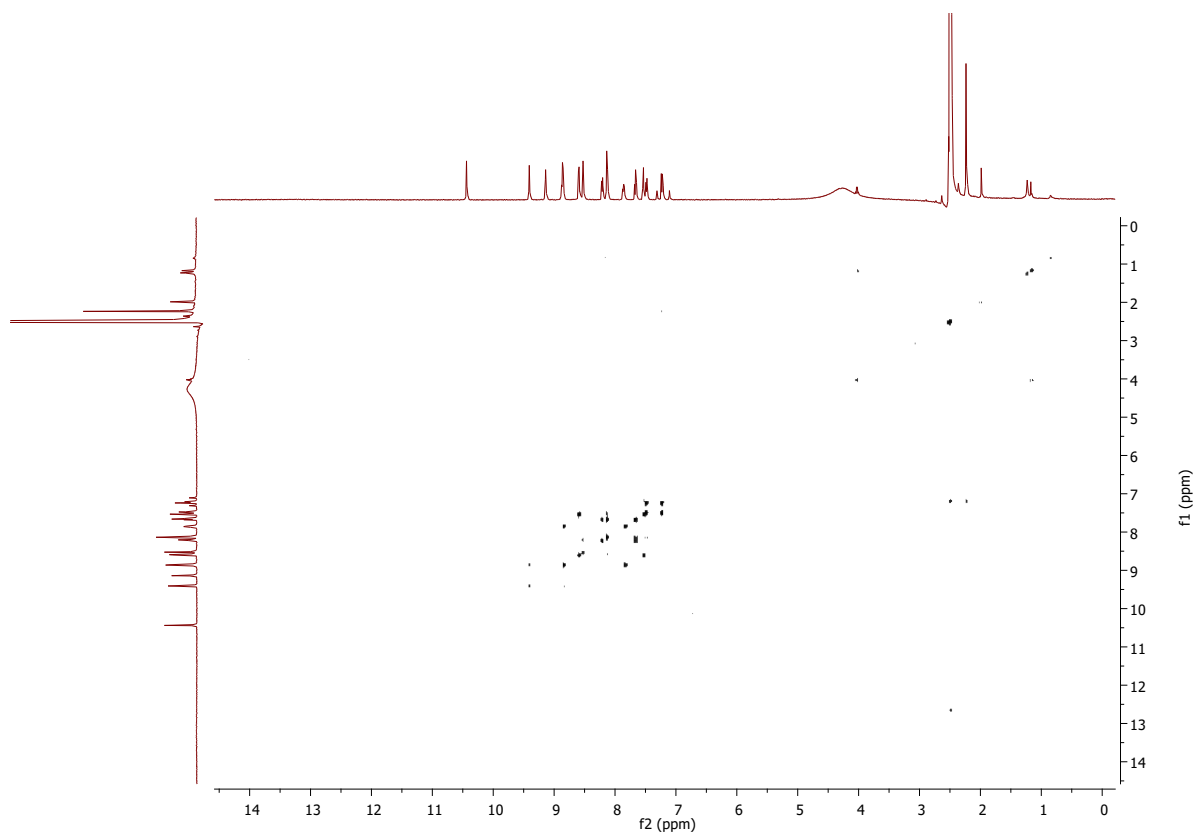


Fig. 2Sc. COSY of **3** in DMSO- d_6

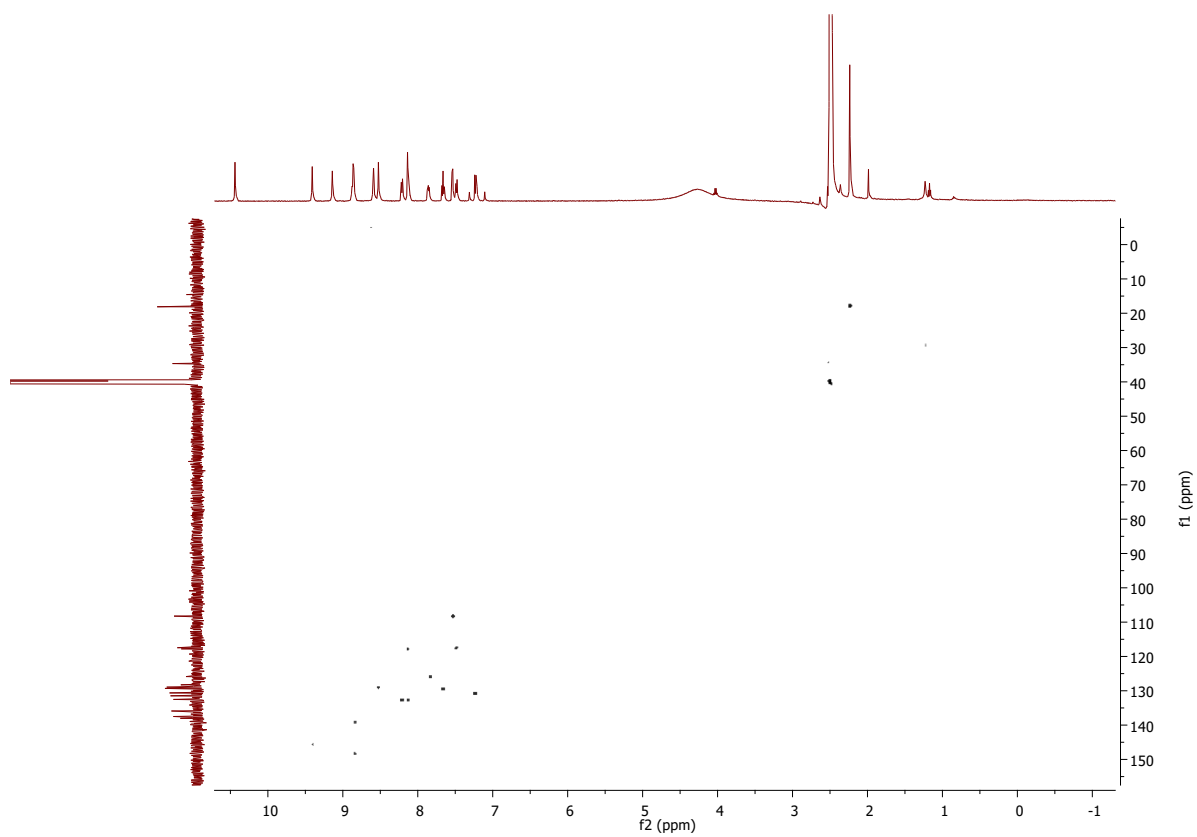


Fig. 2Sd. HSQC of **3** in DMSO- d_6

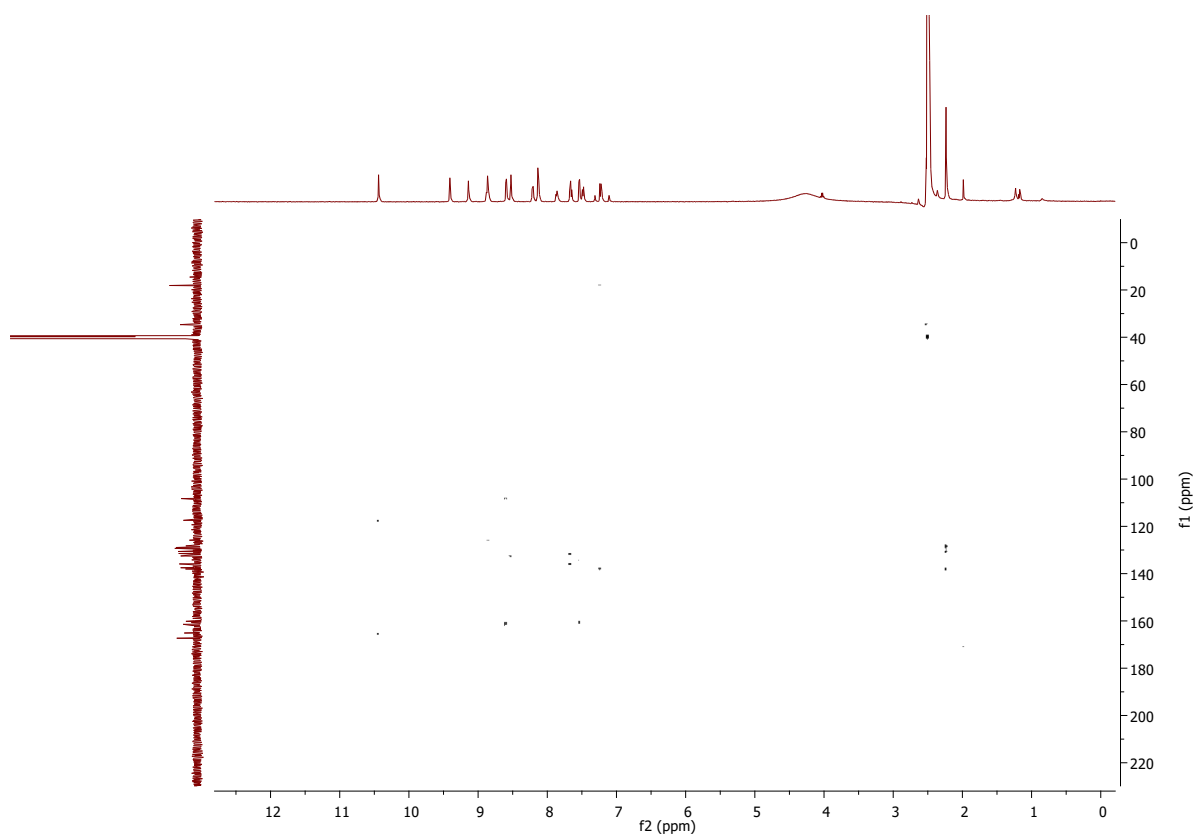


Fig. 2Se. HMBC of **3** in DMSO- d_6

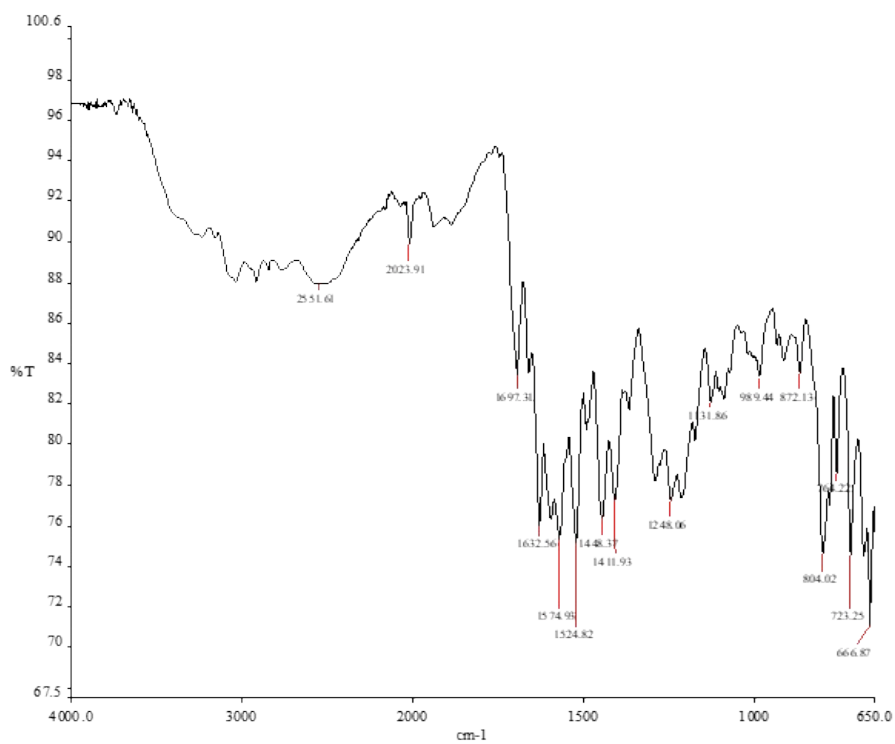


Fig. 2Sf. IR of **3**

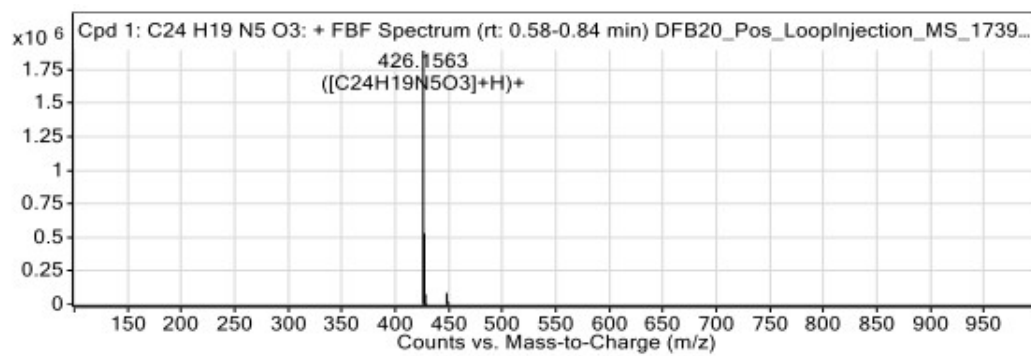


Fig. 2Sg. HRMS of 3

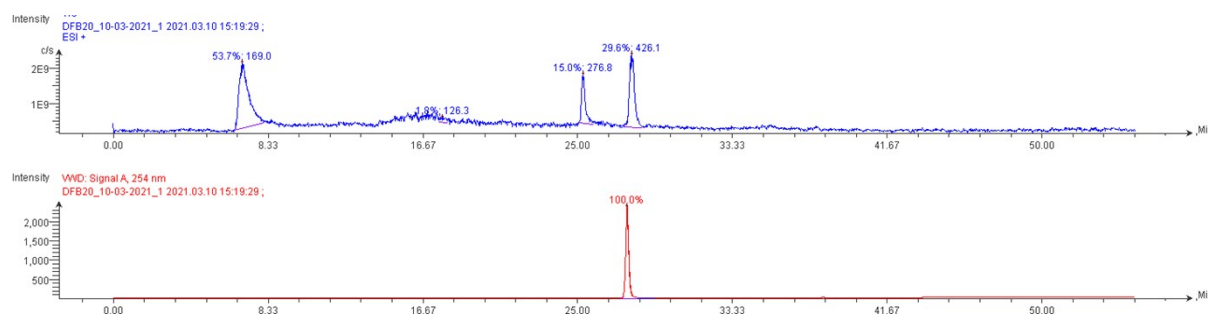


Fig. 2Sh. LCMS of 3

Compound 4

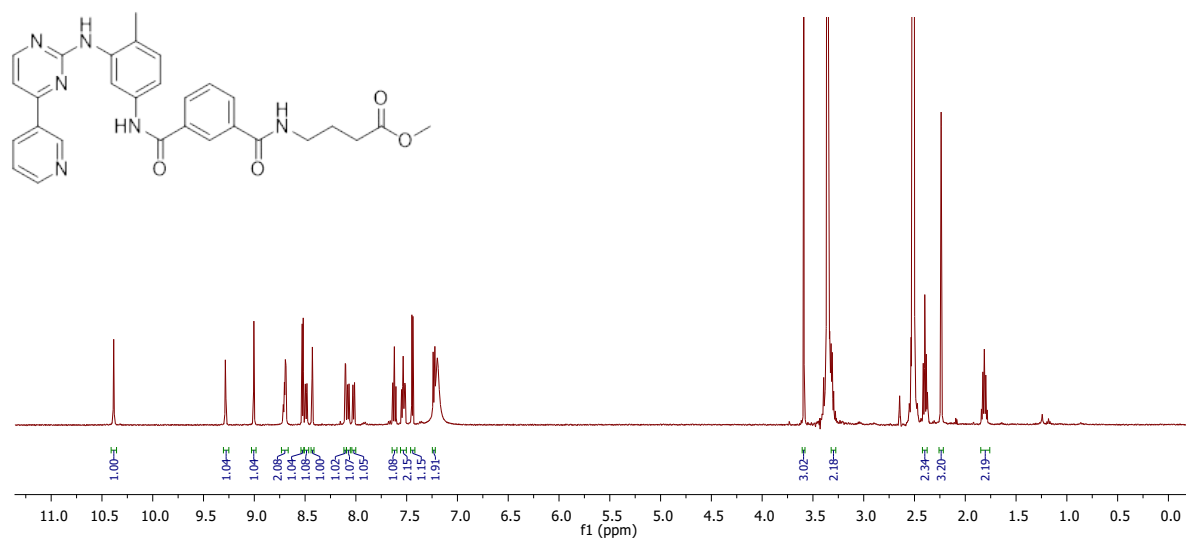


Fig. 3Sa. ¹H NMR of 4 in DMSO-d₆

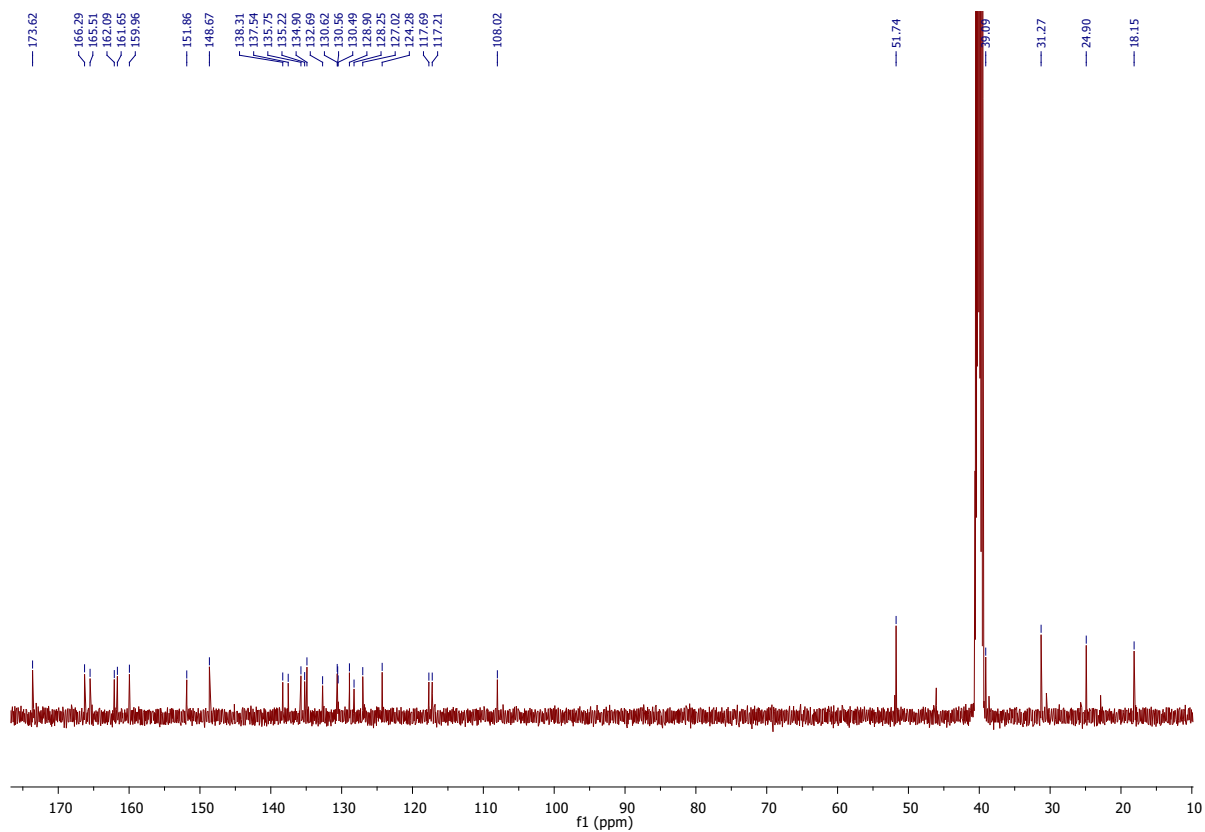


Fig. 3Sb. ^{13}C NMR of **4** in $\text{DMSO-}d_6$

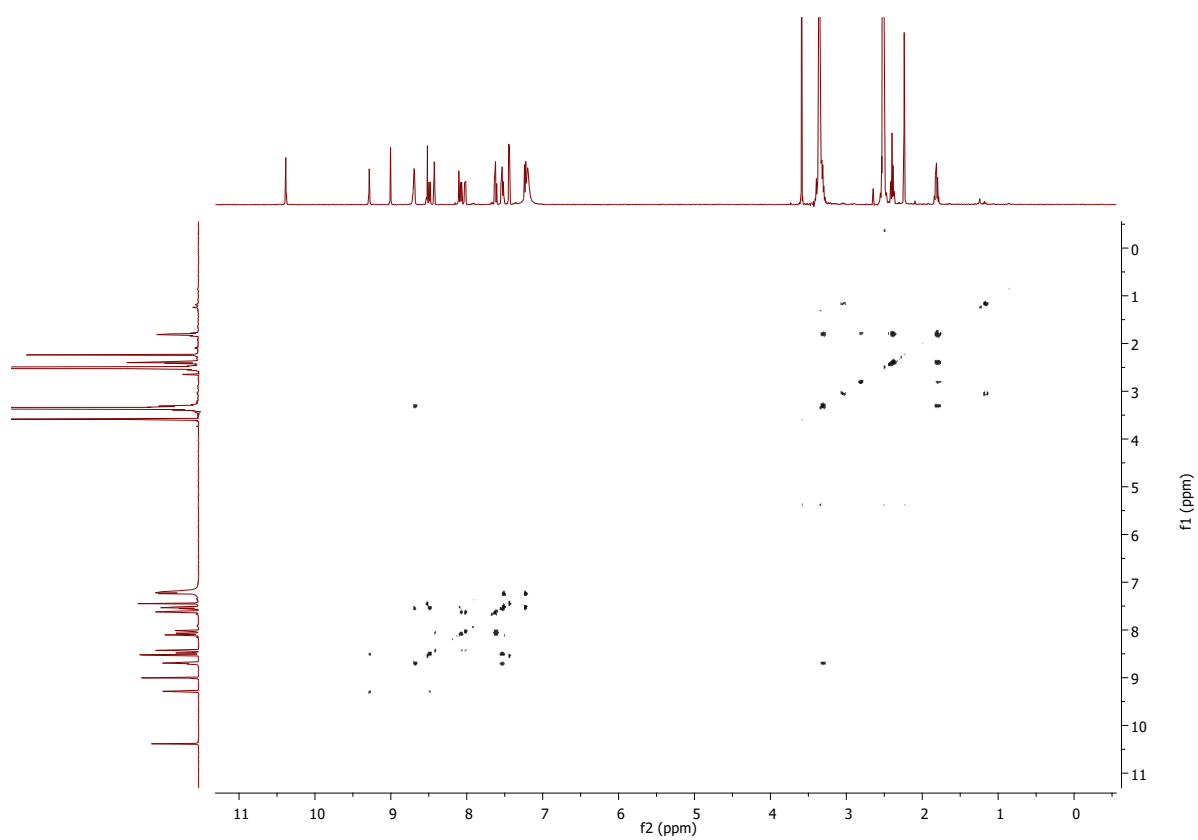


Fig. 3Sc. COSY of **4** in $\text{DMSO-}d_6$

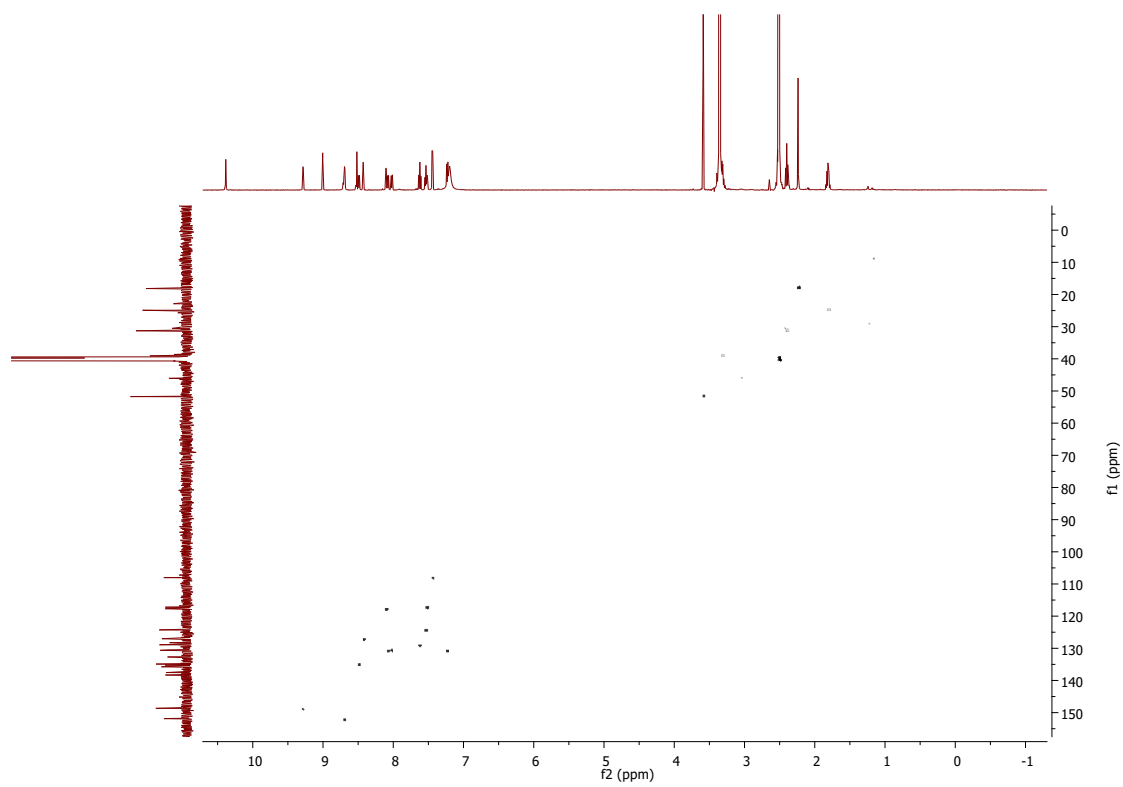


Fig. 3Sd. HSQC of 4 in DMSO- d_6

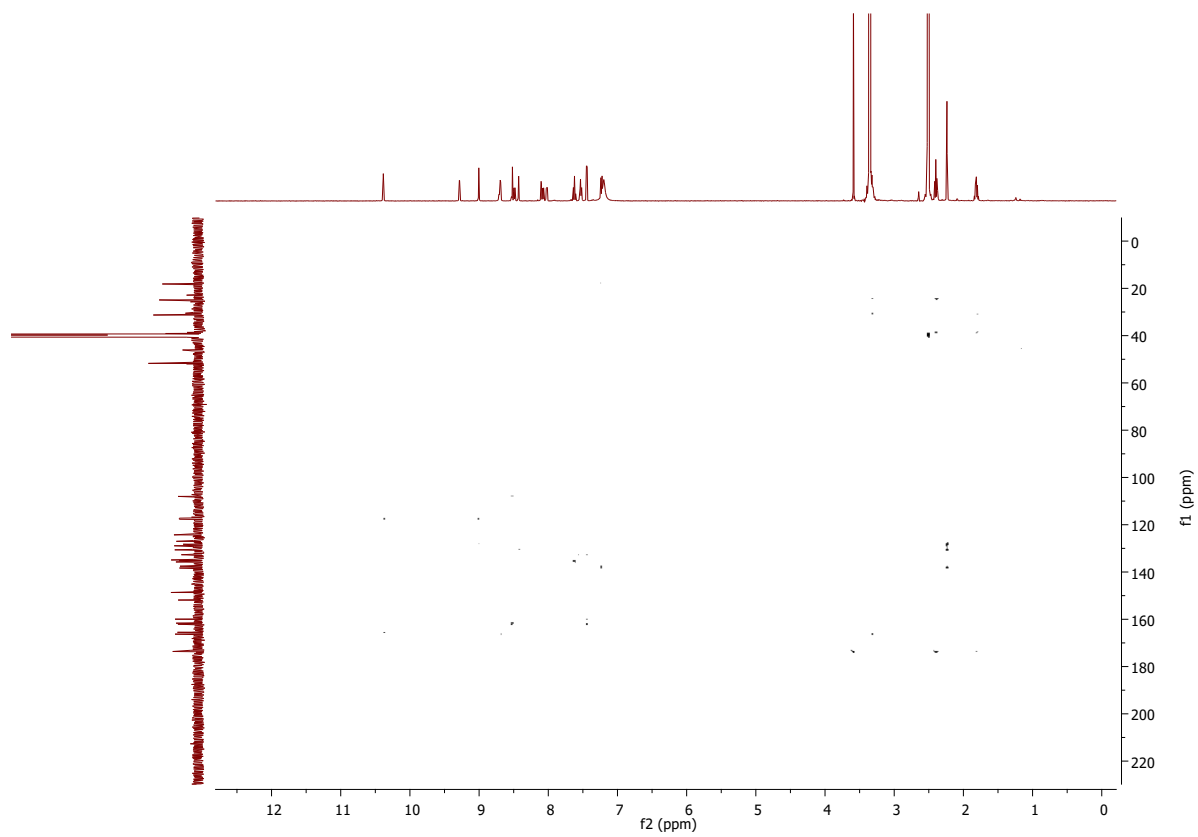


Fig. 3Se. HMBC of 4 in DMSO- d_6

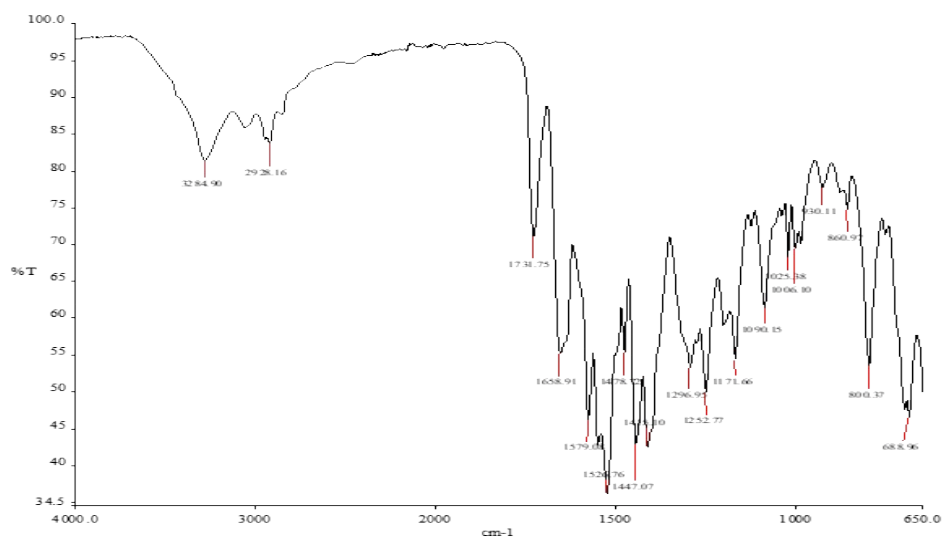


Fig. 3Sf. IR of 4

Figure: Extracted ion chromatogram (EIC) of compound.

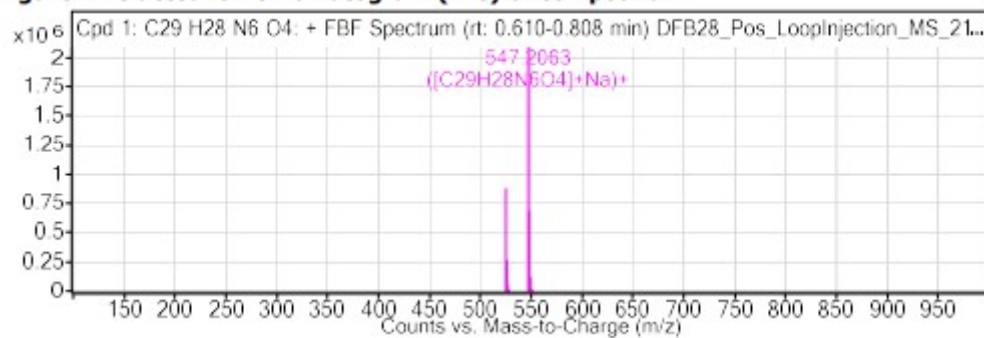


Fig. 3Sg. HRMS of 4

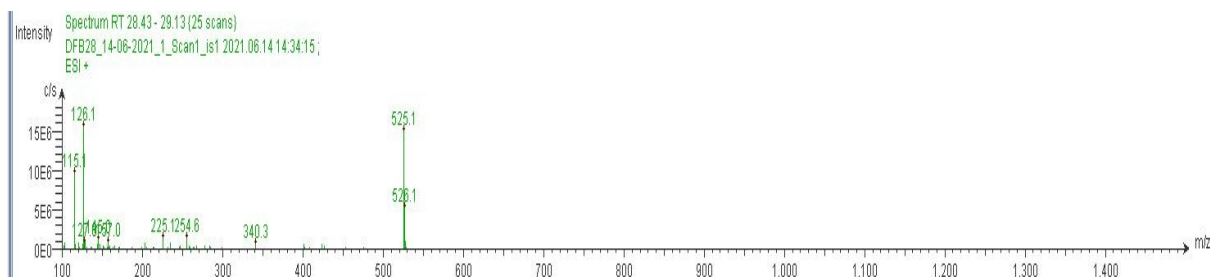
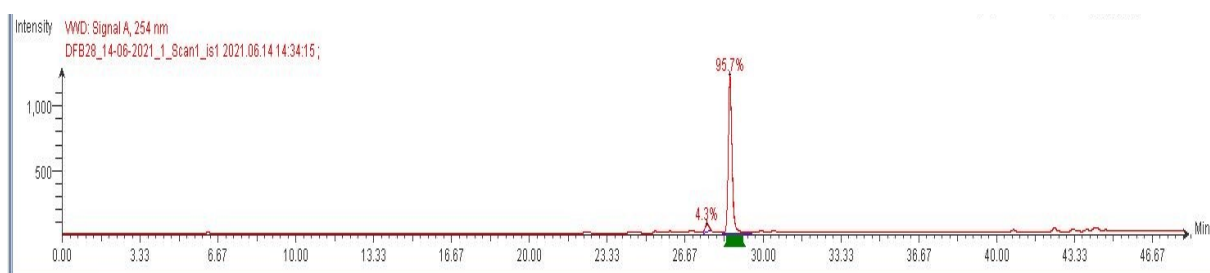


Fig. 3Sh. LCMS of 4

Compound 5

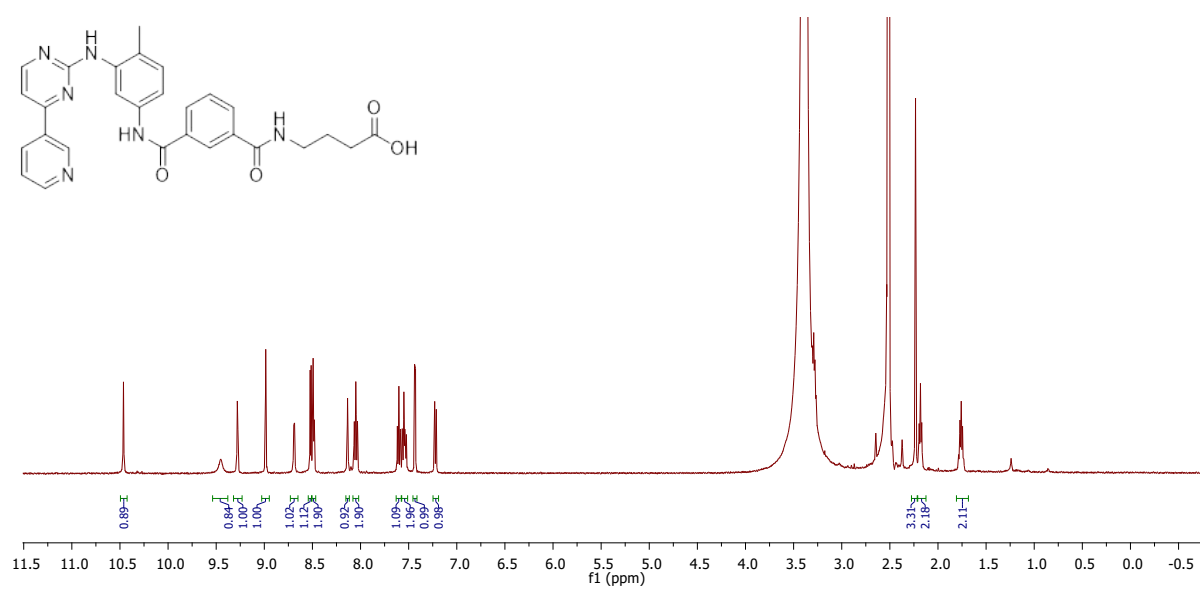


Fig. 4Sa. ¹H NMR of 5 in DMSO-*d*₆

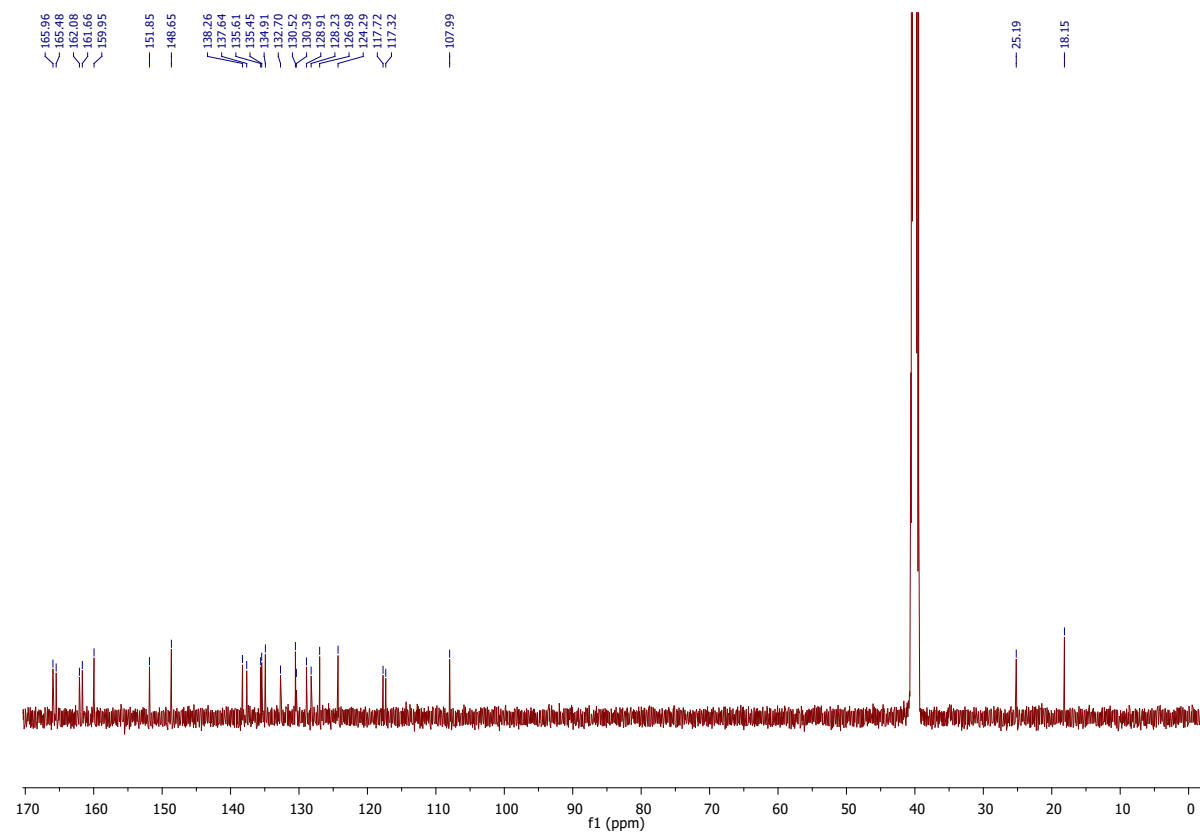


Fig. 4Sb. ¹³C NMR of 5 in DMSO-*d*₆

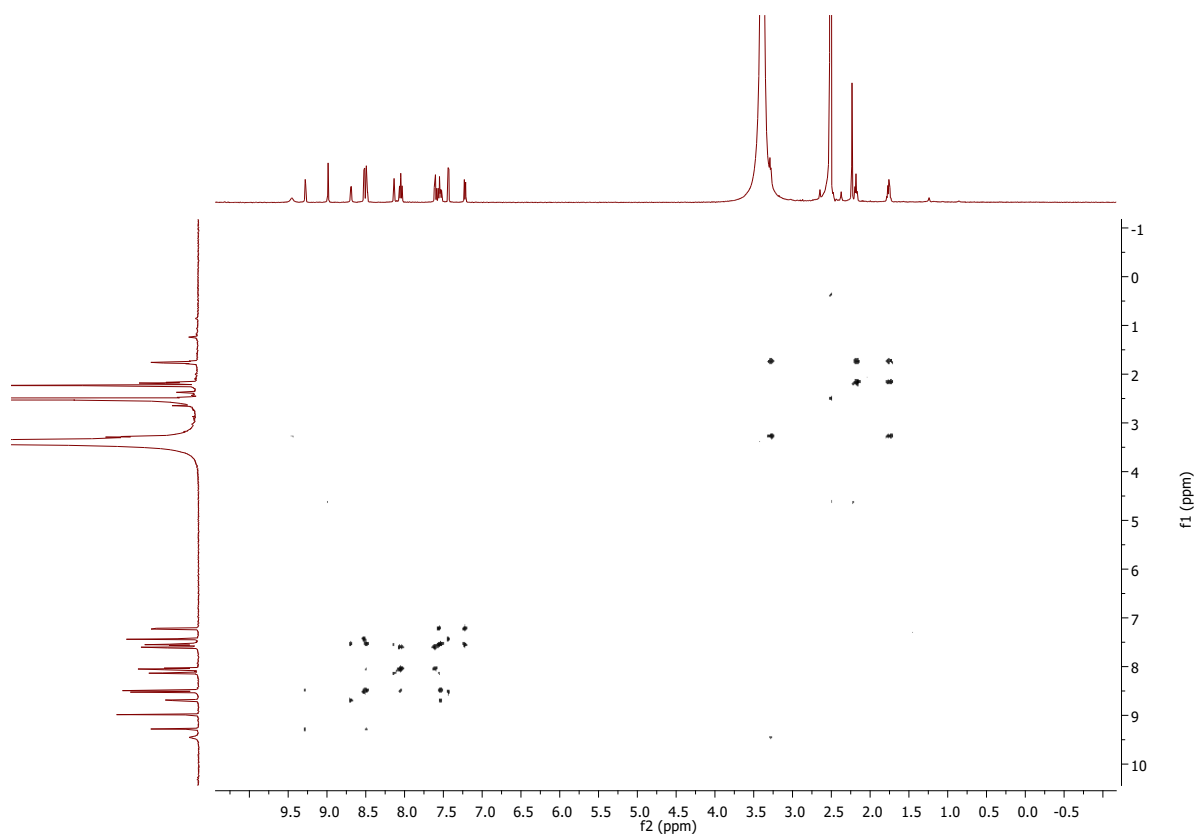


Fig. 4Sc. COSY of 5 in DMSO-*d*₆

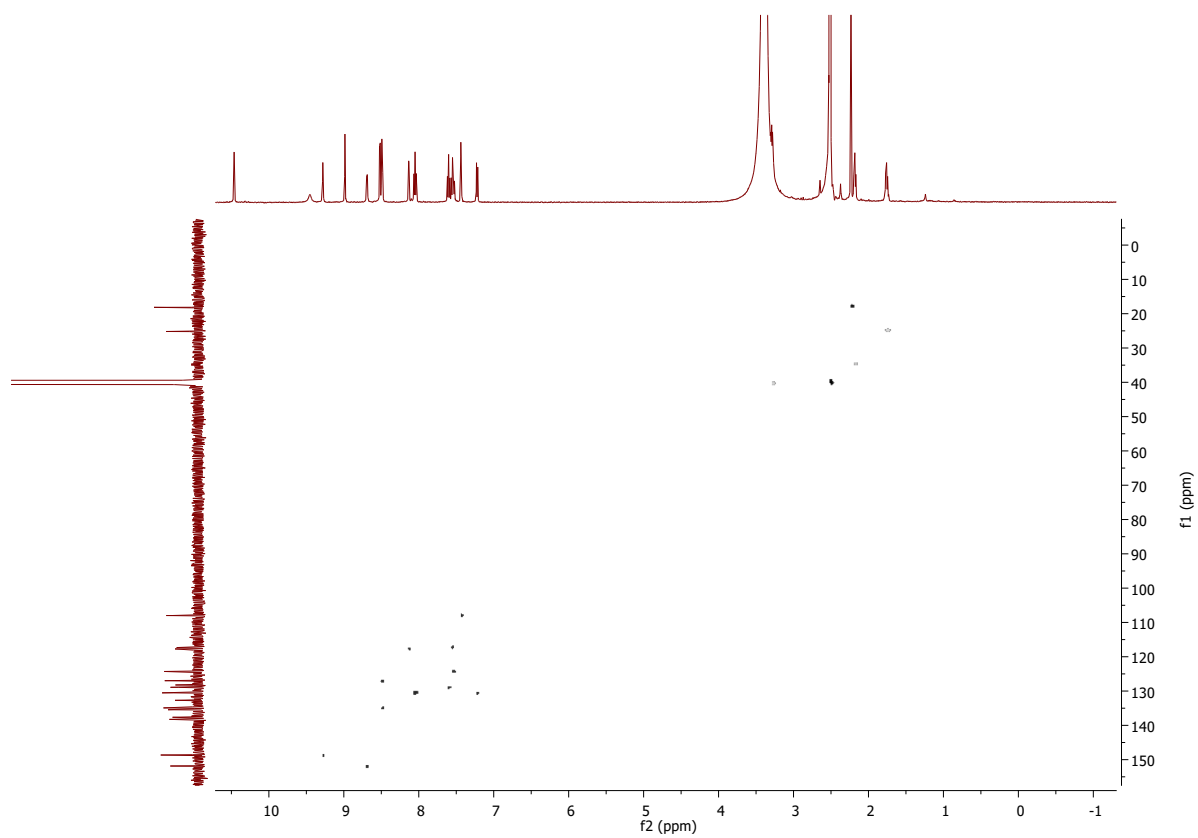


Fig. 4Sd. HSQC of 5 in DMSO- d_6

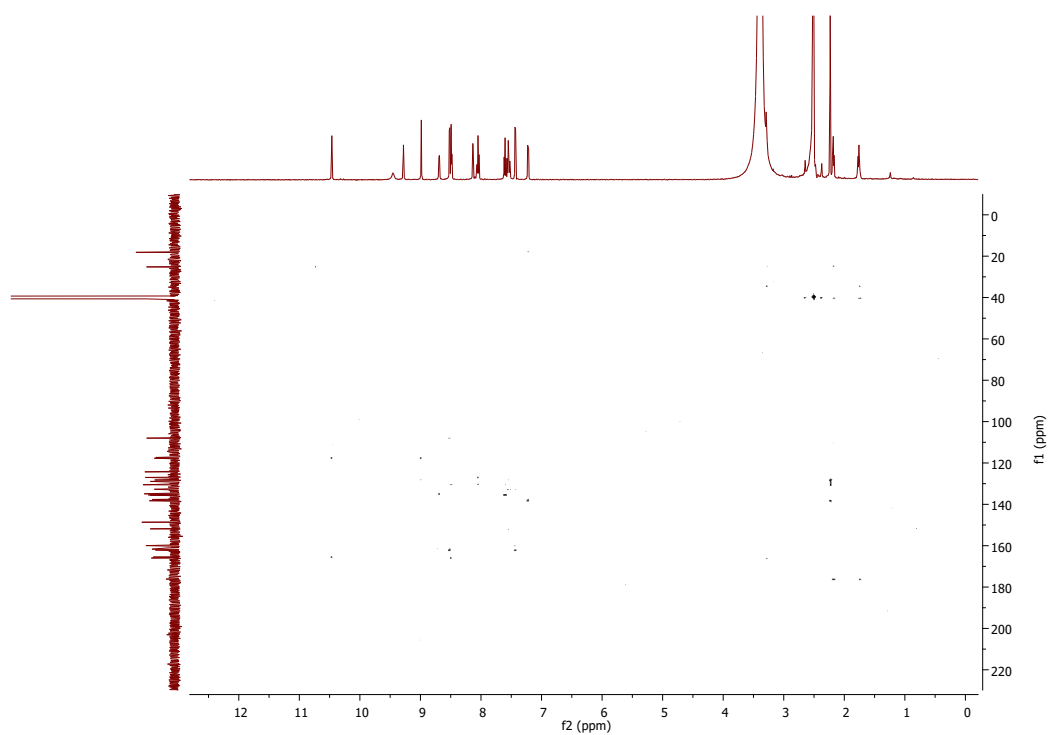


Fig. 4Se. HMBC of 5 in DMSO- d_6

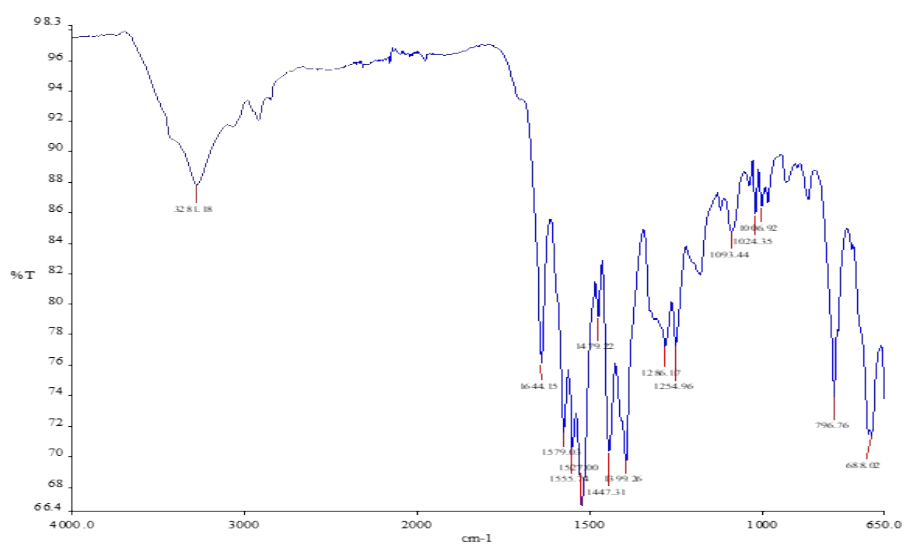


Fig. 4Sf. IR of 5

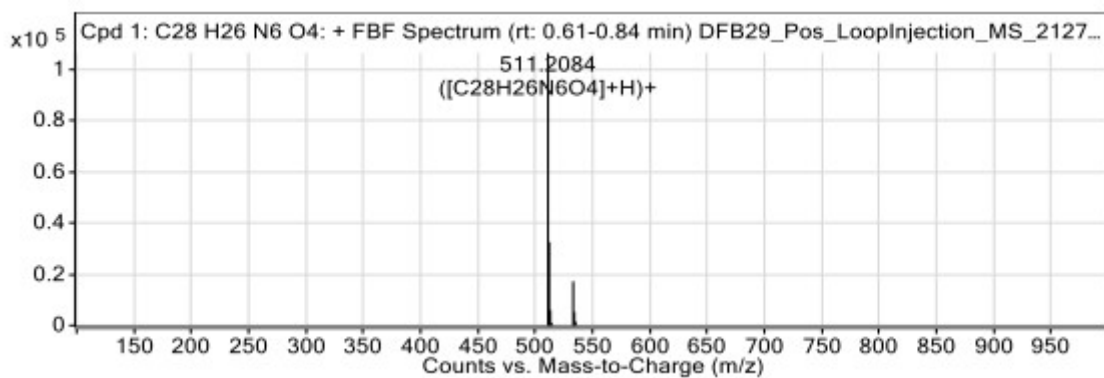


Fig. 4Sg. HRMS of 5

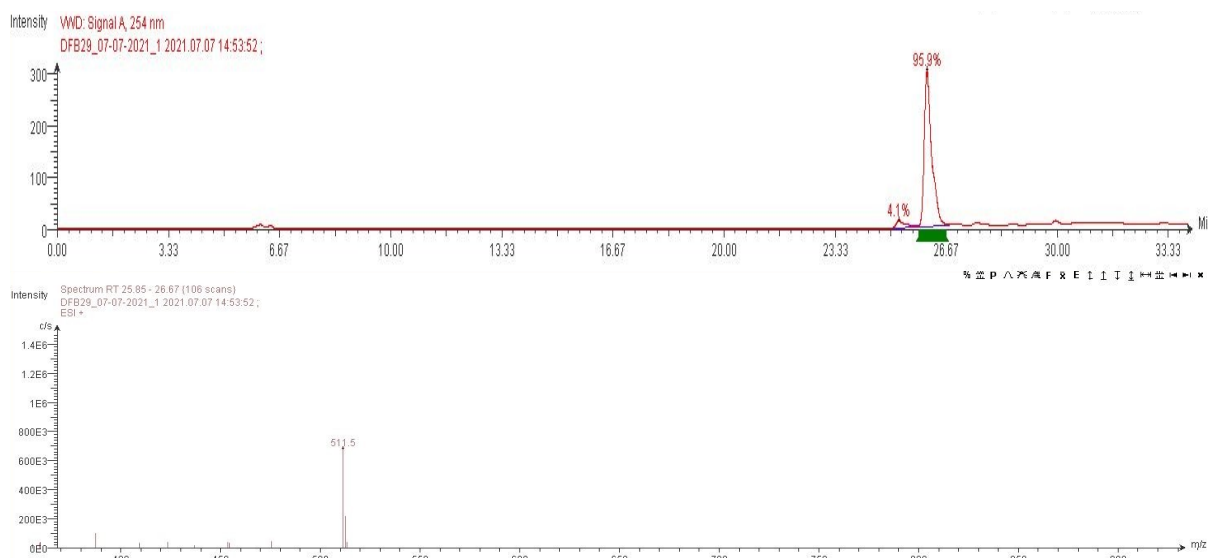


Fig. 4Sh. LCMS of 5

Compound 6

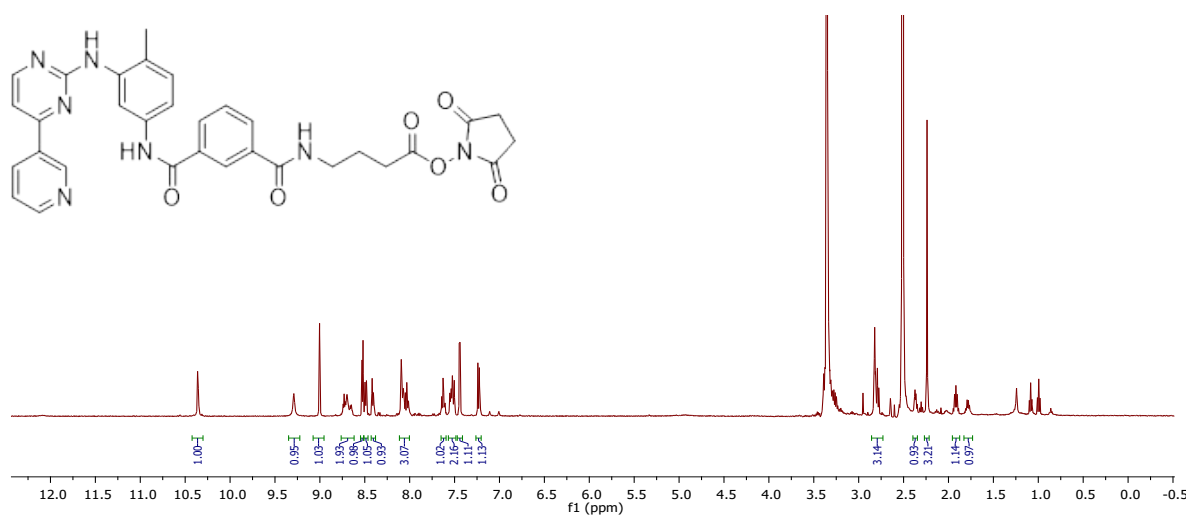


Fig. 5Sa. ^1H NMR of 6 in $\text{DMSO-}d_6$

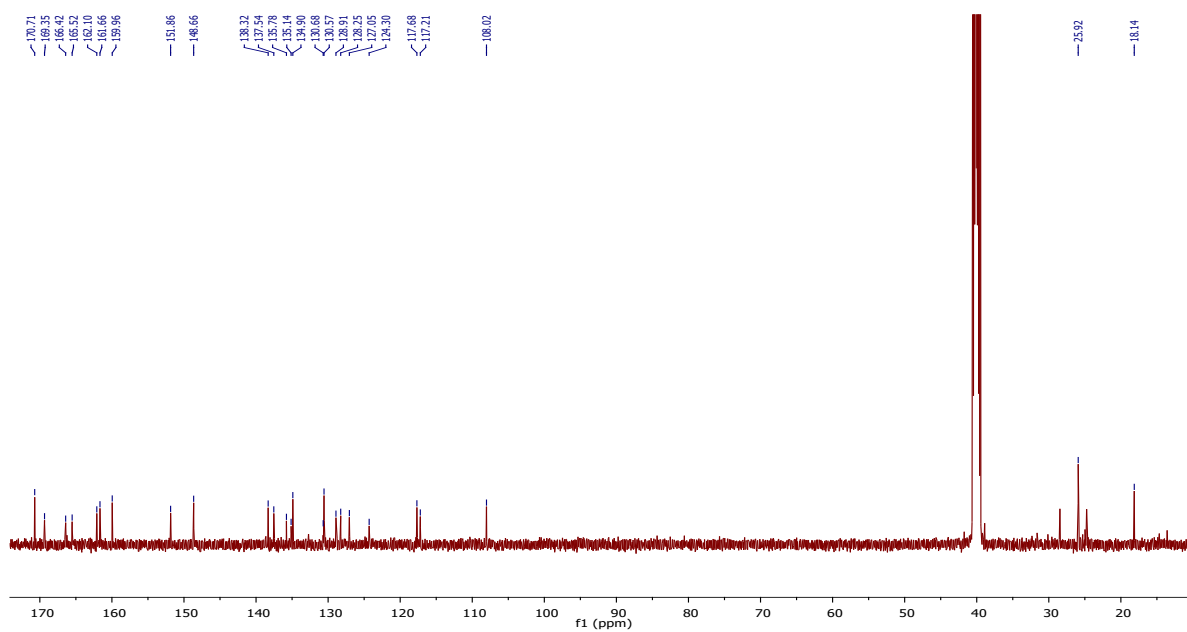


Fig. 5Sb. ^{13}C NMR of **6** in $\text{DMSO-}d_6$

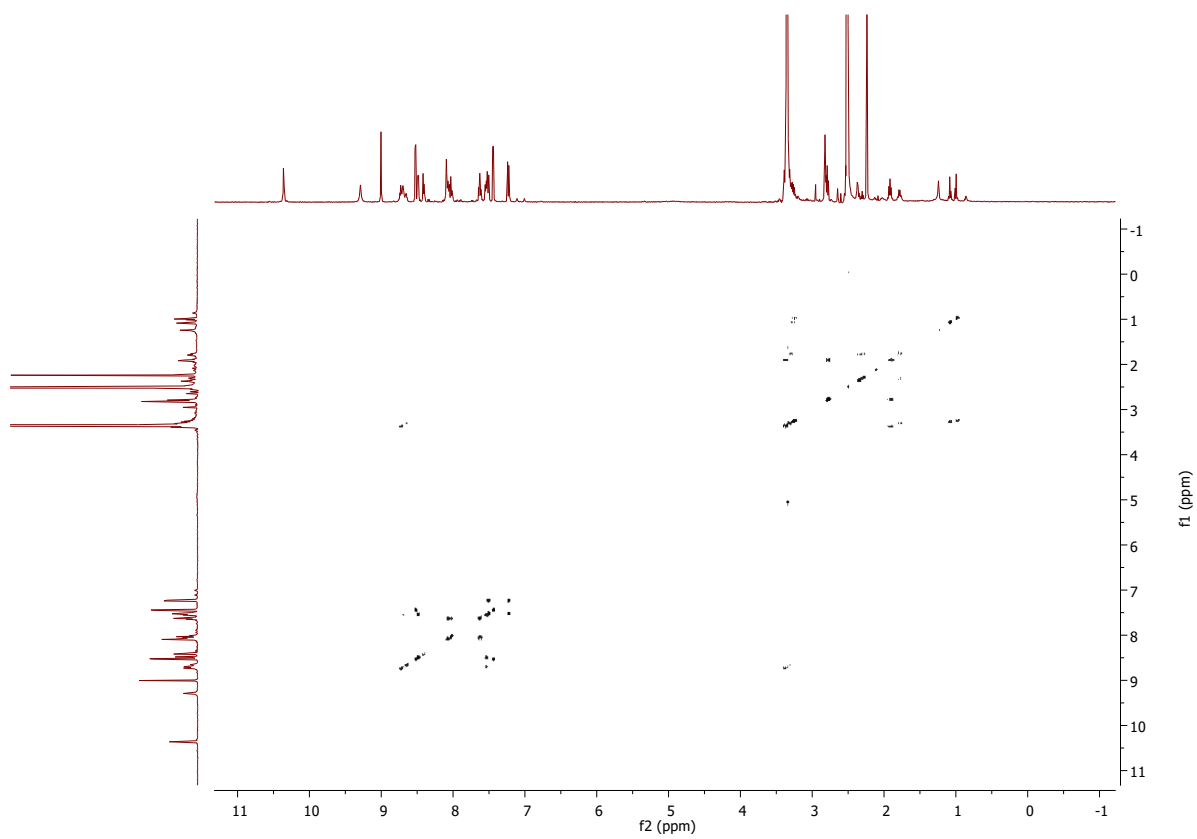


Fig. 5Sc. COSY of **6** in $\text{DMSO-}d_6$

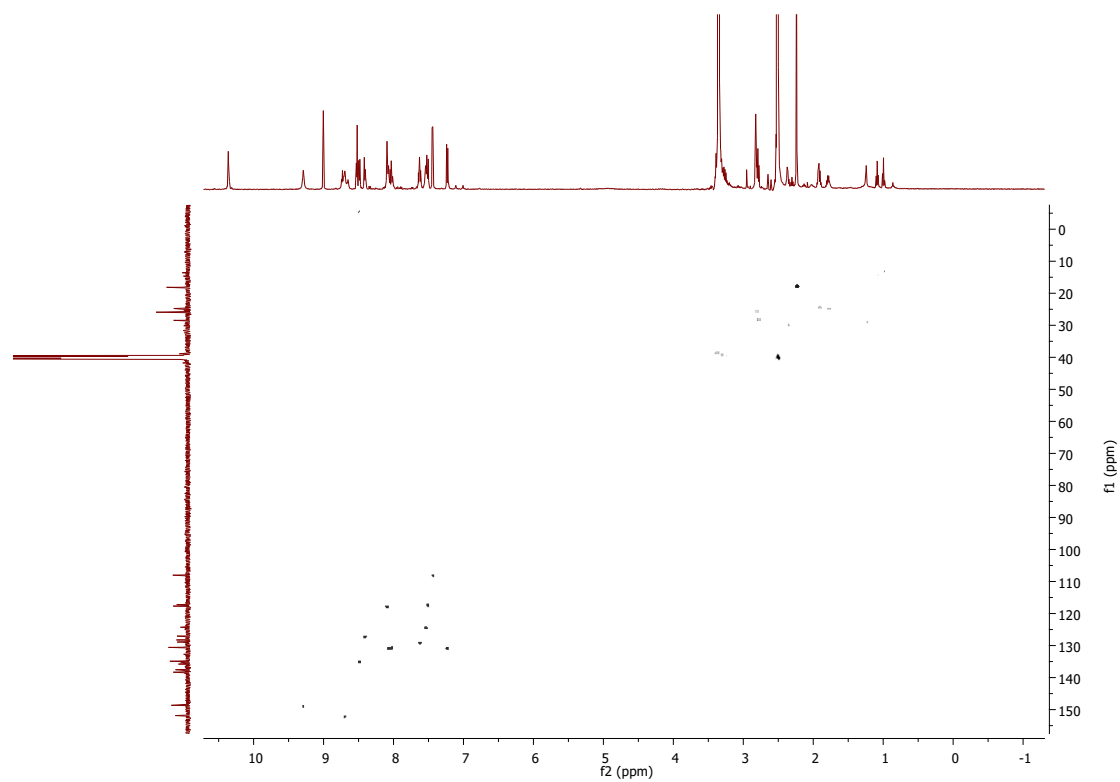


Fig. 5Sd. HSQC of **6** in DMSO- d_6

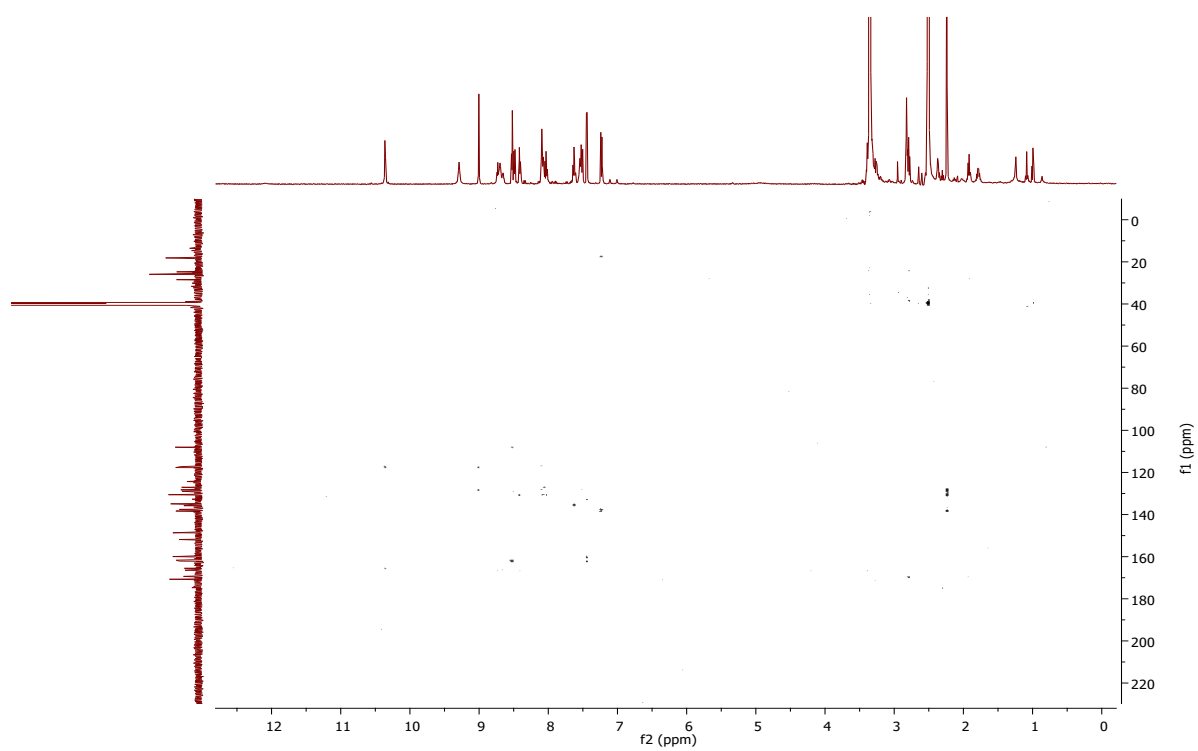


Fig. 5Se. HMBC of **6** in DMSO- d_6

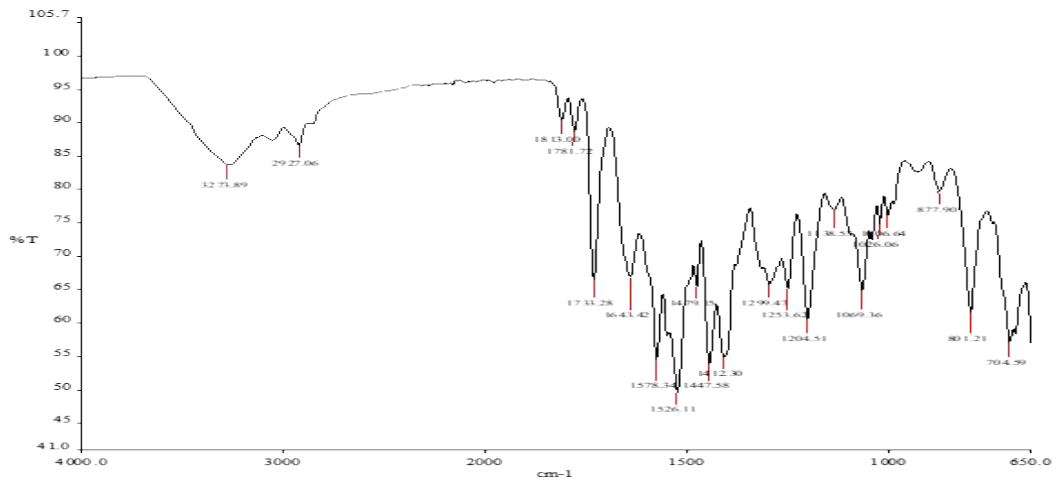


Fig. 5Sf. IR of 6

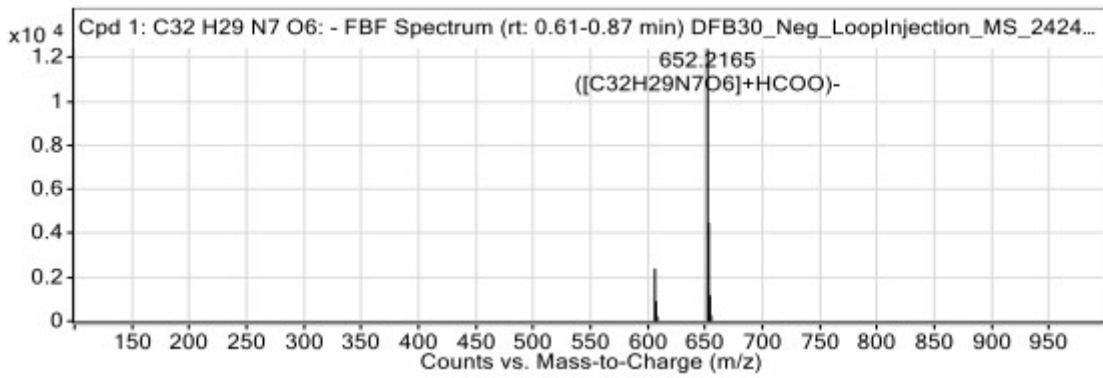


Fig. 5Sg. HRMS of 6

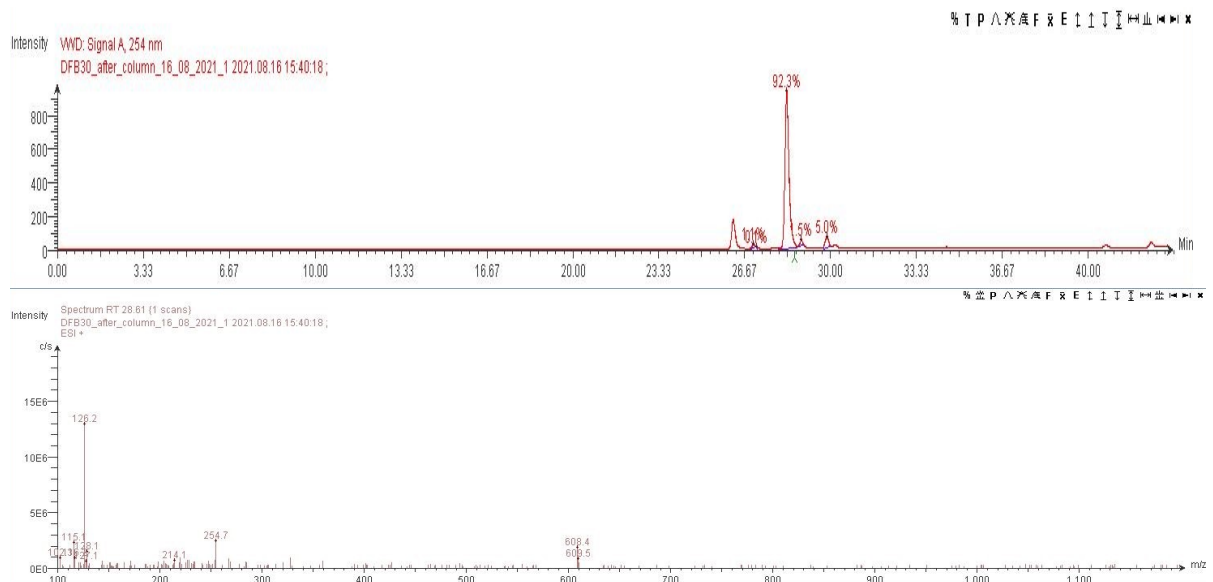


Fig. 5Sh. LCMS of 6

Complex A

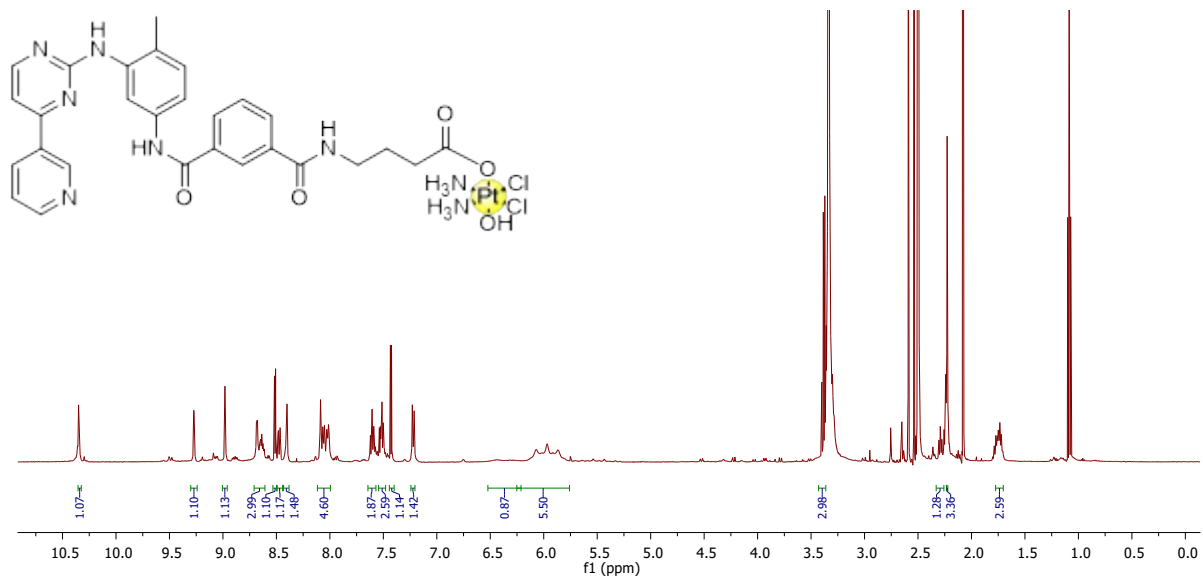


Fig. 6Sa. ^1H NMR of **A** in $\text{DMSO}-d_6$

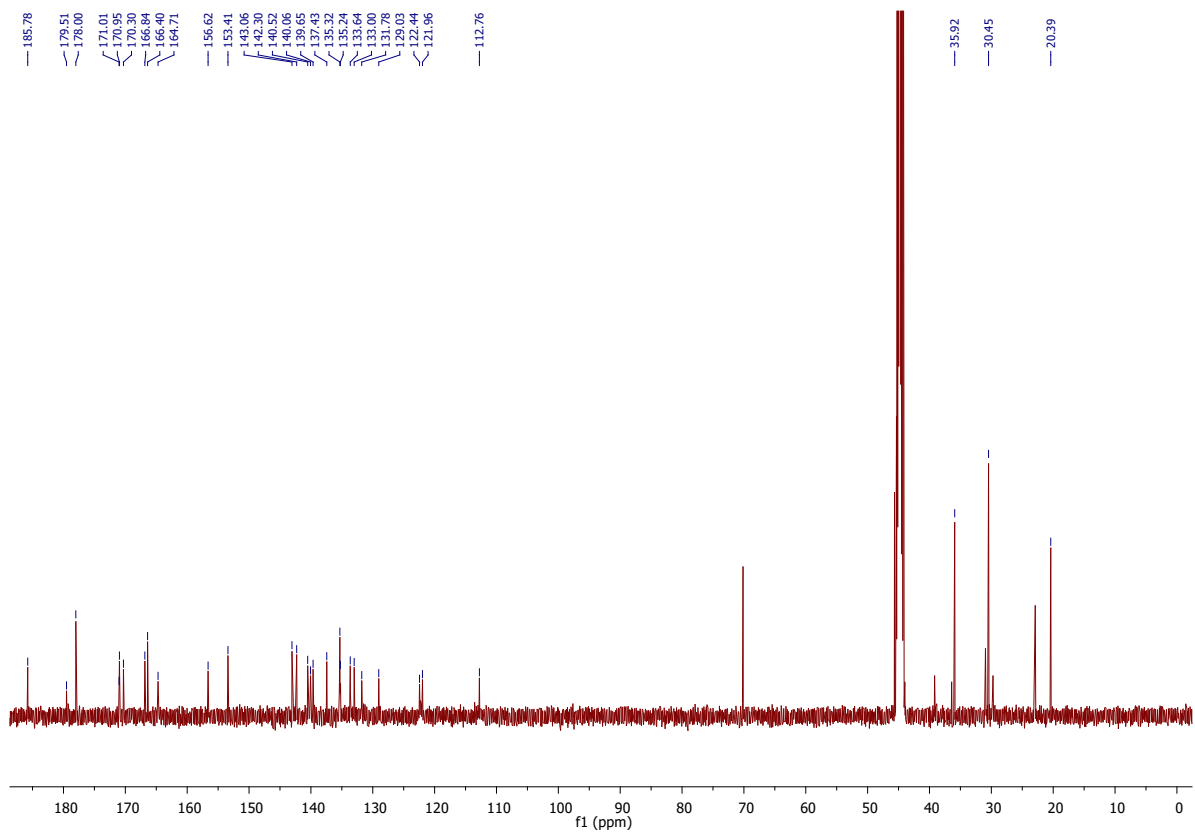


Fig. 6Sb. ^{13}C NMR of **A** in $\text{DMSO}-d_6$

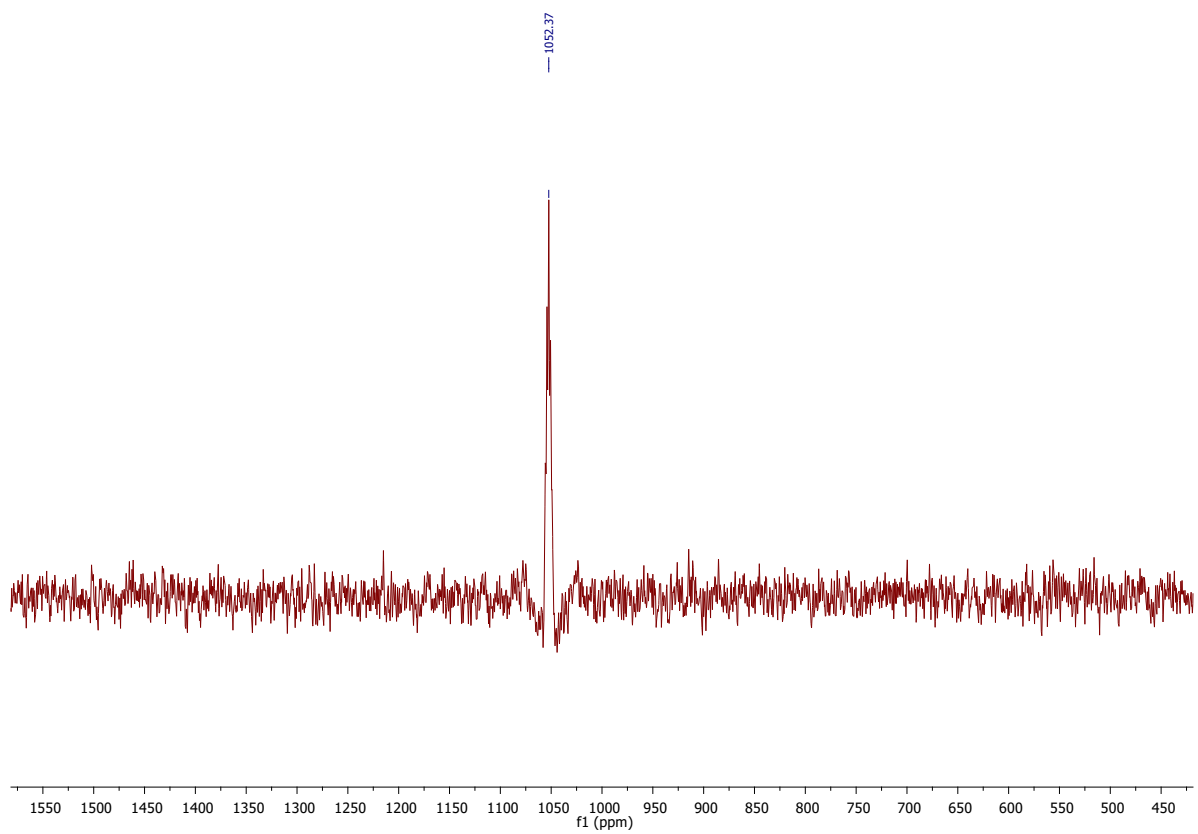


Fig. 6Sc. ^{195}Pt NMR of **A** in $\text{DMSO-}d_6$

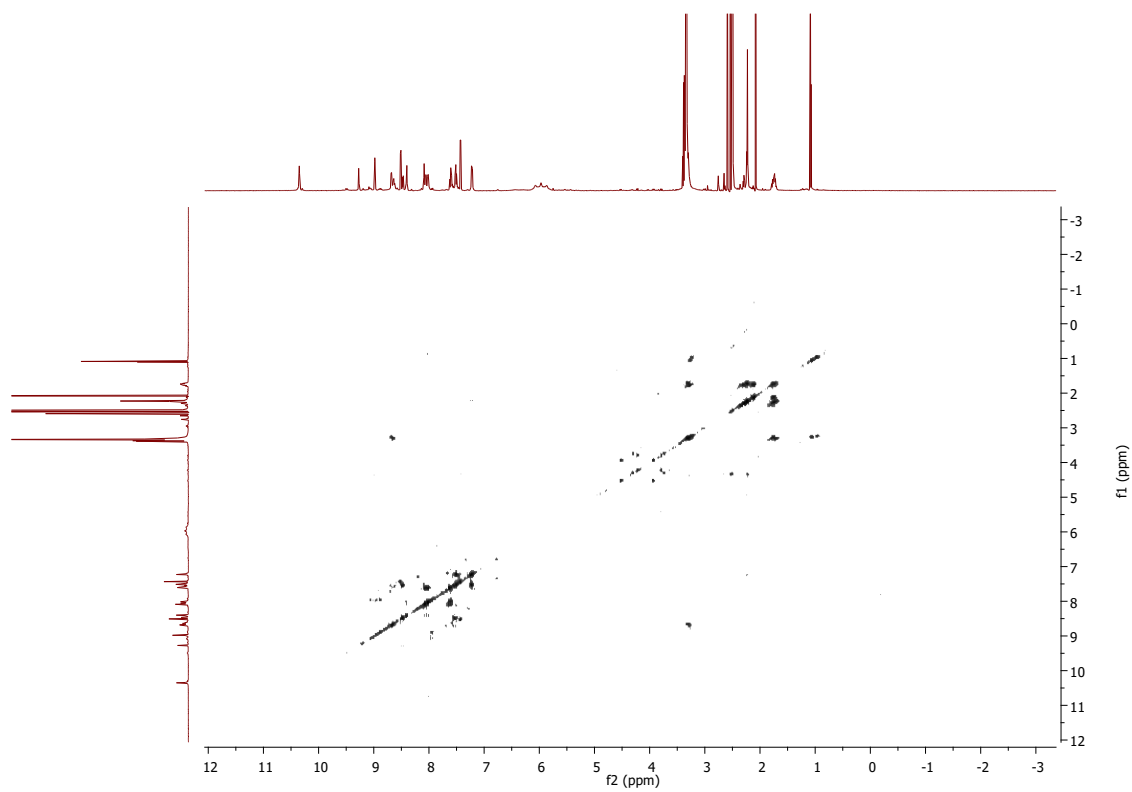


Fig. 6Se. COSY of **A** in $\text{DMSO-}d_6$

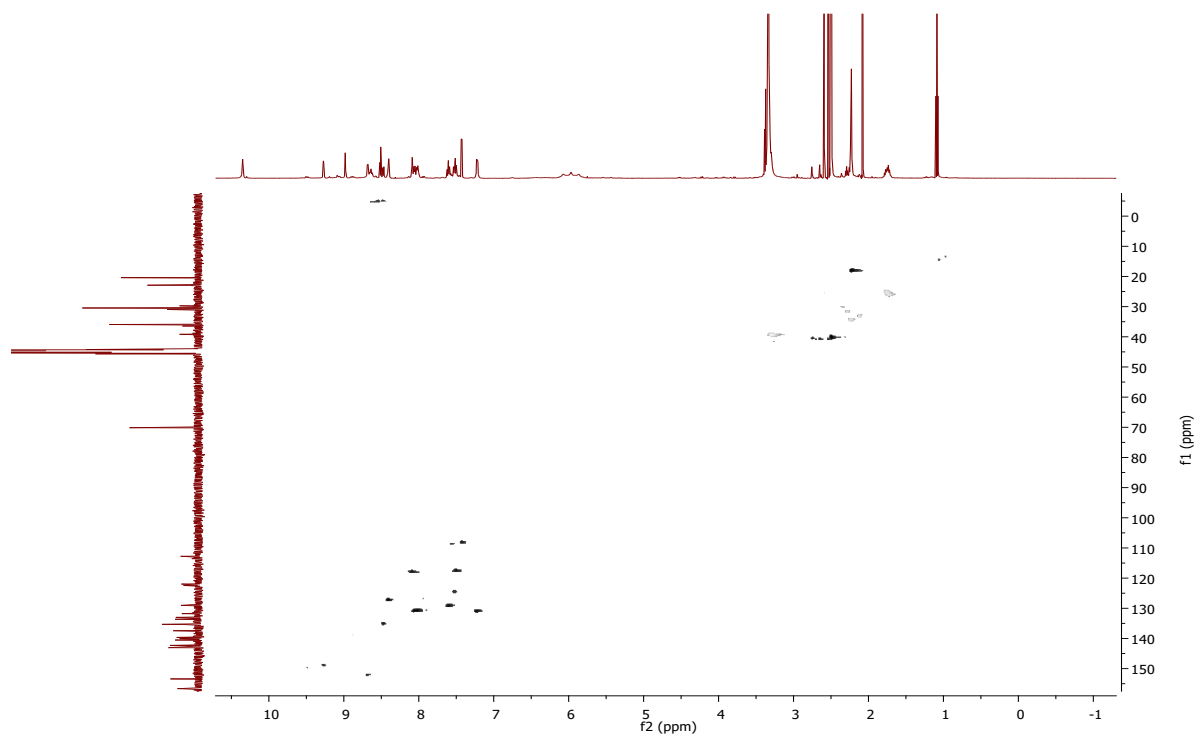


Fig. 6Sf. HSQC of **A** in DMSO- d_6

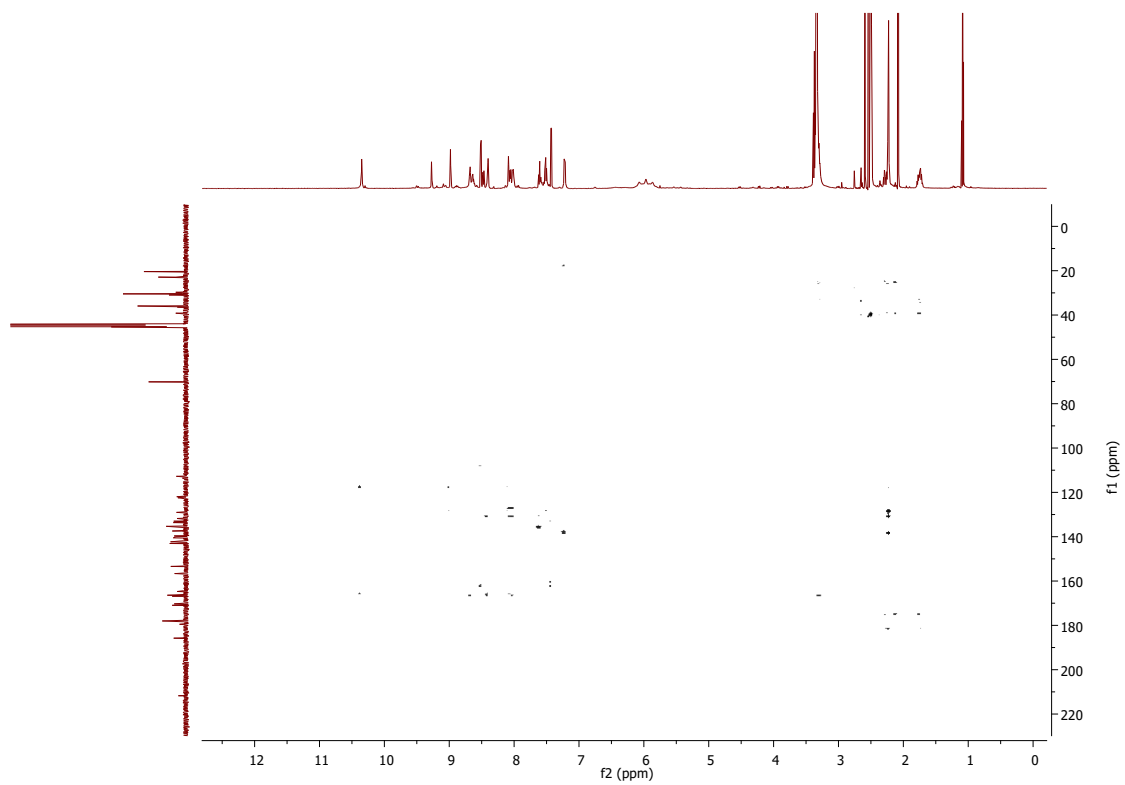


Fig. 6Sg. HMBC of **A** in DMSO- d_6

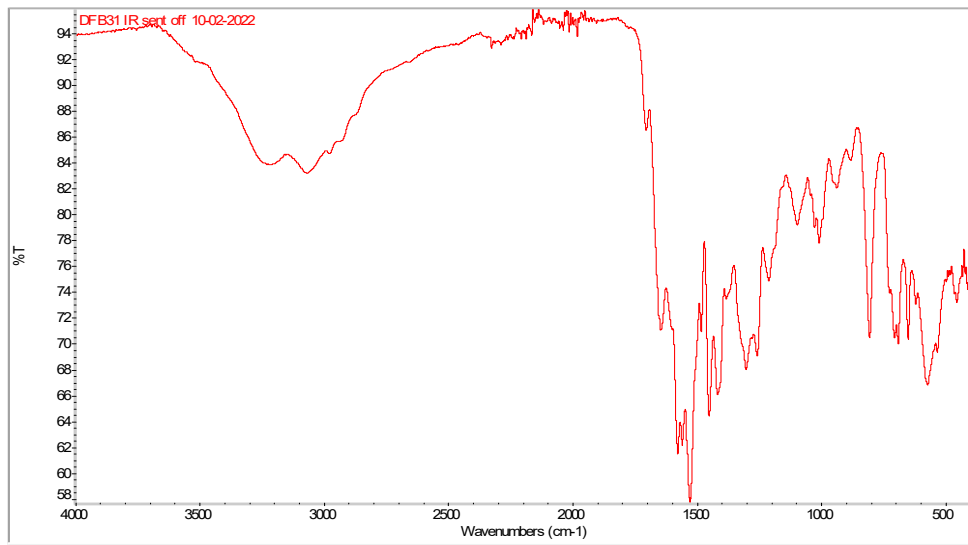


Fig. 6Sh. IR of A

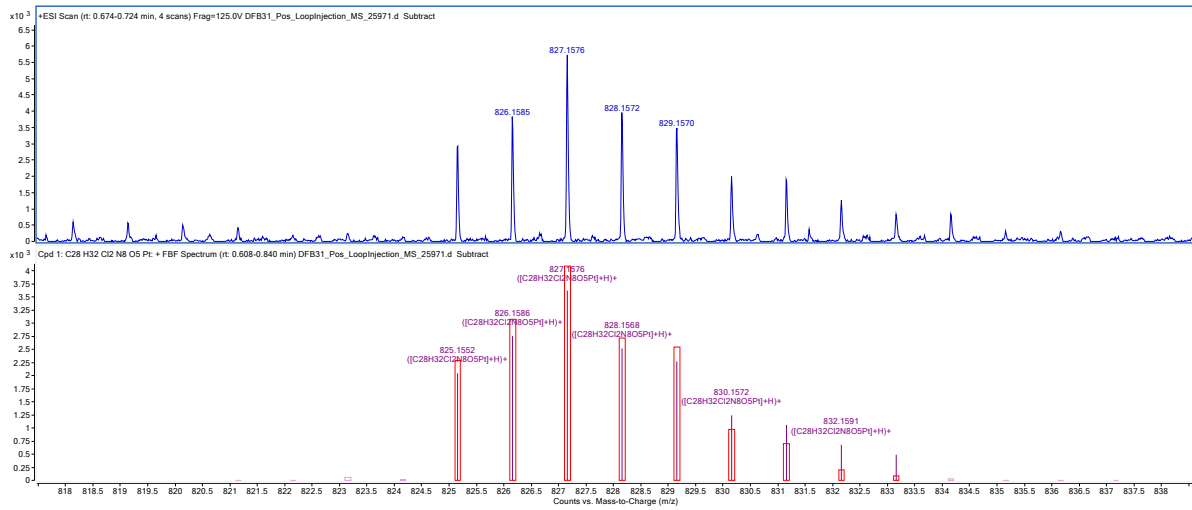


Fig. 6Si. HRMS of A

Compound 9

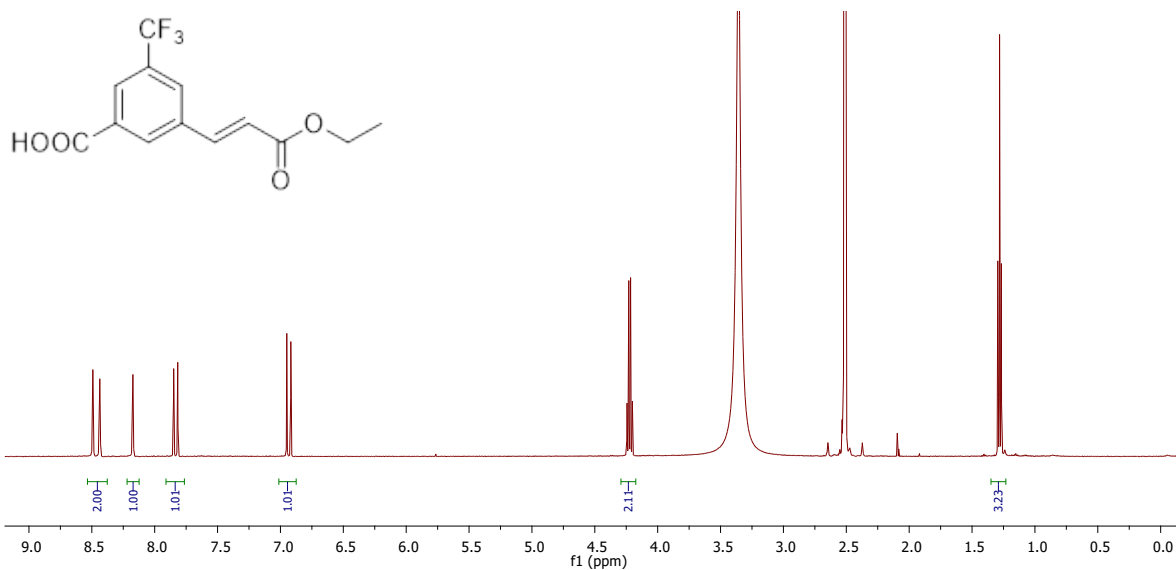


Fig. 7Sa. ¹H NMR of 9 in DMSO-d₆

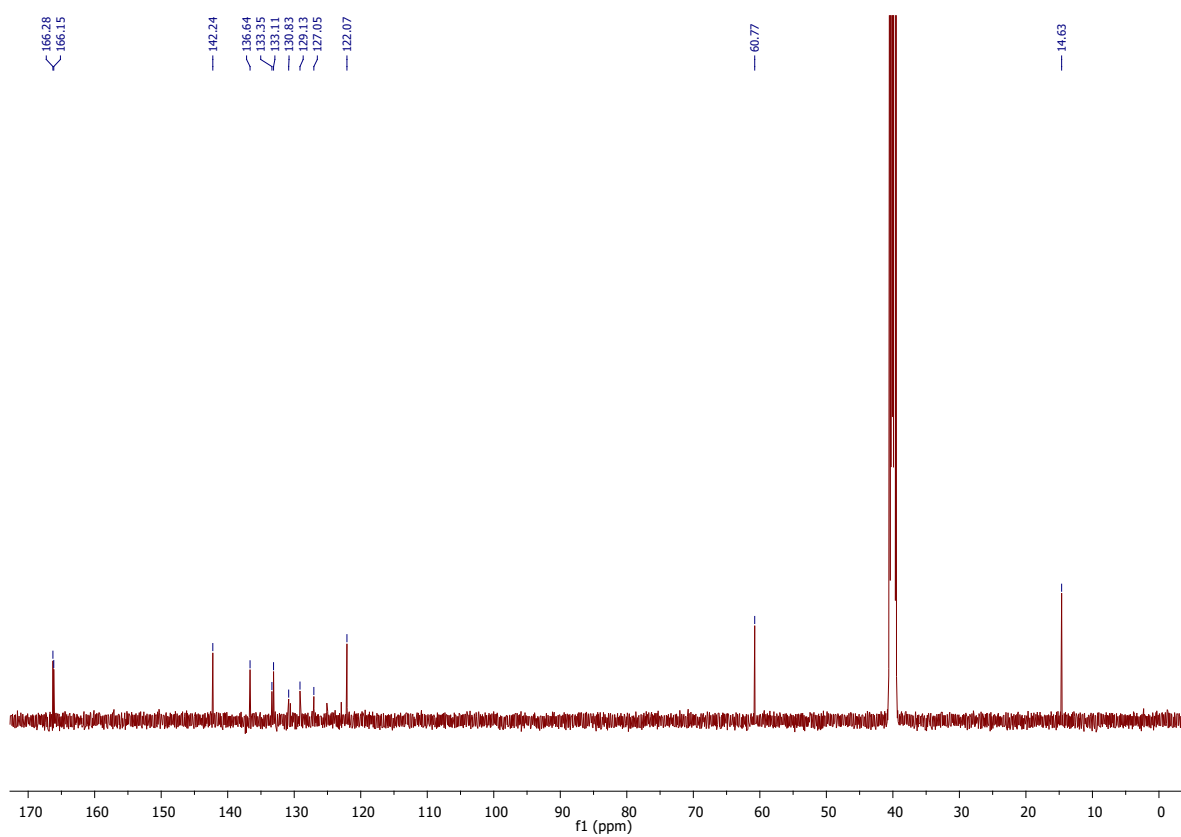


Fig. 7Sb. ¹³C NMR of 9 in DMSO-d₆

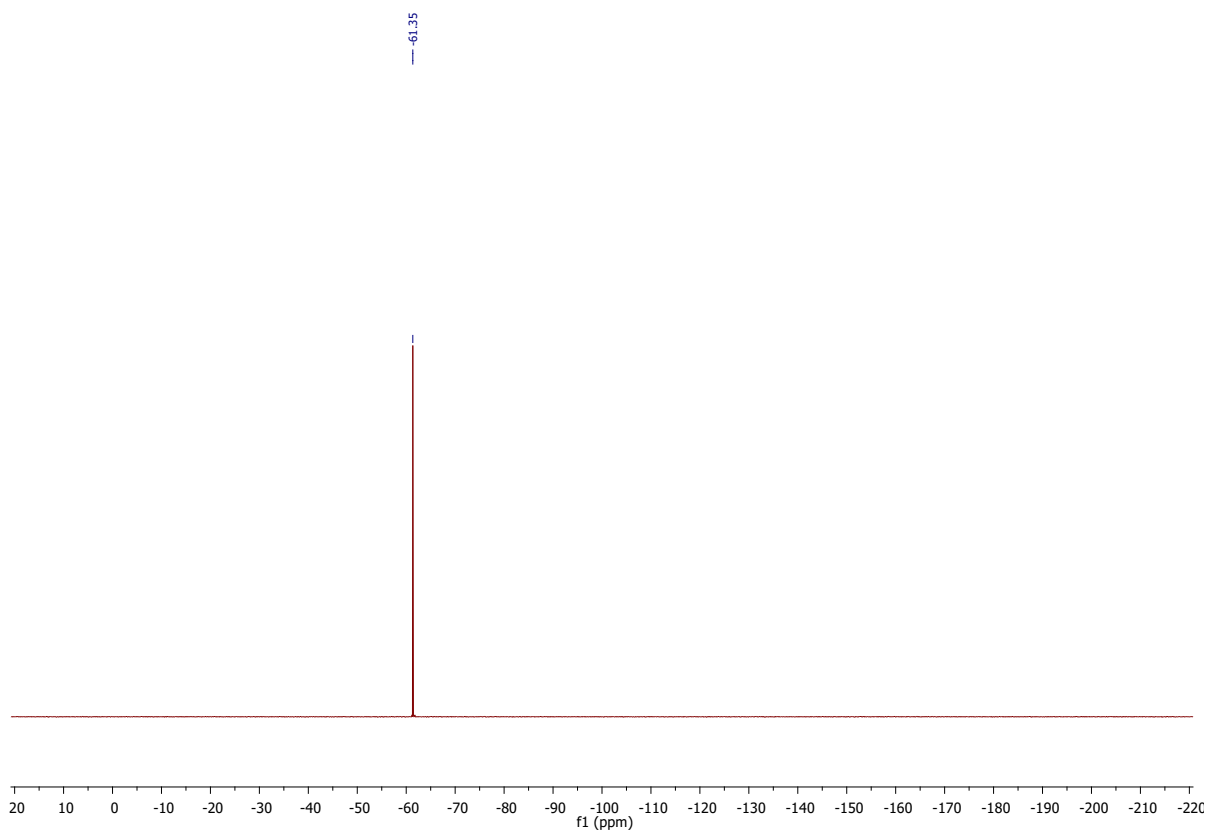


Fig. 7Sc. ¹⁹F NMR of 9 in DMSO-d₆

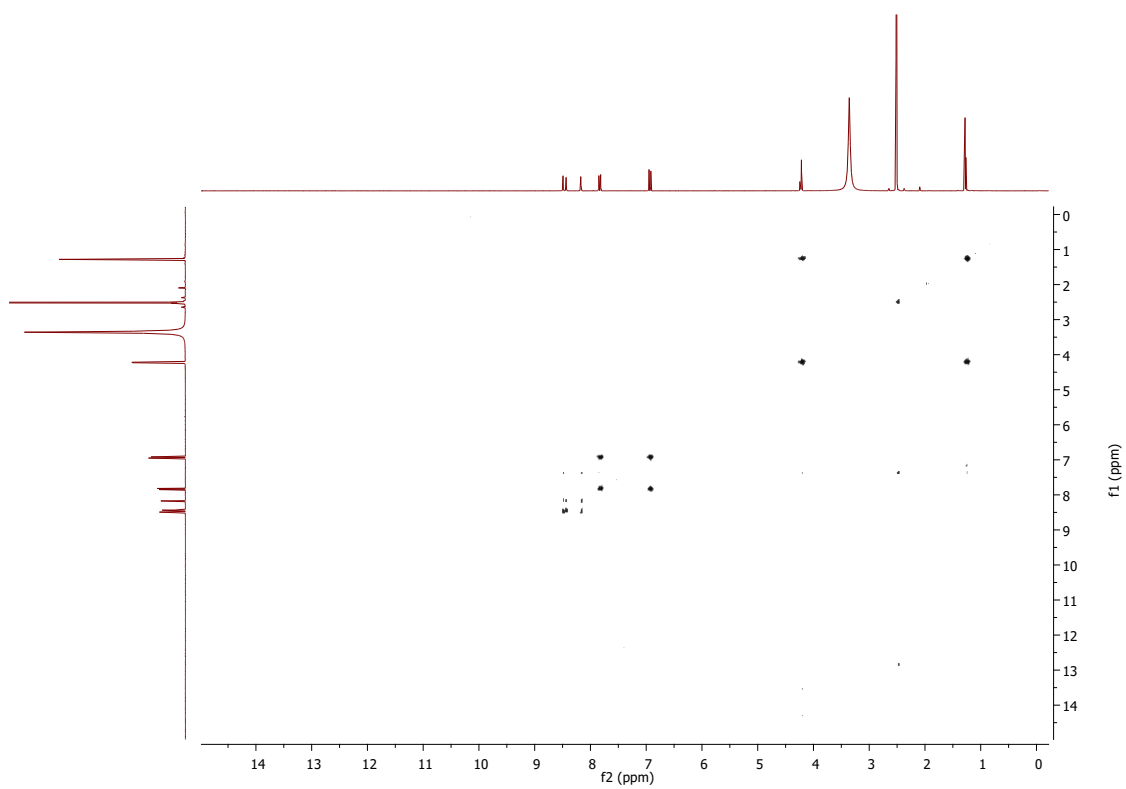


Fig. 7Sd. COSY of 9 in DMSO-d₆

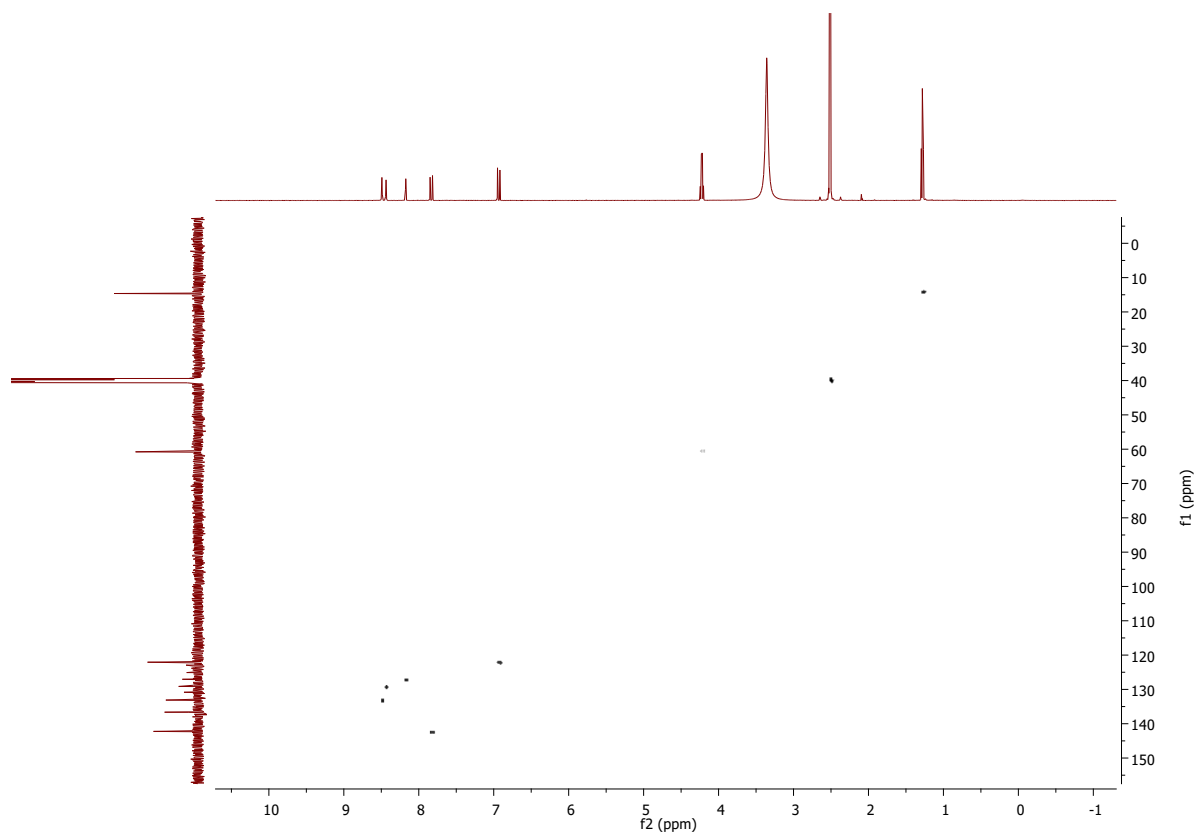


Fig. 7Se. HSQC of 9 in DMSO- d_6

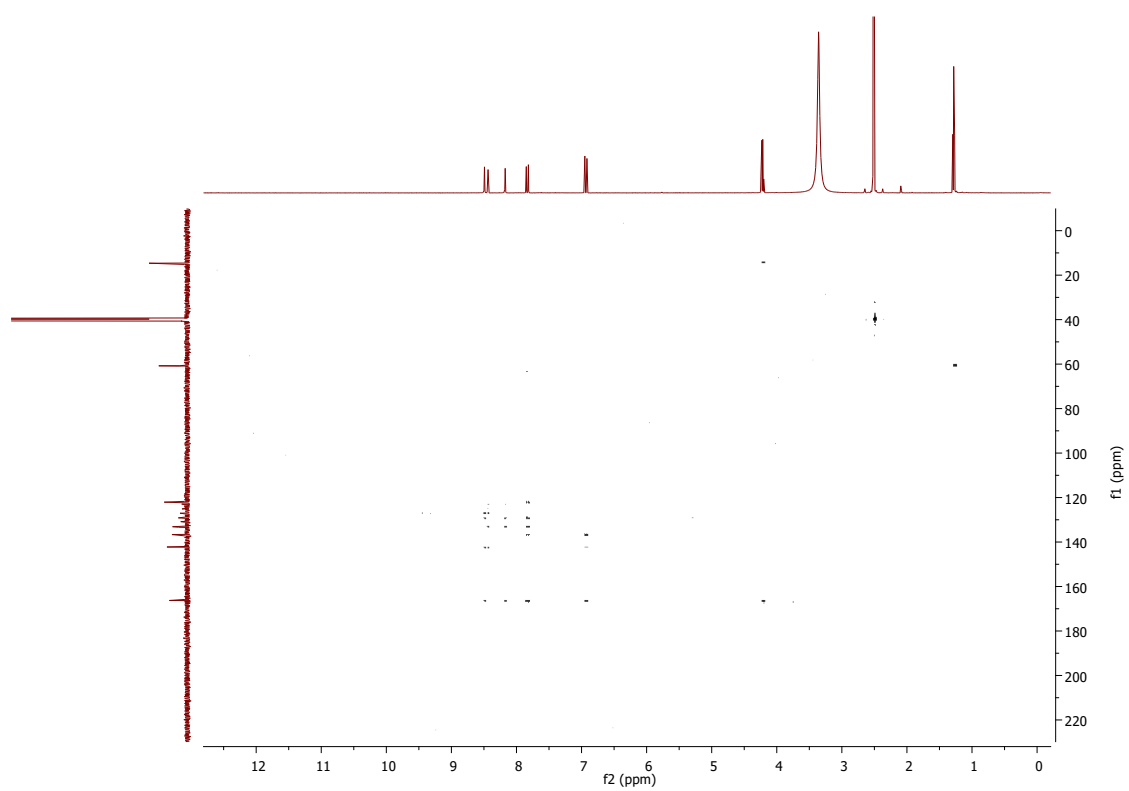


Fig. 7Sf. HMBC of 9 in DMSO- d_6

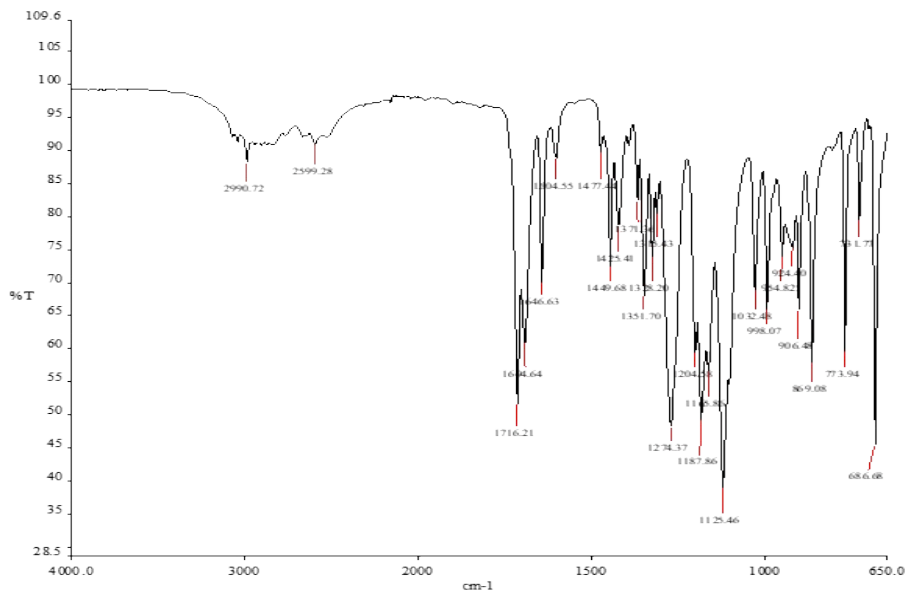


Fig. 7Sg. IR of 9

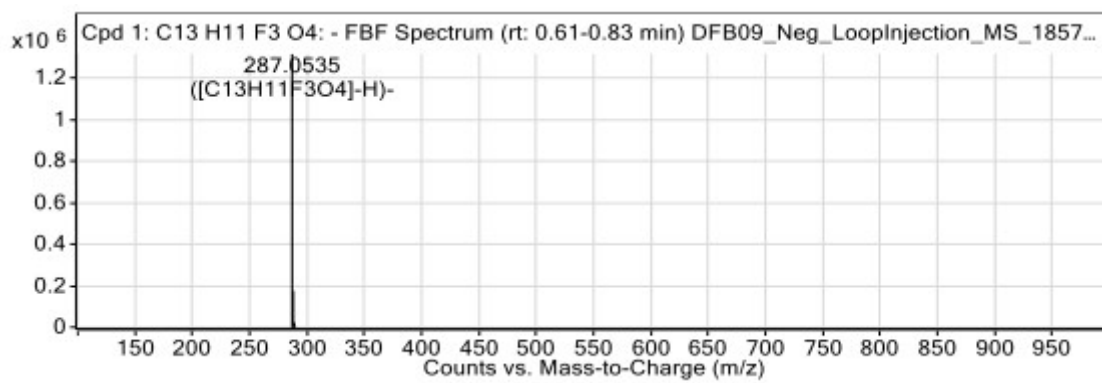


Fig. 7Sh. HRMS of 9

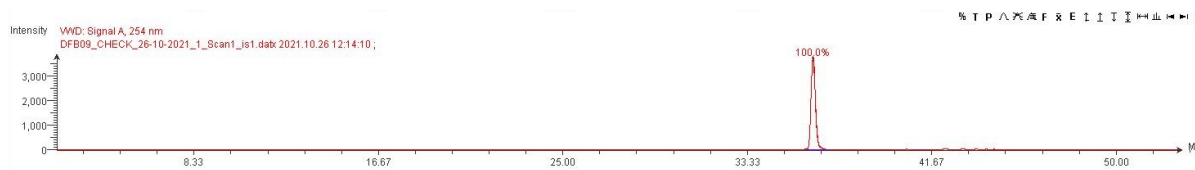


Fig. 7Si. LCMS of 9

Compound 10

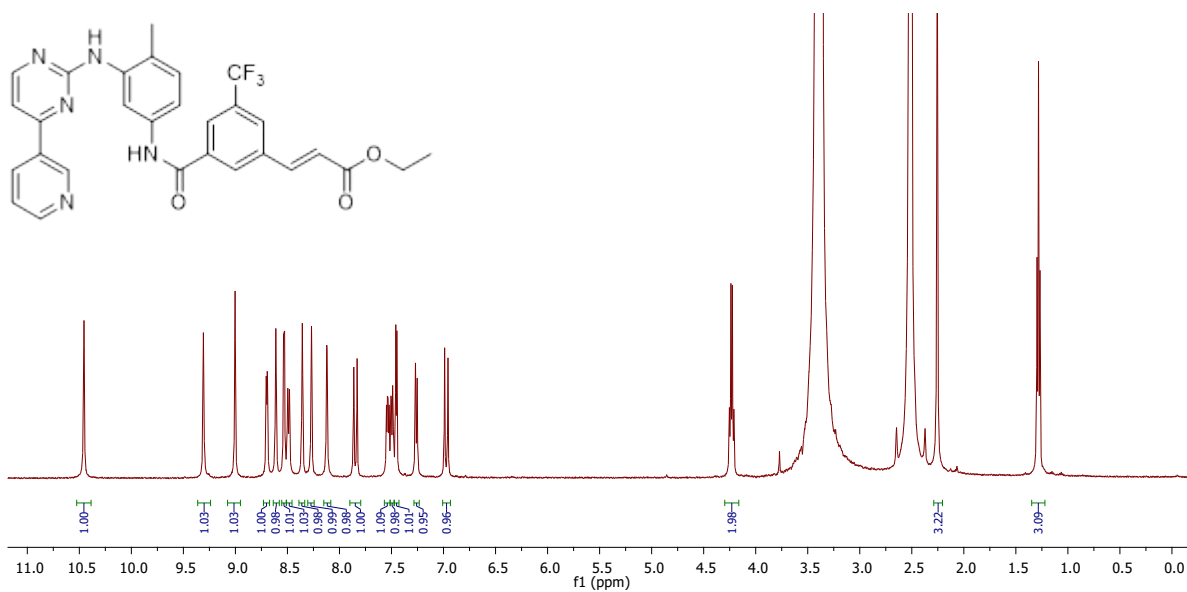


Fig. 8Sa. ¹H NMR of **10** in DMSO-*d*₆

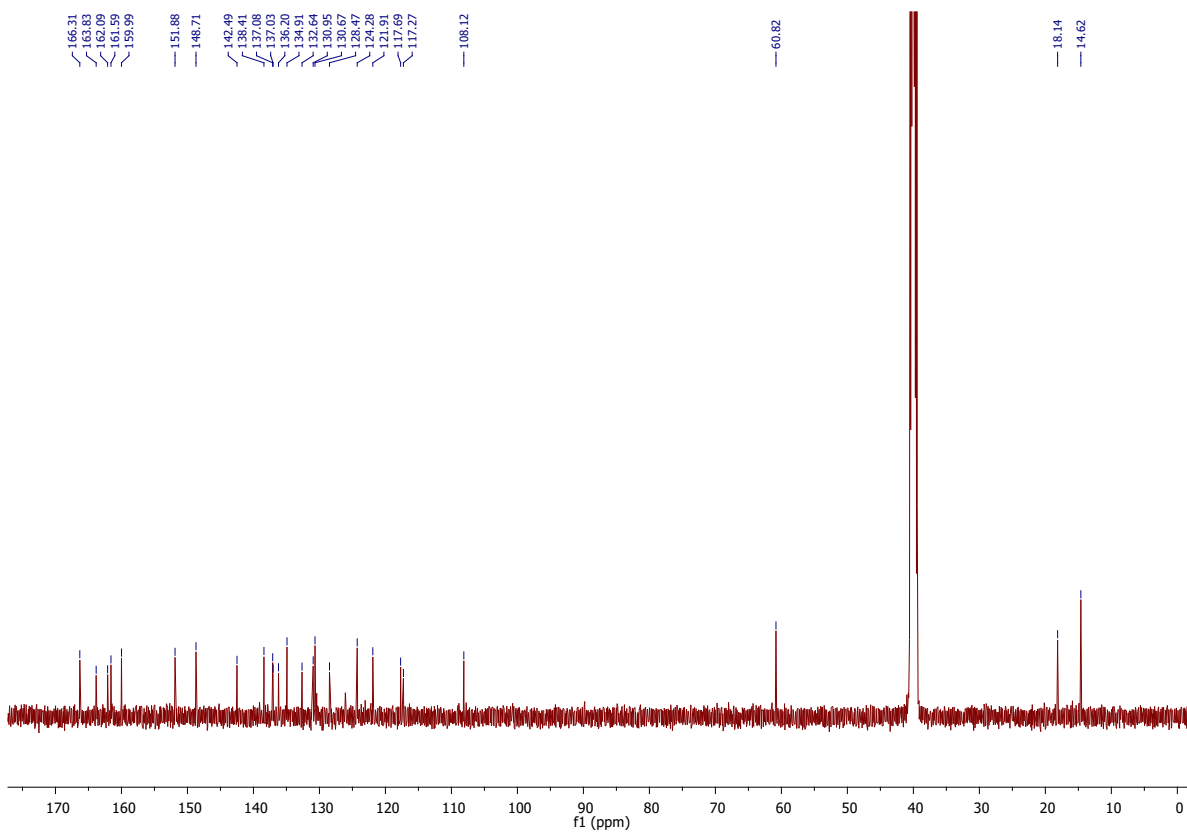


Fig. 8Sb. ¹³C NMR of **10** in DMSO-*d*₆

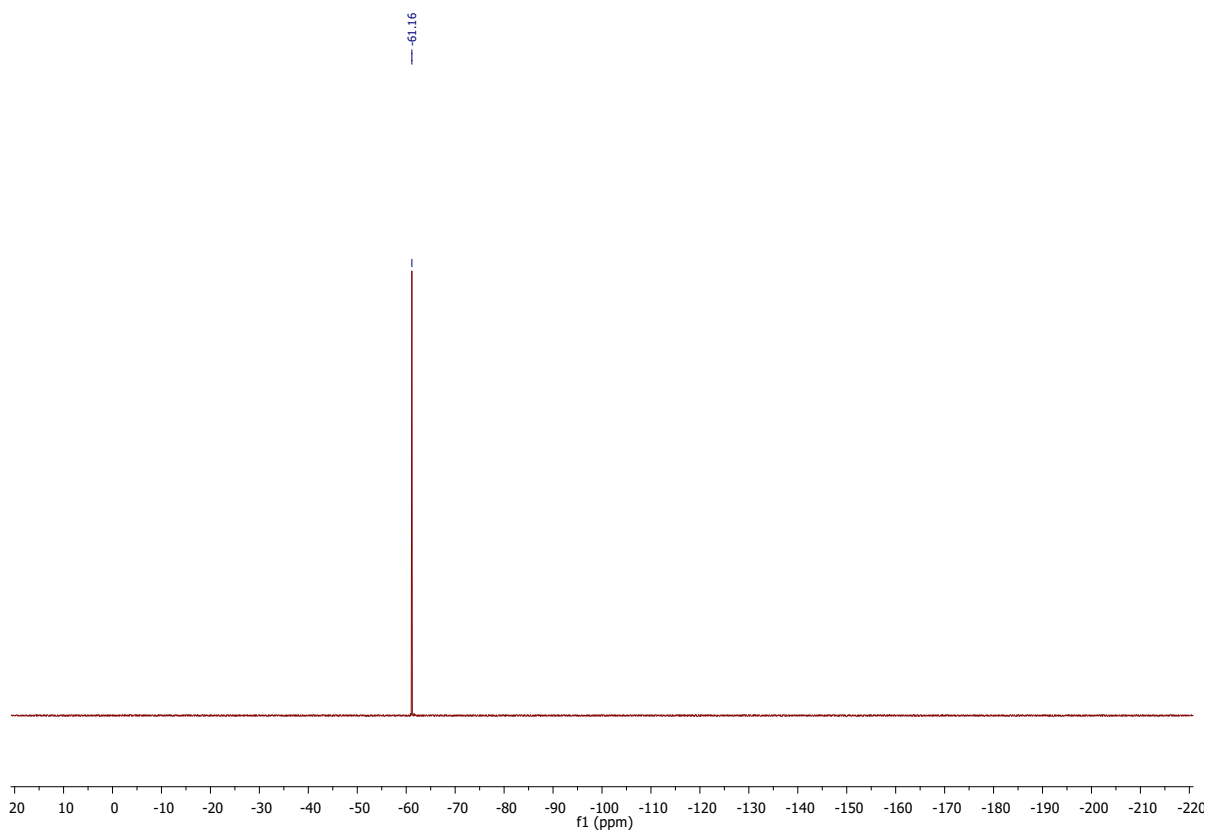


Fig. 8Sc. ^{19}F NMR of **10** in $\text{DMSO-}d_6$

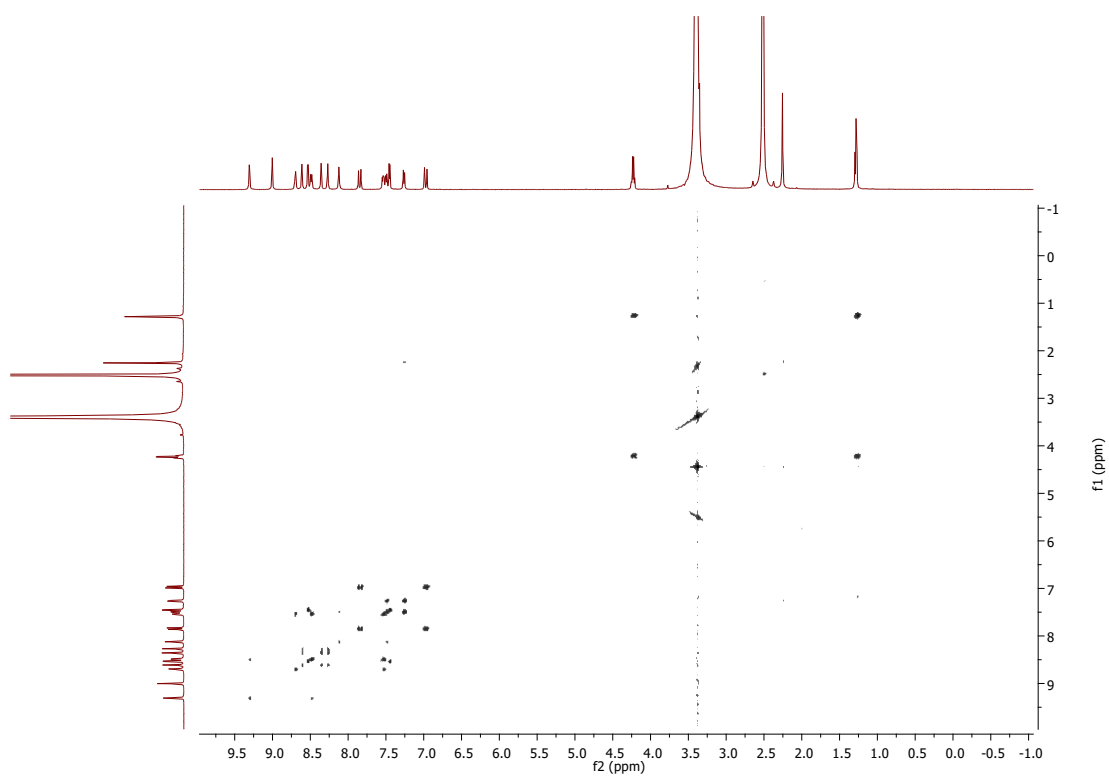


Fig. 8Se. COSY of **10** in $\text{DMSO-}d_6$

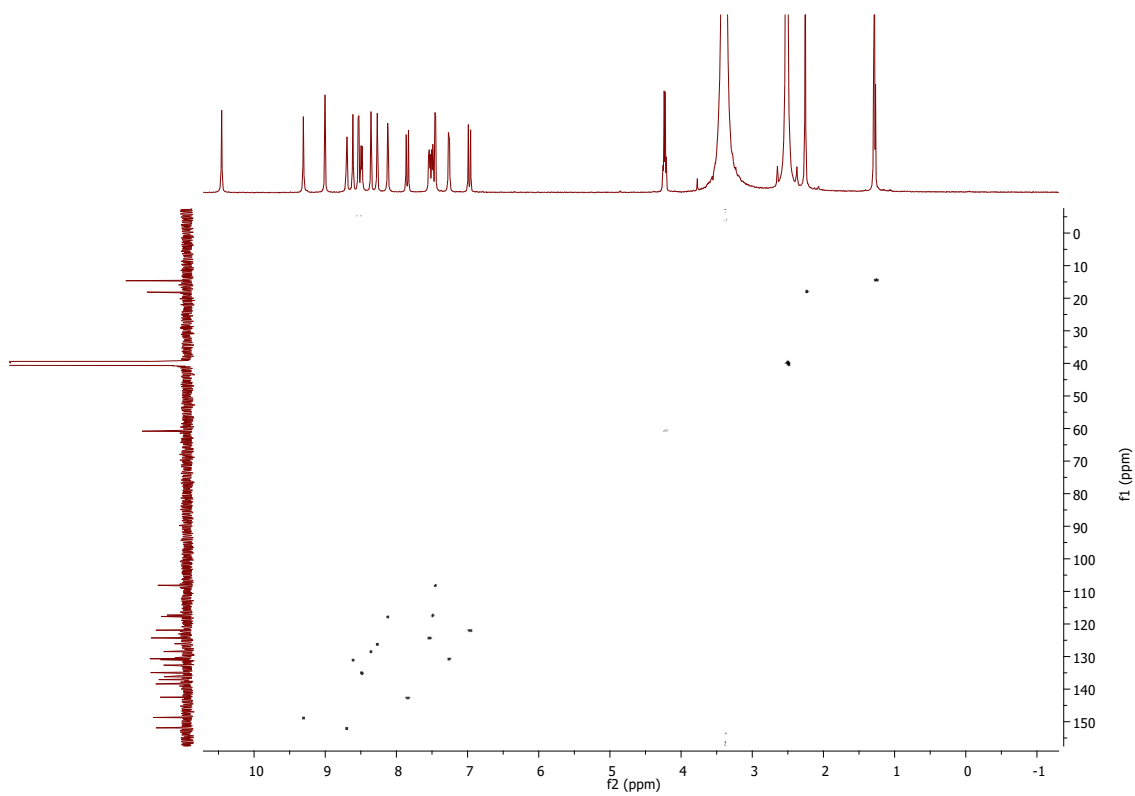


Fig. 8Sf. HSQC of **10** in DMSO- d_6

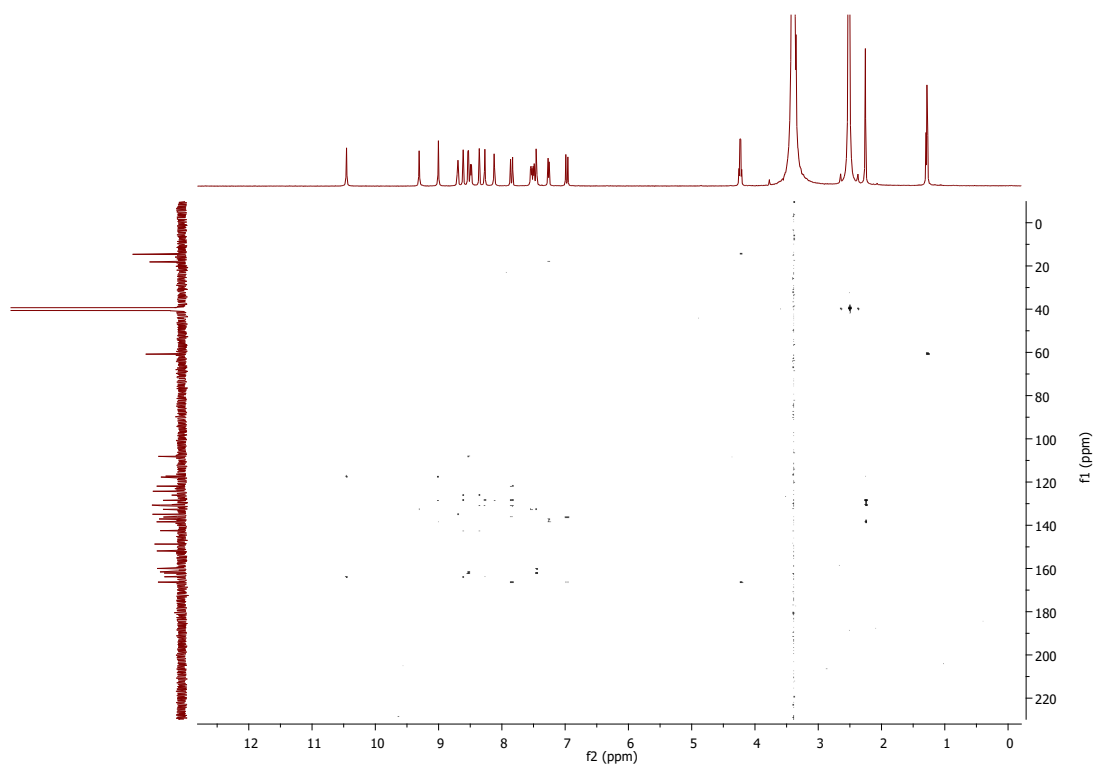


Fig. 8Sg. HMBC of **10** in DMSO- d_6

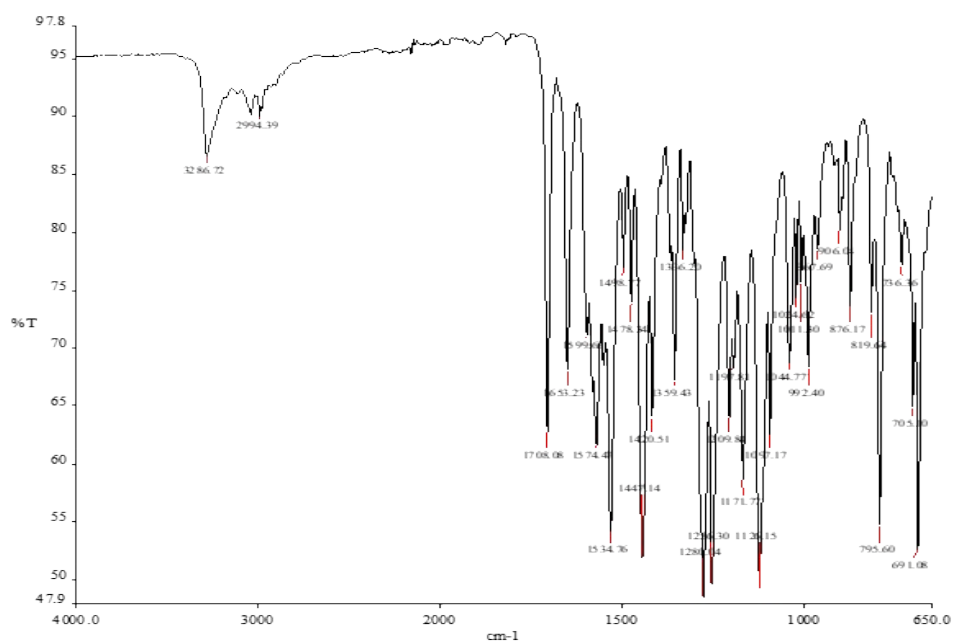


Fig. 8Sh. IR of 10

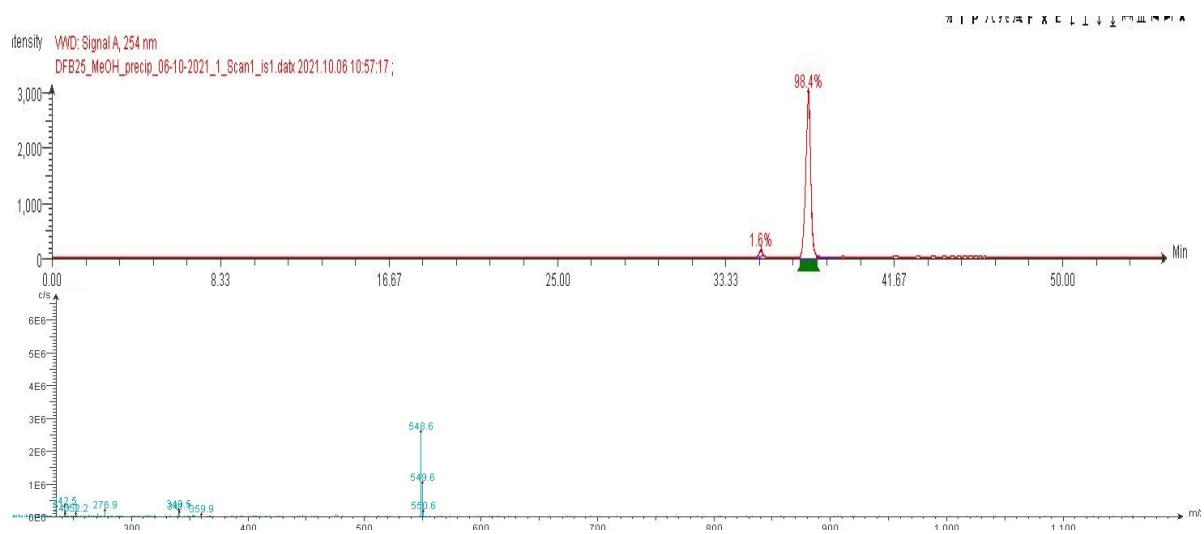


Fig. 8Si. LCMS of 10

Compound 11

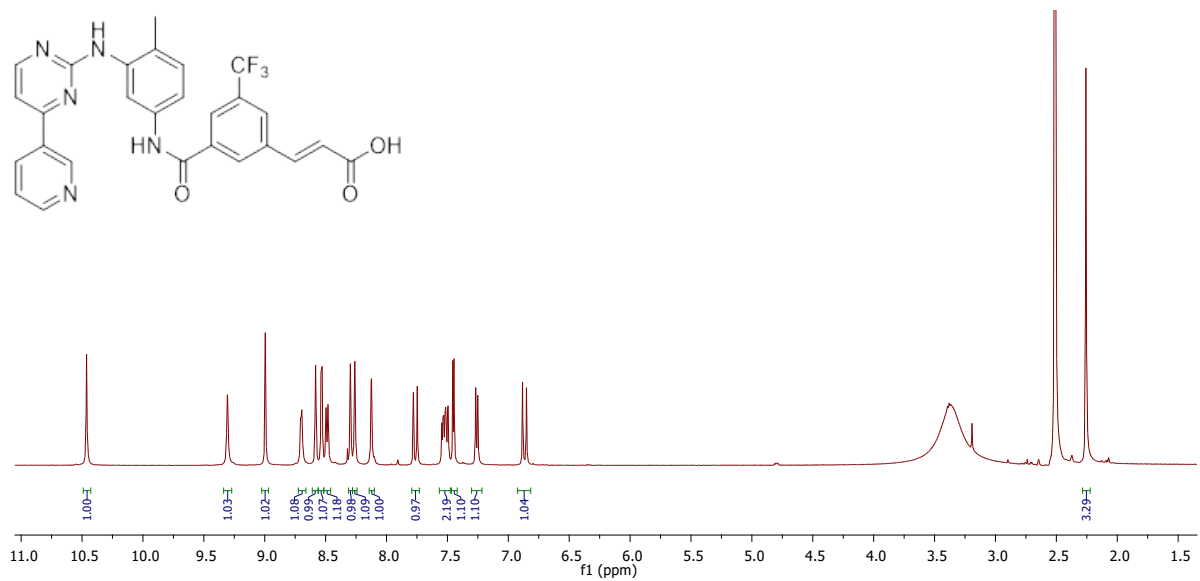


Fig. 9Sa. ¹H NMR of 11 in DMSO-*d*₆

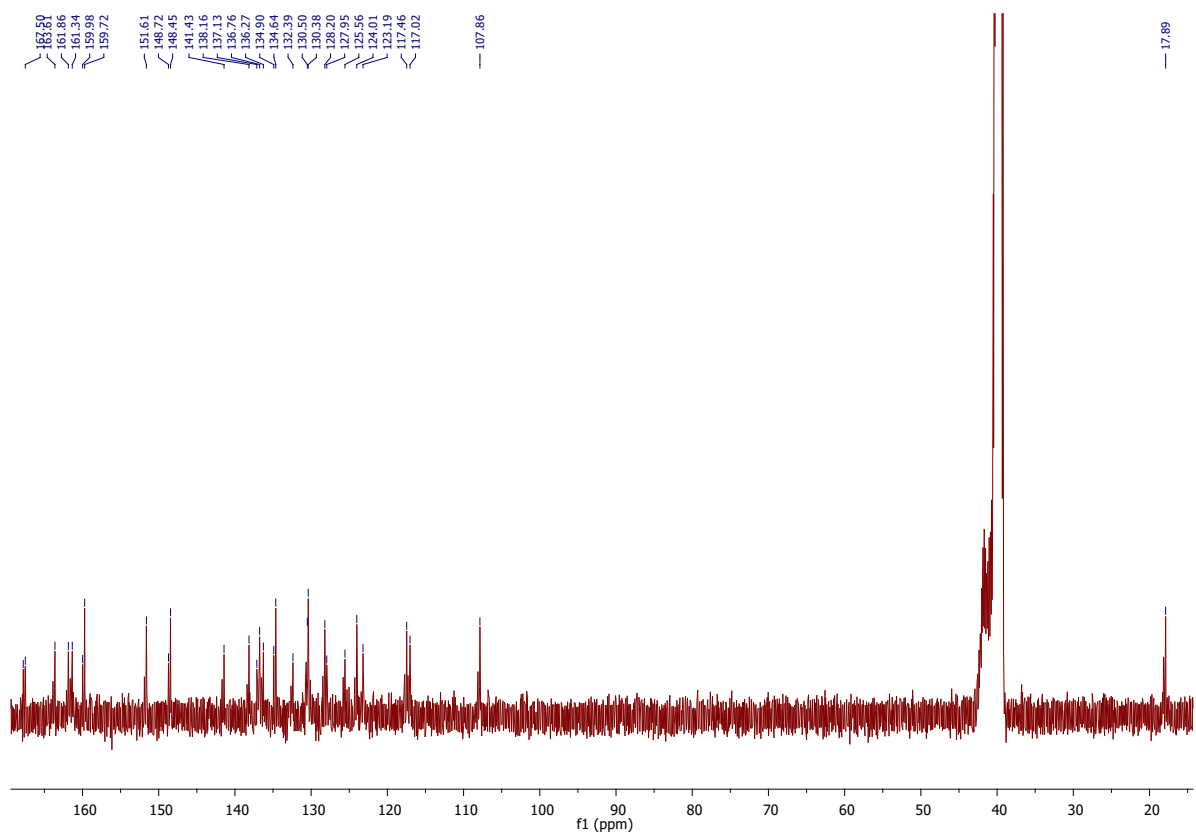


Fig. 9Sb. ¹³C NMR of 11 in DMSO-*d*₆

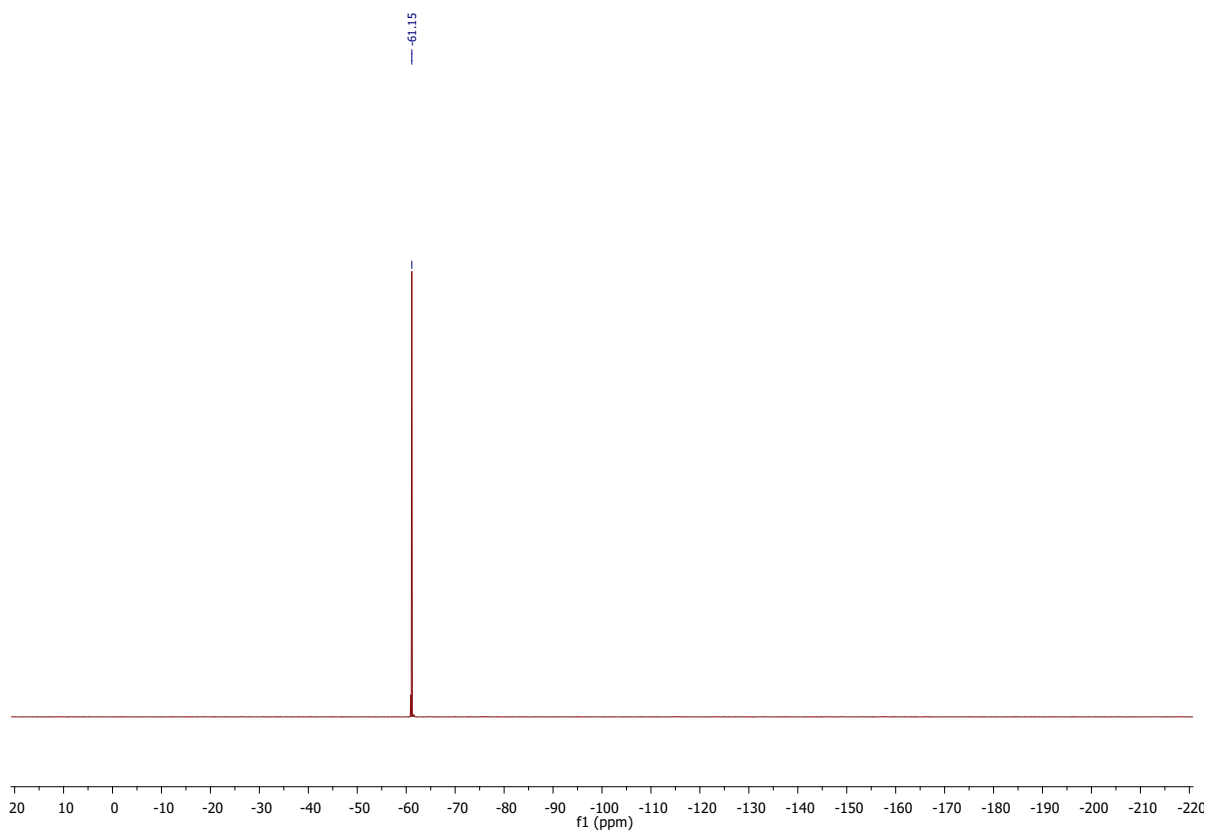


Fig. 9Sc. ^{19}F NMR of **11** in $\text{DMSO-}d_6$

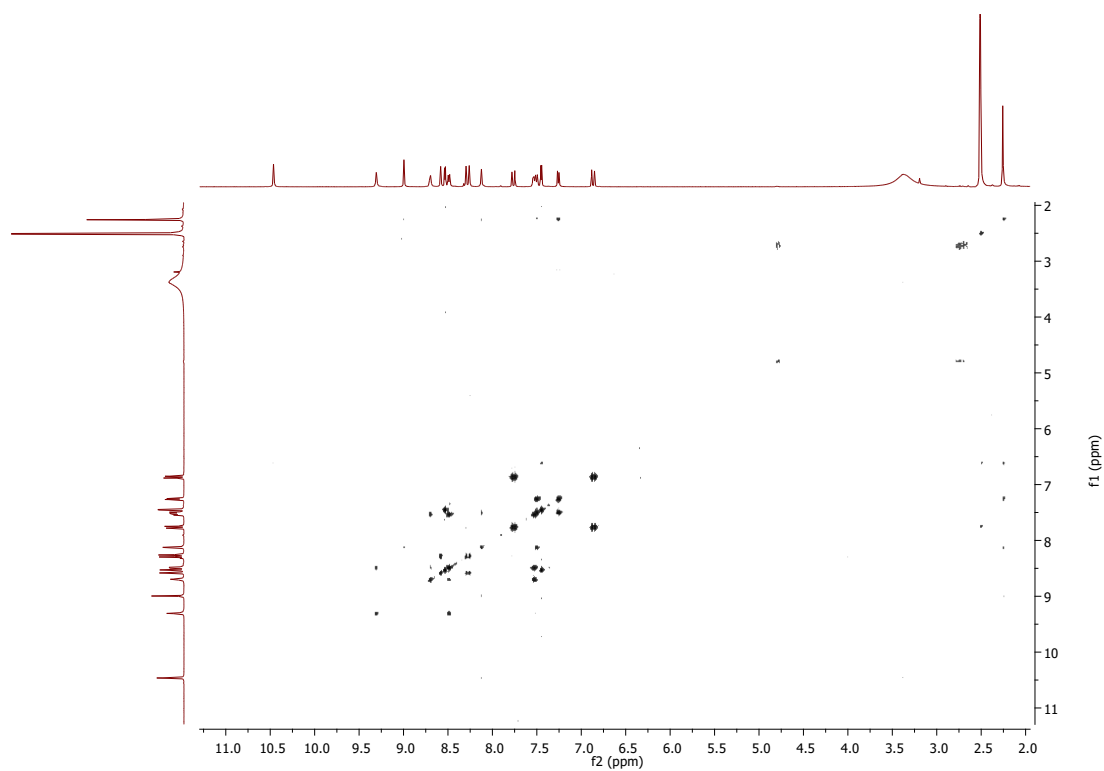


Fig. 9Sd. COSY of **11** in $\text{DMSO-}d_6$

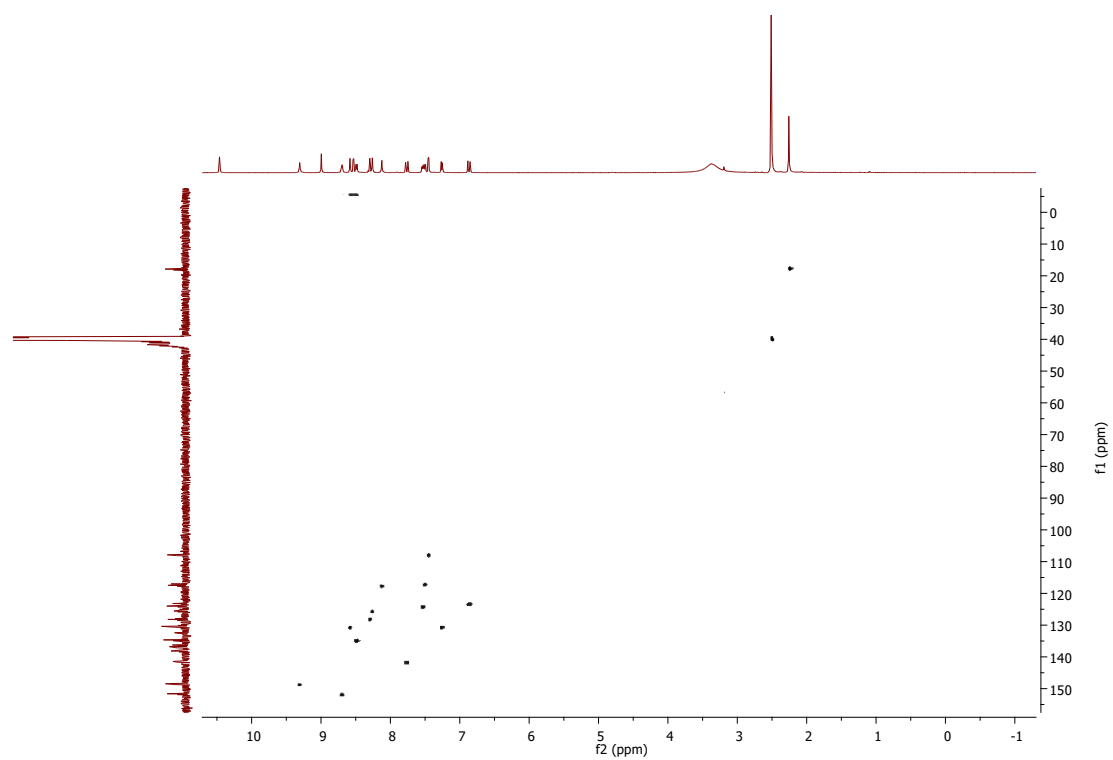


Fig. 9Se. HSQC of **11** in DMSO- d_6

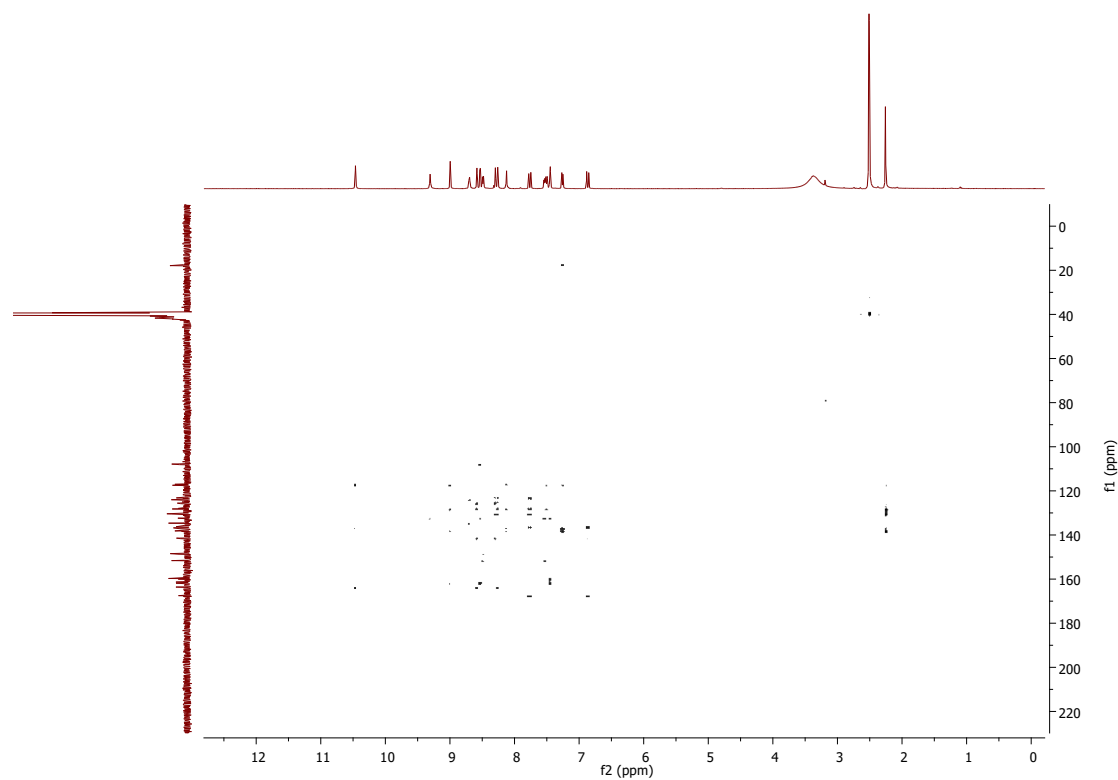


Fig. 9Sf. HMBC of **11** in DMSO- d_6

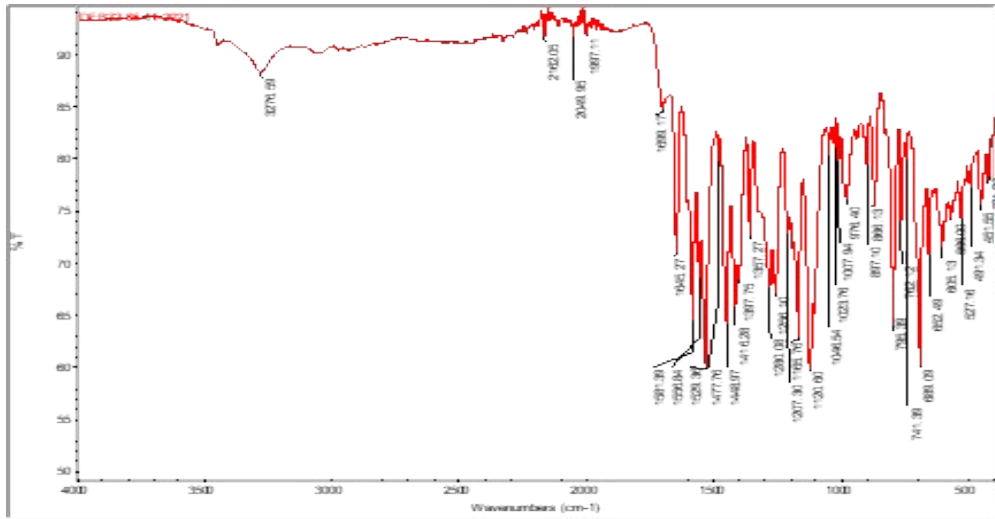


Fig. 9Sg. IR of 11

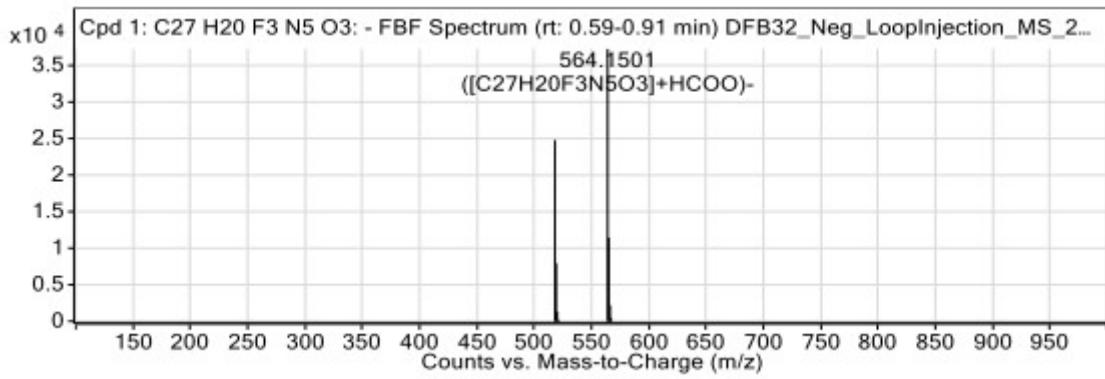


Fig. 9Sh. HRMS of 11

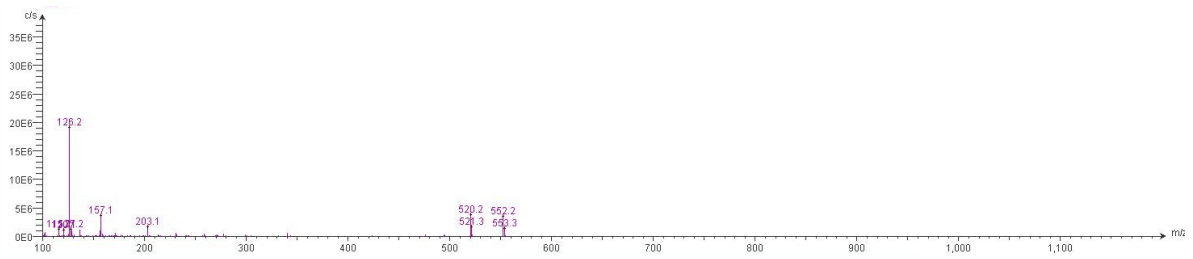
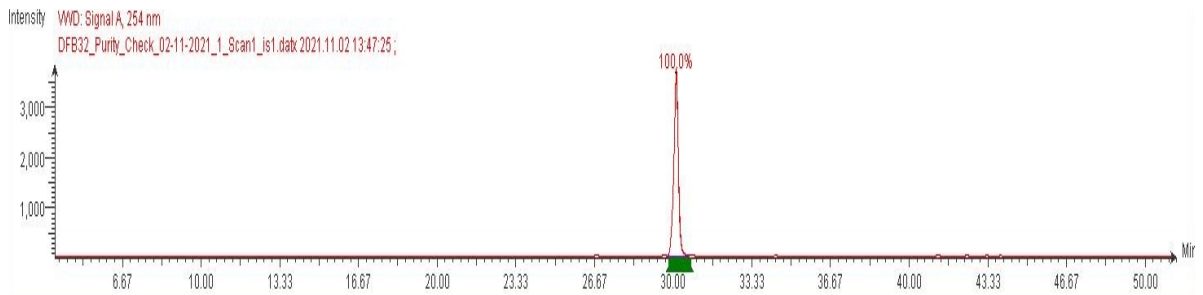


Fig. 9Si. LCMS of 11

Compound 12

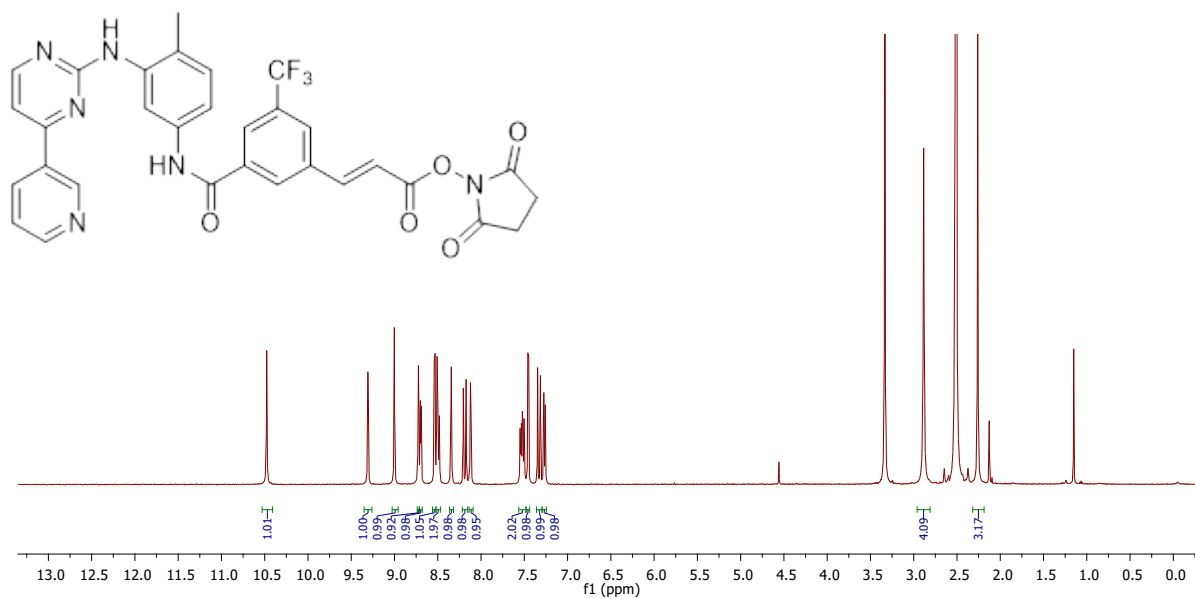


Fig. 10Sa. ^1H NMR of **12** in $\text{DMSO-}d_6$

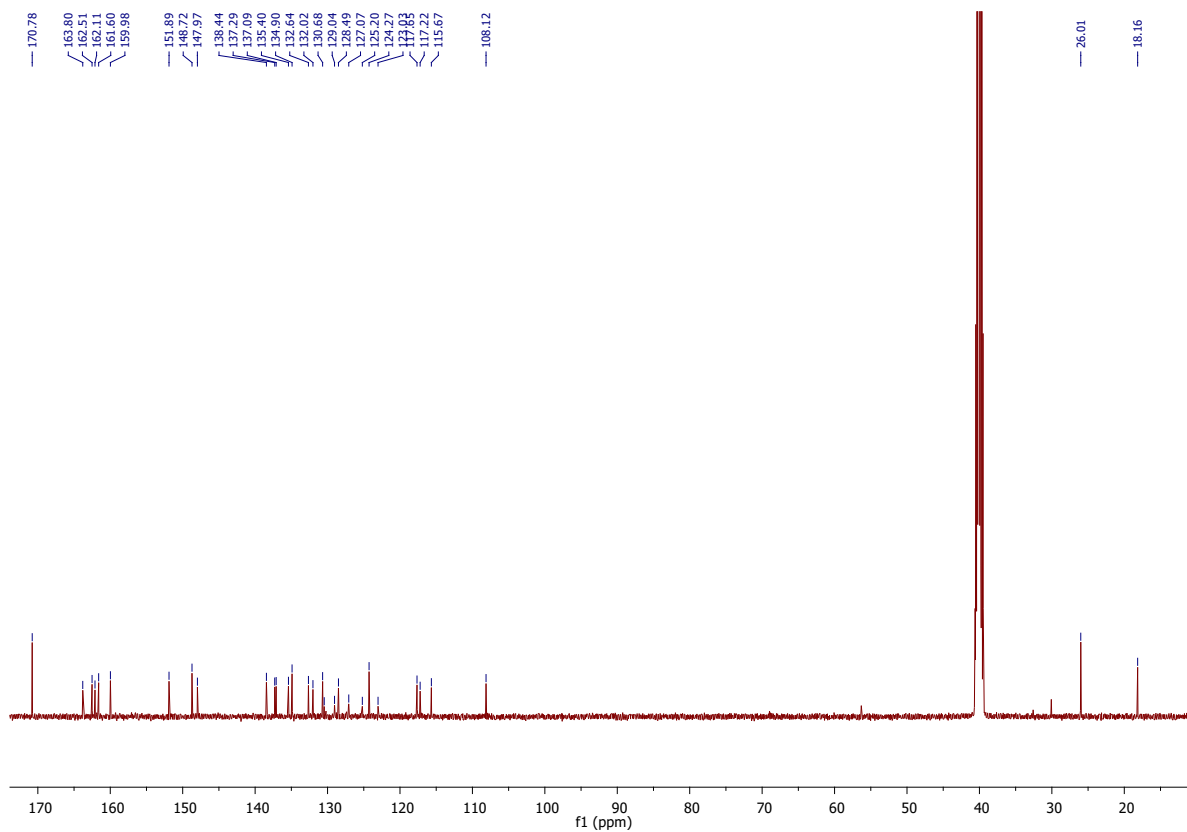


Fig. 10Sb. ^{13}C NMR of **12** in $\text{DMSO-}d_6$

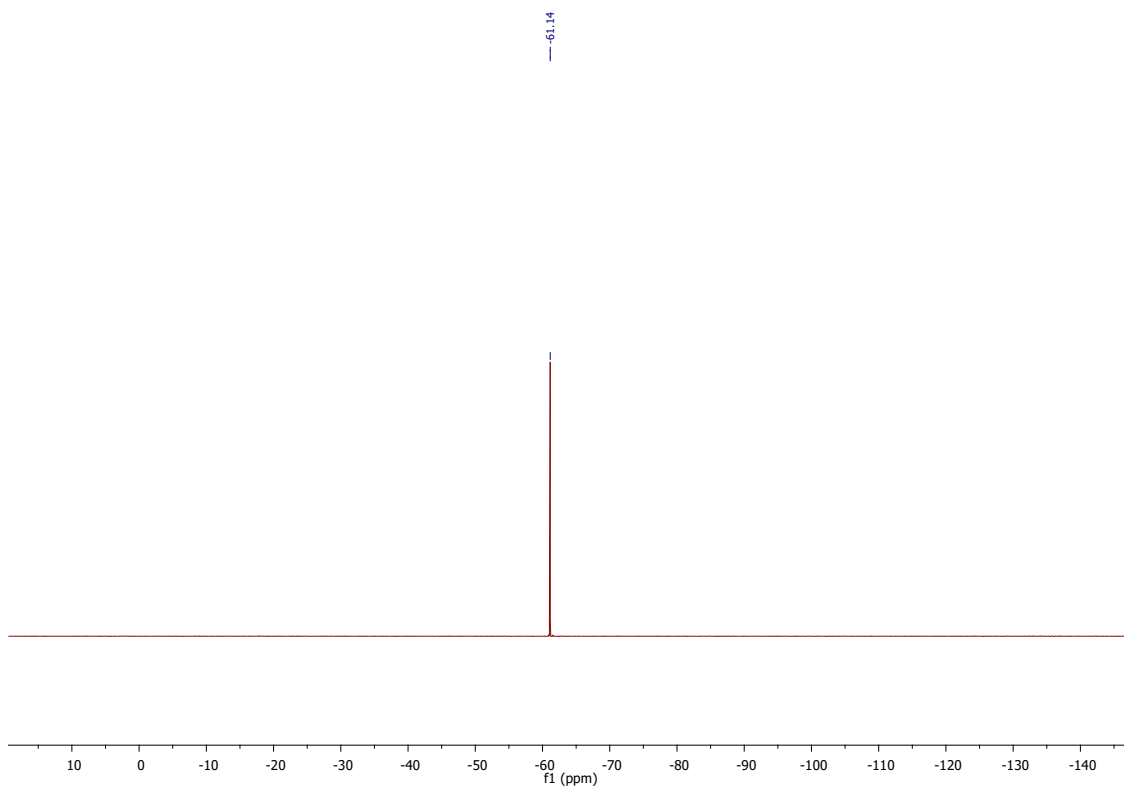


Fig. 10Sc. ^{19}F NMR of **12** in $\text{DMSO-}d_6$

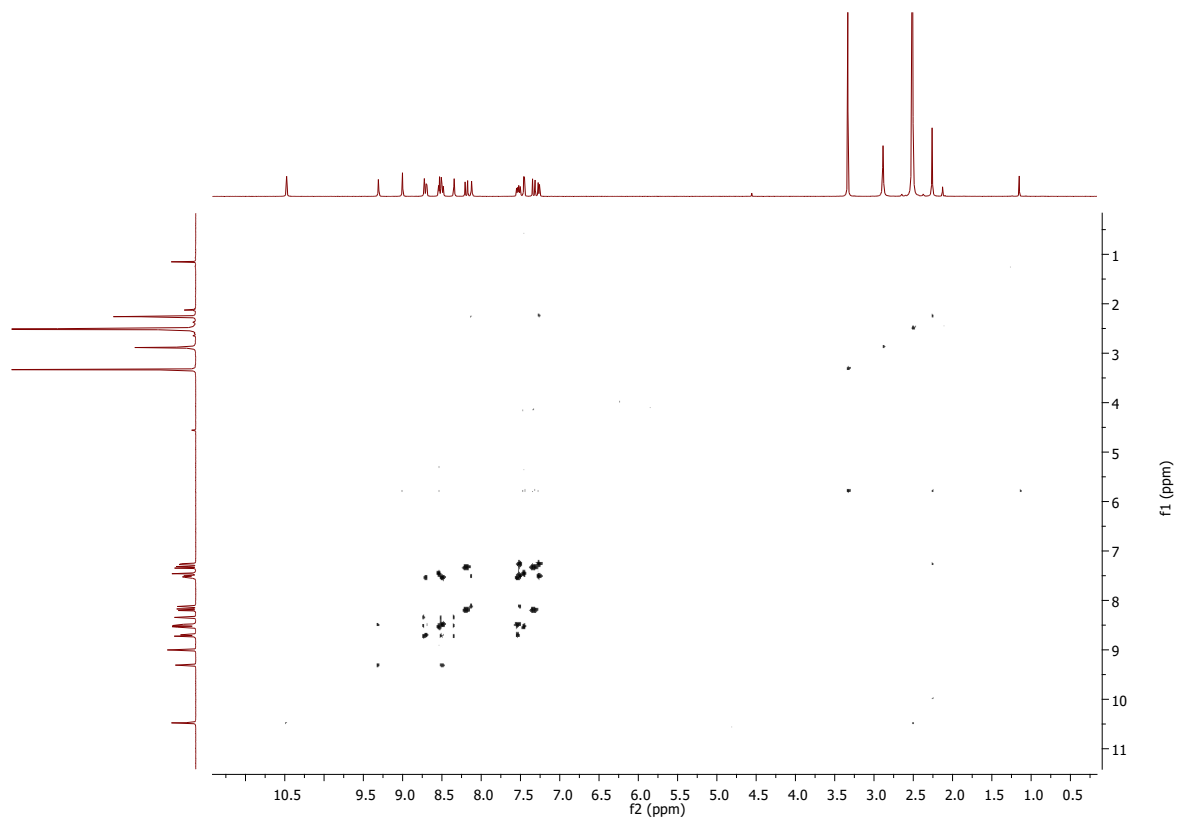


Fig. 10Sd. COSY of **12** in $\text{DMSO-}d_6$

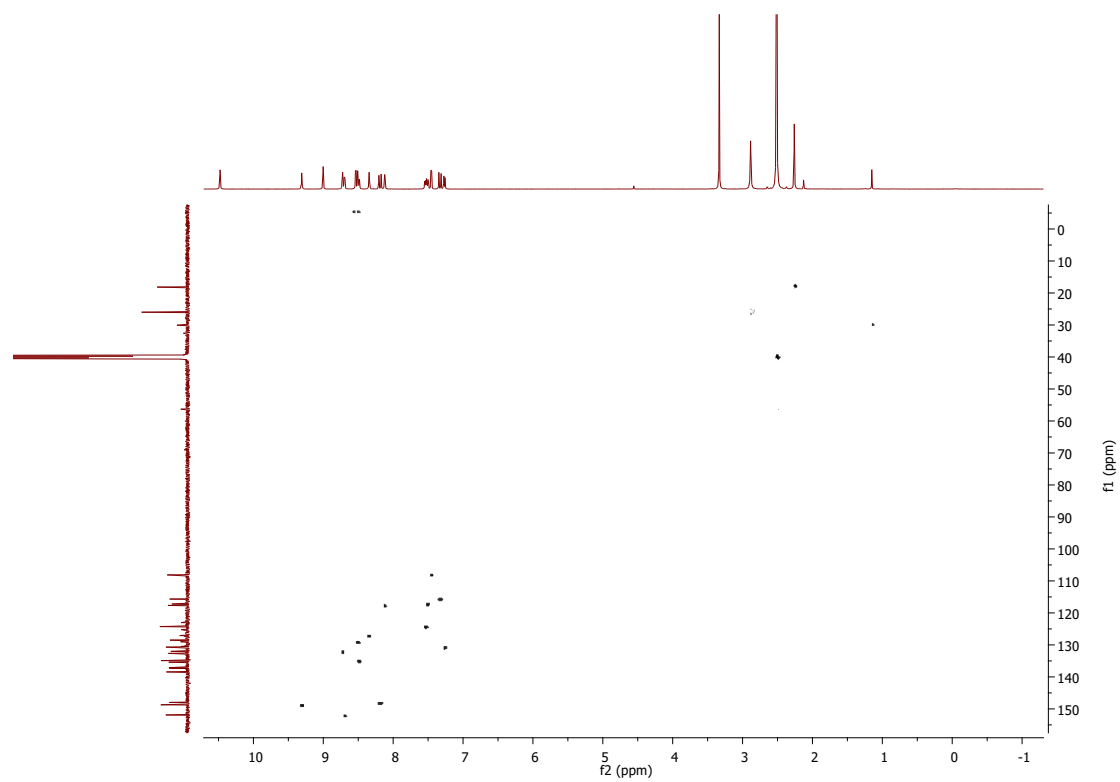


Fig. 10Se. HSQC of **12** in DMSO- d_6

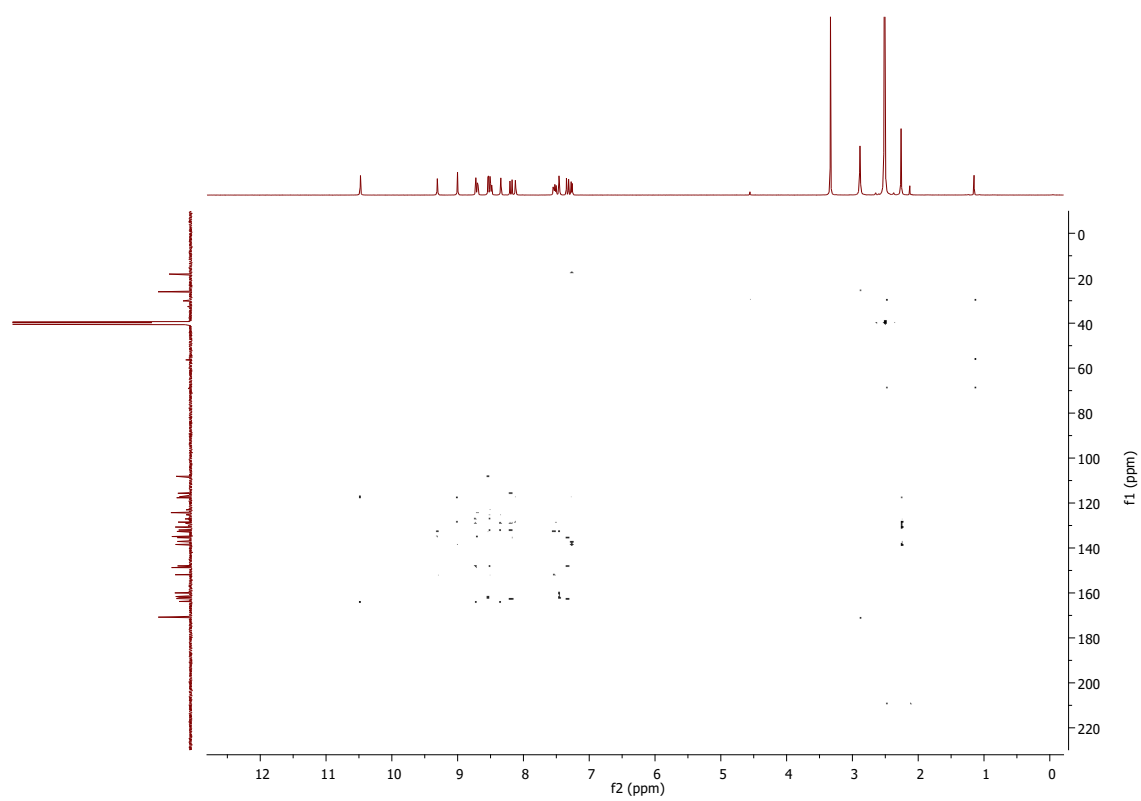


Fig. 10Sf. HMBC of **12** in DMSO- d_6

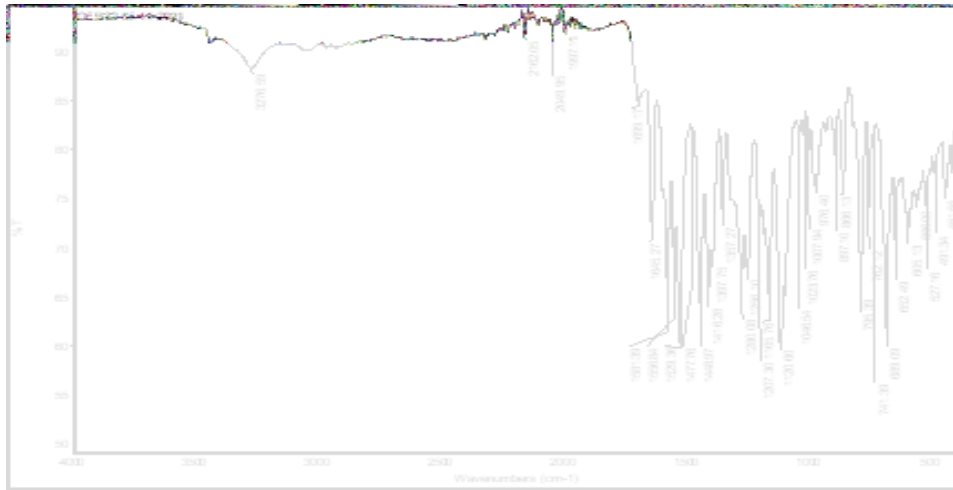


Fig. 10Sg. IR of 12

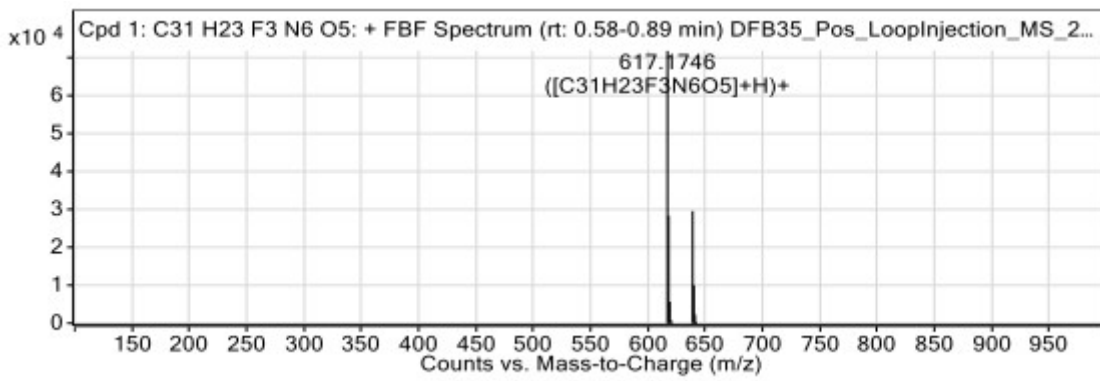


Fig. 10Sh. HRMS of 12

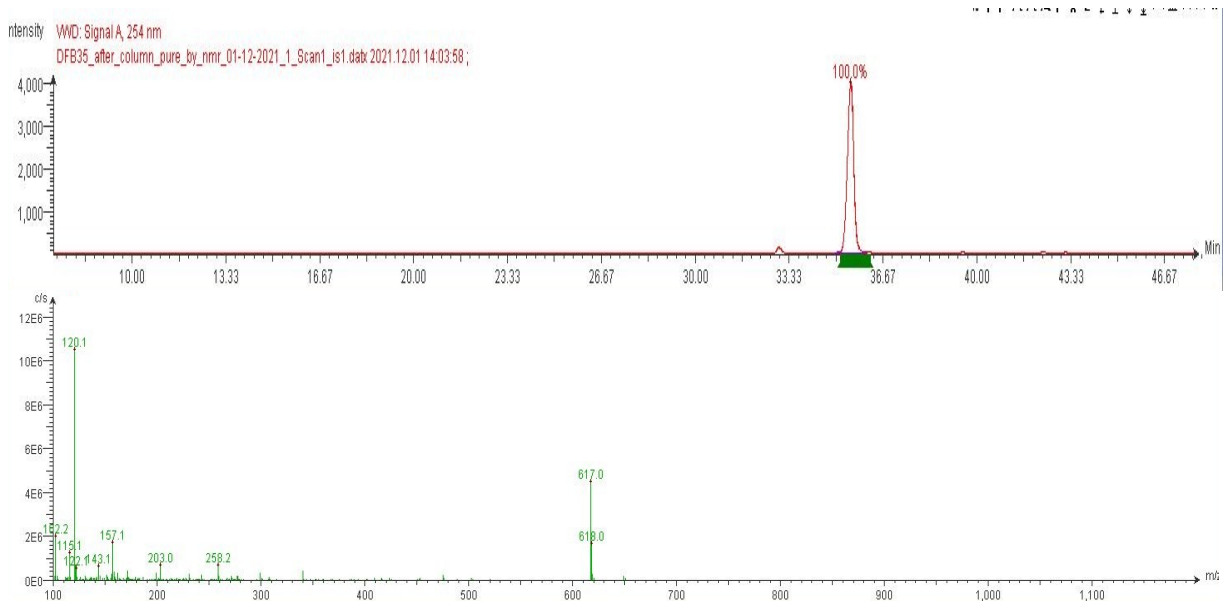


Fig. 10Si. LCMS of 12

Complex B

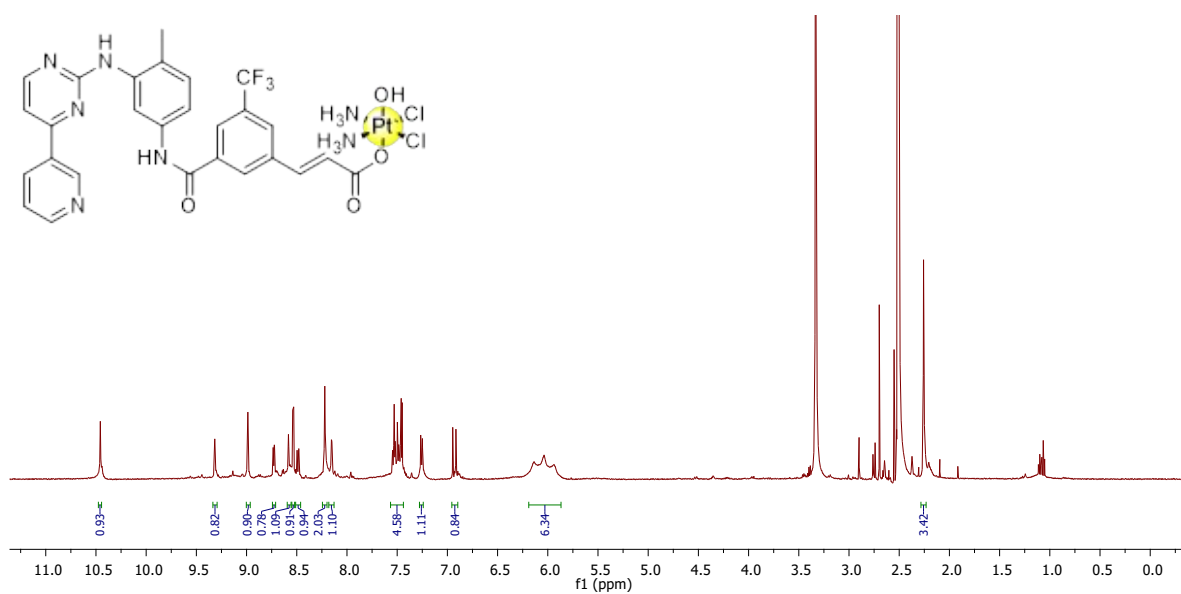


Fig. 11Sa. ¹H NMR of B in DMSO-*d*₆

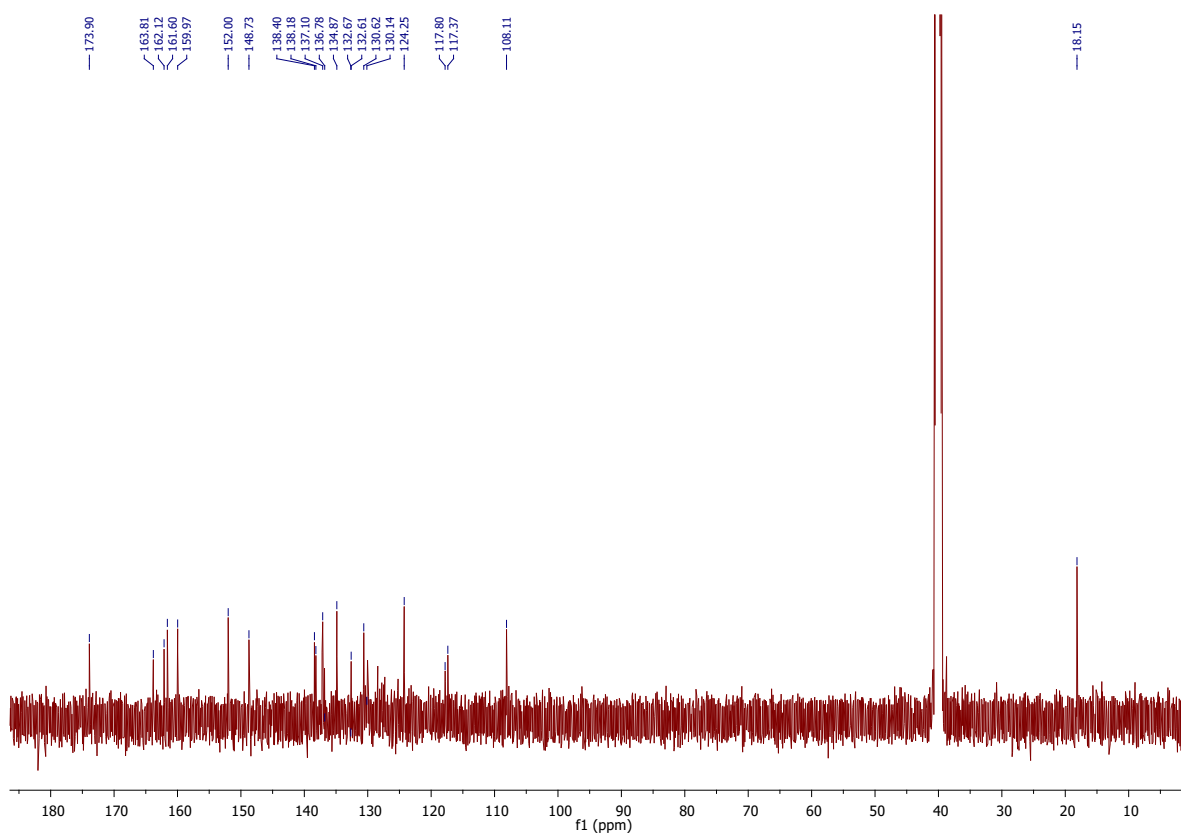


Fig. 11Sb. ¹³C NMR of B in DMSO-*d*₆

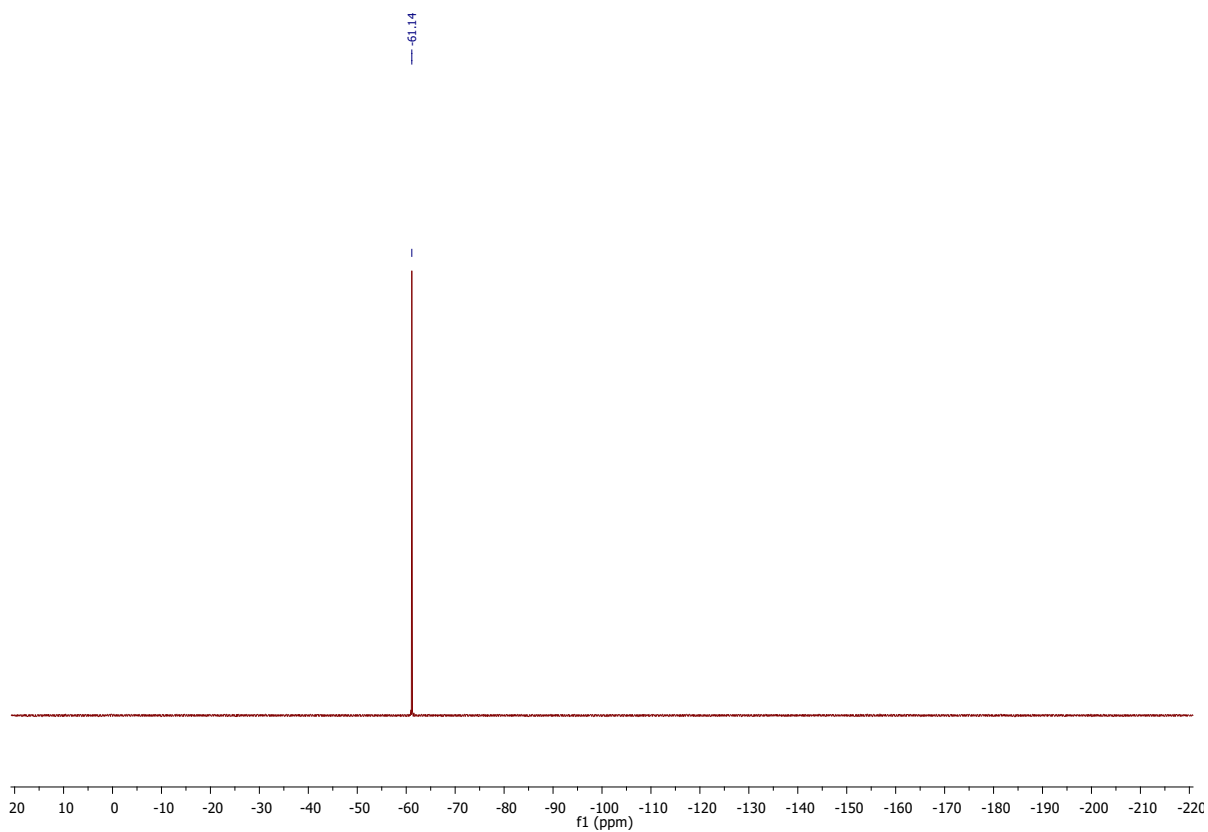


Fig. 11Sc. ^{19}F NMR of **B** in $\text{DMSO-}d_6$

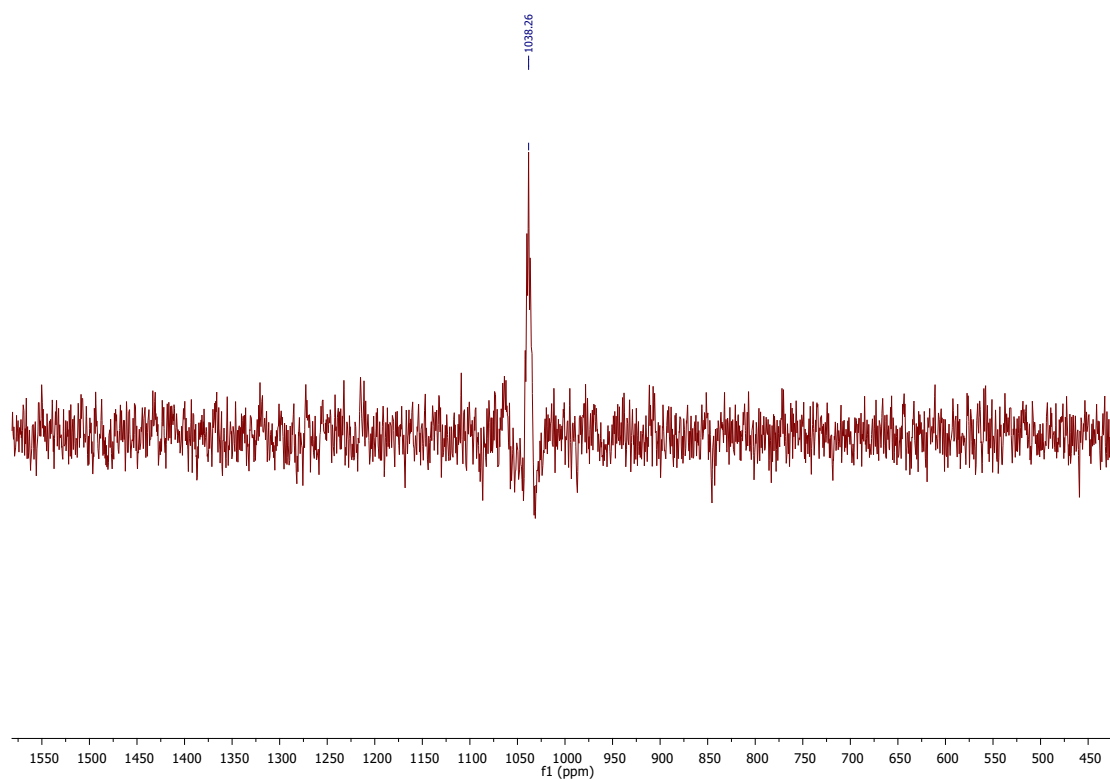


Fig. 11Sd. ^{195}Pt NMR of **B** in $\text{DMSO-}d_6$

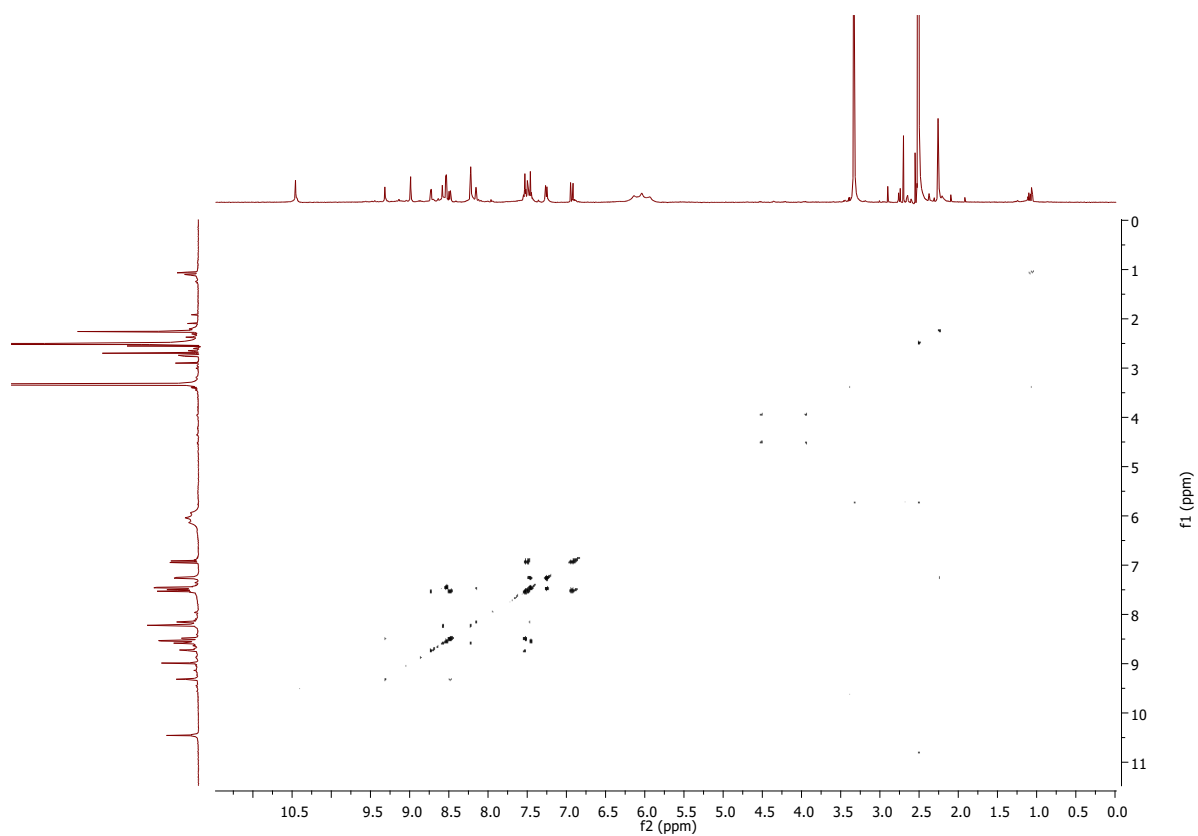


Fig. 11Se. COSY of **B** in DMSO- d_6

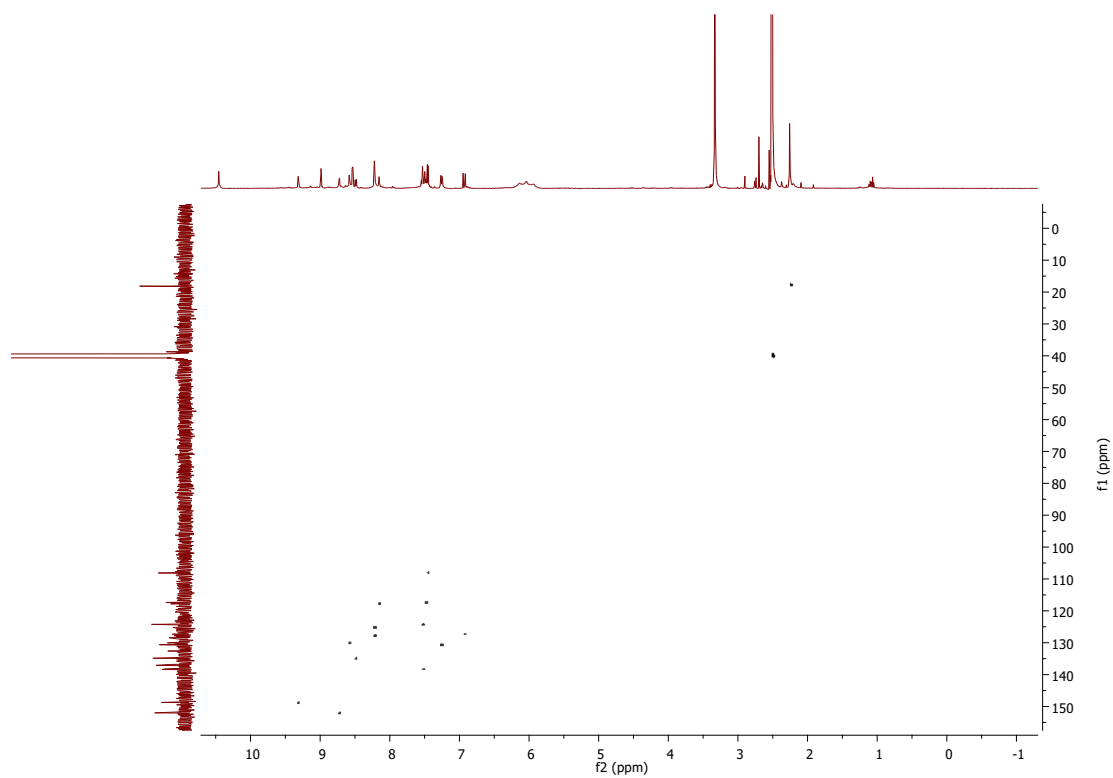


Fig. 11Sf. HSQC of **B** in DMSO- d_6

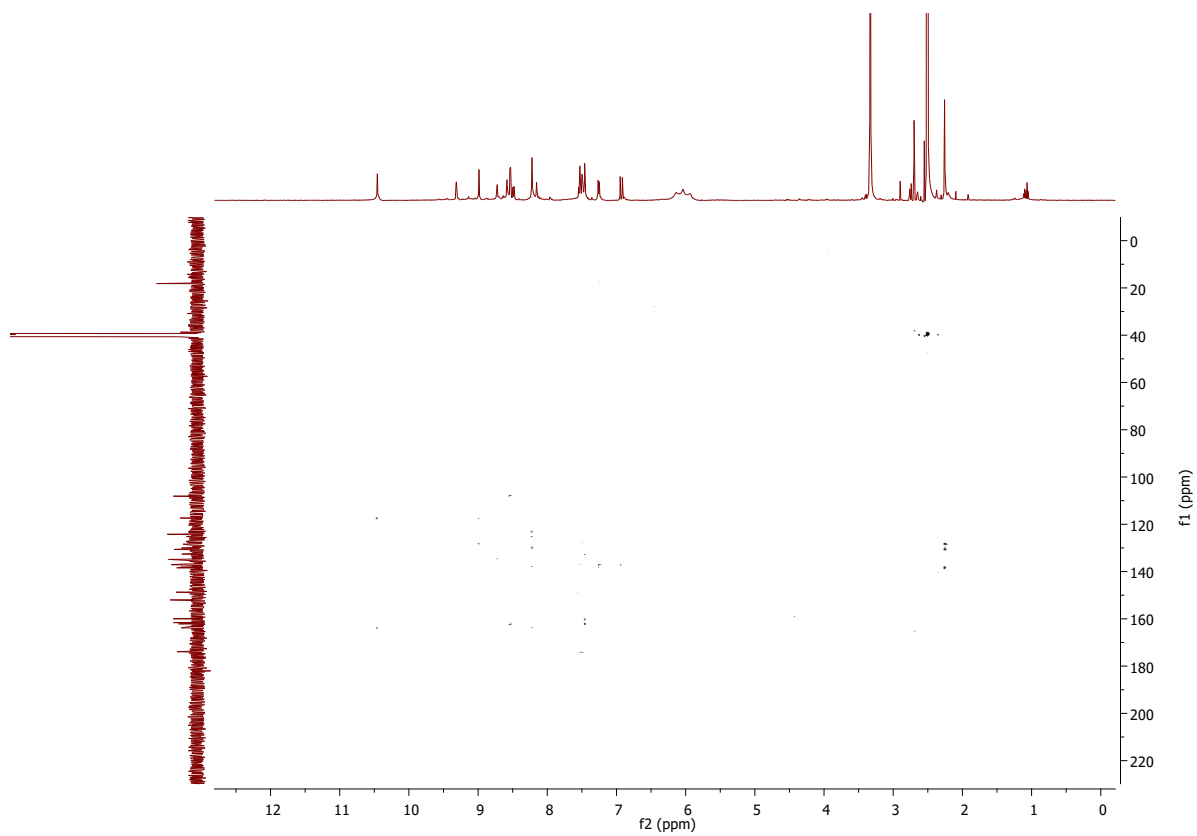


Fig. 11Sg. HMBC of **B** in DMSO- d_6

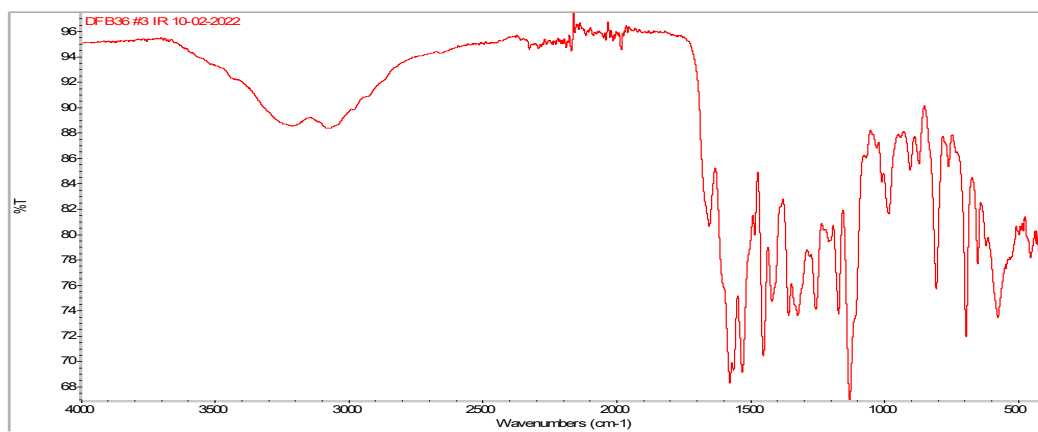


Fig. 11Sh. IR of **B**

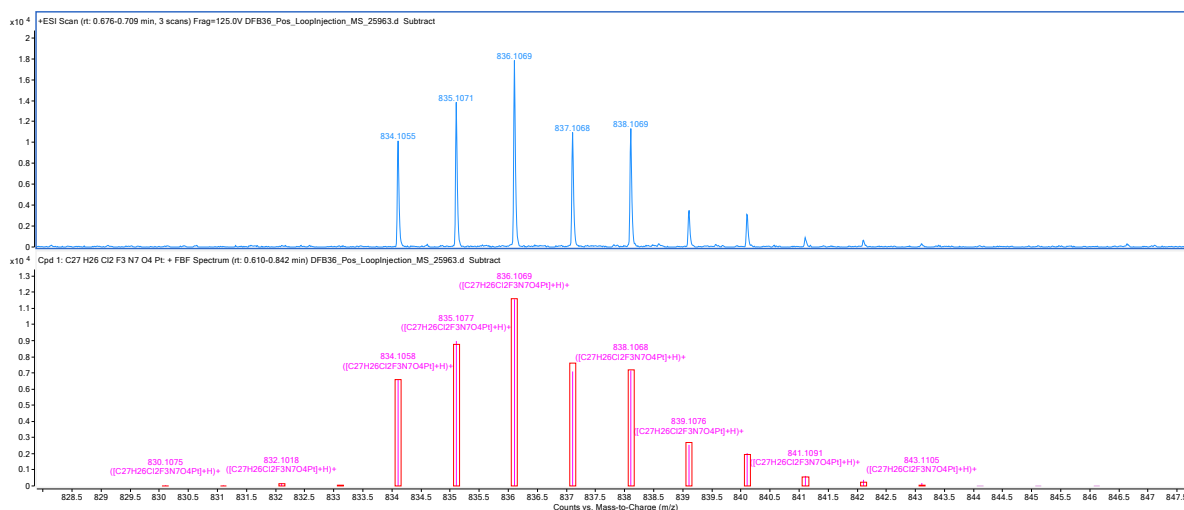


Fig. 11Si. HRMS of B

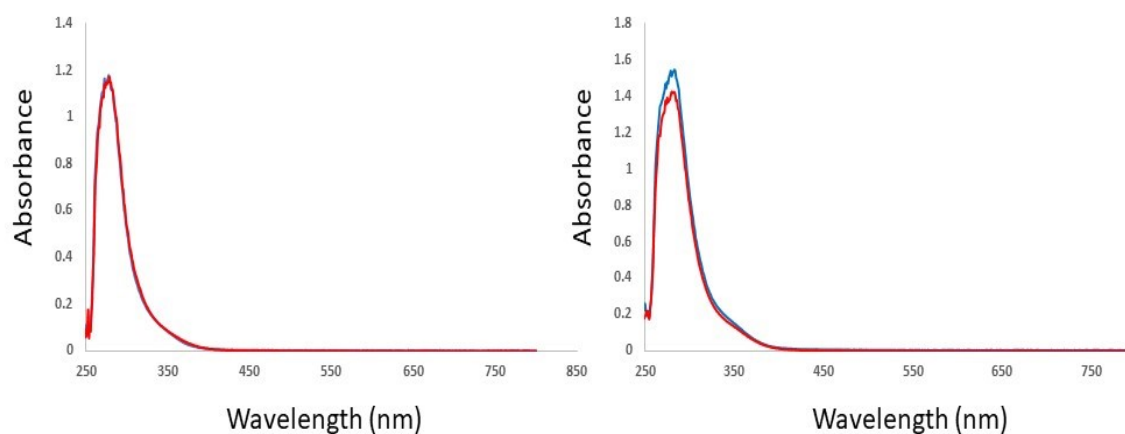


Fig. 12s. UV-VIS stability of complexes A and B in DMSO/PBS buffer (1/9). • t = 0; • t = 24 h; • t = 72 h.

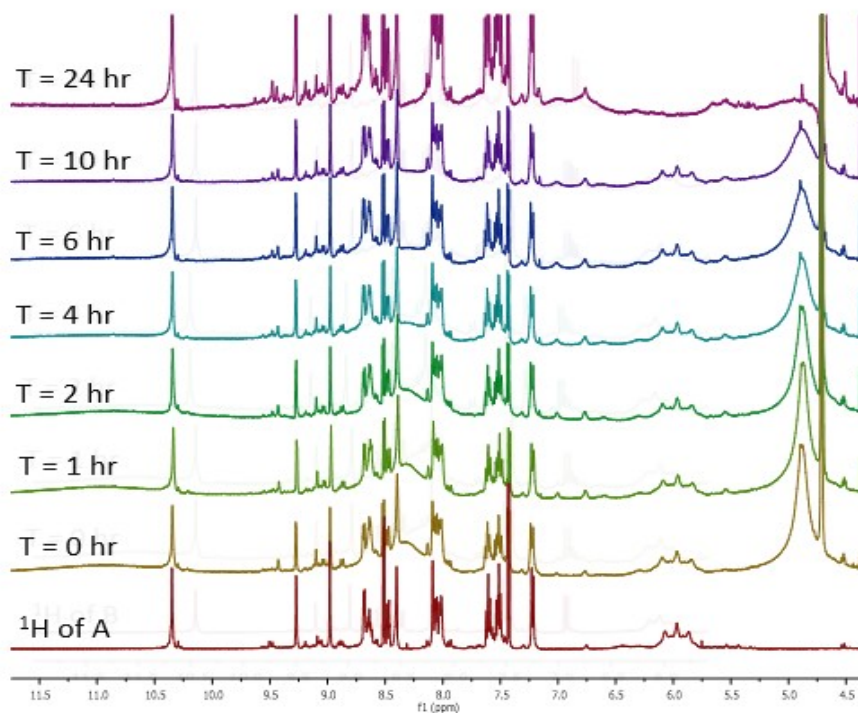


Fig. 13Sa. Reduction behaviour of **A**. ^1H -NMR spectra at different intervals of **A** in the presence of 10 eq. of Ascorbic Acid in $\text{DMSO}-d_6$.

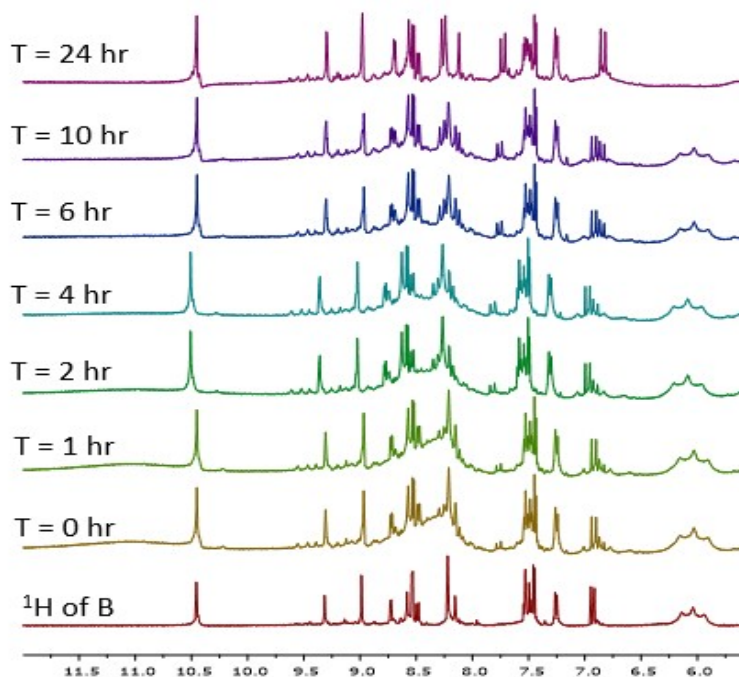


Fig. 13Sb. Reduction behaviour of **B**. ^1H -NMR spectra at different intervals of **B** in the presence of 10 eq. of Ascorbic Acid in $\text{DMSO}-d_6$.

Computational details

DFT Optimisation

Quantum mechanics (QM) simulations were performed to obtain optimised structures of Pt(IV)-imatinib and Pt(IV)-nilotinib using Gaussian 16 Rev C.016 at the wb97cf level of theory.^[1] Double- ξ LANL2DZ basis set consisting of 18 valence electrons associated with the effective core potentials (ECPs) of Hay and Wadt was employed for Pt atoms^[2], and the 6-31+G** basis set has been used for hydrogen, carbon, oxygen, nitrogen, and chlorine atoms.^[3] The solvent effect of water was taken into account using the polarizable continuum model (PCM).^[4] All optimised structures were characterised by positive frequency eigenvalues, indicating that true minima were located for each system.

Docking studies

The 1.90 Å and 1.60 Å x-ray crystal structures of PDGFR- α and c-KIT tyrosine kinase in complex with imatinib were retrieved from the Protein Data Bank (PDB ID codes 6JOL and 1T46). They were pre-processed and refined, including elimination of solvent molecules, addition of missing atoms, and assessment of appropriate protonation states at physiological pH, using the Protein Preparation Wizard employed in the Schrödinger Suite.^[5] c-KIT T670I mutated structure was prepared through Mutate module of the Schrödinger Suite, and appropriate positioning of the new residue and its closest neighbours was assured by their minimisation.

QM optimised structures of Pt(IV) prodrugs were used as inputs with minimal adjustments required to prepare the metal chelate structures for docking with Glide (assignment of zero-order bonds within the metal complex to obviate the need for specific force field parameters involving the metal ion). The coordination geometry of metal centre and complexation fragments was restrained during Glide optimisation and fitting to remain similar to the QM calculated geometry.

Molecular docking was performed with Glide in three steps; rigid docking to identify the best-fit orientation of the compounds into the binding site with single precision (SP) protocol, followed by extra precision (XP) protocol, and finally induced fit docking (IFD) allowing for receptor residues distanced up to 5 Å from the ligand heavy atoms to relax.^[6,7] The appropriate receptor grid was generated based upon the positioning of co-crystallised imatinib molecule within the original X-ray structures employing a grid box 25 Å each side. The larger grid box was necessary to ensure appropriate sampling of any atypical pockets close to the main drug-binding site considering larger sizes of the metal chelates compared to typical small molecules. Docking simulations of pre-bound imatinib were used to evaluate the accuracy of the chosen setup. Comparative docking study hence included original imatinib and nilotinib drugs, the Pt(IV) prodrugs, as well as their acidic form in case of the metal centre detachment, giving a total of 18 systems studied. Validation of the docking protocol was carried out by re-docking imatinib in both receptors with RMSD values of 0.79 and 0.74 Å in comparison to the co-crystallised poses (Figure 13S a/d), confirming the suitability of the approach used.

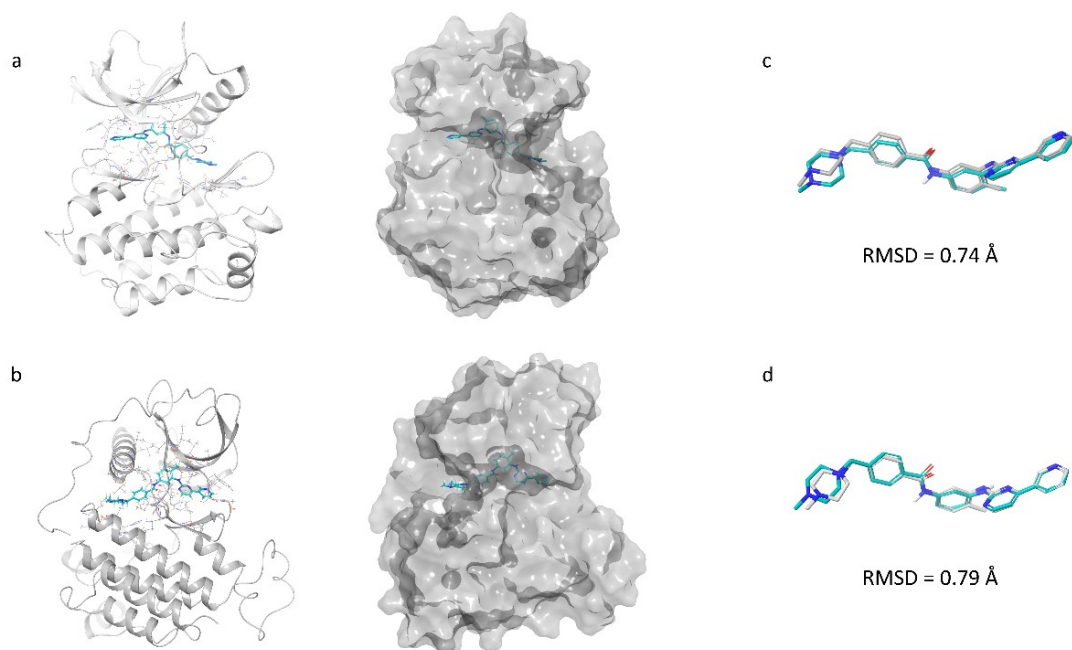


Fig. 14S. (a) Ribbon and surface representation of imatinib co-crystallised within PDGFR- α (PDB ID 6JOL). (b) Ribbon and surface representation of imatinib co-crystallised within c-kit tyrosine kinase (PDB ID 1T46). (c) Overlap of co-crystallised imatinib (grey) and imatinib docked in PDGFR- α using Glide (cyan). (d) Overlap of co-crystallised imatinib (grey) and imatinib docked in c-kit tyrosine kinase using Glide (cyan).

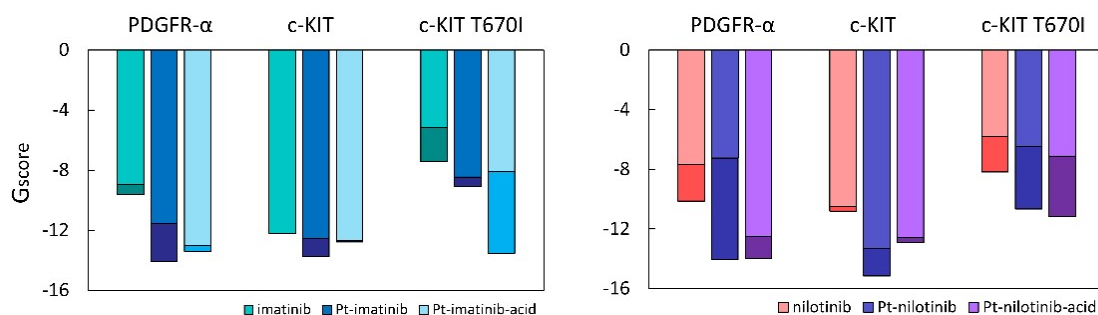


Fig. 15S. Docking scores (G_{score}) of imatinib, nilotinib, Pt(IV) complexes **A** and **B** and the A_{-} and B_{-} ligand-COOH structures in PDGFR- α , c-KIT, and mutated c-KIT T670I as obtained by Glide. Lighter shaded colours correspond to rigid docking scores, whereas docking scores from IFD flexible binding site protocol are shown as dimmed.

Contacts formed between the six ligands and PDGFR- α in the flexible docking with Glide

The binding poses of the six ligands within PDGFR- α as modelled by IFD in Glide are shown in Figure 3, and their two-dimensional interaction profiles are presented in Figure 15S. Several potential hydrogen bonds (HB) and other non-bonding interactions were observed to reoccur throughout the six studied systems. HB of the nitrogen from the terminal pyridine ring with the amino backbone group of CYS677 is maintained with all the ligands, as is the π - π stacking of pyrimidine moiety with PHE837. Except for the best scoring pose of Pt-nilotinib, HB between the amino group connecting pyrimidine and tri-substituted phenyl rings and THR674 is also seen in all the systems. Major differences in binding modes

arise from the remaining ligand fragments, namely amide connected phenyl rings with piperazine, imidazole, and Pt-complexed tails. In the case of both imatinib and nilotinib, amide functional group is the last fragment which interacts with the target, where NH acts as a hydrogen donor to GLU644, and carbonyl group of nilotinib forms an HB with ASP836. Neither of the two rings that extend towards out of the enclosed binding cavity contribute to non-covalent interactions with nearby residues. Acidic tails and metal centres of Pt-prodrug conjugates allow formation of hydrogen and halogen bonds well outside the binding pocket. Hydroxyl group of the Pt-imatinib metal complex established a HB with THR872, whereas that of the Pt-nilotinib metal complex formed a HB with ARG817. Complexation of Pt-nilotinib also benefited from two interactions between a chlorine and ARG817, one being a salt bridge and the other a halogen bond. Acidic Pt-prodrug forms with detached metal centre have each established a HB with the backbone amino groups of ARG817 in the case of Pt-imatinib-acid and that of LEU839 in the case of Pt-nilotinib-acid.

From the binding pose overlaps also shown in Figure 3, it can be concluded that the 4-pyridyl-pyrimidine core which is shared across all six ligands remains locked in the hydrophobic end of the binding pocket containing a series of non-polar amino acids (LEU599, VAL607, ALA625, VAL658, LEU825, PHE837) and two aromatic residues (TYR676 and PHE837) with consistent π - π bonding. Positively charged side-chain of LYS627 conveniently positioned in the centre of the cavity followed by hydrogen accepting carboxyl groups of GLU644 and ASP836 allows for efficient HB and π -cation network, securing the ligand binding. The entrance to the cavity is highly hydrophobic, surrounded by side chains of ILE647, LEU651, and LEU809. As the surface of the protein opens up, more points for a strong hydrogen and/or salt-based interaction arise, including SER643 and TYR872 with hydroxyl functional groups and very flexible nitrogen rich tails of LYS646 and ARG817. To reach these reactive residues, long ligands whose fragments can extend beyond the enclosed cavity, such as those containing flexible carbon chains functionalised with hydrogen deficient and/or negatively charged groups, as in the case of acidic form of the Pt-imatinib or Pt-nilotinib, are necessary.

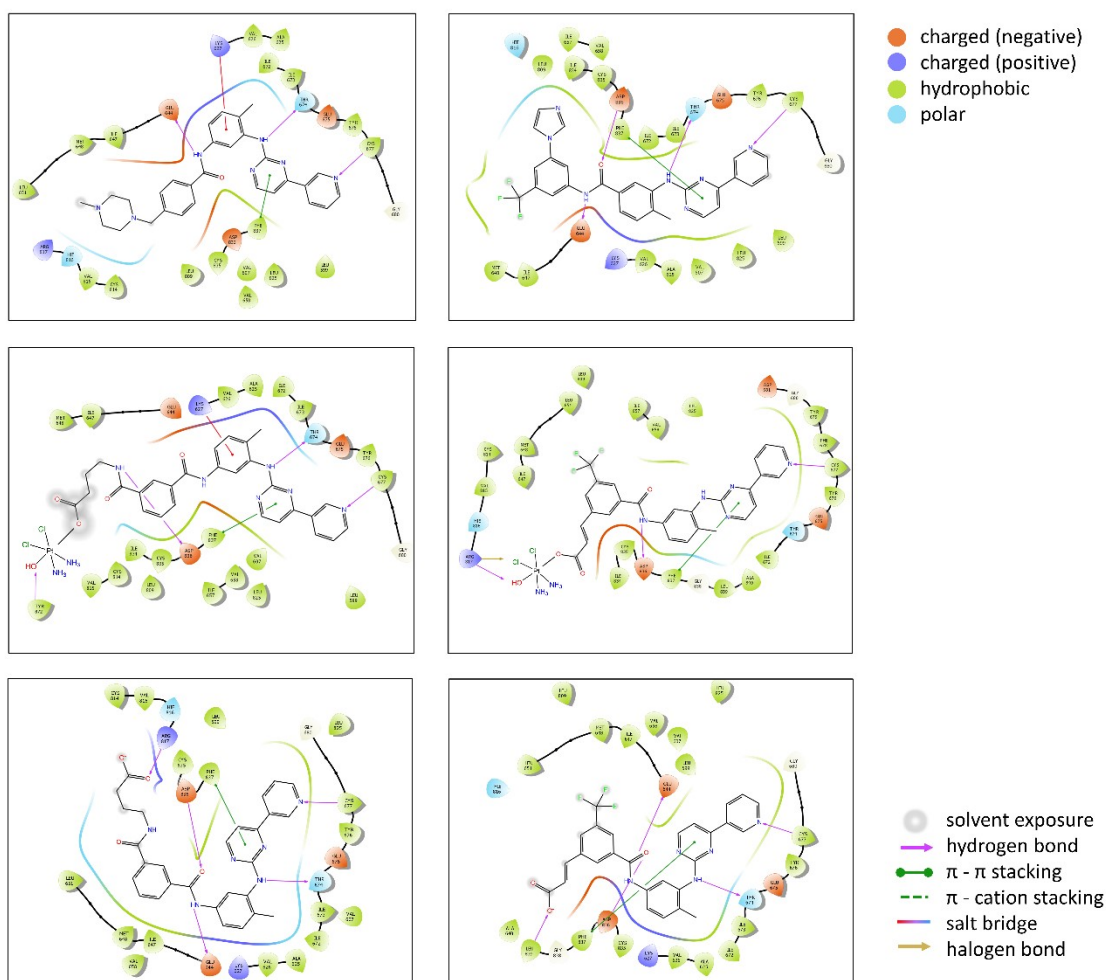


Fig. 16S. Two-dimensional interaction diagrams for best scoring poses of imatinib, **A** and **A_ligand-COOH** (left panel top to bottom), and nilotinib, **B** and **B_ligand-COOH** (right panel top to bottom) after induced fit (IFD) docking in PDGFR- α with Glide. Legend for amino acid residues and interaction types is given on the right.

Contacts formed between the six ligands and c-KIT in the flexible docking with Glide

The binding poses of the six ligands within c-KIT as modelled by IFD in Glide are shown in Figure 4, and their two-dimensional interaction profiles are presented in Figure 16S. As the binding cavity shows similar features as those of PDGFR- α , allowing for dual inhibition of the two proteins, as shown in Figure 17S, the positioning and type of interactions established during the binding of the six ligands in the two targets are also similar. The 4-pyridyl-pyrimidine core sits comfortably in the hydrophobic cocoon enclosed by non-polar LEU595, VAL603, ALA621, VAL654, and LEU799, and two π -aromatic clouds of PHE811 and TYR672. Position of terminating pyridine is additionally ensured through HB with the amino backbone group of CYS673. Cationic end of LYS623 can be seen to form π -cation interactions with the central phenyl ring and nearby GLU640 and ASP810 are seen securing the surrounding amide and amine linkers of ligands through hydrogen bonds. Outside the binding cavity, ARG791 is the most successful in stabilising the position of metal complexed chains of Pt imatinib and nilotinib prodrugs. Position of the acidic chains after the metal centre detachment is less defined.

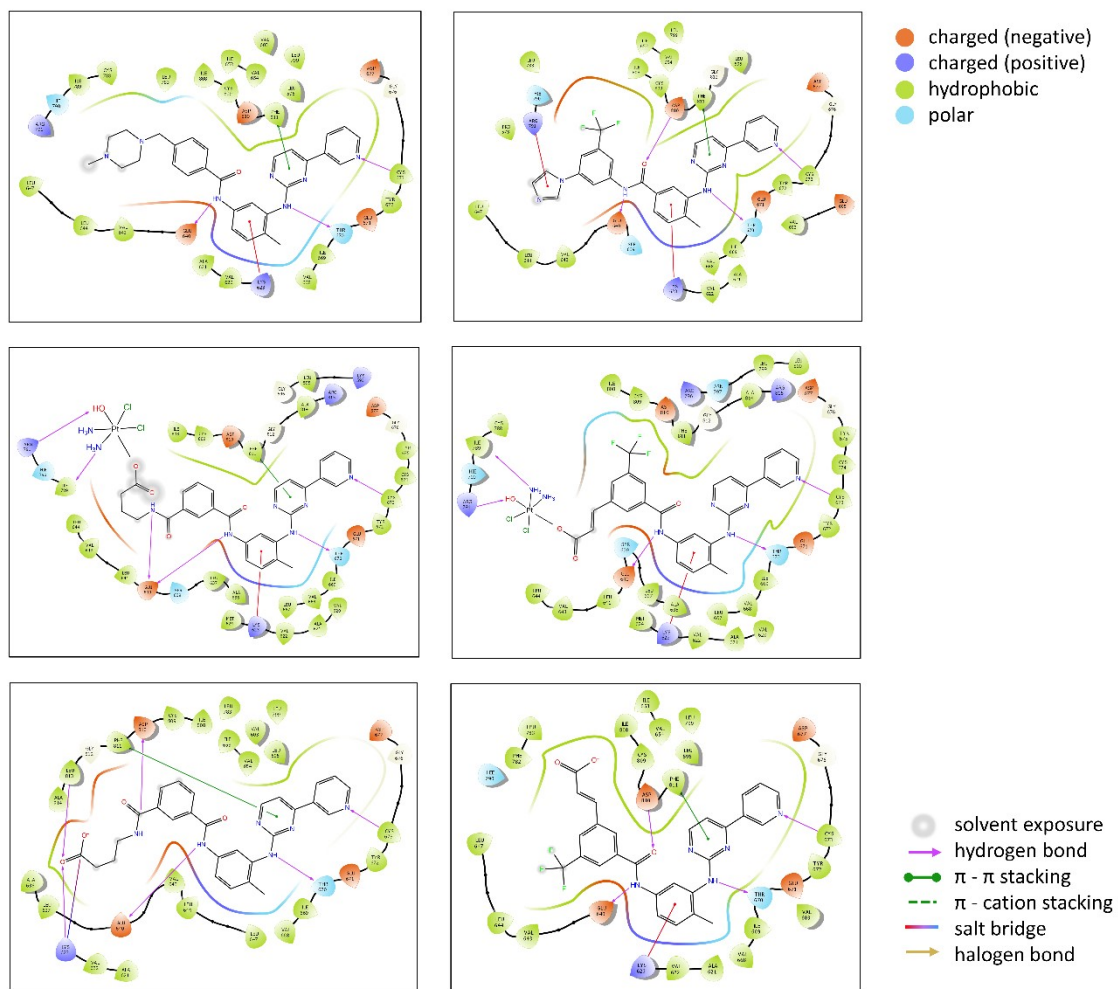


Fig. 17S. Two-dimensional interaction diagrams for best scoring poses of imatinib, **A**, and **5** (left panel top to bottom), and nilotinib, **B**, and **11** (right panel top to bottom) after induced fit (IFD) docking in c-KIT with Glide. Legend for amino acid residues and interaction types is given on the right.

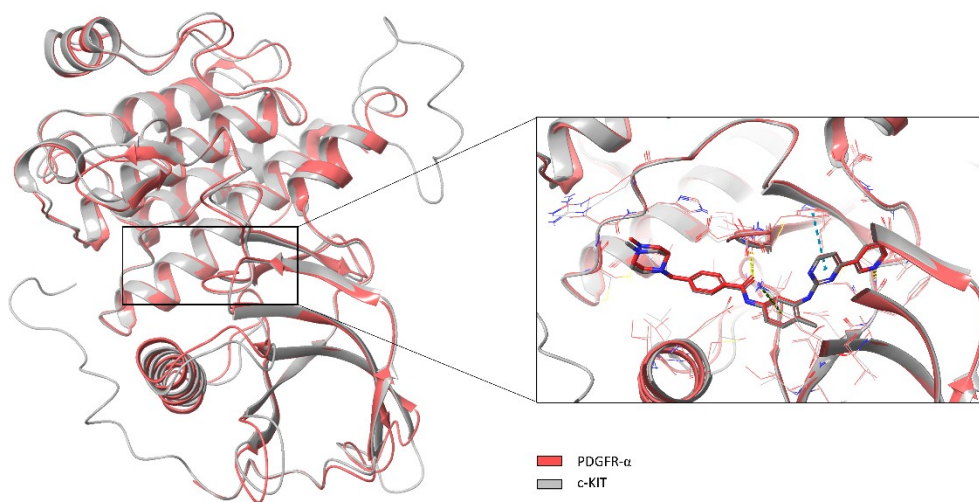


Fig. 18S. Alignment of PDGFR- α and c-KIT proteins and enlarged area of their binding sites with imatinib.

Contacts formed between the six ligands and T670I mutated c-KIT in the flexible docking with Glide

IFD docked poses of the six ligands in c-KIT with T670I mutation are shown in Figure 18S and their two-dimensional interaction diagrams can be seen in Figure 19S. This crucial mutation of a polar residue in the centre of the binding pocket of c-KIT, THR670, which was seen to be an active hydrogen bond acceptor for a studied set of ligands, into a hydrophobic ILE with an ethyl side chain pointing into the binding pocket, is known to significantly hinder the inhibiting activity of imatinib and nilotinib. Loss of this HB interaction affects the ability of 4-pyridyl-pyrimidine core to bury itself deeply into the binding site, causing a reduced depth of entry of the whole ligand molecule into the binding cavity, as well as a less than ideal volume fit with a significant empty space, shown on the example of imatinib in 19S left. This, in turn, distances pyridine ring from CYS673 which was also captured as a consistent hydrogen donor for the six ligands. Instead, any interactions of the terminal 4-pyridyl-pyrimidine fragment are established through pyrimidine ring only, π - π stacking and HB with PHE811 and LYS623 for imatinib, and π -cation and HB interaction with LYS623 and ASP810 for nilotinib. In addition to a single HB formed between an amide NH and GLU640 (imatinib) or ASP810 (nilotinib), there are no other interactions between ligands and mutated receptor.

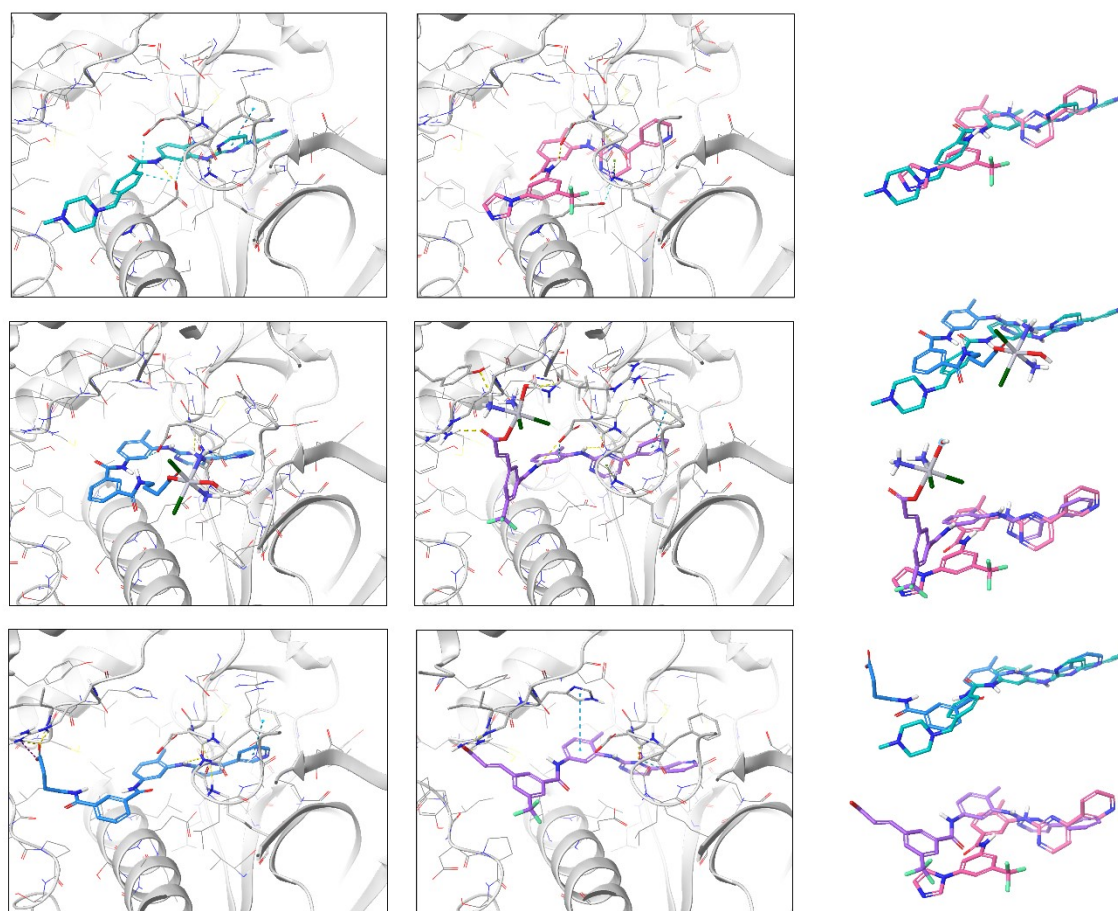


Fig. 19S. Best scoring poses of imatinib, **A** and **A_ligand-COOH** (left panel, top to bottom), and nilotinib, **B** and **B_ligand-COOH** (middle panel, top to bottom) after induced fit (IFD) in c-KIT with T-I mutation in position 670 docking with Glide. Alignment of ligand pairs is shown in the right panel (top to bottom), colouring matching the colouring in the ligand-receptor figures. For interaction colour scheme follow the caption of Figure 3.

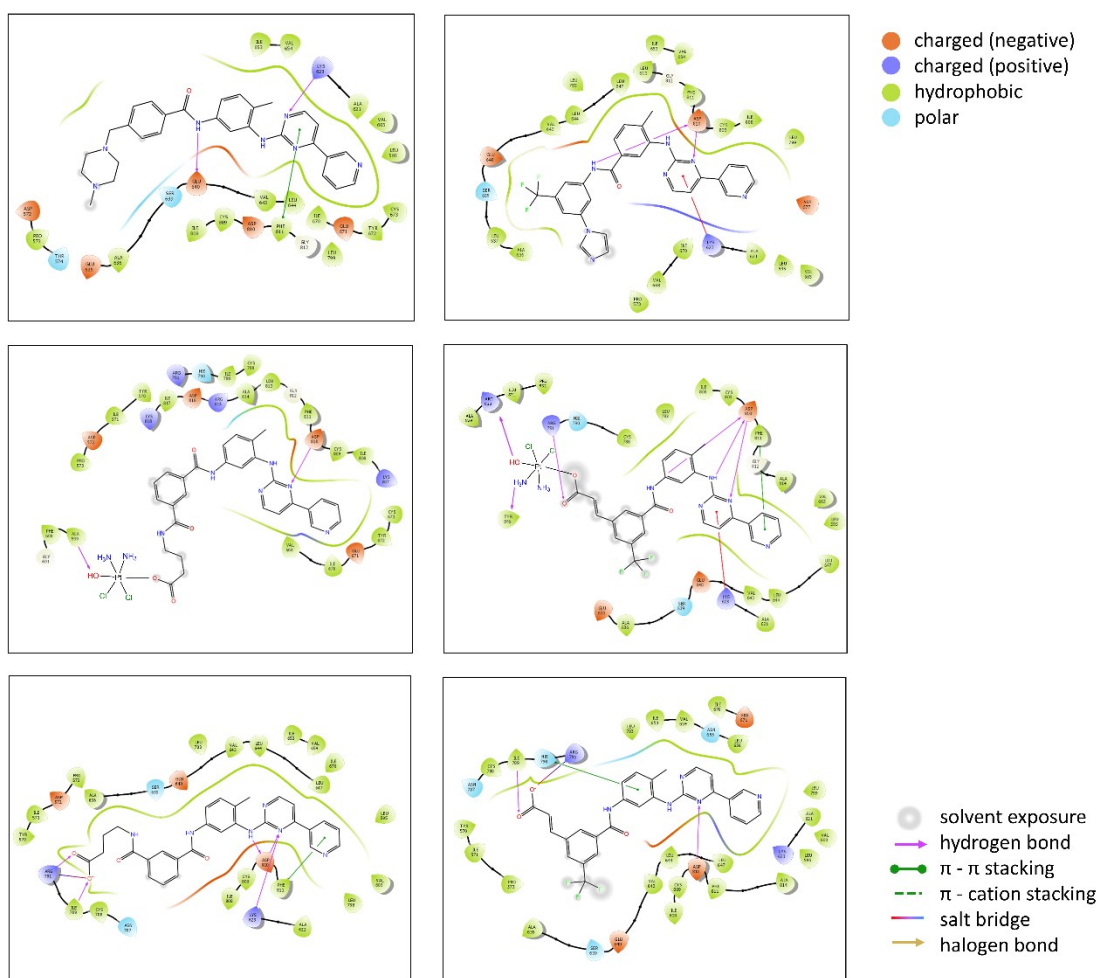


Fig. 20S. Two-dimensional interaction diagrams for best scoring poses of imatinib, **A** and **A_ligand-COOH** (left panel top to bottom), and nilotinib, **B** and **B_ligand-COOH** (right panel top to bottom) after induced fit (IFD) docking in T670I mutated c-KIT with Glide. Legend for amino acid residues and interaction types is given on the right.

Molecular Dynamics

Docking scores are very approximate, qualitative estimates of the binding affinity of the ligand for the protein and it has been shown they do not correlate with experimentally measured binding constants.^[8] This is mainly due to the protein conformational rigidity as well as solvation/desolvation effects which are not taken into the account. Additional caveat is the stability of the predicted pose in dynamical environment protein-ligand complexes find themselves in. Molecular dynamics (MD) simulations are an excellent approach to consider both the dynamics and the solvation.

The bottleneck of MD simulations, on the other hand, are force fields. The incompleteness of force field parameters has been a long-standing problem, especially for metal-related systems. For small organic molecules, generation of parameters has been well developed and automatized by a range of programmes such as ANTECHAMBER^[9] and CGenFF.^[10] To derive force field parameters for metal-containing systems, force constants can be directly derived from the Cartesian-based Hessian matrix after the QM calculation, as proposed in Seminario^[11] and Ayer methods.^[12] In this work, CHARMM36 force field was implemented for receptors, CGenFF platform was used to generate parameters of imatinib, nilotinib, and acid prodrug derivatives, and Seminario method as implemented in Visual Force Field Derivation Toolkit (VFFDT)^[13] was employed for derivation of force and angle constants for the metal centre and its chelating agents based on Hessian matrixes from Gaussian QM calculations. For solvent molecules, a CHARMM TIP3P water model was used.^[14]

To assess the stability of the docking poses obtained from Glide, MD simulations were performed in Gromacs.^[15,16] First, the ligand binding structures obtained through docking were solvated with approximately 14 000 water molecules at a physiological concentration of NaCl. Then, a simple energy minimisation was performed, followed by a short 10 ps equilibration in the NVT ensemble, and a longer 10 ns equilibration in the NPT ensemble with positional restraints on protein and ligand heavy atoms. After the system equilibration, 100 ns production MD runs were conducted under 310 K and 1 atm NPT conditions without any restraints. The Nose-Hoover thermostat^[17], with a relaxation time of 1 ps, and the Berendsen barostat^[18], with a relaxation time of 2 ps, were used. The cutoff radius of the Lennard-Jones (LJ) and electrostatic interactions were set to 1.2 nm, and the MD time step to 2 fs. To describe long-range electrostatic interactions, the particle mesh Ewald (PME) method was used.^[19] Root-mean-square deviation (RMSD), root-mean-square fluctuation (RMSF), and other interactions were analysed using internal Gromacs tools (gmx rms, rmsf, hbond etc) over full trajectories, taking configurations in every 50 ps.

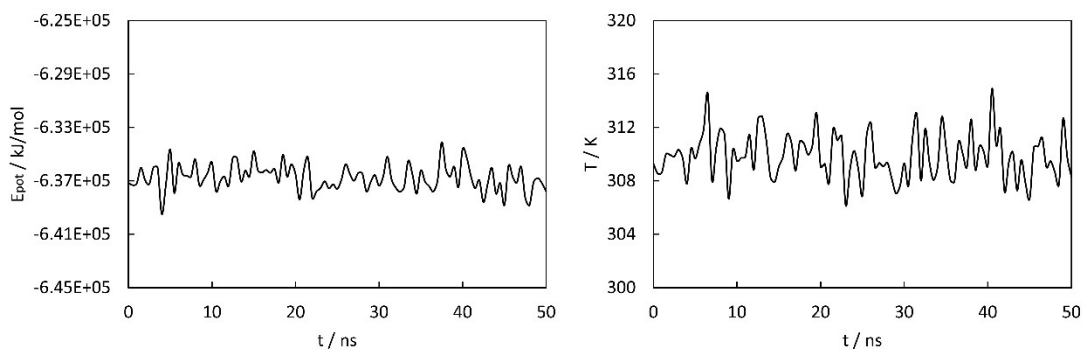


Fig. 21S. Potential energy, E_{pot} (left), and temperature, T (right), time evolution over a 50 ns MD simulation of imatinib-PDGFR- α complex **A**.

Detailed analysis of MD production for imatinib and its derivatives complexed with PDGFR- α is showcased through a series of structural graphs in Figure 21S (SI). The average deviations observed in protein RMSD, 0.13, 0.12, and 0.12 nm and ligand RMSD, 0.11, 0.14, and 0.09 nm for PDGFR- α complexed with imatinib, **A** and **A_ligand-COOH**, respectively, indicate that complexes are very stable. The radius of gyration shows moderate modifications in the secondary structure of PDGFR- α , but also reflects the overall stability of the complexes, meaning that despite the structural changes caused by the compound binding, the protein remains folded, and no denaturation occurs negating any termination of the ligand inhibitory pathway. The flexibility patterns of the individual residues about their mean positions were studied through the RMSF analysis. The imatinib-PDGFR- α and **A** and **A_ligand-COOH** showed minimal fluctuations with an average RMSF of 0.11 nm in all cases. The complexes were relatively more stable near the interface domain with the HB network (ALA640-GLY680 and LEU809-ASP836), whereas the fluctuations of a higher magnitude were observed for the hydrophobic subdomain of the binding cavity and other residues within the same beta-sheet and belonging loops (LEU599-VAL624). A flexible coil (SER890-ASP902) exposed at the protein surface far from the binding site also showed more pronounced fluctuations.

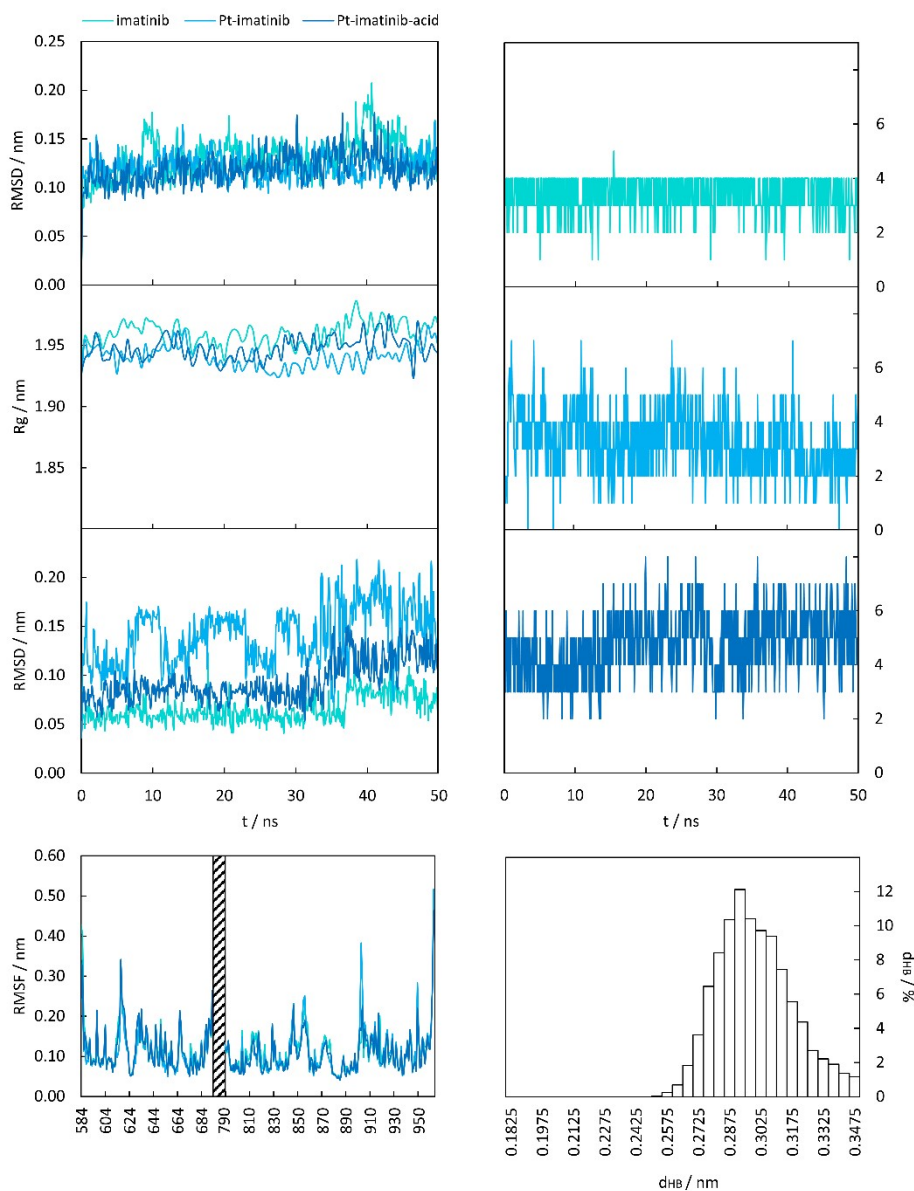


Fig. 22S. Analysis of MD trajectories after the 50 ns NPT production runs conducted on imatinib- (cyan), **A** (blue), and **A_ligand-COOH** with PDGFR- α (dark blue) complexes. Protein RMSD (nm), protein radius of gyration (R_g , nm), ligand RMSD (nm), and RMSF (nm) per residue are shown in the left panel (top to bottom). Hydrogen bond (HB) count and length (d_{HB} , nm) distribution are shown in the bottom right panel.

Principal component analysis was conducted in order to determine the relationship between statistically meaningful conformations sampled during the trajectory and recover a partial complex free energy profile correlated to the major global motions of the ligand. Through an eigenvalue rank plot it was discovered that the first two principal components (PC1 and PC2) are responsible for more than 85% of the total variance, and their correlation is projected in Figure 22S. Multiple energy clusters per system depict the structural transition between distinct active states, and by retrieving the two lowest energy structures it can be seen that different clusters appear due to the fluctuation in the position of the piperazine ring of imatinib and that of long tails with Pt-complex **A** or the corresponding ligand **A_ligand-COOH**.

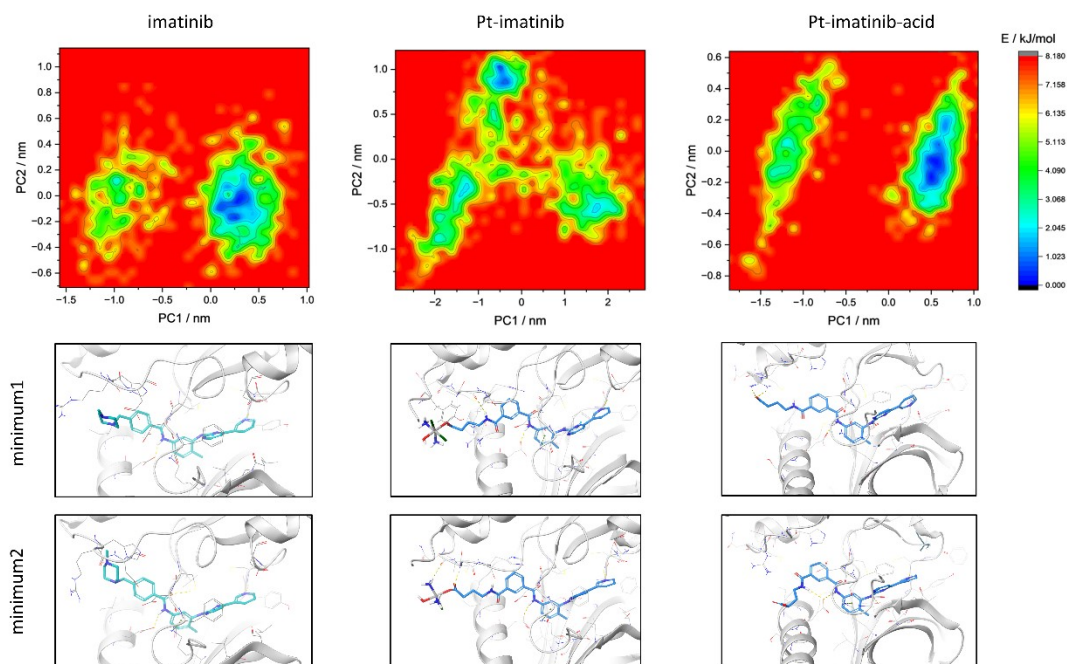


Fig. 23S. Principal component analysis of the 50 ns NPT production runs conducted on imatinib- (left), complex A (middle), and A_{ligand-COOH} -PDGFR- α (right) complexes. Projection of principle component 1 (PC1) on principal component 2 (PC2) with corresponding complex structures belonging to the energy minima.

To better understand which residues of the receptors are relevant for the binding process, trajectories were analysed by considering the statistical distribution in terms of contacts between ligands and single residues and the corresponding maps are shown in the top panel of Figure 22S. The contact frequency is defined as a fraction of the trajectory in which a certain contact is made, considering all contacts with atoms in the query residue, with contact defined within a cut-off distance of 4.0 Å.

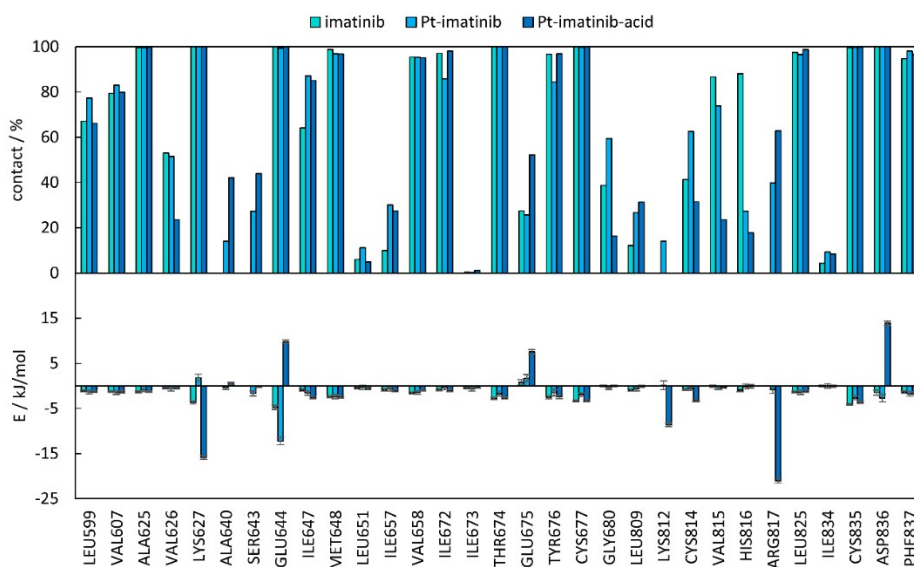


Fig. 24S. Analysis of contacts between the ligand and binding site residues and decomposed contribution of those residues to the free binding energy of imatinib (cyan), A (blue), and A_{ligand-COOH} (dark blue) within PDGFR- α .

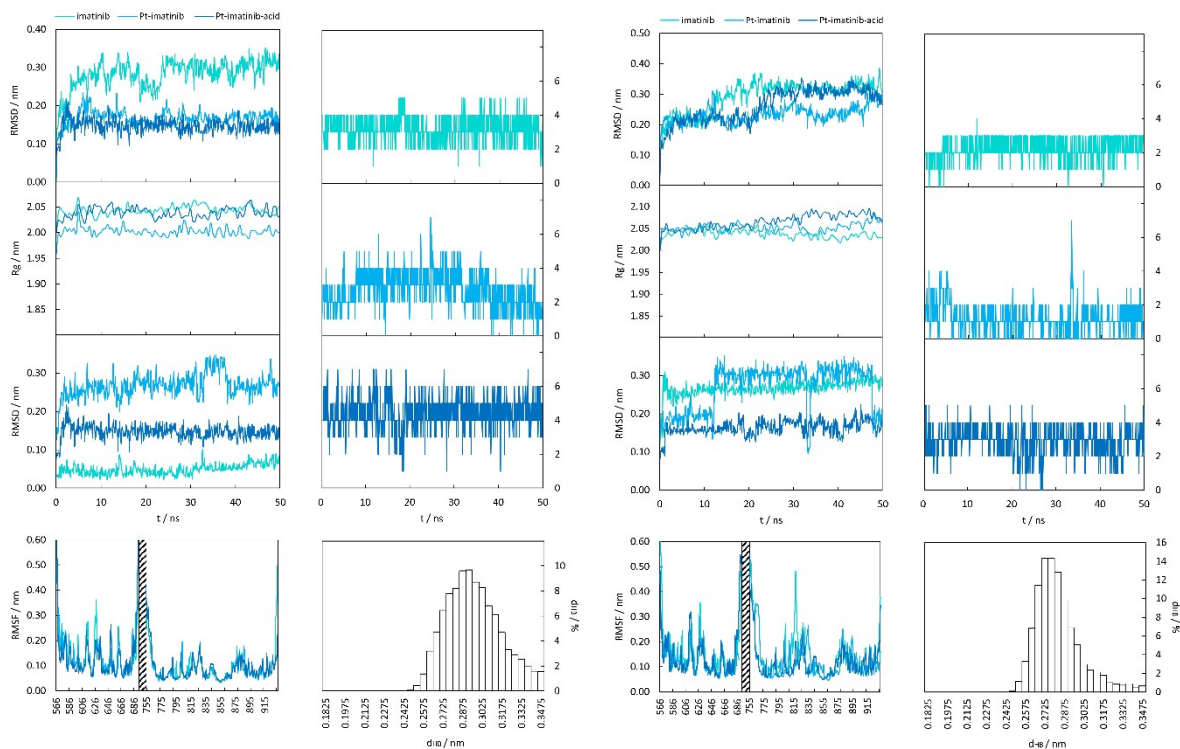


Fig. 255. Analysis of MD trajectories after the 50 ns NPT production runs conducted on imatinib- (cyan), A (blue), and A_ligand-COOH (dark blue) complexes with c-KIT (left panel) and T670I mutated c-KIT (right panel).

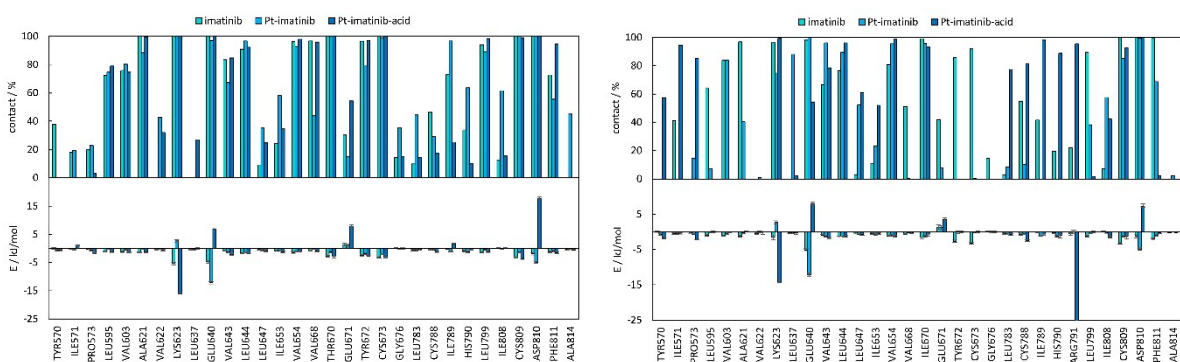


Fig. 265. Analysis of contacts between the ligand and binding site residues and decomposed contribution of those residues to the free binding energy of imatinib (cyan), A (blue), and A_ligand-COOH (dark blue) within c-KIT (left) and c-KIT with T670I mutation (right).

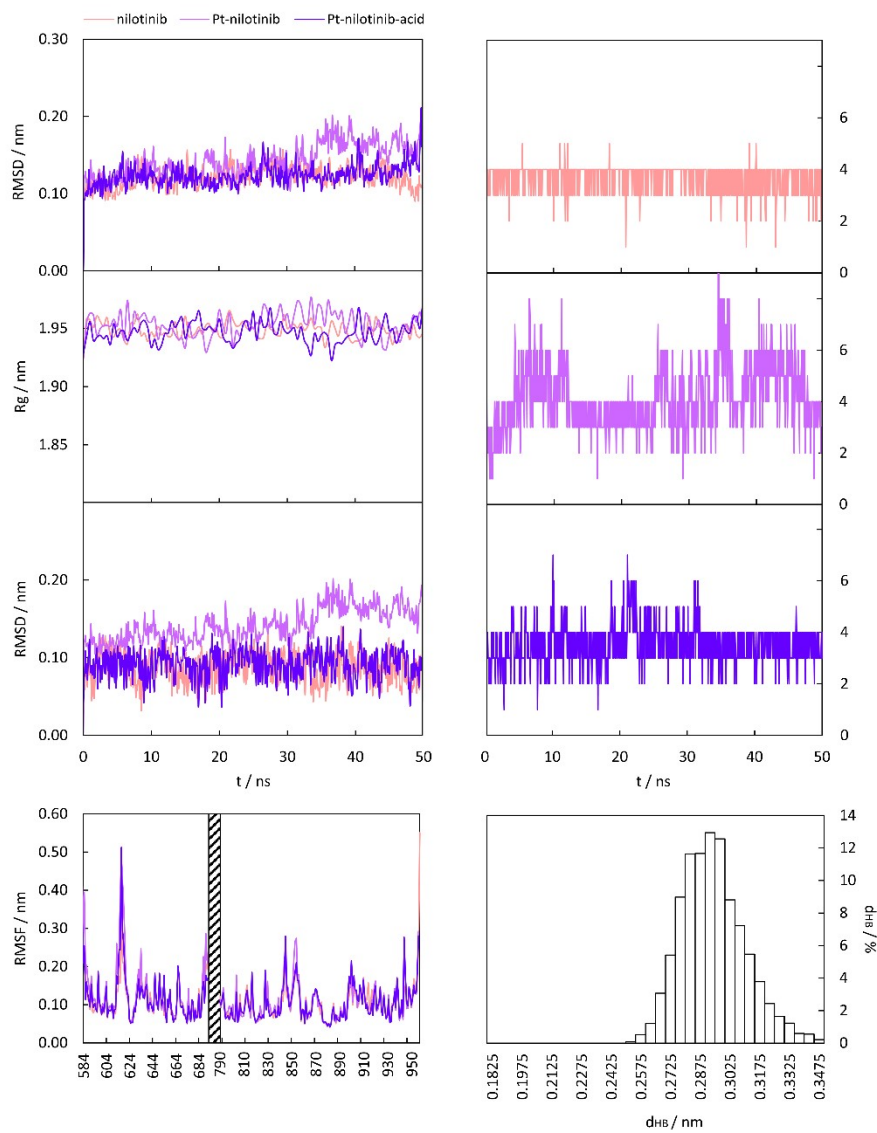


Fig. 27S. Analysis of MD trajectories after the 50 ns NPT production runs conducted on nilotinib- (pink), **B** (purple), and **B_ligand-COOH** PDGFR- α (dark purple) complexes. Protein RMSD, protein radius of gyration (R_g), ligand RMSD, and RMSF per residue are shown in the left panel. Hydrogen bond (HB) count and length (d_{HB}) distribution are shown in the right panel.

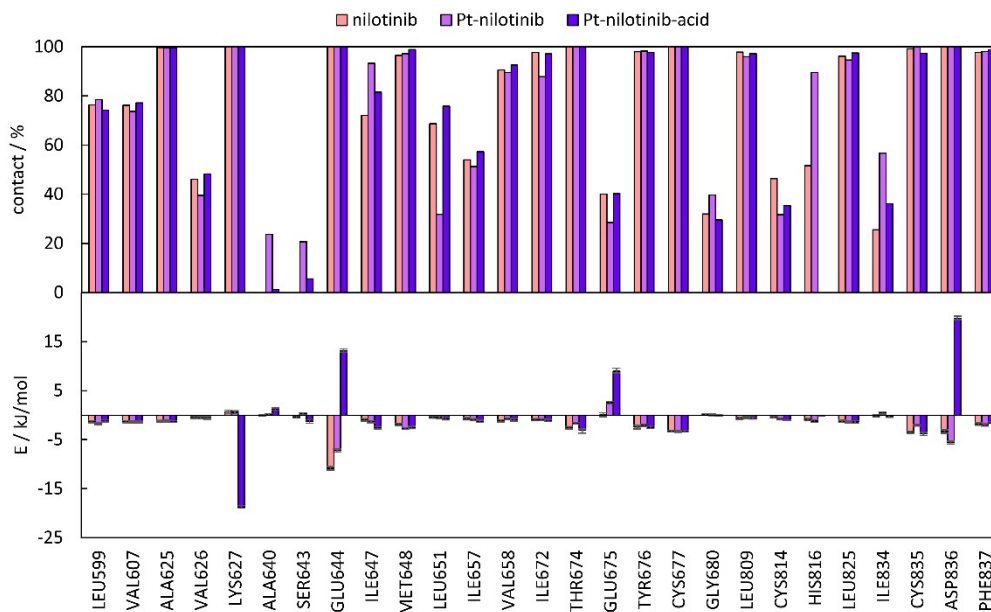


Fig. 28S. Analysis of contacts between the ligand and binding site residues and decomposed contribution of those residues to the free binding energy of nilotinib- (pink), **B** (purple), and **B_ligand-COOH** (dark purple) within PDGFR- α .

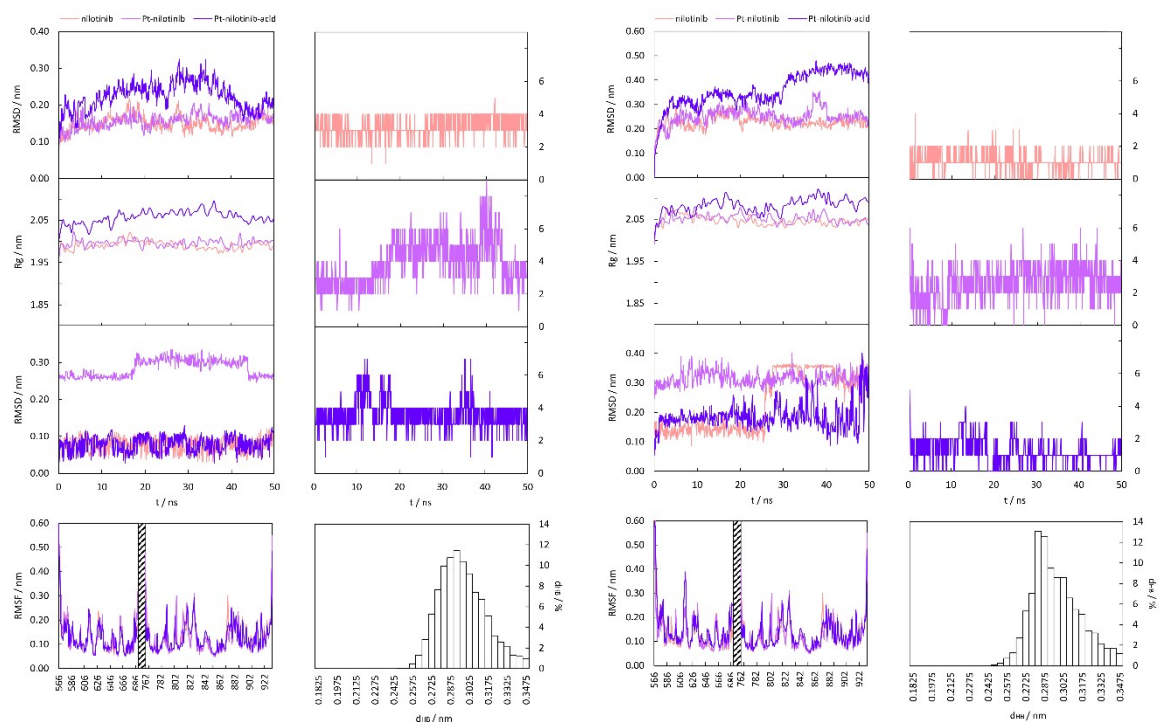


Fig. 29S. Analysis of MD trajectories after the 50 ns NPT production runs conducted on nilotinib- (pink), **B** (purple), and **B_ligand-COOH** (dark purple) complexes with c-KIT (left panel) and T670I mutated c-KIT (right panel).

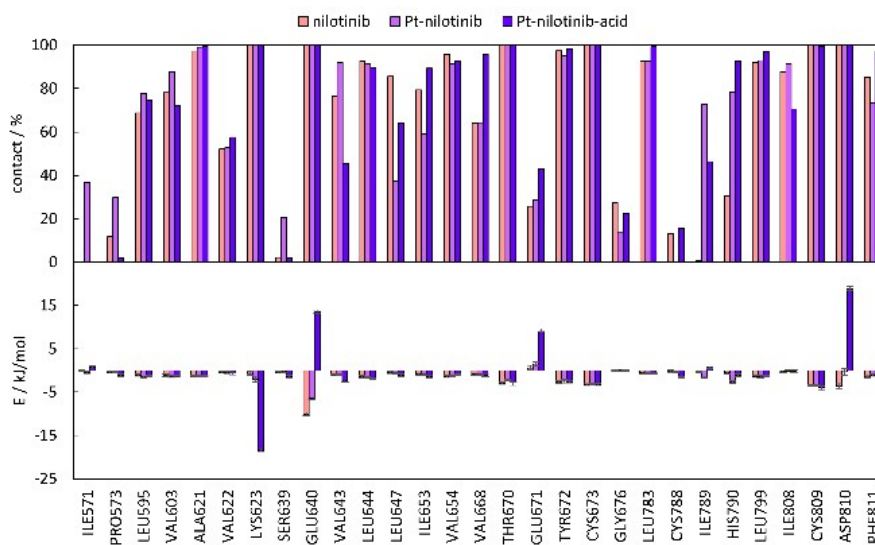


Fig. 30S. Analysis of contacts between the ligand and binding site residues and decomposed contribution of those residues to the free binding energy of nilotinib- (pink), **B** (purple), and **B_ligand-COOH** (dark purple) within c-KIT (up) and c-KIT with T670I mutation (down).

To calculate a quantitative approximation to the free binding energy, a MMPBSA approach [20,21, 22] which assesses individually solvation energies of free and complexed ligand as well as interaction energy of the ligand-receptor complex was used as implemented in gmx_MMPBSA tool.^[23,24]

Table 1S. Free binding energy (E_{bin}) and its components: van der Waals energy (ΔvdW), electrostatic energy (ΔE_{el}), polar solvation energy based on Poisson-Boltzmann approach (ΔEPB), non-polar solvation energy based on SASA approach (ΔnP), and dispersion energy (ΔE_{disp}) calculated using the MMPBSA method for imatinib, nilotinib, **A**, **B**, **5** and **11** interacting with PDGFR- α , c-KIT, and c-KIT mutated in position 670 (T-I). All energies are expressed in kJ/mol.

		imatinib	A	5	nilotinib	B	11
PDGFR- α	ΔvdW	-	-	-	-60.58±0.75	-66.91±1.31	-61.84±0.72
	ΔE_{el}	63.82±1.10	66.71±0.81	62.98±0.69	-8.49±0.09	-5.80±1.11	-14.36±0.29
	ΔEPB	-7.53±0.26	-6.79±1.20	-	12.12±0.12	14.36±0.64	19.51±0.12
	ΔnP	11.41±0.13	14.63±0.61	26.79±0.02	-44.31±0.22	-50.11±0.23	-44.24±0.18
	ΔE_{disp}	47.51±0.13	48.26±0.32	46.90±0.13	76.57±0.25	85.63±0.22	76.25±0.24
	E_{bin}	80.11±0.12	85.31±0.06	79.88±0.14	-	-	-
		27.36±1.45	21.86±2.02	26.94±1.25	24.69±1.10	22.84±2.08	24.68±1.23
c-KIT	ΔvdW	-	-	-	-60.38±0.66	-64.62±0.98	-62.40±1.05
	ΔE_{el}	63.96±0.90	66.63±1.19	65.08±0.52	-9.03±0.05	-8.29±0.87	-5.07±0.29
	ΔEPB	-7.44±0.09	-	-	12.38±0.10	13.52±0.43	11.83±0.34
	ΔnP	12.68±0.06	18.01±0.10	23.59±0.18	-44.65±0.08	-50.87±0.06	-45.63±0.05
	ΔE_{disp}	47.05±0.14	52.77±0.38	47.58±0.09	77.49±0.07	86.94±0.25	78.36±0.21
	E_{bin}	82.15±0.08	91.91±0.16	84.28±0.01	-24.20±1.11	-23.32±1.62	-22.92±1.50
		23.62±1.30	20.44±2.08	24.19±1.18			
c-KIT T670I	ΔvdW	-	-	-	-45.70±1.03	-58.00±0.67	-43.96±1.13
	ΔE_{el}	59.87±0.38	55.25±1.17	46.81±0.89	-5.34±0.04	-6.93±0.91	-10.29±1.23
	ΔEPB	-4.64±0.22	-5.45±1.10	-	9.61±0.29	12.75±0.40	15.07±1.14
	ΔnP	10.05±0.07	13.78±0.55	19.71±0.57	-36.66±0.24	-44.10±0.46	-34.44±0.01
	ΔE_{disp}	43.67±0.20	42.72±0.48	38.33±0.37	64.74±0.28	79.62±0.12	60.08±0.28
	E_{bin}	79.74±0.60	75.98±0.16	68.75±0.38	-	-	-
		18.39±1.20	13.67±2.07	13.15±1.78	13.34±1.45	16.67±1.50	13.54±2.20

Biological Details

Experiments with Cultured Human Cancer Cells

All tested compounds were dissolved in DMSO just before the experiment, and a calculated amount of drug solution was added to the cell growth medium to a final solvent concentration of 0.5%, which had no detectable effects on cell viability. Cisplatin was dissolved in 0.9 % NaCl solution. MTT (3-(4,5-dimethylthiazol-2-yl)-2,5-diphenyltetrazolium bromide) and DTNB were obtained from Sigma Chemical Co, St. Louis, USA.

Cell Cultures

Human SH-SY5Y neuroblastoma carcinoma cells were obtained by ATCC (American Type Culture Collection, Rockville, MD, USA). The human ovarian cancer cell line 2008 were kindly provided by Prof. G. Marverti (Department of Biomedical Science of Modena University, Italy). Cell lines were maintained in the logarithmic phase at 37 °C in a 5% carbon dioxide atmosphere using RPMI-1640 medium (EuroClone) containing 10% fetal calf serum (EuroClone, Milan, Italy), antibiotics (50 units/mL penicillin and 50 µg/mL streptomycin) and 2 mM l-glutamine.

MTT Assay

The growth inhibitory effect on tumor cells was evaluated by means of the MTT assay. Briefly, 3–8 x 10³ cells/well, dependent upon the growth characteristics of the cell line, were seeded in 96-well microplates in growth medium (100 µL). After 24 h, the medium was removed and replaced with a fresh one containing the compound to be studied at the appropriate concentration. Triplicate cultures were established for each treatment. After 72 h, each well was treated with 10 µL of a 5 mg/mL MTT saline solution, and following 5 h of incubation, 100 µL of a sodium dodecyl sulfate (SDS) solution in HCl 0.01 M was added. After overnight incubation, cell growth inhibition was detected by measuring the absorbance of each well at 570 nm using a Bio-Rad 680 microplate reader. The mean absorbance for each drug dose was expressed as a percentage of the control untreated well absorbance and plotted vs. drug concentration. IC₅₀ values, the drug concentrations that reduce the mean absorbance at 570 nm to 50% of those in the untreated control wells, were calculated by the four-parameter logistic (4-PL) model. The evaluation was based on means from at least three independent experiments.

Inhibition of PDGFR α and c-KIT Kinase Activity

The inhibition of the kinase activity PDGFR- α and c-KIT was assessed through the KinomeScan assay service (DiscoverX) which is run in parallel with known inhibitors. An exhaustive description of the assay is given in ref.^[25]

References

1. J. Da Chai, M. Head-Gordon, *Phys. Chem. Chem. Phys.* 2008, **10**, 6615–6620.
2. P. J. Hay, W. R. Wadt, *J Chem Phys* 1985, **82**, 299–310.
3. M. J. Frisch, J. A. Pople, J. S. Binkley, *J Chem Phys* 1984, **80**, 3265–3269.
4. B. Mennucci, J. Tomasi, R. Cammi, J. R. Cheeseman, M. J. Frisch, F. J. Devlin, S. Gabriel, P. J. Stephens, *J. Phys. Chem. A* 2002, **106**, 6102–6113.
5. G. Madhavi Sastry, M. Adzhigirey, T. Day, R. Annabhimoju, W. Sherman, *J. Comput. Aided Mol. Des.* 2013, **27**, 221–234.
6. R. A. Friesner, J. L. Banks, R. B. Murphy, T. A. Halgren, J. J. Klicic, D. T. Mainz, M. P. Repasky, E. H. Knoll, M. Shelley, J. K. Perry, D. E. Shaw, P. Francis, P. S. Shenkin, *J. Med. Chem.* 2004, **47**, 1739–1749.
7. W. Sherman, H. S. Beard, R. Farid, *Chem. Biol. Drug. Des.* 2006, **67**, 83–84.
8. X.-Y. Meng, H.-X. Zhang, M. Mezei, M. Cui, *Curr. Comput. Aided Drug. Des.* 2011, **7**, 145–157.
9. J. Wang, W. Wang, P. A. Kollman, D. A. Case, *J. Mol. Graph. Model* 2006, **25**, 247–260.
10. K. Vanommeslaeghe, A. D. MacKerell, *J. Chem. Inf. Model* 2012, **52**, 3144–3154.
11. J. M. Seminario, *Int. J. Quantum Chem.* 1996, **60**, 1271–1277.

12. S. K. Burger, M. Lacasse, T. Verstraelen, J. Drewry, P. Gunning, P. W. Ayers, *J. Chem. Theory Comput.* 2012, **8**, 554–562.
13. S. Zheng, Q. Tang, J. He, S. Du, S. Xu, C. Wang, Y. Xu, F. Lin, *J. Chem. Inf. Model* 2016, **56**, 811–818.
14. S. Boonstra, P. R. Onck, E. Van Der Giessen, *J. Phys. Chem. B* 2016, **120**, 3692–3698.
15. H. J. C. Berendsen, D. Van Der Spoel, R. Van Drunen, *Comp. Phys. Comm.* 1995, **91**, 43 - 56
16. S. Páll, A. Zhmurov, P. Bauer, M. Abraham, M. Lundborg, A. Gray, B. Hess, E. Lindahl, *J. Chem. Phys.* 2020, **153**, 134110.
17. D. J. Evans, B. L. Holian, *J. Chem. Phys.* 1985, **83**, 4069–4074.
18. H. J. C. Berendsen, J. P. M. Postma, W. F. Van Gunsteren, A. Dinola, J. R. Haak, *J. Chem. Phys.* 1984, **81**, 3684–3690
19. U. Essmann, L. Perera, M. L. Berkowitz, T. Darden, H. Lee, L. G. Pedersen, *J. Chem. Phys.* 1995, **103**, 8577–8593.
20. J. Srinivasan, T. E. Cheatham, P. Cieplak, P. A. Kollman, D. A. Case, *J. Am. Chem. Soc.* 1998, **120**, 9401- 9409.
21. P. A. Kollman, I. Massova, C. Reyes, B. Kuhn, S. Huo, L. Chong, M. Lee, T. Lee, Y. Duan, W. Wang, O. Donini, P. Cieplak, J. Srinivasan, D. A. Case, T. E. Cheatham, *Acc. Chem. Res.* 2000, **33**, 889–897.
22. C. Wang, D. Greene, L. Xiao, R. Qi, R. Luo, *Front. Mol. Biosci.* 2018, **4**, 87.
23. B. R. Miller, T. D. McGee, J. M. Swails, N. Homeyer, H. Gohlke, A. E. Roitberg, *J. Chem. Theor. Comput.* 2012, **8**, 3314–3321.
24. M. S. Valdés-Tresanco, M. E. Valdés-Tresanco, P. A. Valiente, E. Moreno, *J. Chem. Theor. Comput.* 2021, **17**, 6281–6291.
25. Available online: https://www.discoverx.com/products-applications/kinase-solutions?gclid=EAlaIqobChMI5-3mrL2V_gIVIM13Ch0RrAK8EAAYAiAAEgJEsPD_BwER.J.

Electronic Supporting Information (ESI)

Novel design of dual-action Pt(IV) anticancer pro-drugs based on cisplatin and derivatives of the Tyrosine Kinase Inhibitors imatinib and nilotinib

Darren Fergal Beirne, Barbara Farkaš, Chiara Donati, Valentina Gandin, Isabel Rozas, Trinidad Velasco-Torrijos, Diego Montagner

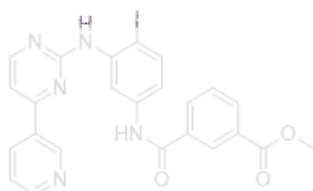
Table of contents

Materials and Methods.....	2
Characterisation Data:	
$^1\text{H}/^{13}\text{C}$ NMR, COSY, HSQC, HMBC, IR, HRMS & LCMS of 2	2-5
$^1\text{H}/^{13}\text{C}$ NMR, COSY, HSQC, HMBC, IR, HRMS & LCMS of 3	6-9
$^1\text{H}/^{13}\text{C}$ NMR, COSY, HSQC, HMBC, IR, HRMS & LCMS of 4	9-12
$^1\text{H}/^{13}\text{C}$ NMR, COSY, HSQC, HMBC, IR, HRMS & LCMS of 5	13-16
$^1\text{H}/^{13}\text{C}$ NMR, COSY, HSQC, HMBC, IR, HRMS & LCMS of 6	16-19
$^1\text{H}/^{13}\text{C}/^{195}\text{Pt}$ NMR, COSY, HSQC, HMBC, IR & HRMS of A	20-23
$^1\text{H}/^{13}\text{C}/^{19}\text{F}$ NMR, COSY, HSQC, HMBC, IR, HRMS & LCMS of 9	24-27
$^1\text{H}/^{13}\text{C}/^{19}\text{F}$ NMR, COSY, HSQC, HMBC, IR, HRMS & LCMS of 10	28-31
$^1\text{H}/^{13}\text{C}/^{19}\text{F}$ NMR, COSY, HSQC, HMBC, IR, HRMS & LCMS of 11	32-35
$^1\text{H}/^{13}\text{C}/^{19}\text{F}$ NMR, COSY, HSQC, HMBC, IR, HRMS & LCMS of 12	36-39
$^1\text{H}/^{13}\text{C}/^{19}\text{F}/^{195}\text{Pt}$ NMR, COSY, HSQC, HMBC, IR & HRMS of B	40-44
Uv-Vis Stability of A & B	44
NMR Reduction Studies of A & B	45
Computational Details: DFT Optimisation & Docking Studies.....	46-52
Computational Details: Molecular Dynamics.....	53-61
Biological Details: Experiments with Cultured Human Cancer Cells.....	62
Biological Details: Cell Cultures.....	62
Biological Details: MTT Assay.....	62
Biological Details: Inhibition of PDGFR α and c-KIT Kinase Activity.....	62
References.....	62-63

Materials and Methods

All reagents, solvents and reactants were purchased from commercial sources (Sigma-Aldrich and Flourochem) and used without further purification unless specified. [Tetrakis-(triphenylphosphine) palladium(0)] was provided by Johnson Matthey through the JM PGM Award Scheme PGMAS54. *Elemental Analyses* (Carbon, Hydrogen and Nitrogen) were performed with a PerkinElmer 2400 series II analyser. *Infrared (IR)* spectrometry was conducted on a Perkin Elmer Spectrum 100 FT-IR. Attenuated Total Reflectance Fourier transform Infrared (ATR-FTIR) spectra were taken in the region 4000 cm^{-1} to 650 cm^{-1} , using 4 scans with a resolution of 4 cm^{-1} . *ESI Mass Spectra* were recorded with a Waters LCT Premier XE Spectrometer. Microwave assisted organic syntheses were conducted using a CEM Discover microwave synthesis reactor equipped with an Explorer 12 Hybrid Autosampler. *NMR analyses* were conducted with a Bruker Advance spectrometer at 500 MHz for ^1H , 126 MHz for ^{13}C , 107 MHz for ^{195}Pt and 470 MHz for ^{19}F nuclei. Samples were typically dissolved in $\text{DMSO-}d_6$ and CDCl_3 and added to 5-mm sample tubes. The probe temperature was maintained at 298 K, unless stated otherwise. The residual solvent peaks were used as an internal standard for ^1H and ^{13}C experiments. For ^{195}Pt , an external reference of Na_2PtCl_4 in D_2O (adjusted to $\delta = -1628$ ppm from Na_2PtCl_6) was used. Chemical shifts were recorded in parts per million (ppm), while the coupling constant (J) was recorded in Hz when applicable. *TLC* was conducted using TLC Silica gel 60 RP-2 (silanized) plates with a fluorescent indicator at 254 nm, bought from Sigma-Aldrich Ireland. Lyophilisation was conducted on a Labconco Freezone 1 Dry system. *LC-MS* was performed on an Agilent Technologies 1200 Series instrument consisting of a G1322A Quaternary pump and a G1314B UV detector (254 nm) coupled to an Advion Expression L Compact Mass spectrometer (ESI) operating in positive mode. *UV-Stability Studies*: complexes A and B were dissolved in a mixture of DMSO/PBS buffer (1/9) and the UV-VIS spectra were recorded at different interval using a Varian CARY 50 spectrophotometer with a wavelength range of 200-800 nm and a scan rate of 600 nm min^{-1} . *Reduction Studies*: complexes A and B were dissolved in 500 μL of $\text{DMSO-}d_6$ (18 mM solution) and 10 eq. of ascorbic acid were added. The reduction was followed by $^1\text{H-NMR}$ and $^{195}\text{Pt NMR}$. $^1\text{H NMR}$ spectra were recorded at $t = 0\text{h}$, 1h; 2h; 4h; 6h; 10h and 24h. $^{195}\text{Pt NMR}$ spectrum was recorded at $t = 24\text{h}$.

Compound 2



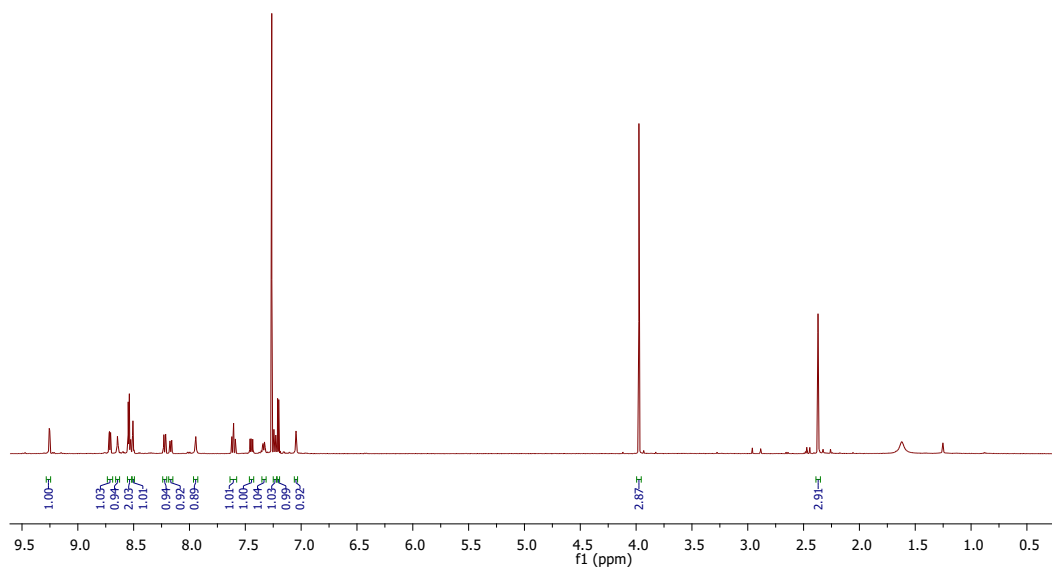


Fig. 1Sa. ^1H NMR of **2** in CDCl_3

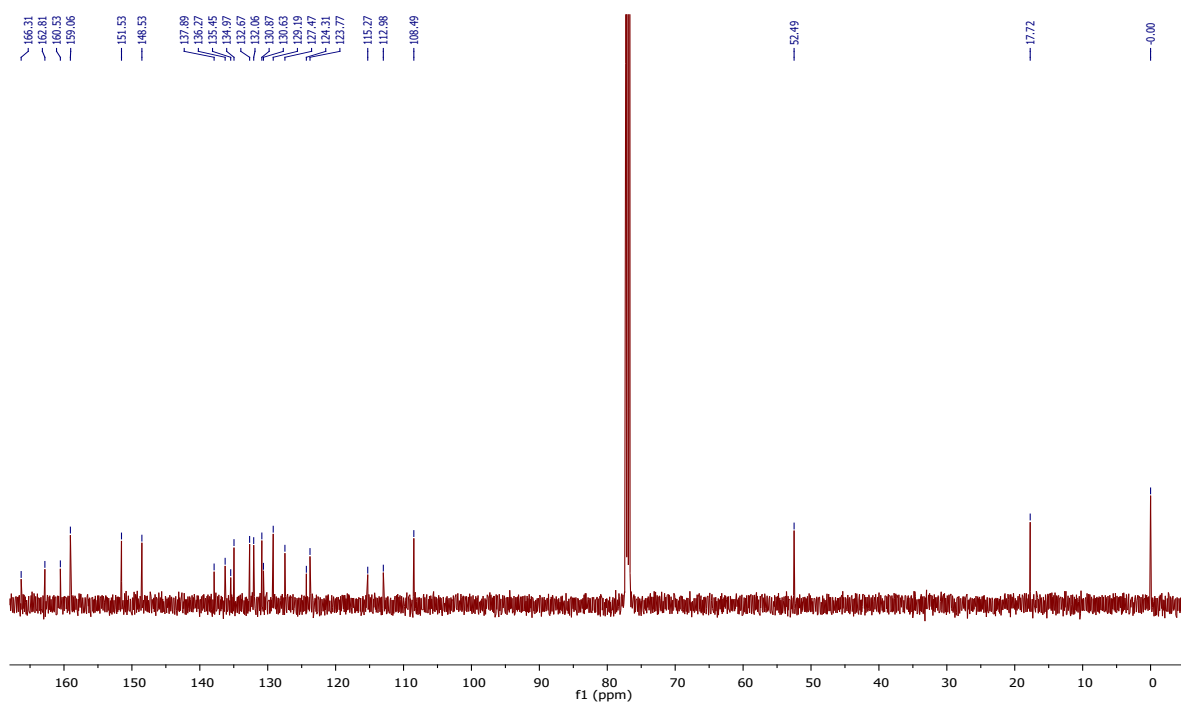


Fig. 1Sb. ^{13}C NMR of **2** in CDCl_3

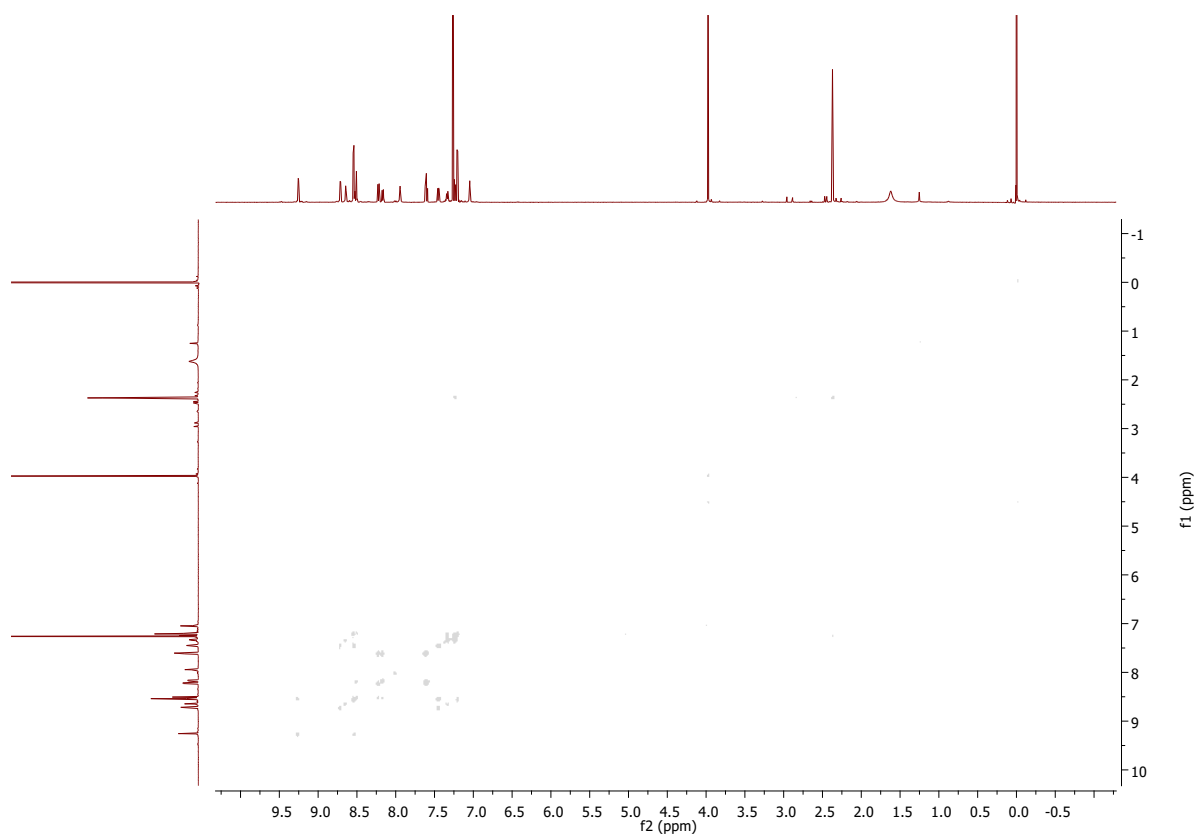


Fig. 1Sc. COSY of **2** in CDCl_3

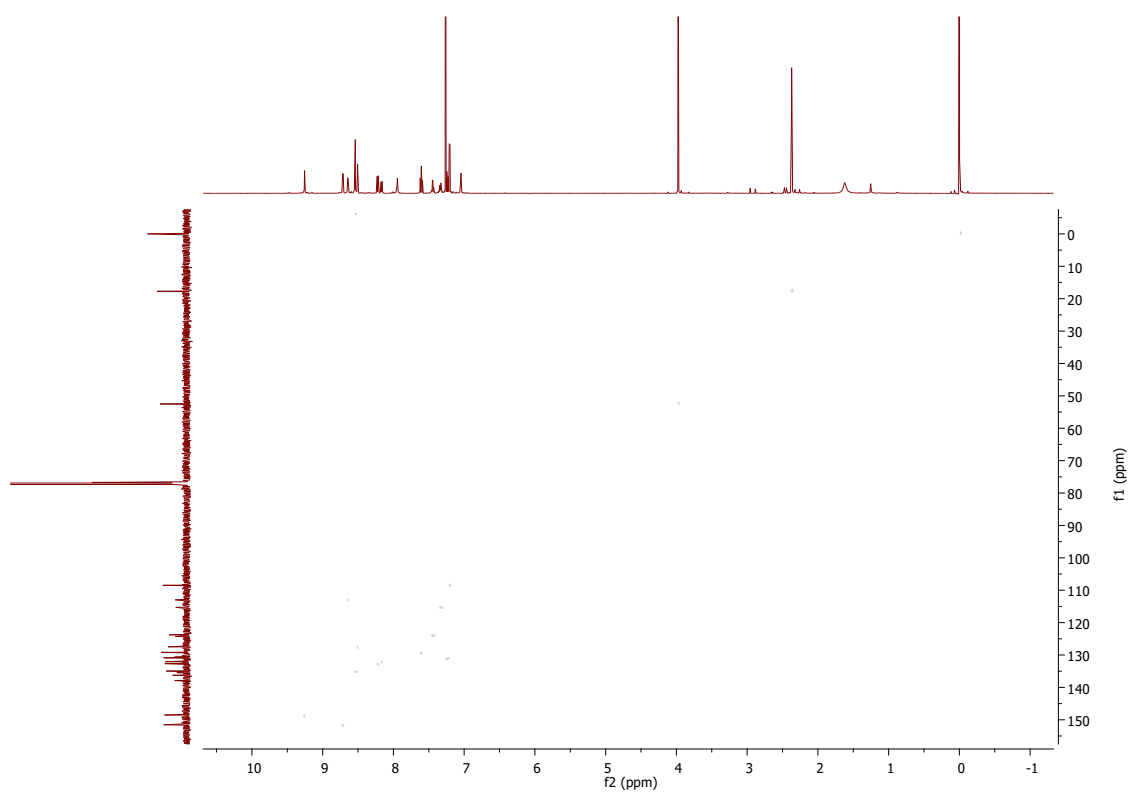


Fig. 1Sd. HSQC of **2** in CDCl_3

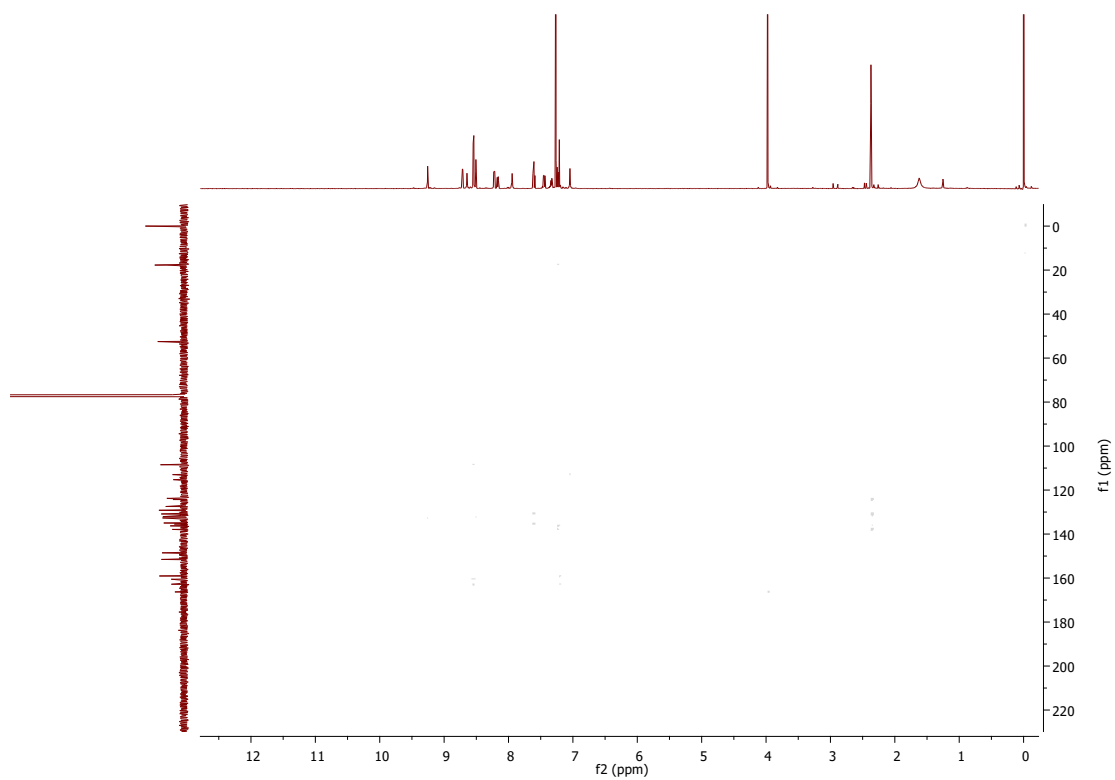


Fig. 1Se. HMBC of 2 in CDCl₃

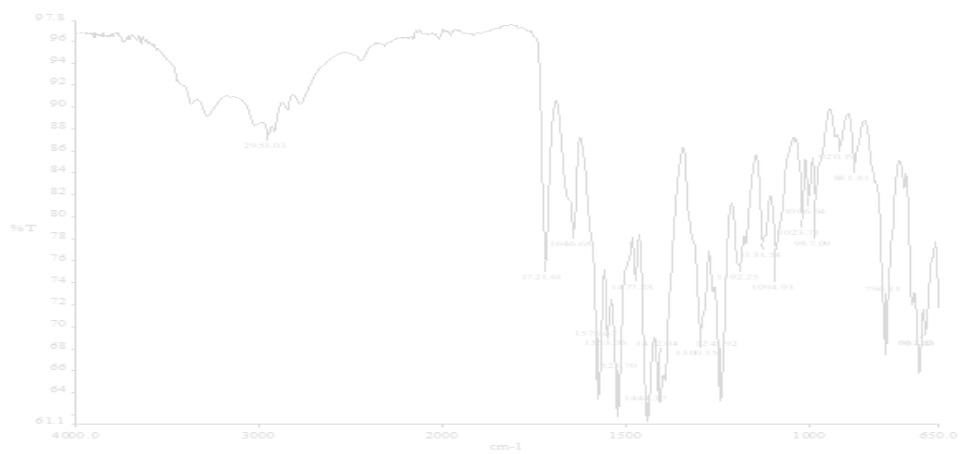


Fig. 1Sf. IR of 2



Fig. 1Sg. HRMS of 2

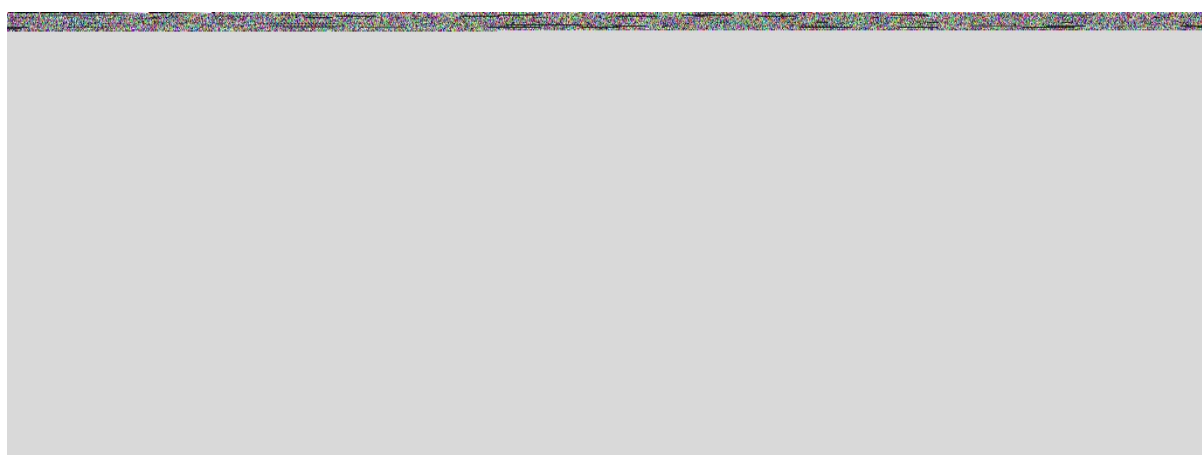


Fig. 1Sh. LCMS of 2

Compound 3

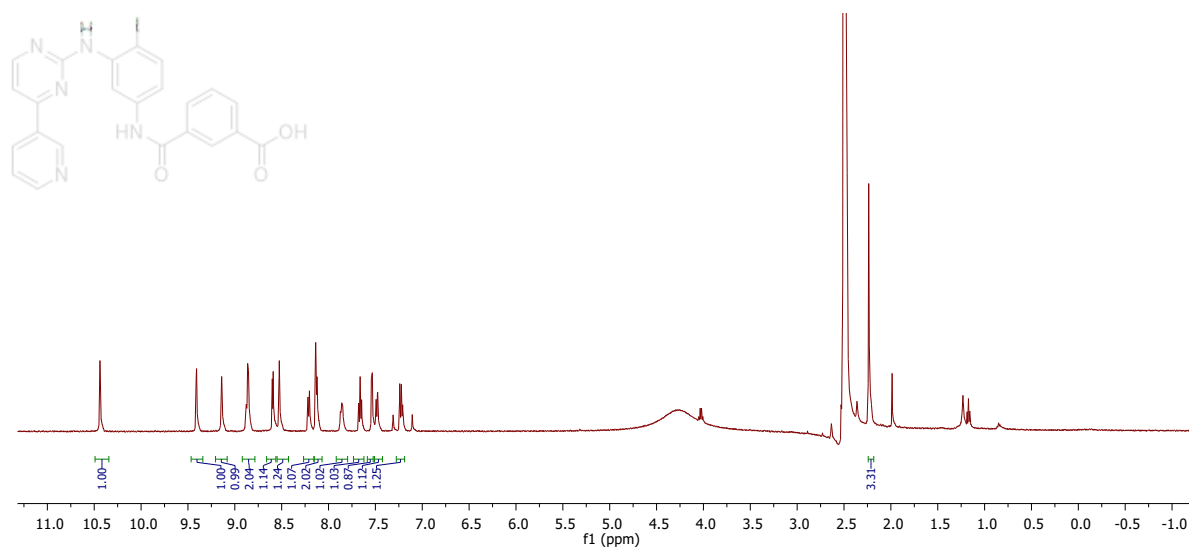


Fig. 2Sa. ^1H NMR of 3 in $\text{DMSO-}d_6$

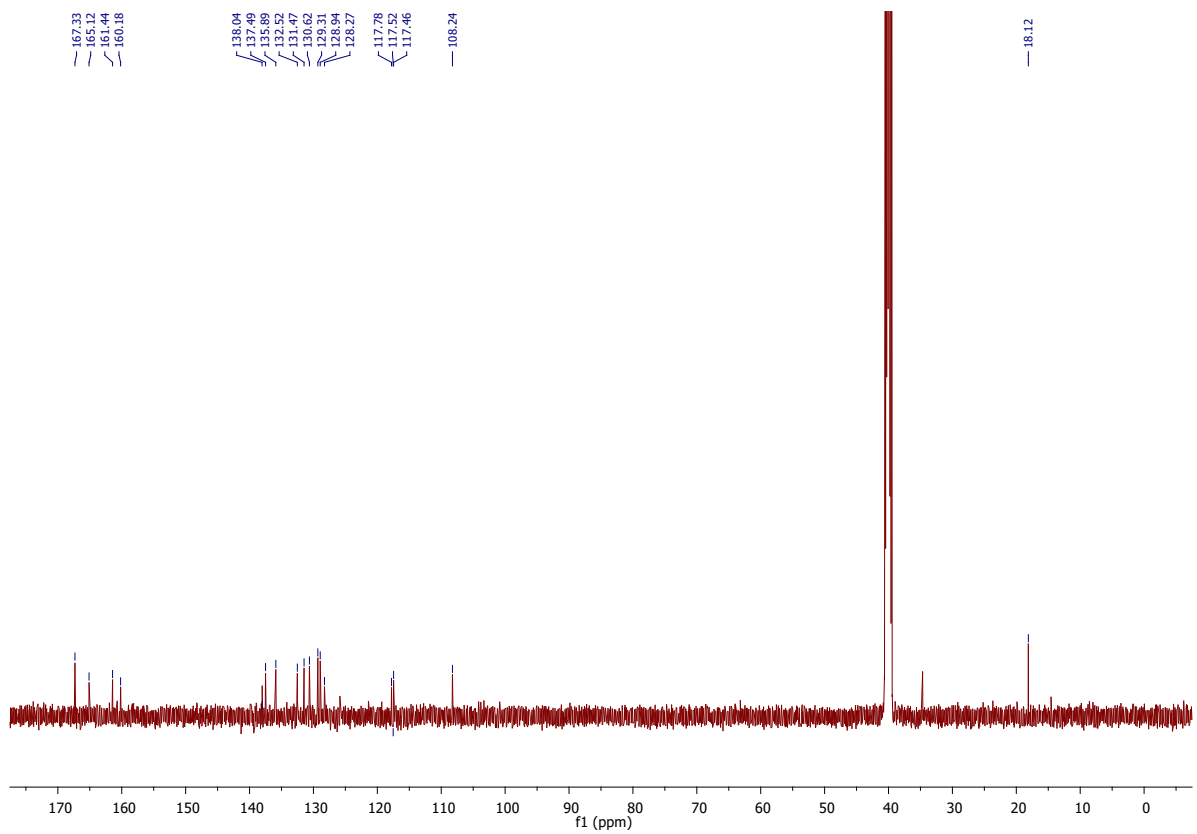


Fig. 2Sb. ^{13}C NMR of **3** in $\text{DMSO-}d_6$

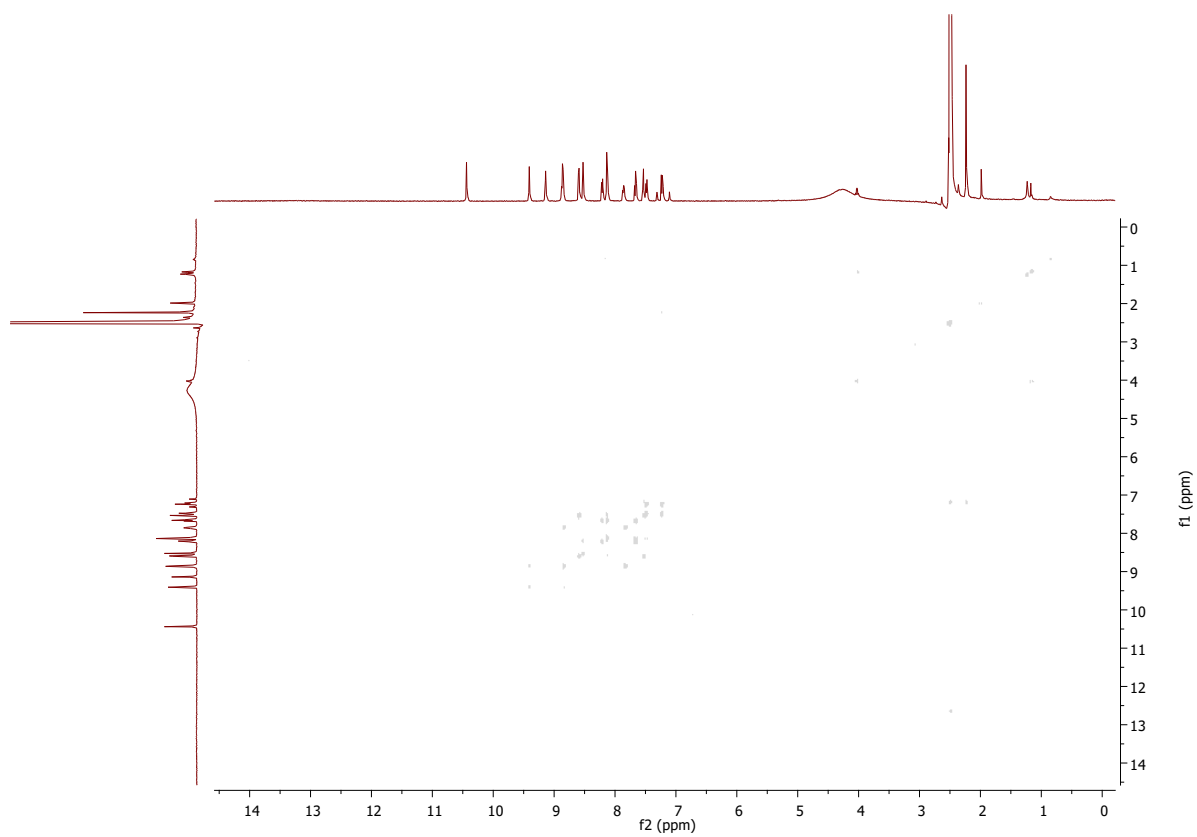


Fig. 2Sc. COSY of **3** in $\text{DMSO-}d_6$

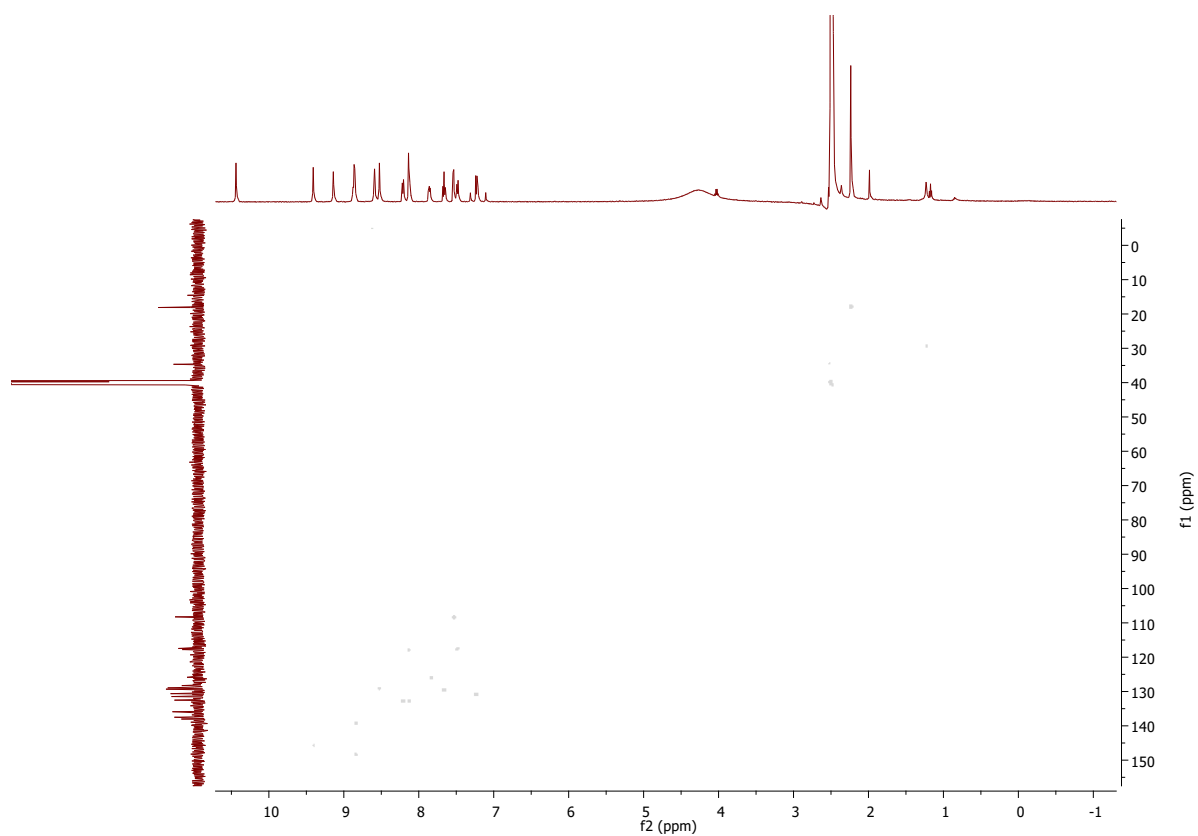


Fig. 2Sd. HSQC of **3** in DMSO- d_6

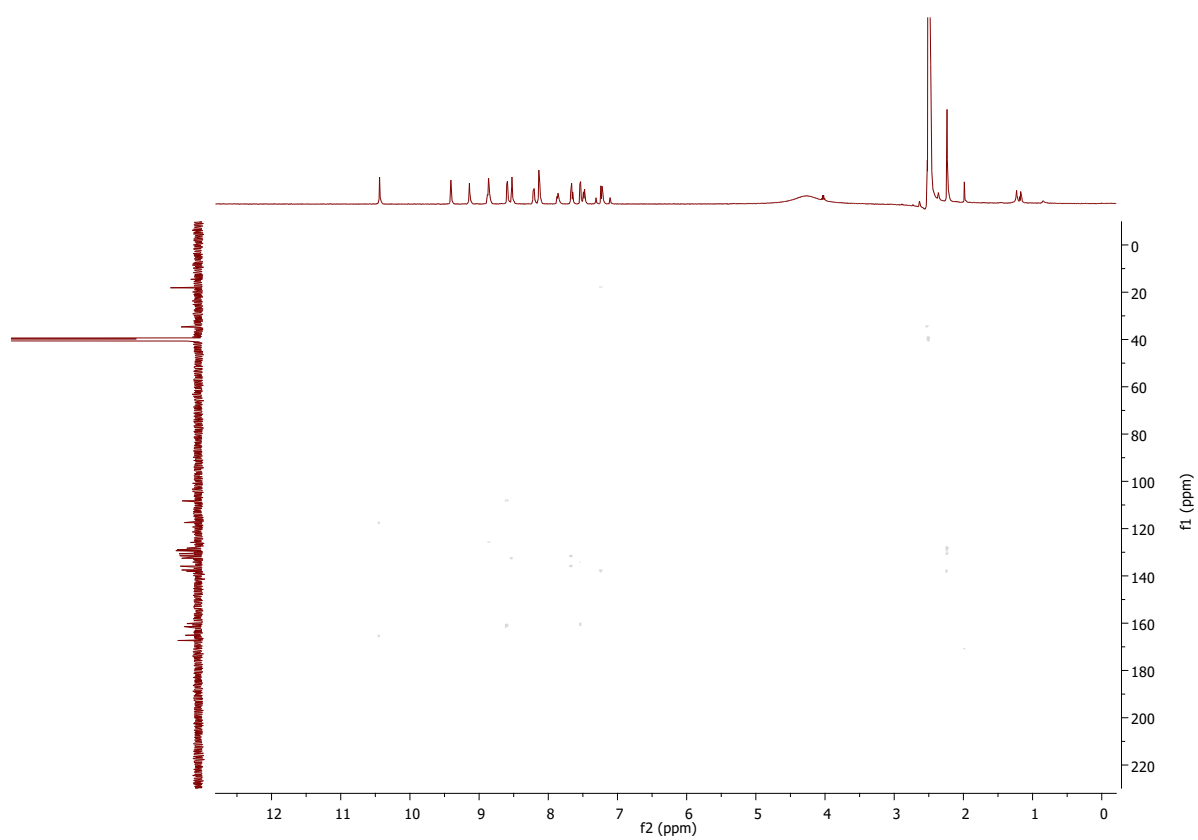


Fig. 2Se. HMBC of **3** in DMSO- d_6

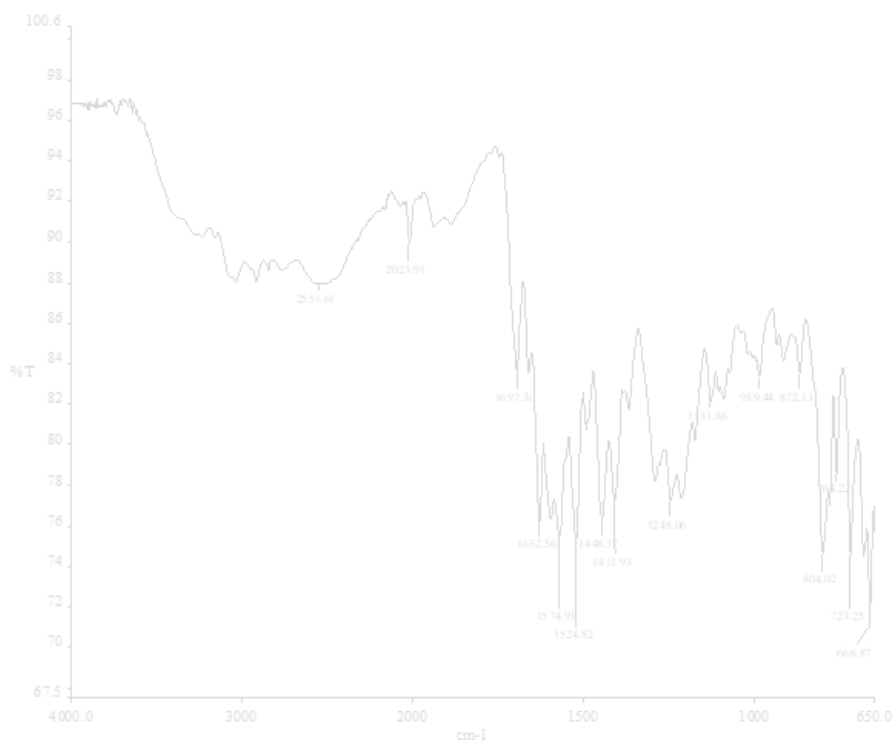


Fig. 2Sf. IR of 3



Fig. 2Sg. HRMS of 3



Fig. 2Sh. LCMS of 3

Compound 4

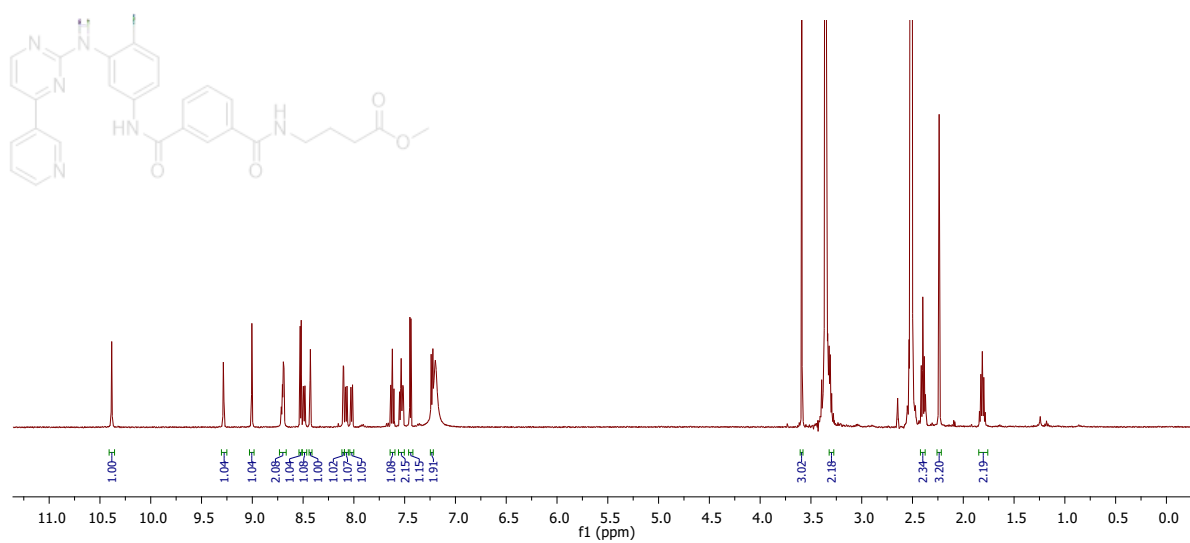


Fig. 3Sa. ^1H NMR of 4 in $\text{DMSO}-d_6$

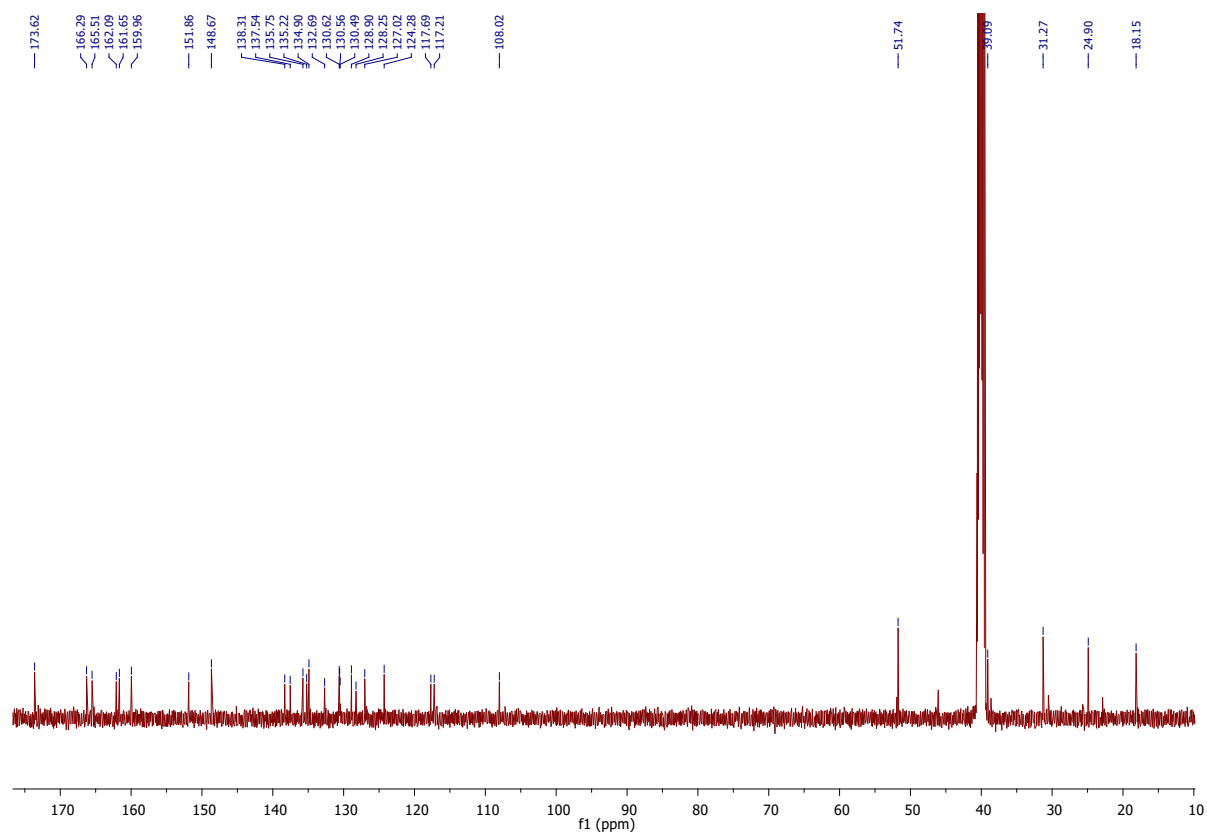


Fig. 3Sb. ^{13}C NMR of 4 in $\text{DMSO}-d_6$

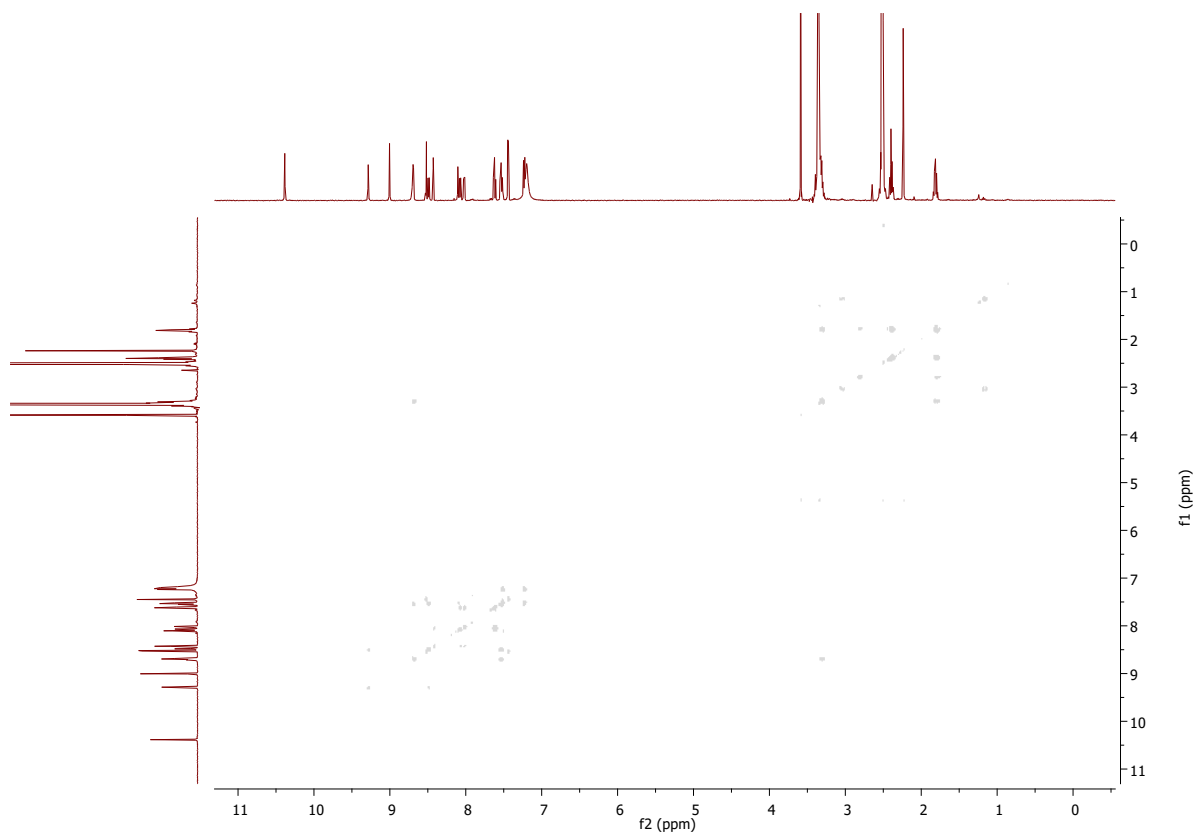


Fig. 3Sc. COSY of **4** in DMSO- d_6

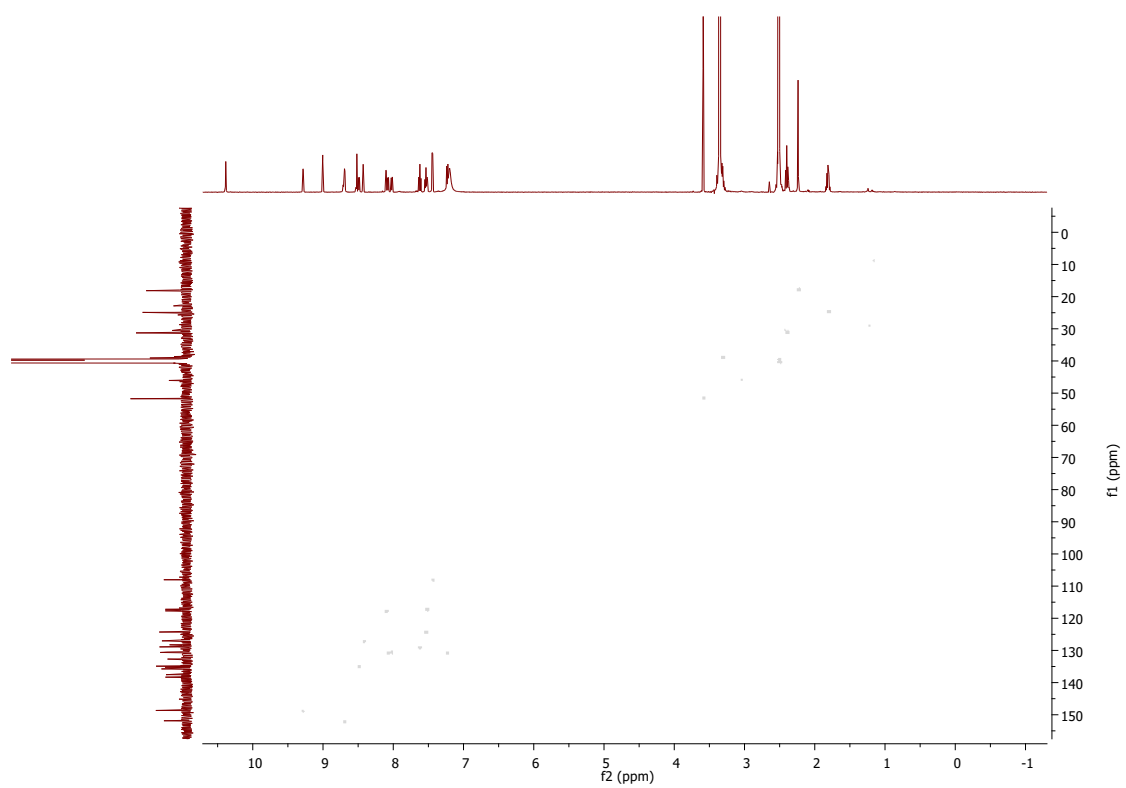


Fig. 3Sd. HSQC of **4** in DMSO- d_6

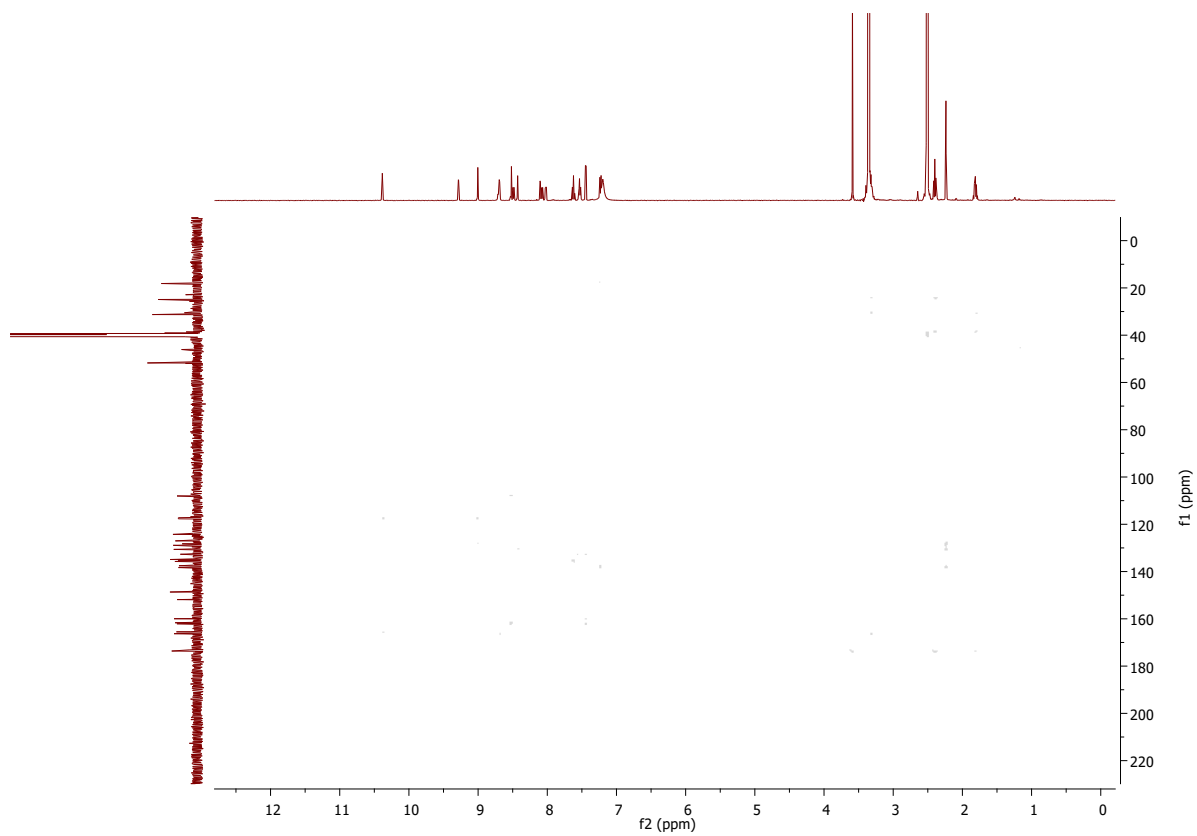


Fig. 3Se. HMBC of 4 in DMSO- d_6

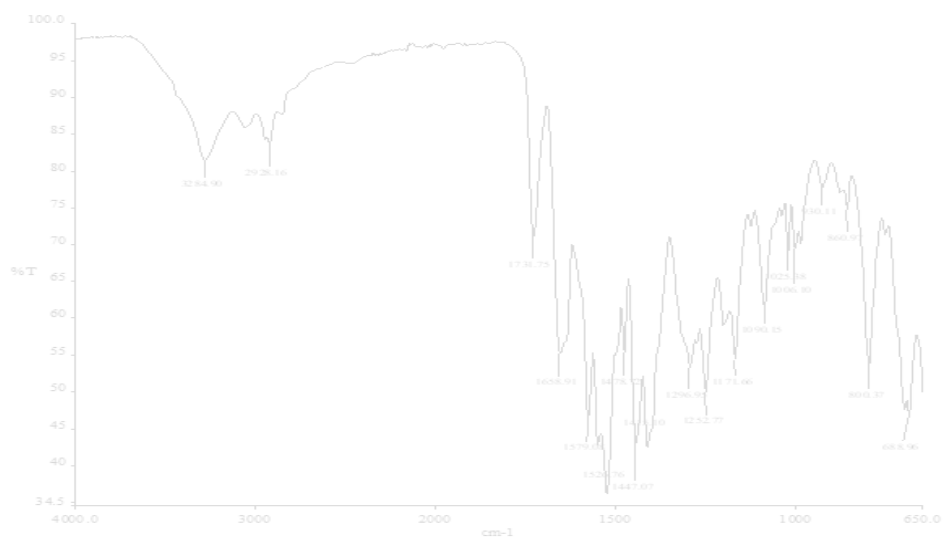


Fig. 3Sf. IR of 4



Fig. 3Sg. HRMS of **4**

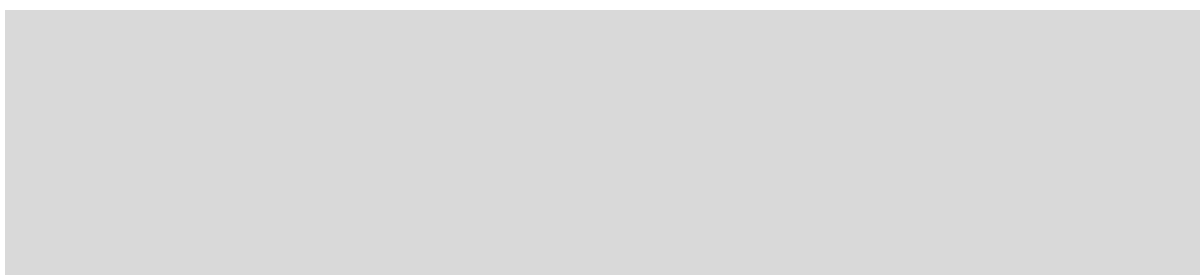
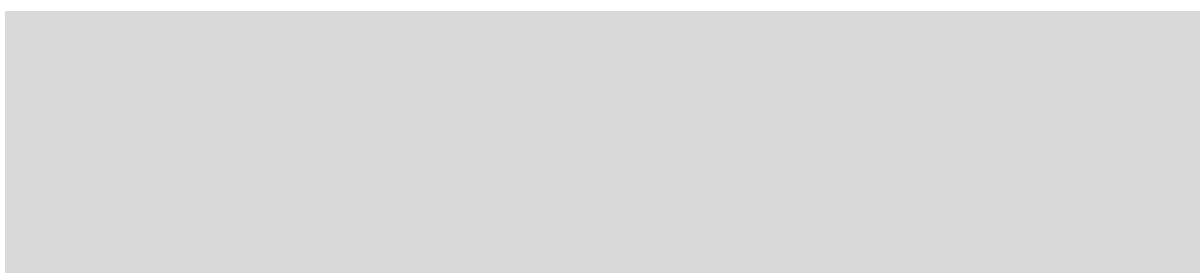


Fig. 3Sh. LCMS of **4**

Compound 5

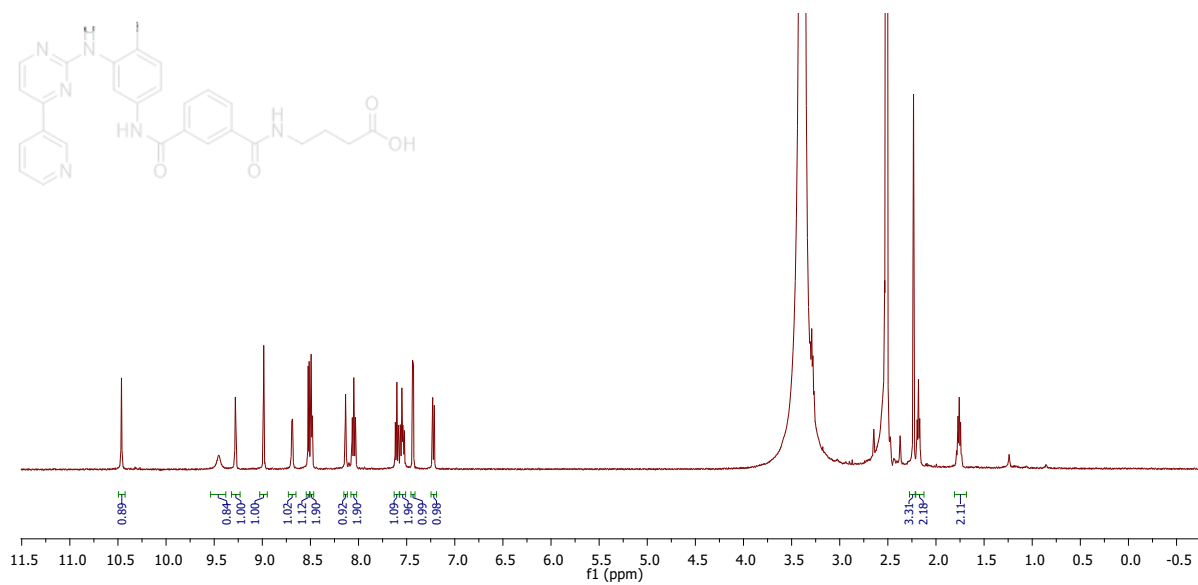


Fig. 4Sa. ¹H NMR of 5 in DMSO-*d*₆

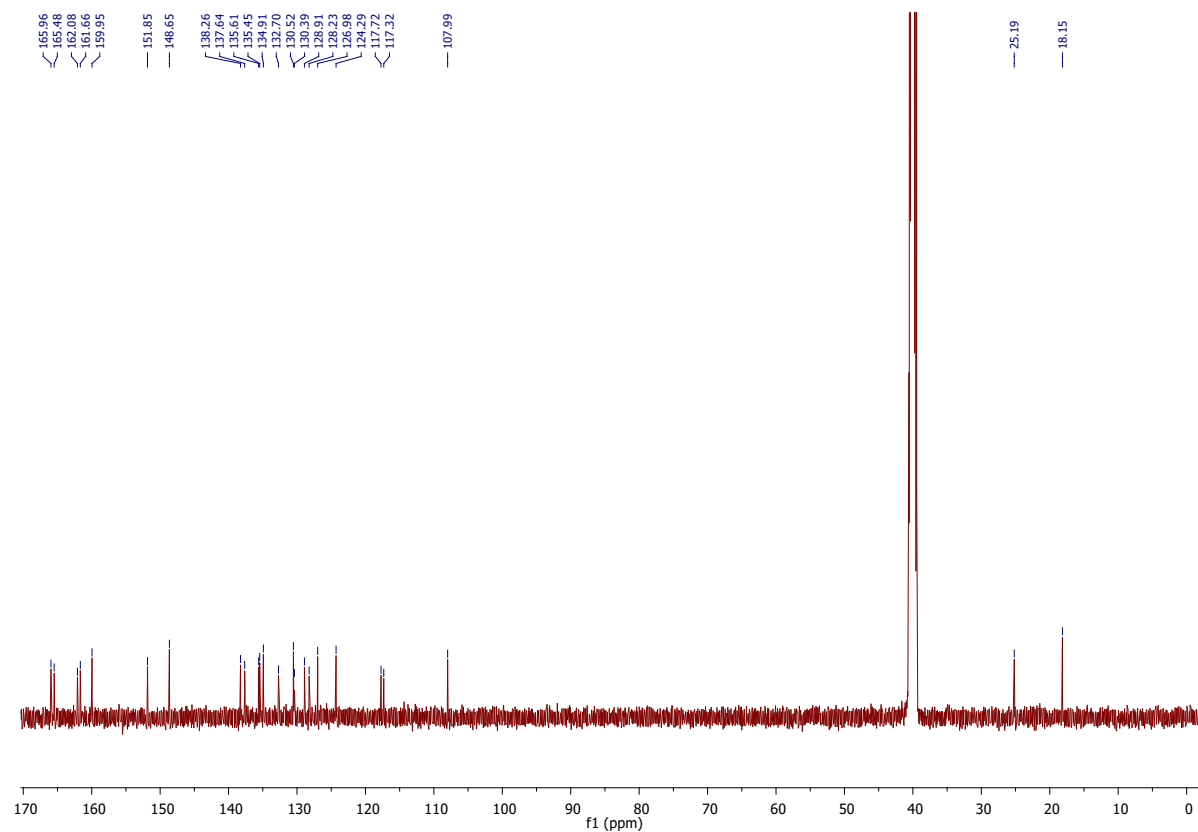


Fig. 4Sb. ¹³C NMR of 5 in DMSO-*d*₆

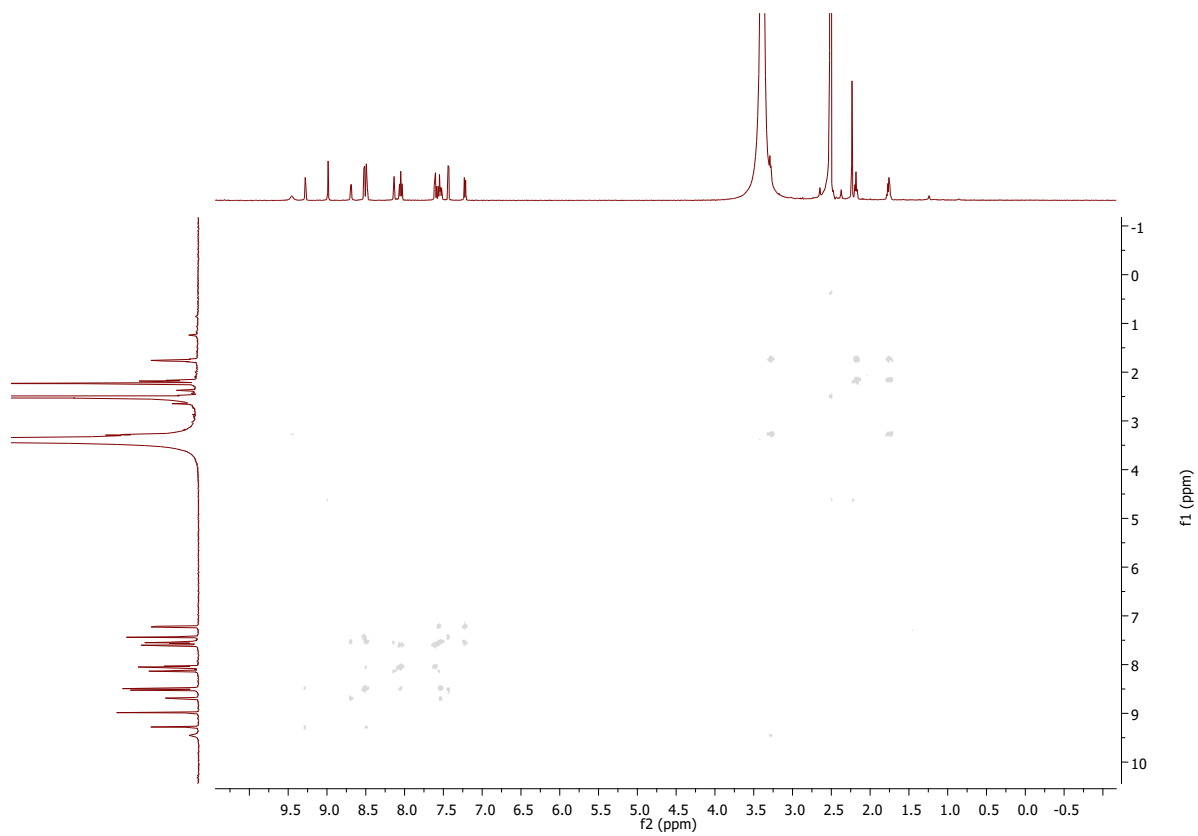


Fig. 4Sc. COSY of **5** in DMSO- d_6

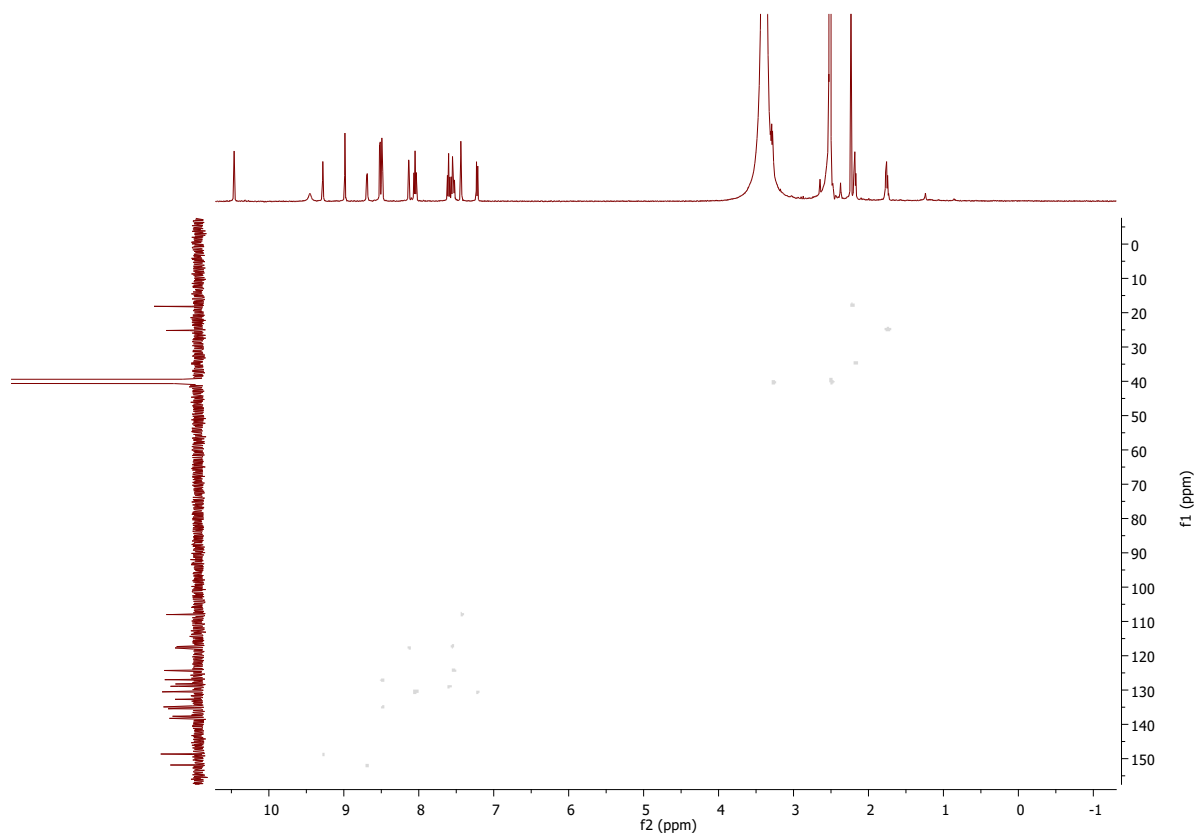


Fig. 4Sd. HSQC of **5** in DMSO- d_6

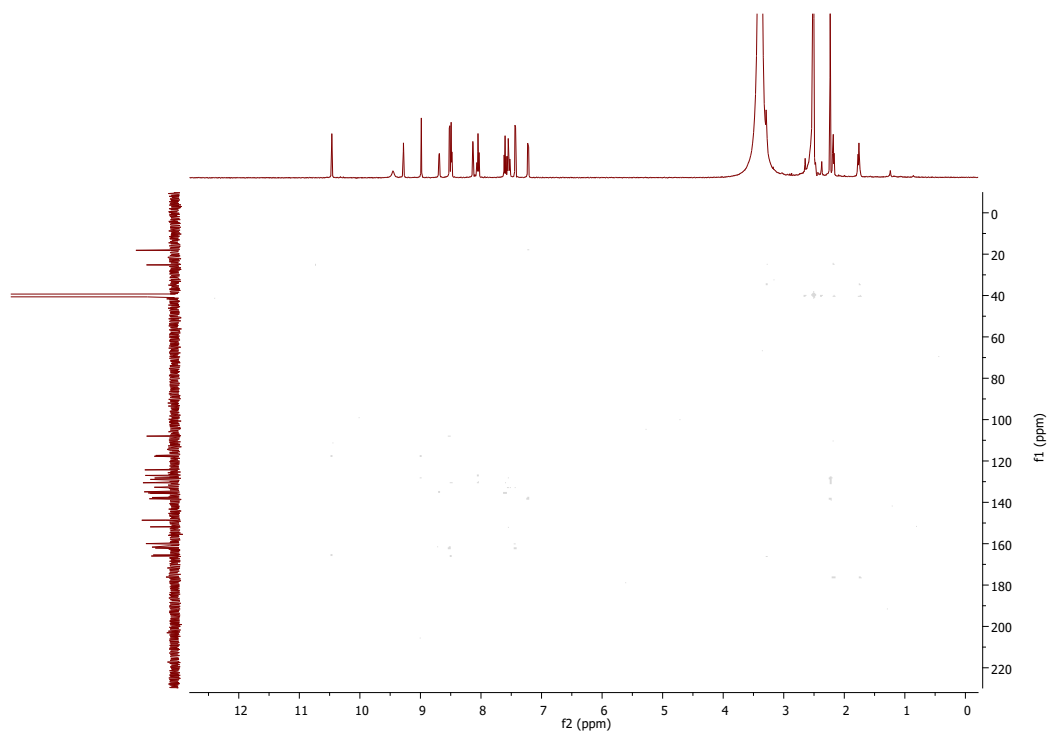


Fig. 4Se. HMBC of 5 in DMSO- d_6

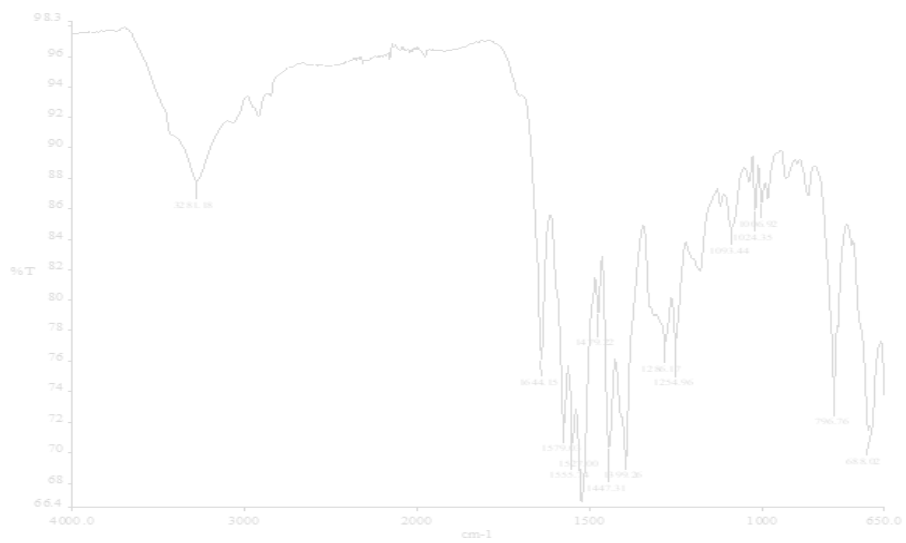


Fig. 4Sf. IR of 5



Fig. 4Sg. HRMS of 5

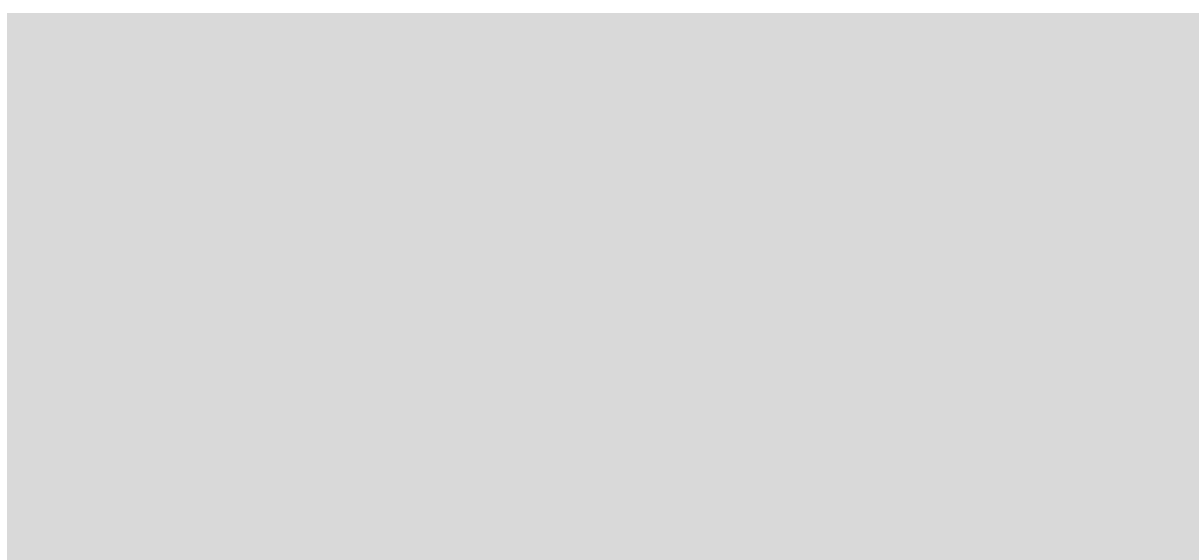


Fig. 4Sh. LCMS of 5

Compound 6

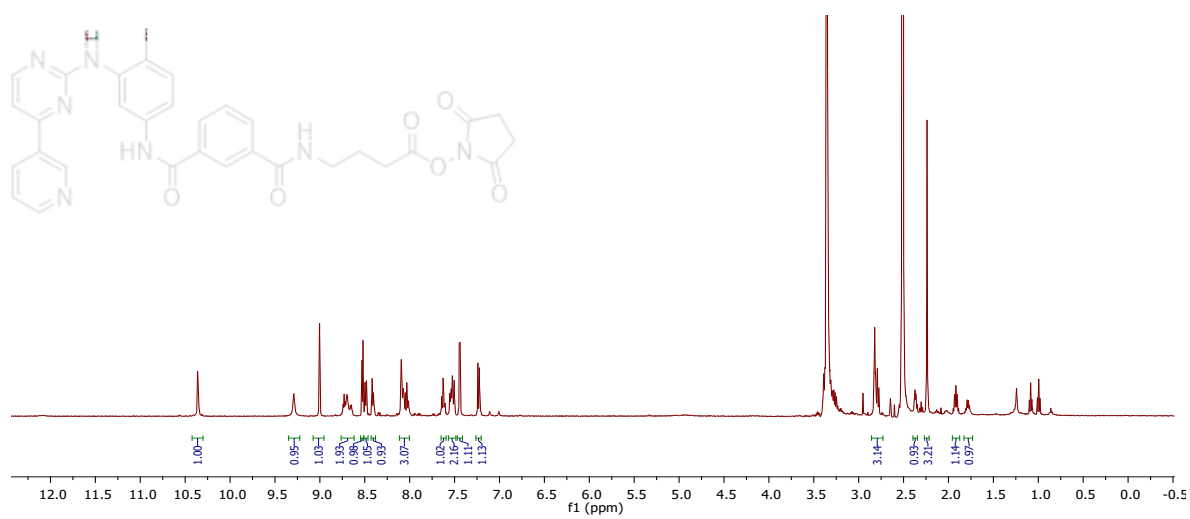


Fig. 5Sa. ^1H NMR of 6 in $\text{DMSO-}d_6$

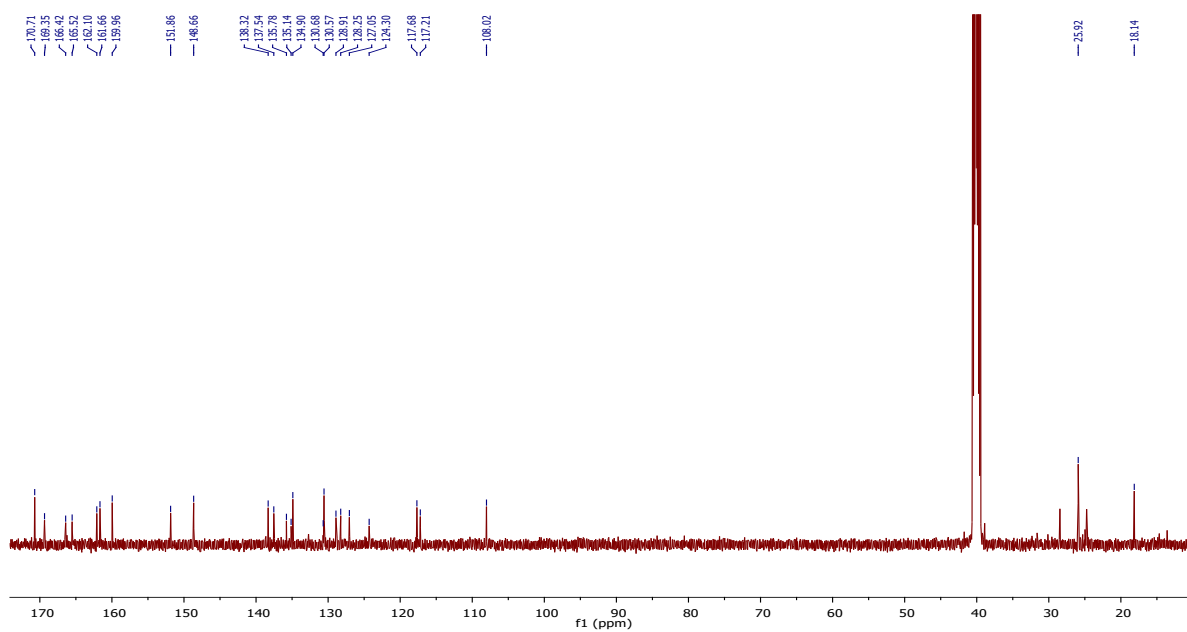


Fig. 5Sb. ^{13}C NMR of **6** in $\text{DMSO-}d_6$

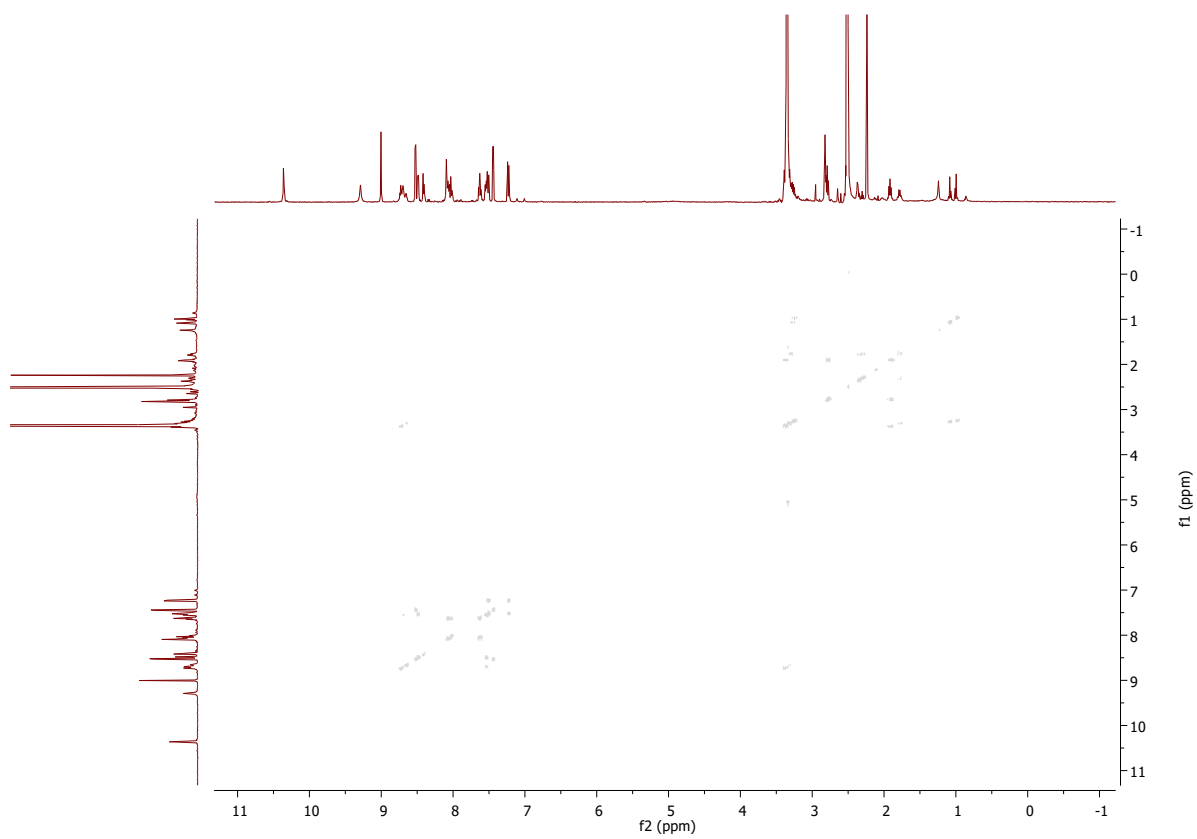


Fig. 5Sc. COSY of **6** in $\text{DMSO-}d_6$

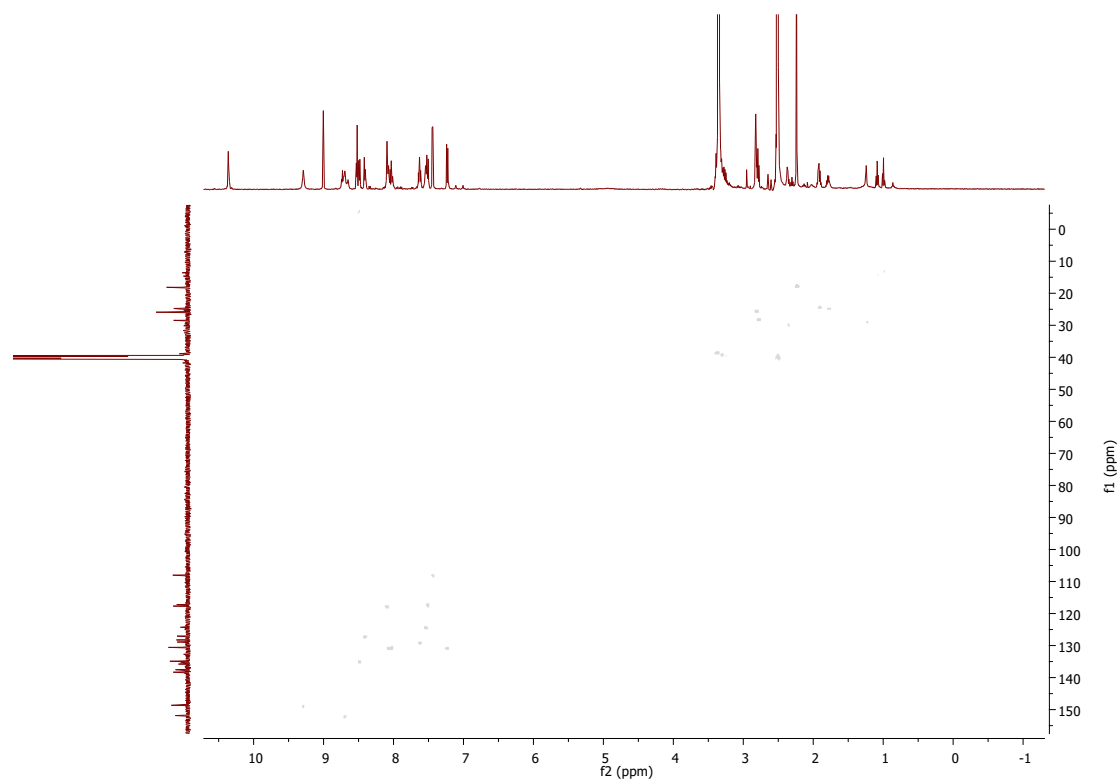


Fig. 5Sd. HSQC of **6** in DMSO- d_6

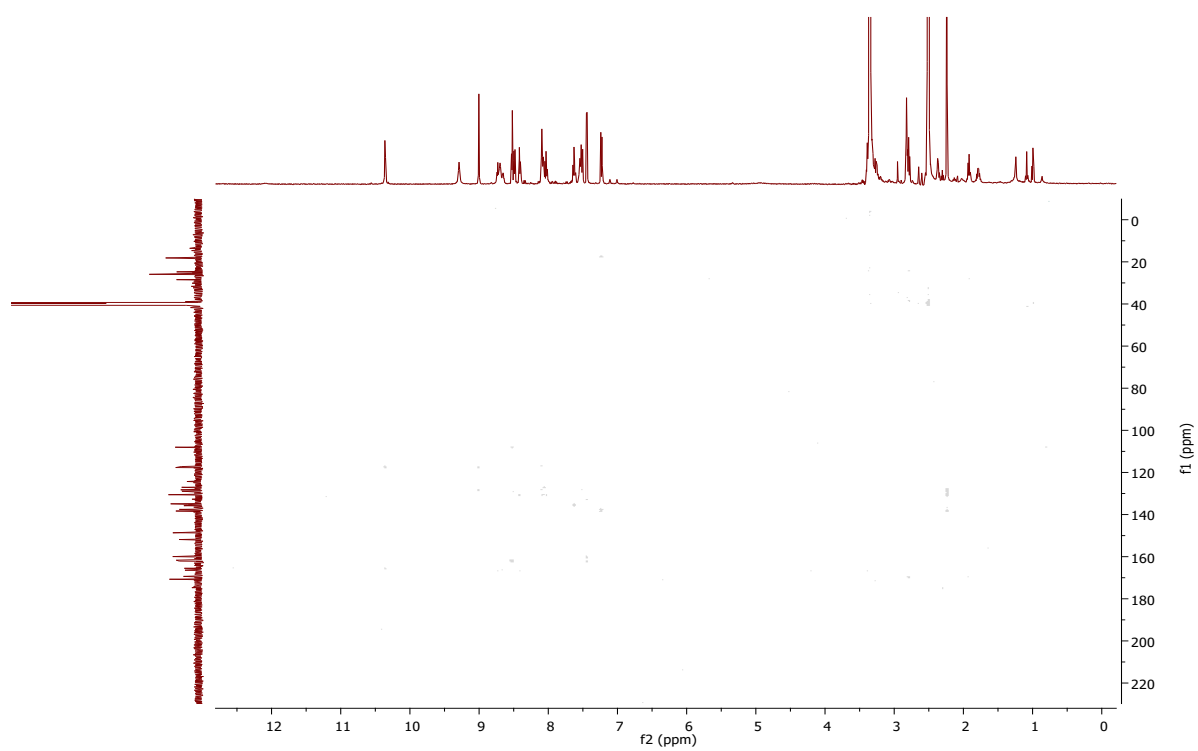


Fig. 5Se. HMBC of **6** in DMSO- d_6

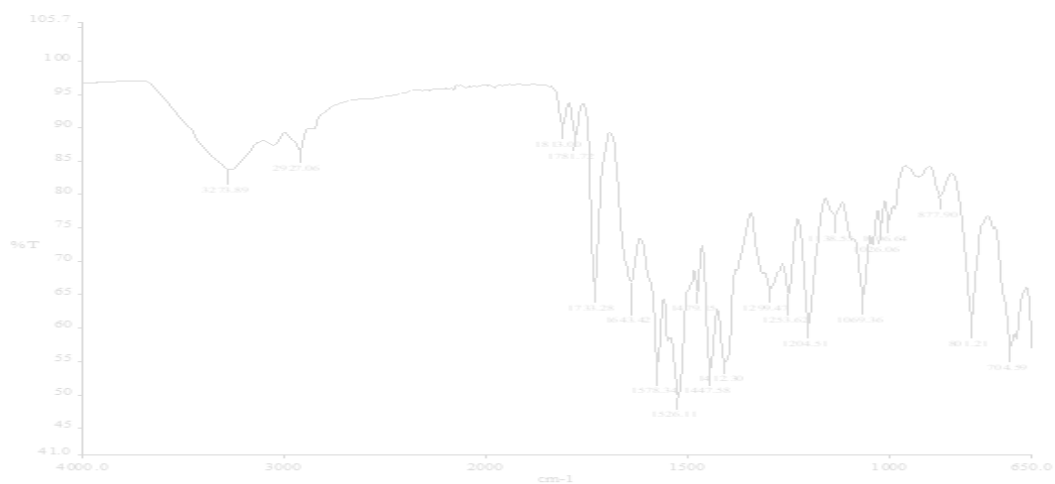


Fig. 5Sf. IR of 6



Fig. 5Sg. HRMS of 6

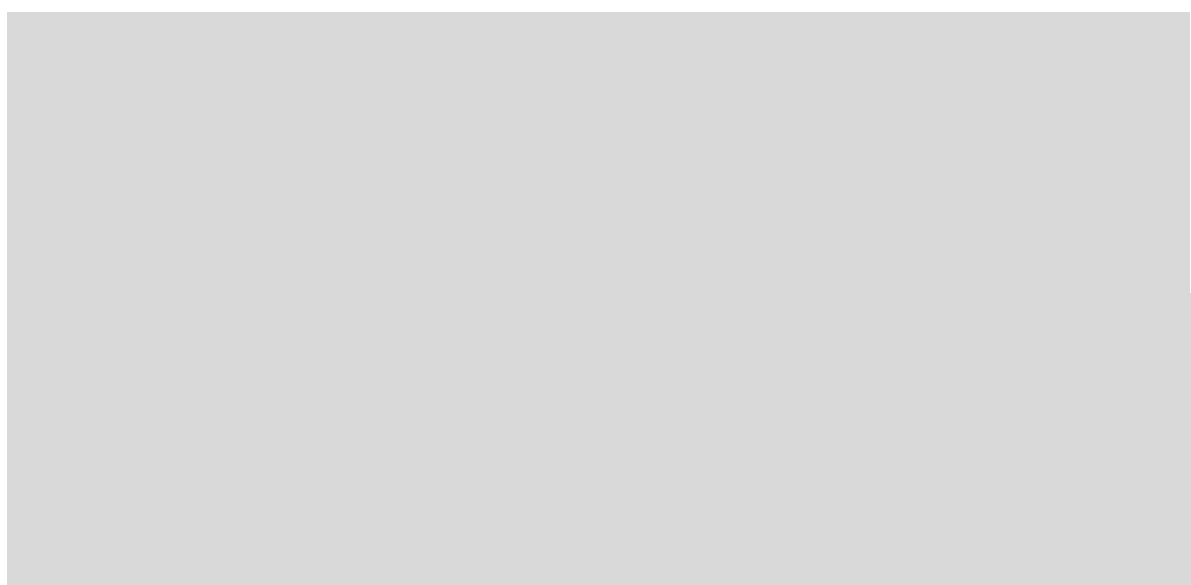


Fig. 5Sh. LCMS of 6

Complex A

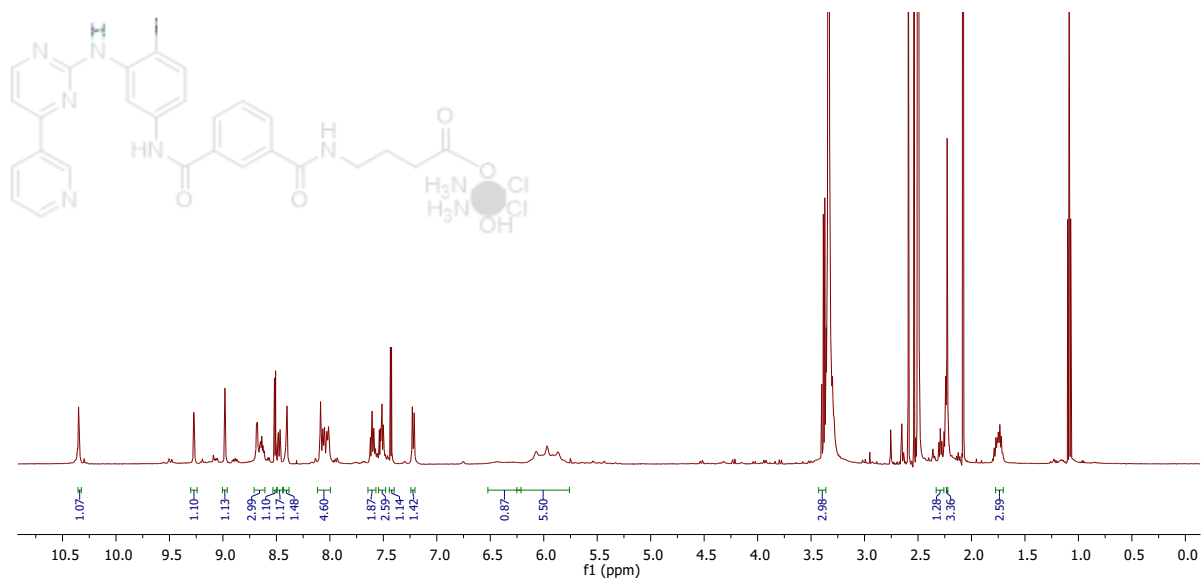


Fig. 6Sa. ^1H NMR of A in $\text{DMSO}-d_6$

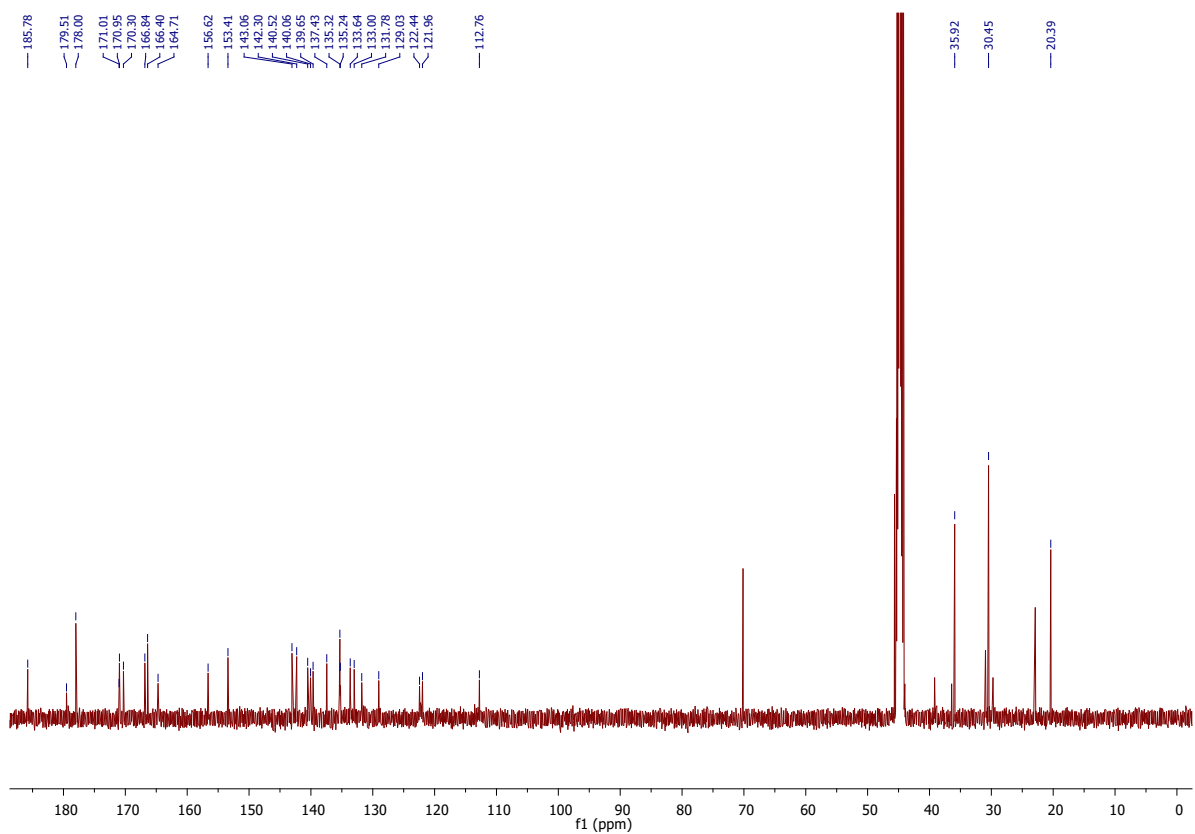


Fig. 6Sb. ^{13}C NMR of A in $\text{DMSO}-d_6$

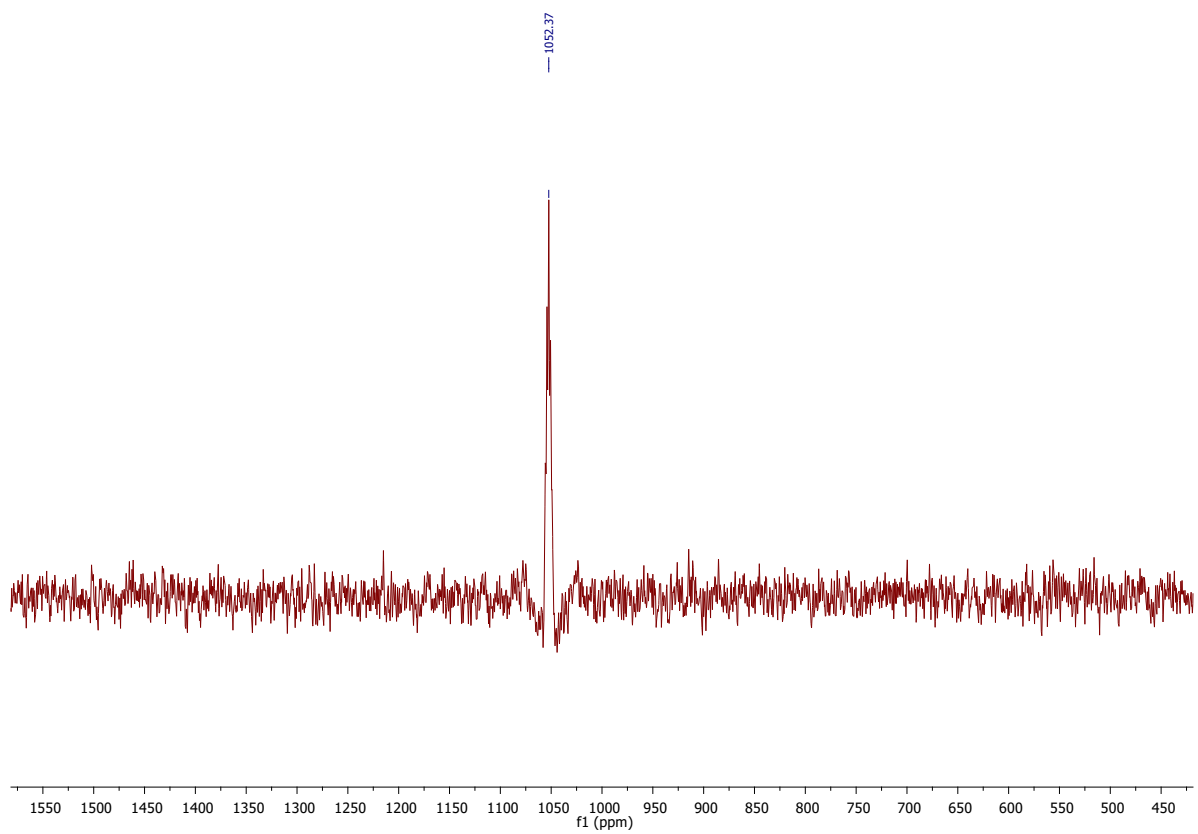


Fig. 6Sc. ^{195}Pt NMR of **A** in $\text{DMSO-}d_6$

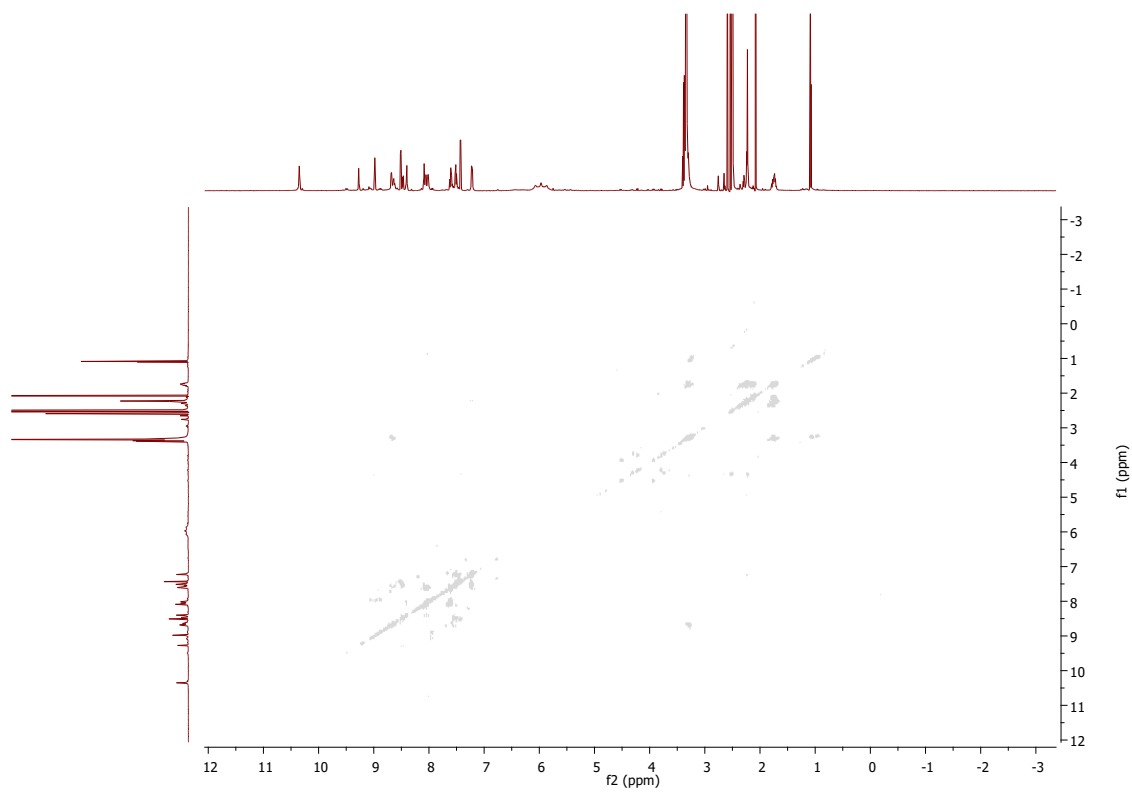


Fig. 6Se. COSY of **A** in $\text{DMSO-}d_6$

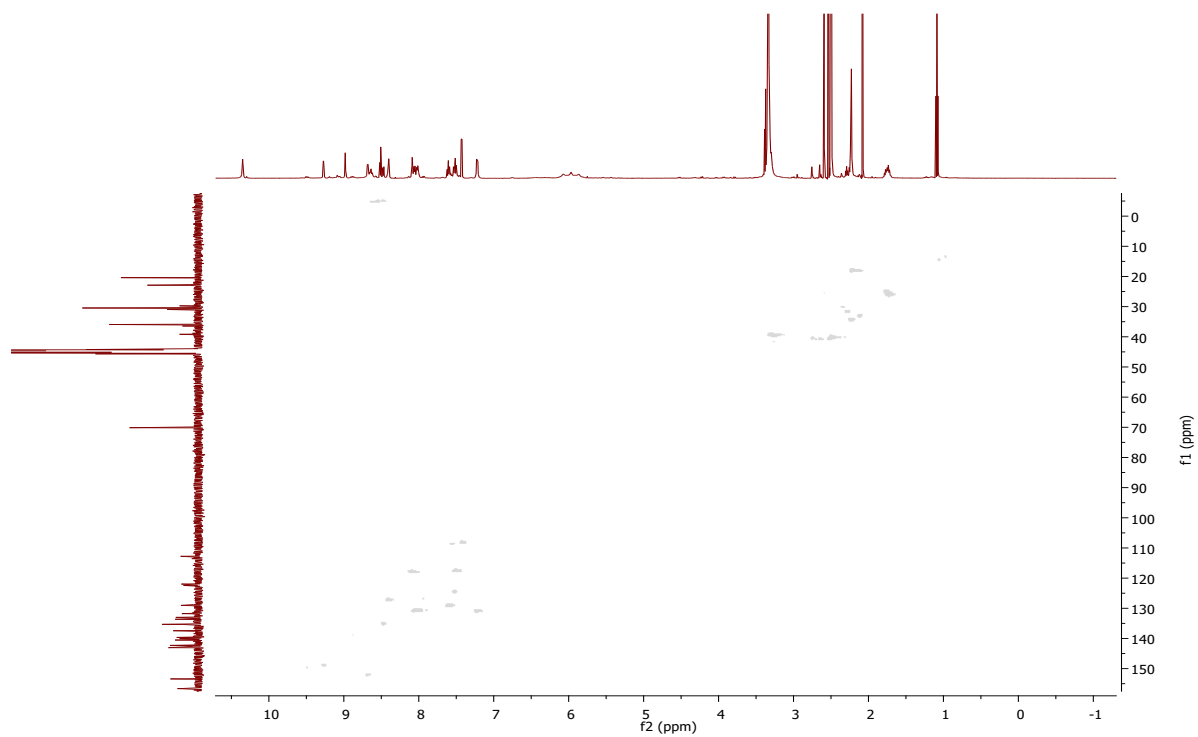


Fig. 6Sf. HSQC of **A** in DMSO- d_6

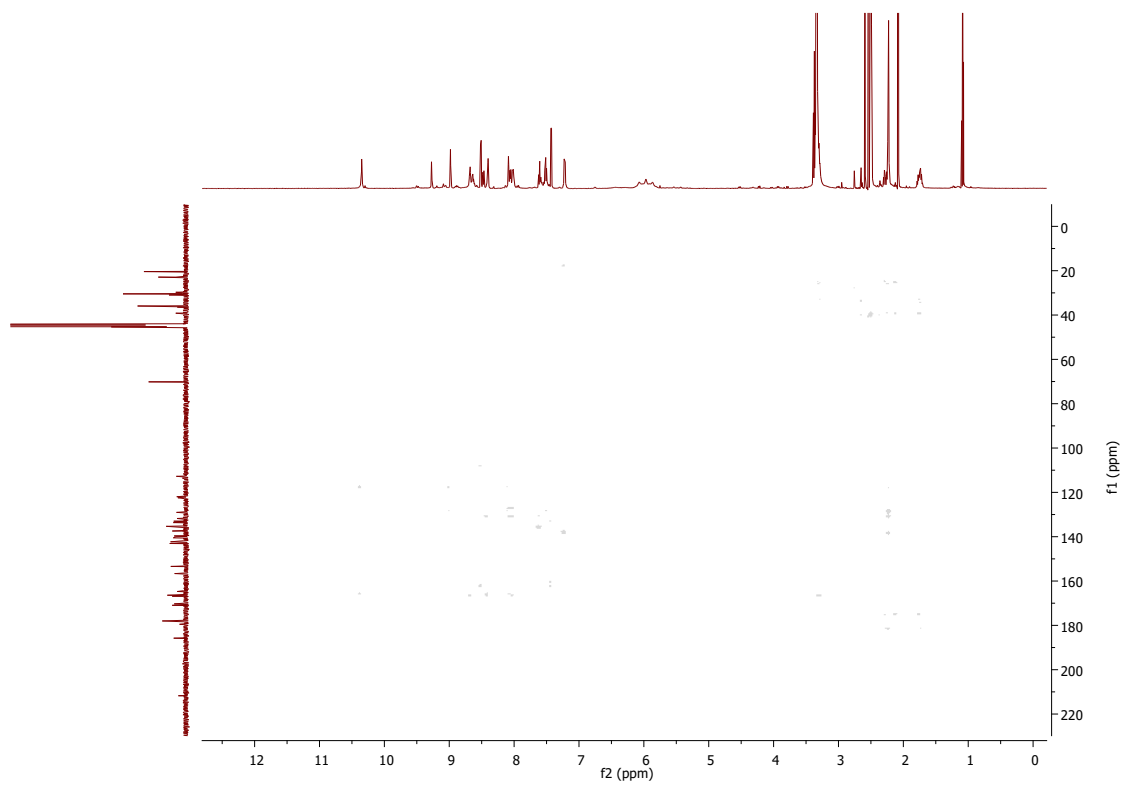


Fig. 6Sg. HMBC of **A** in DMSO- d_6

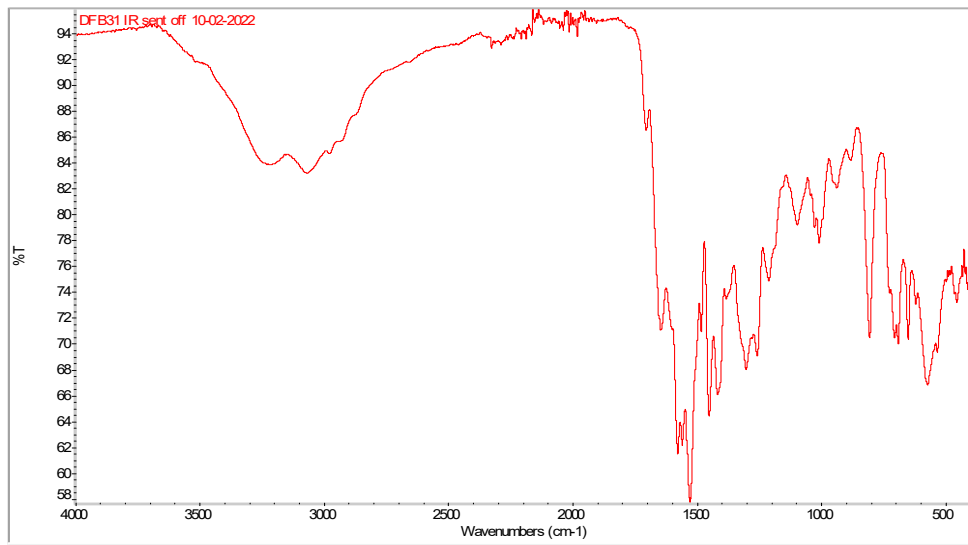


Fig. 6Sh. IR of A

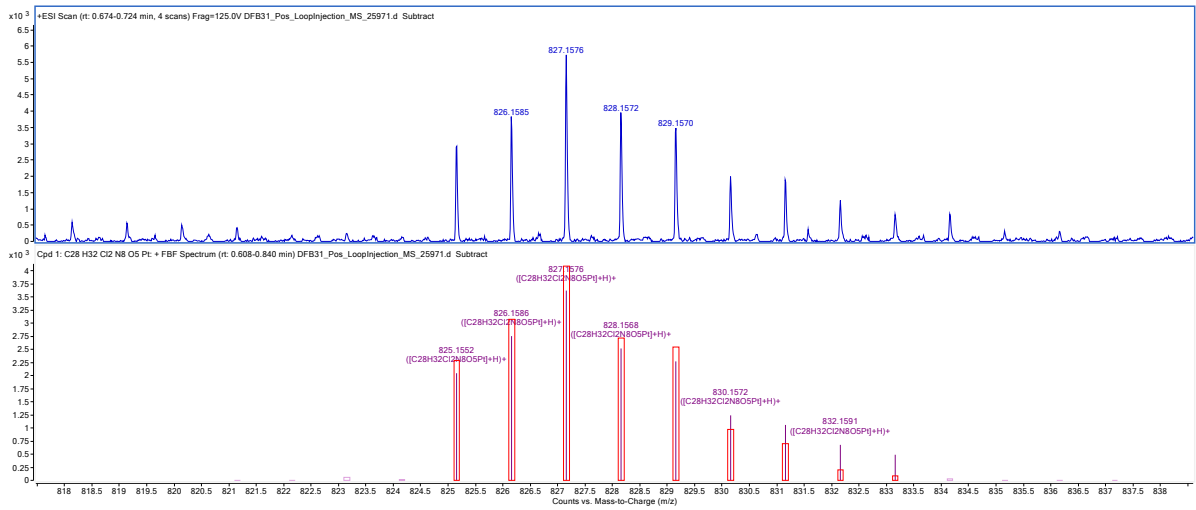


Fig. 6Si. HRMS of A

Compound 9

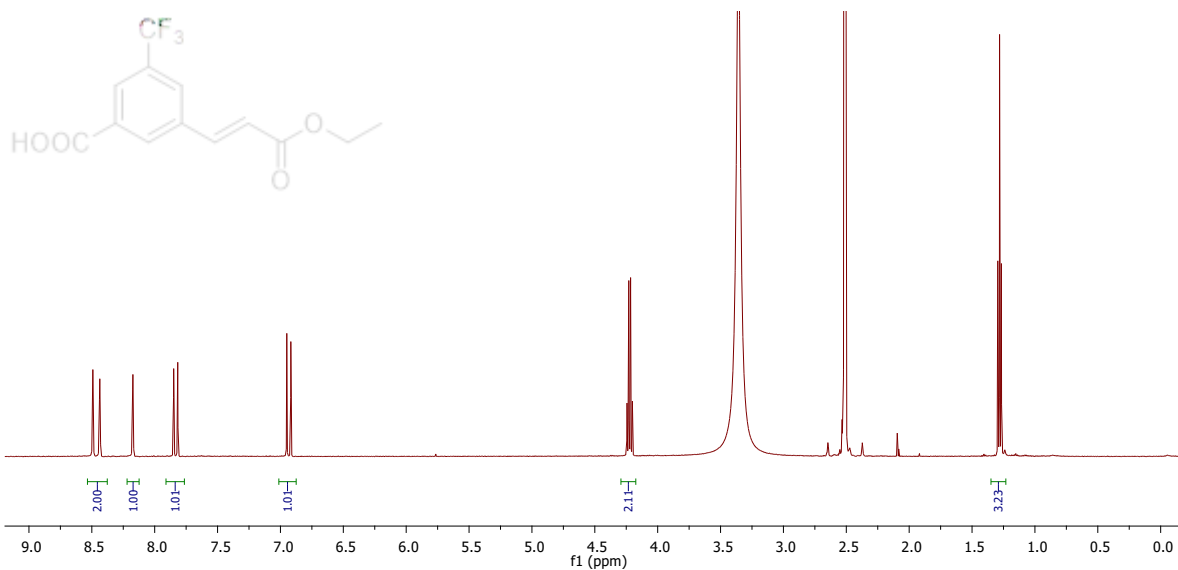


Fig. 7Sa. ¹H NMR of 9 in DMSO-d₆

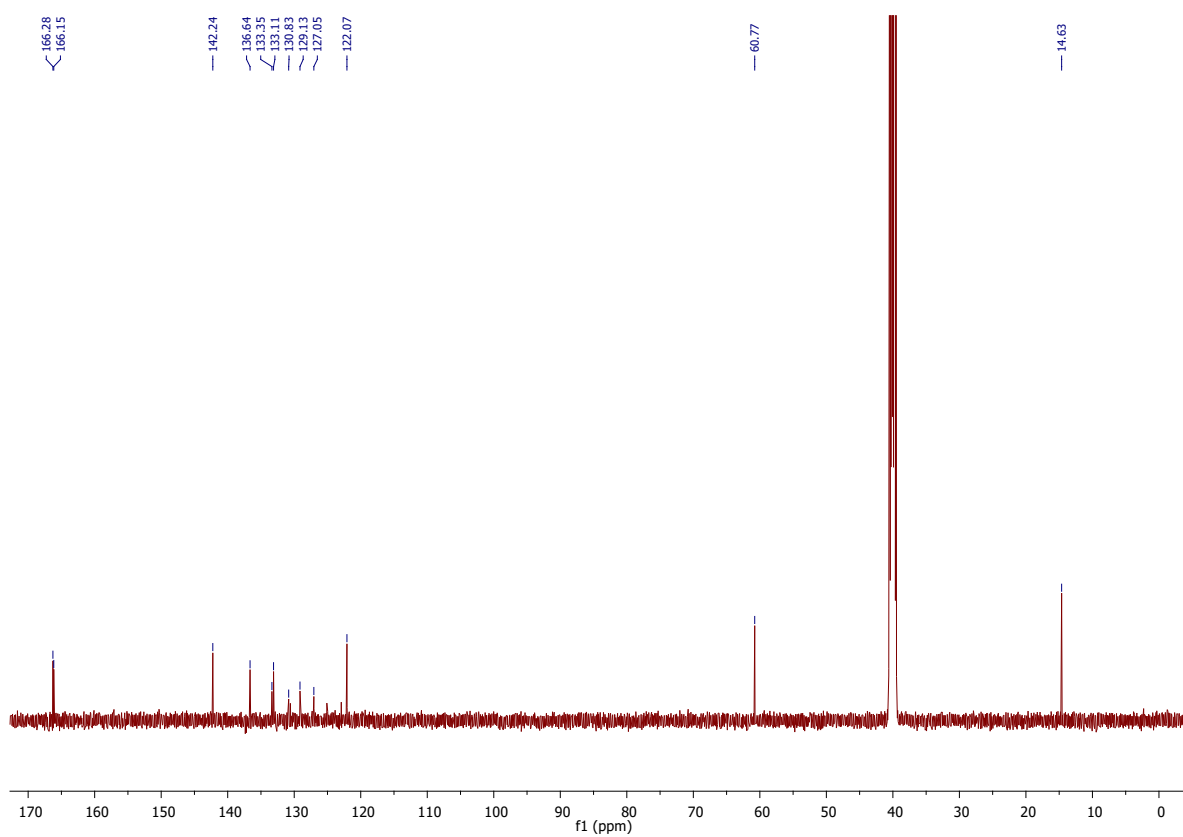


Fig. 7Sb. ¹³C NMR of 9 in DMSO-d₆

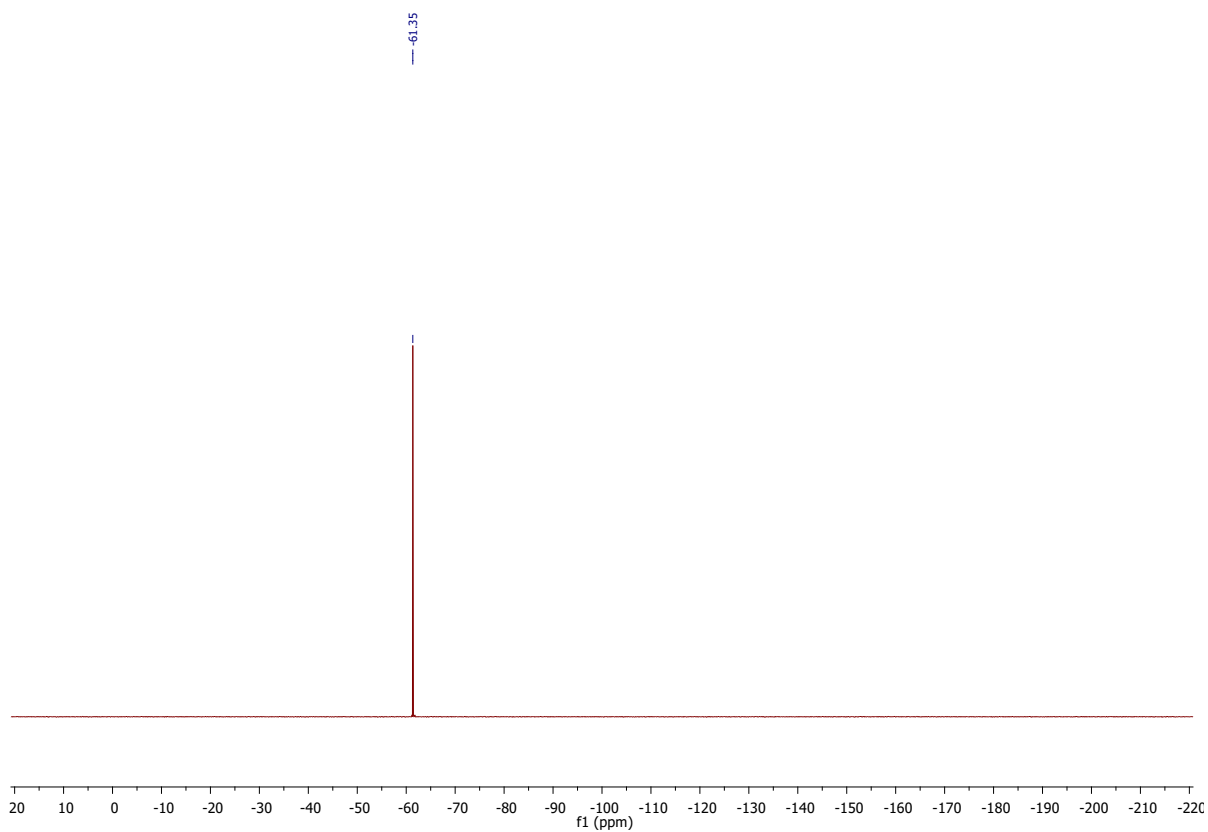


Fig. 7Sc. ^{19}F NMR of **9** in $\text{DMSO-}d_6$

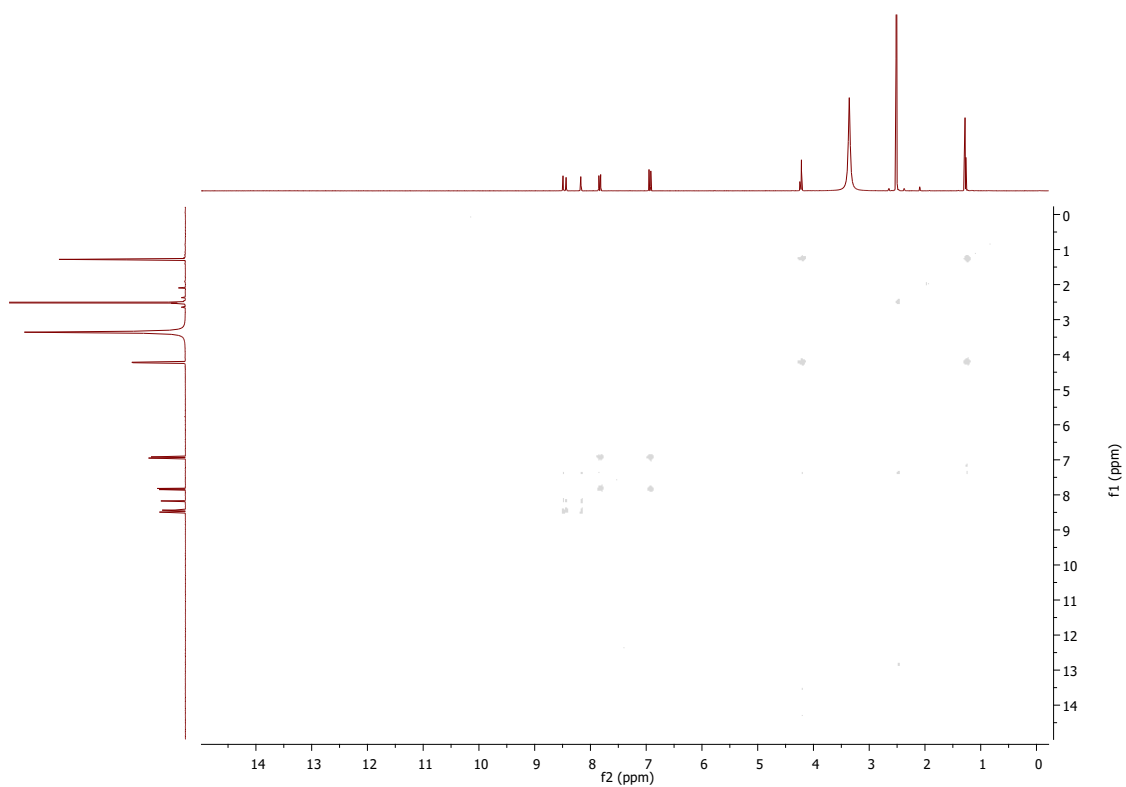


Fig. 7Sd. COSY of **9** in $\text{DMSO-}d_6$

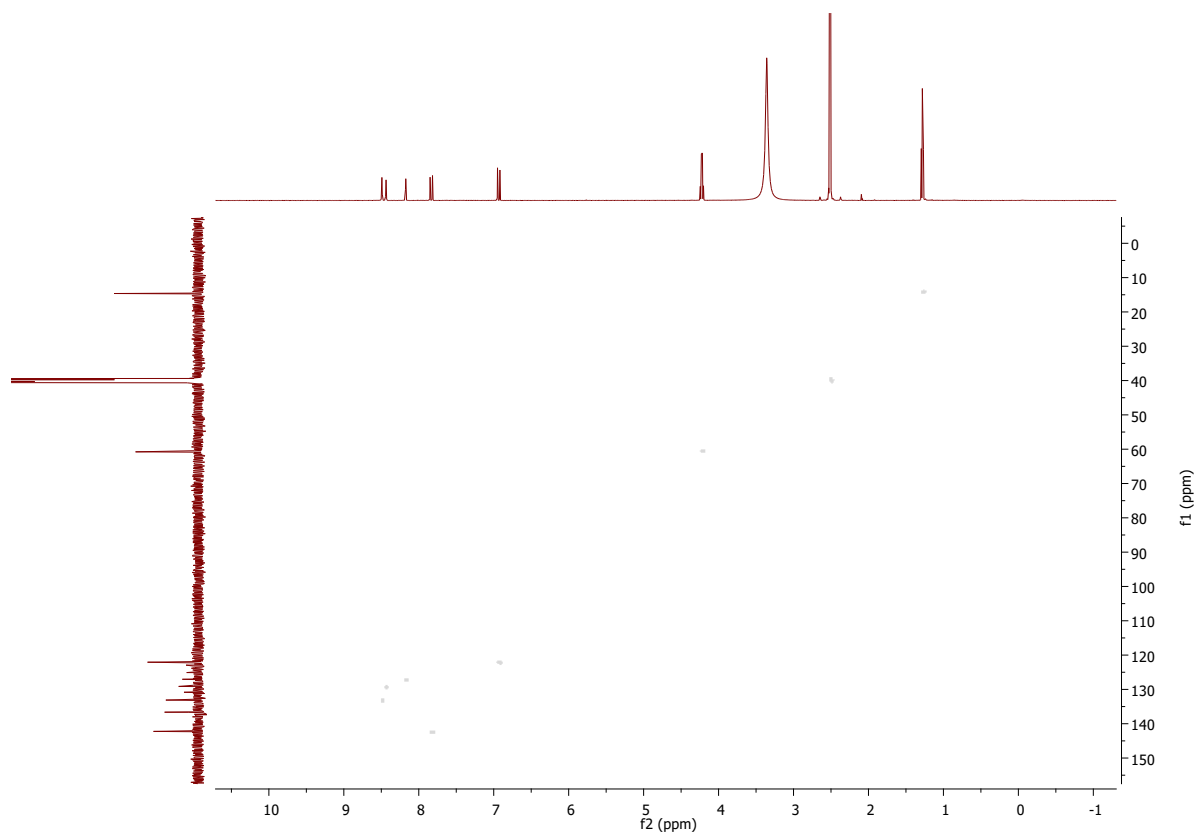


Fig. 7Se. HSQC of 9 in DMSO- d_6

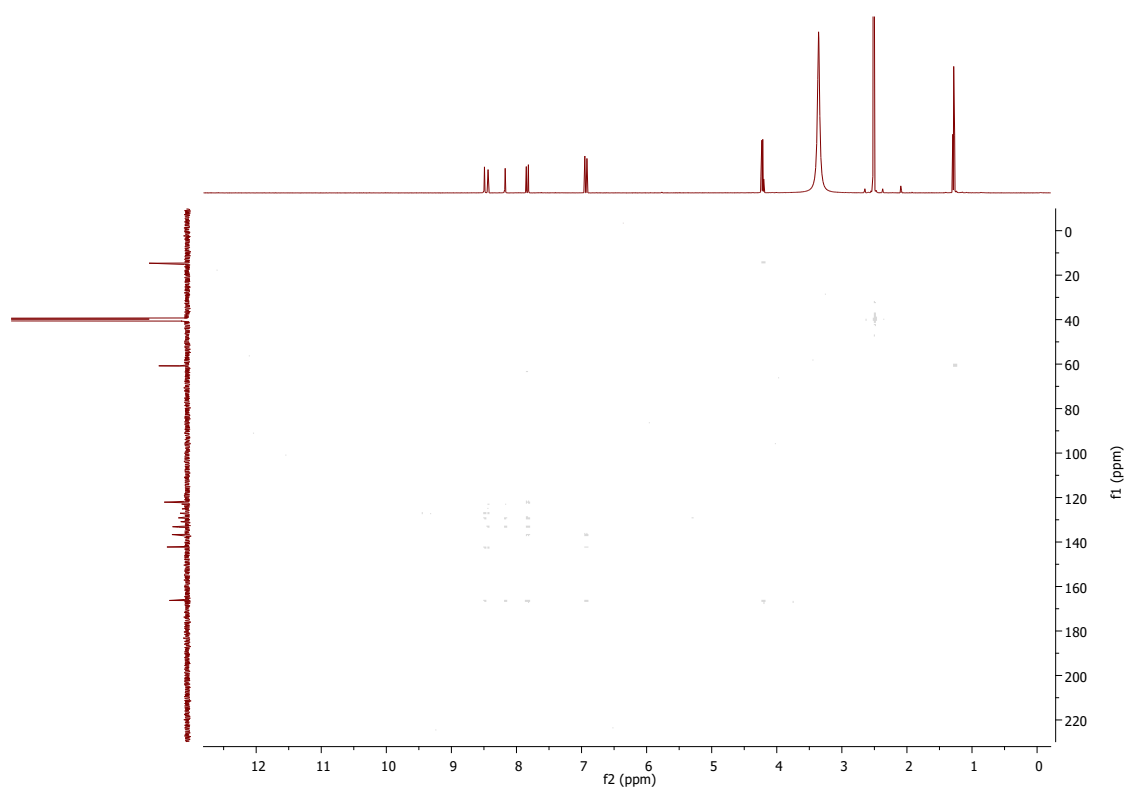


Fig. 7Sf. HMBC of 9 in DMSO- d_6

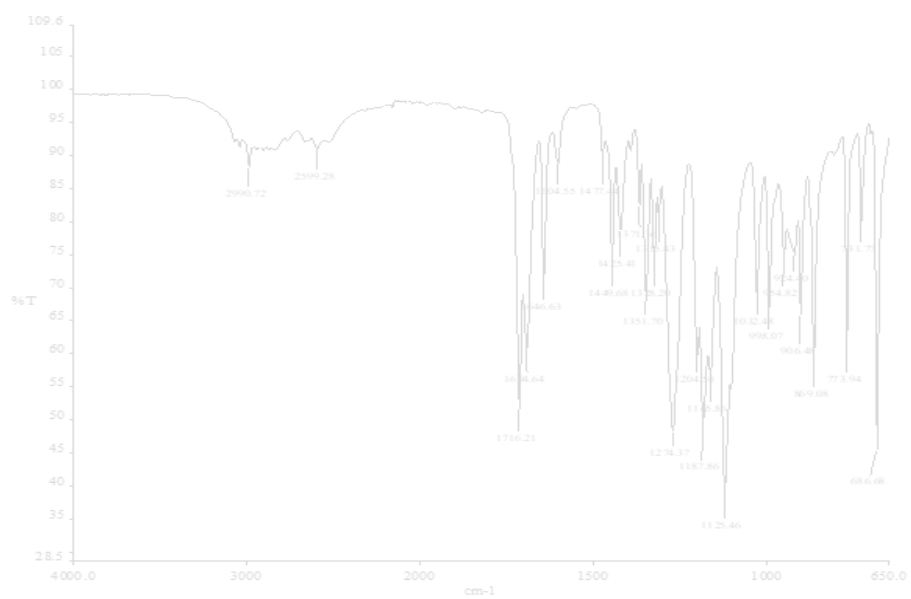


Fig. 7Sg. IR of **9**



Fig. 7Sh. HRMS of **9**

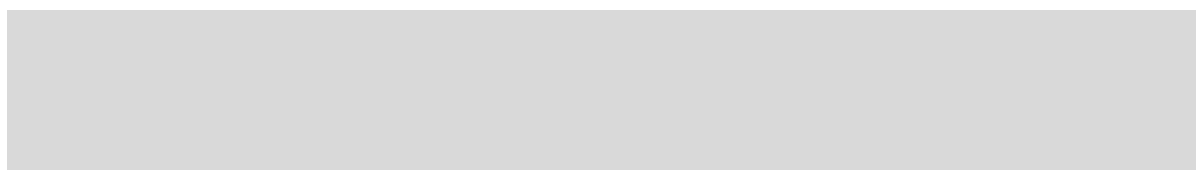


Fig. 7Si. LCMS of **9**

Compound 10

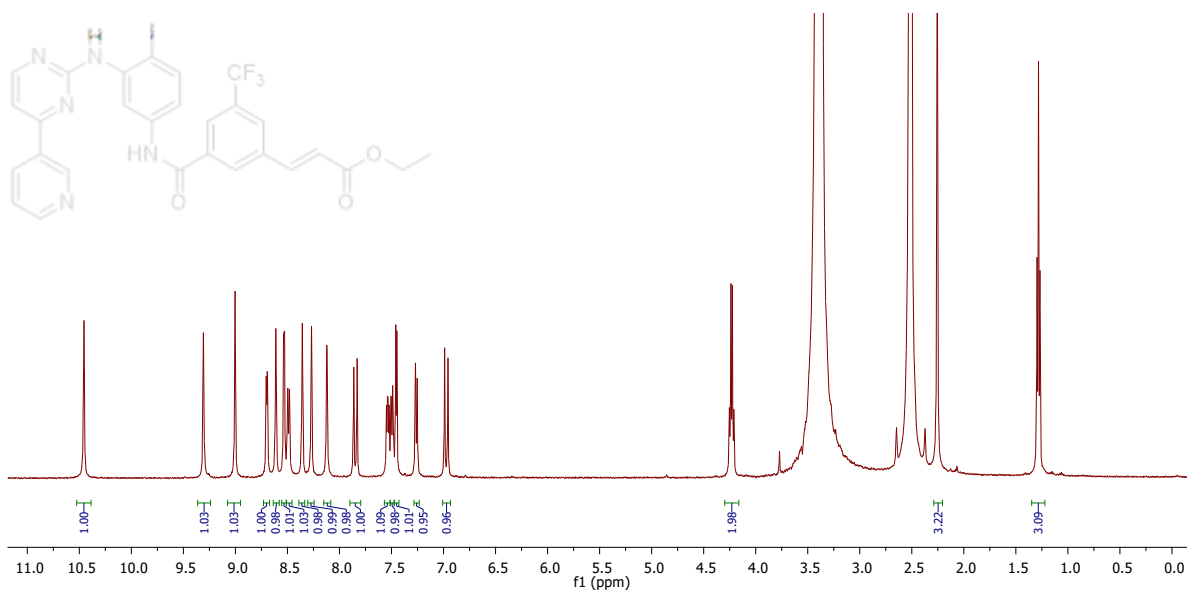


Fig. 8Sa. ¹H NMR of 10 in DMSO-d₆

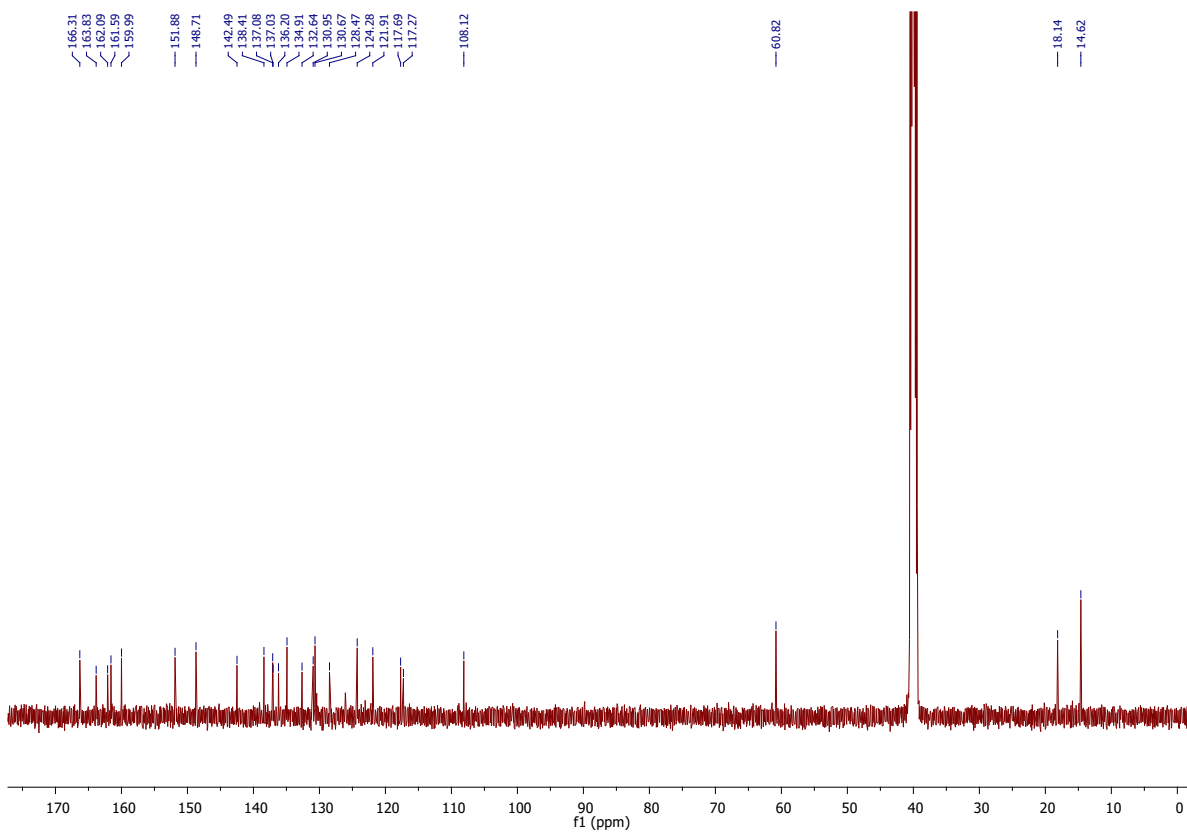


Fig. 8Sb. ¹³C NMR of 10 in DMSO-d₆

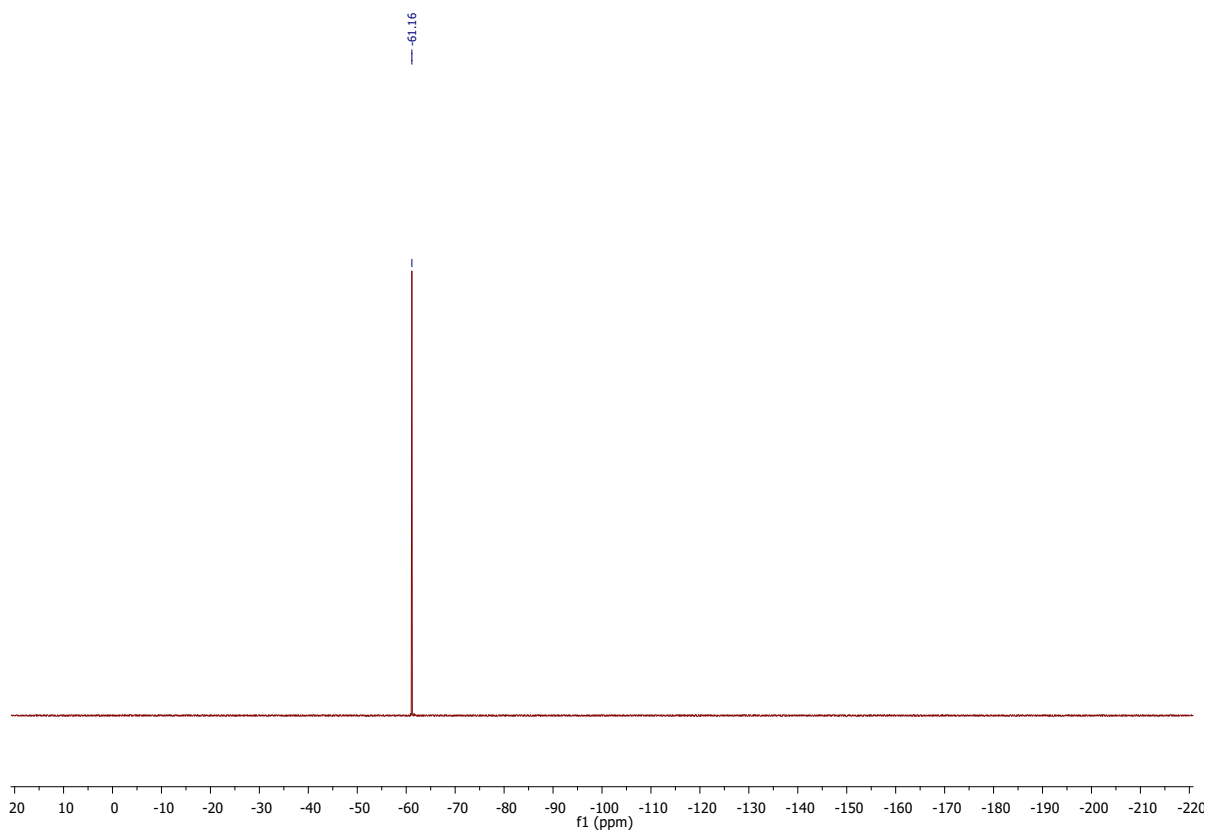


Fig. 8Sc. ¹⁹F NMR of **10** in DMSO-*d*₆

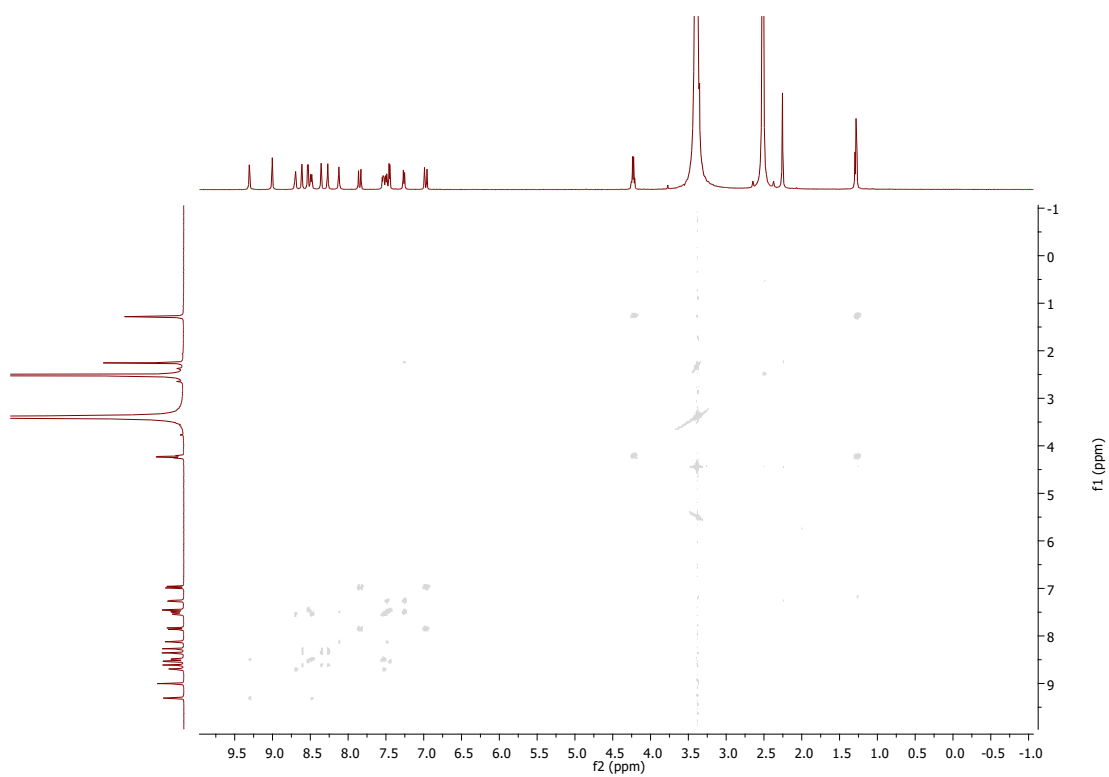


Fig. 8Se. COSY of **10** in DMSO-*d*₆

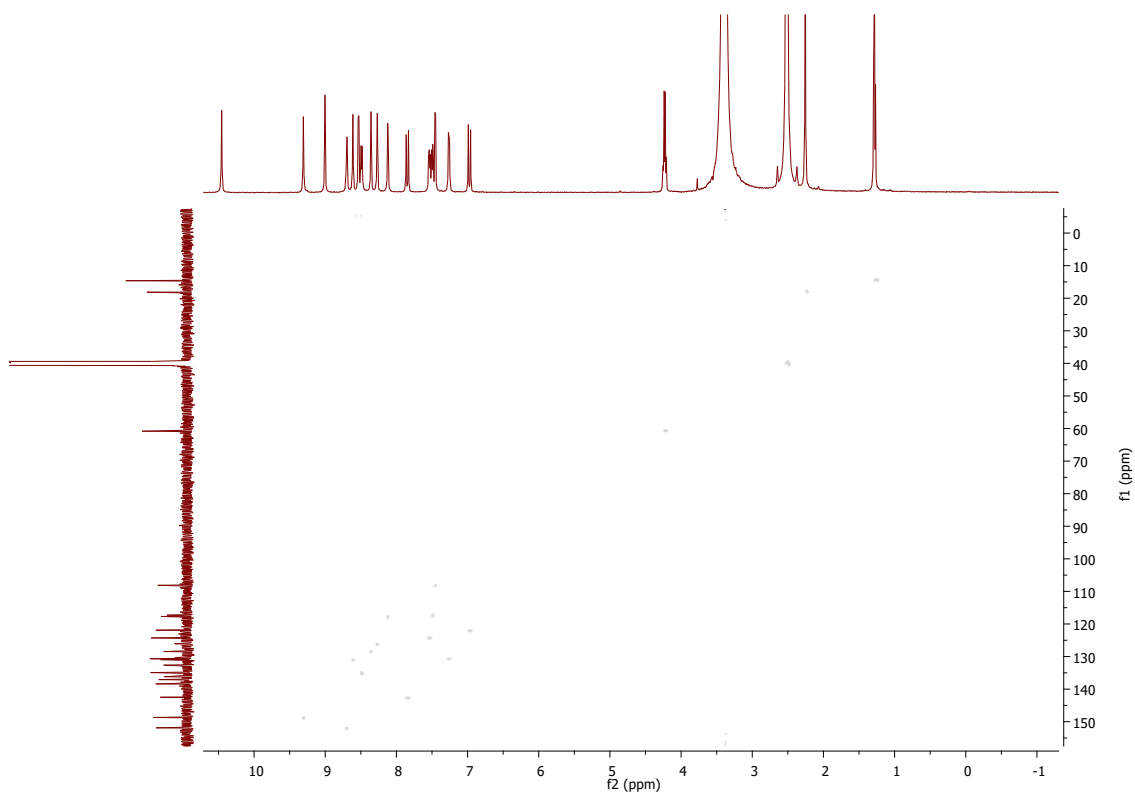


Fig. 8Sf. HSQC of **10** in DMSO- d_6

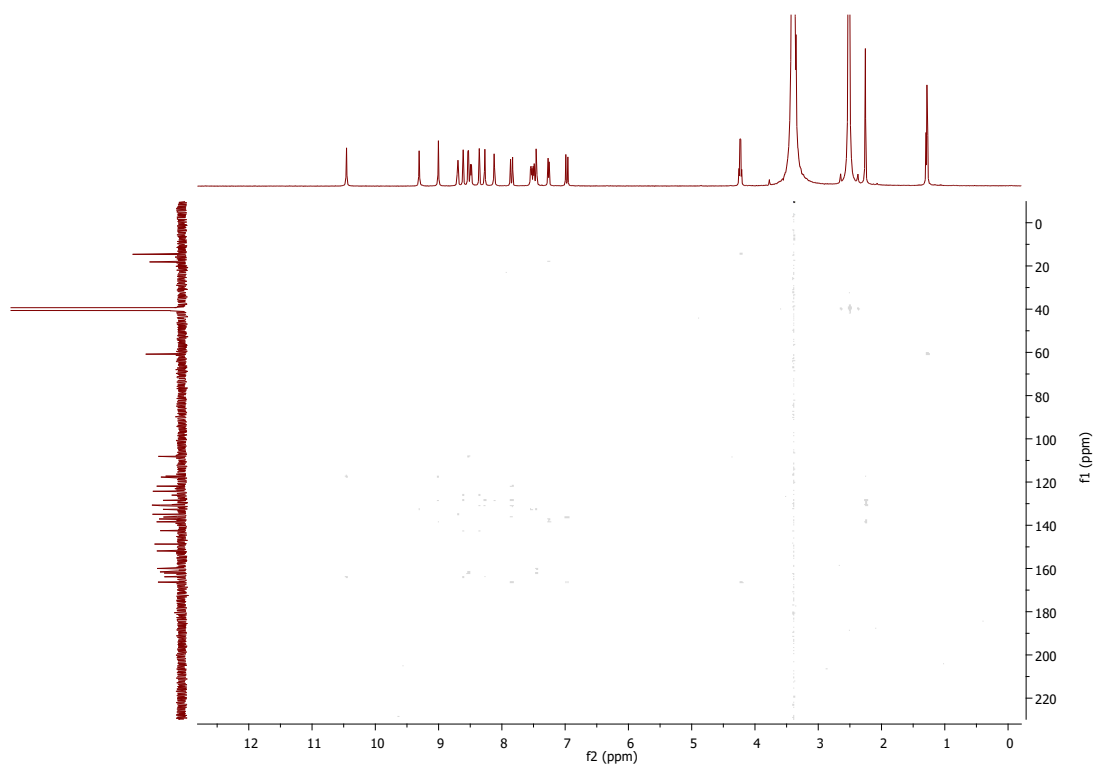


Fig. 8Sg. HMBC of **10** in DMSO- d_6

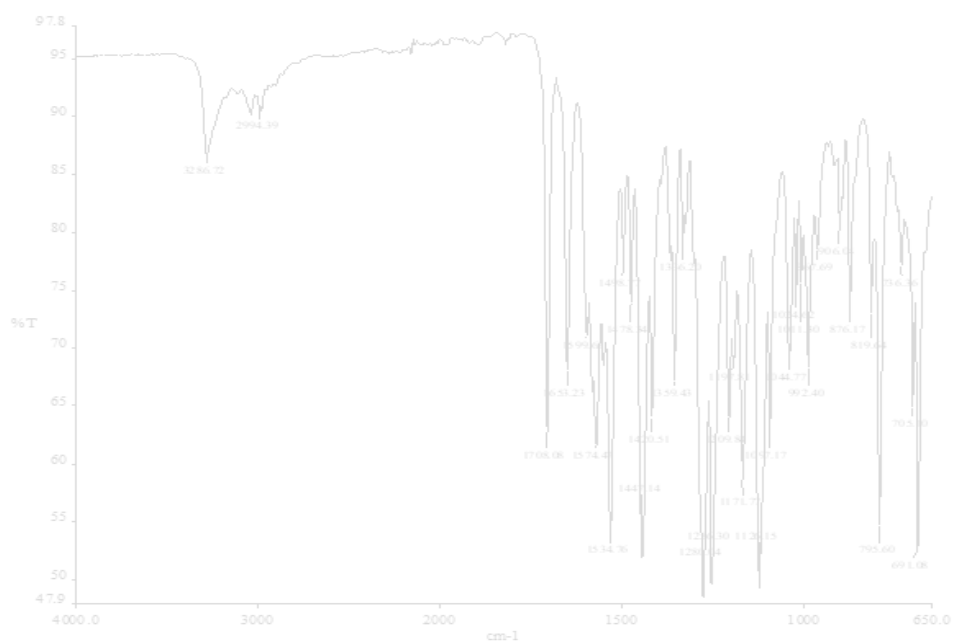


Fig. 8Sh. IR of **10**

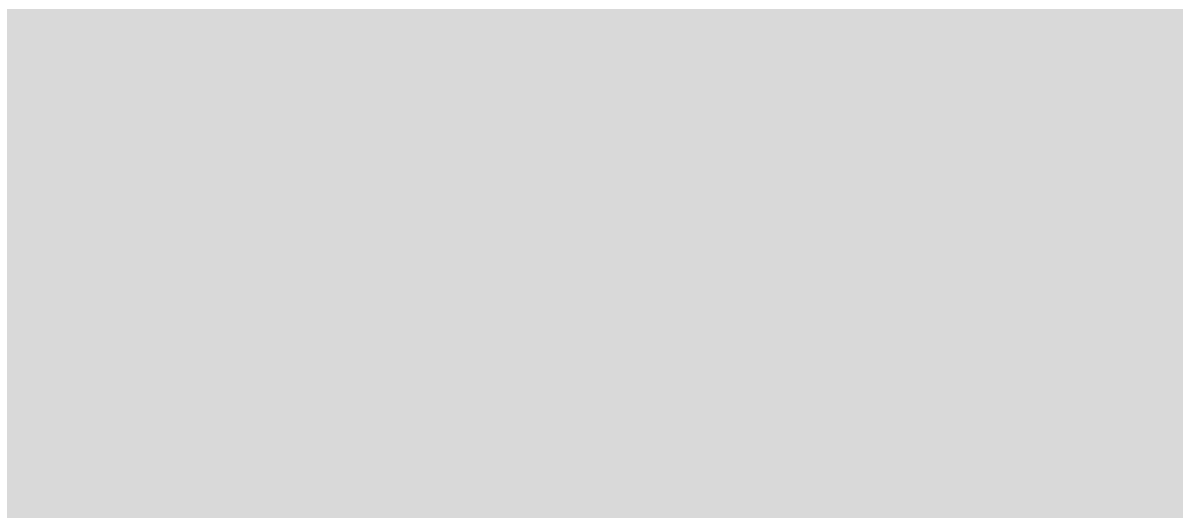


Fig. 8Si. LCMS of **10**

Compound 11

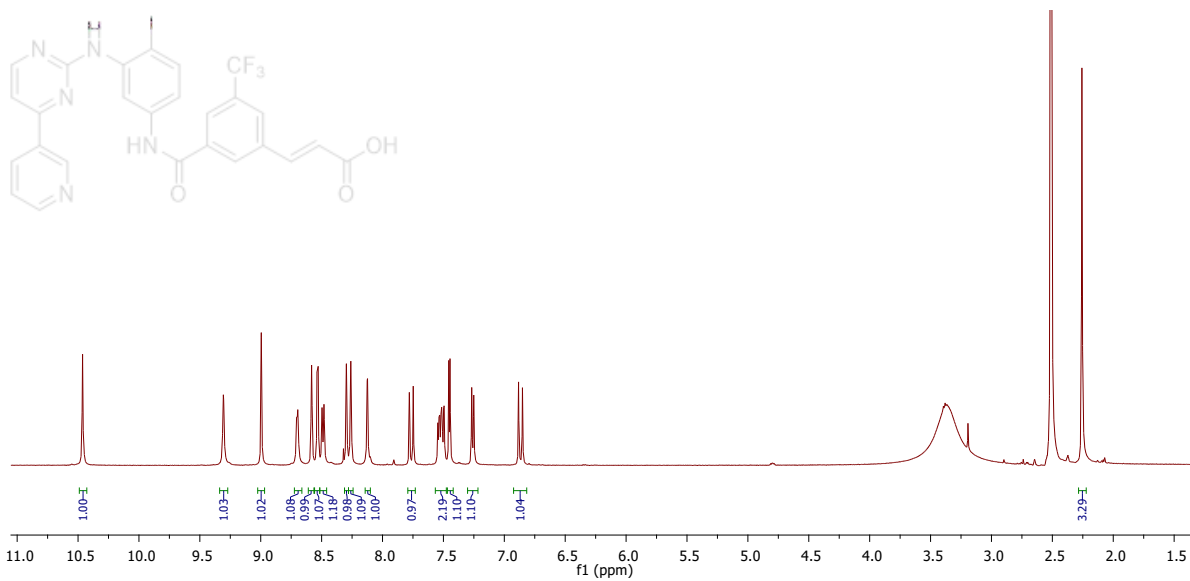


Fig. 9Sa. ¹H NMR of 11 in DMSO-d₆

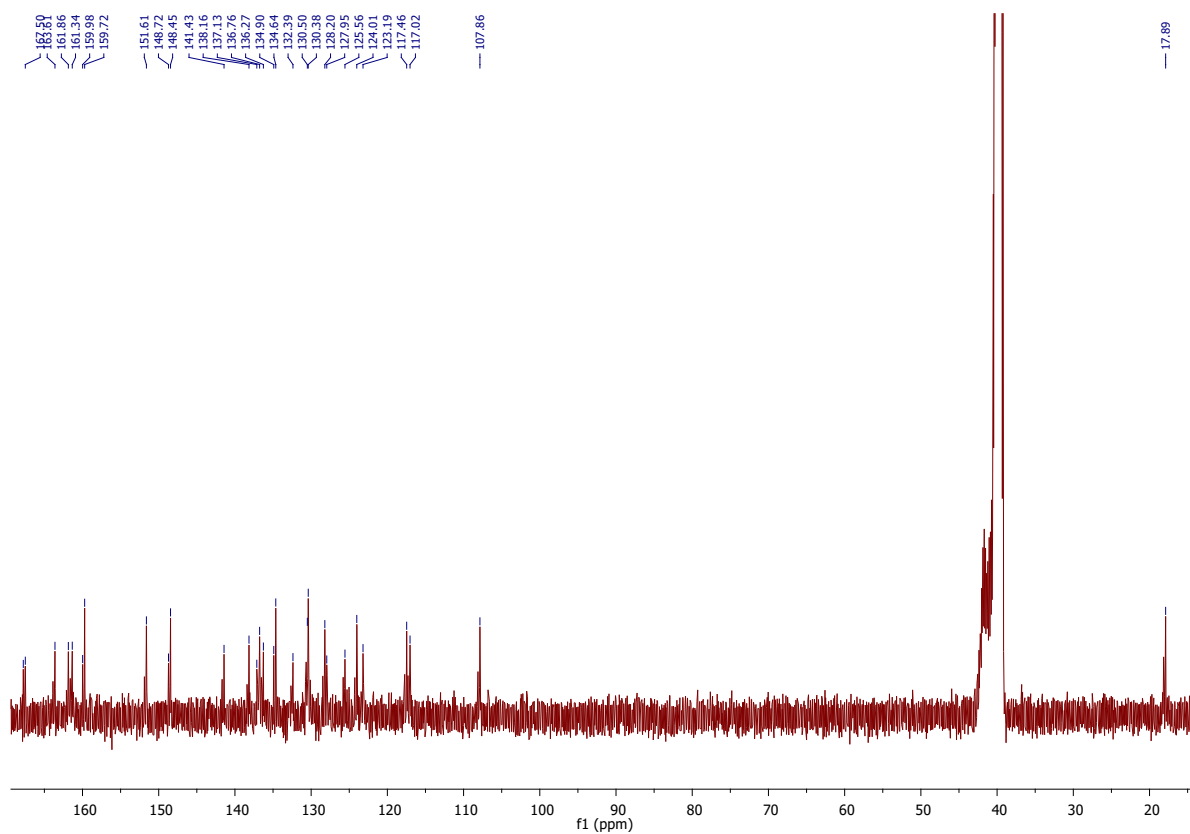


Fig. 9Sb. ¹³C NMR of 11 in DMSO-d₆

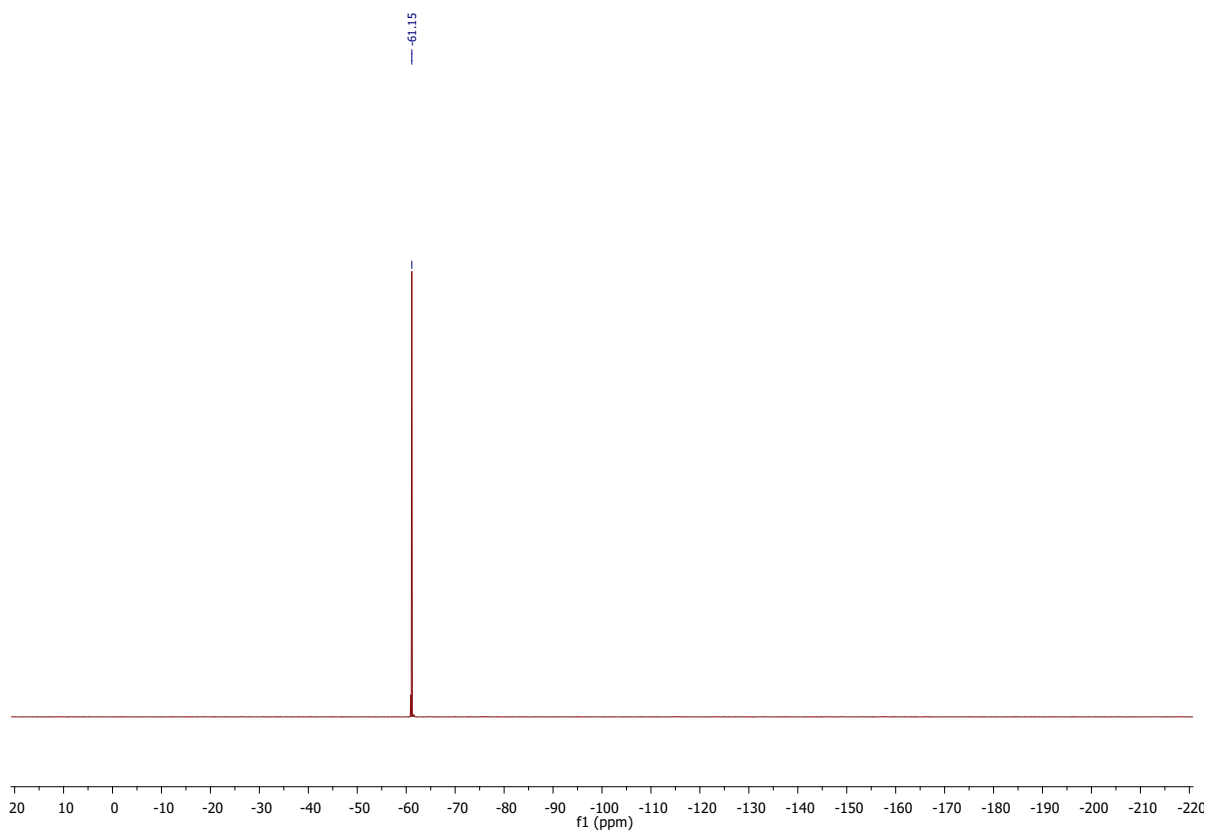


Fig. 9Sc. ^{19}F NMR of **11** in $\text{DMSO-}d_6$

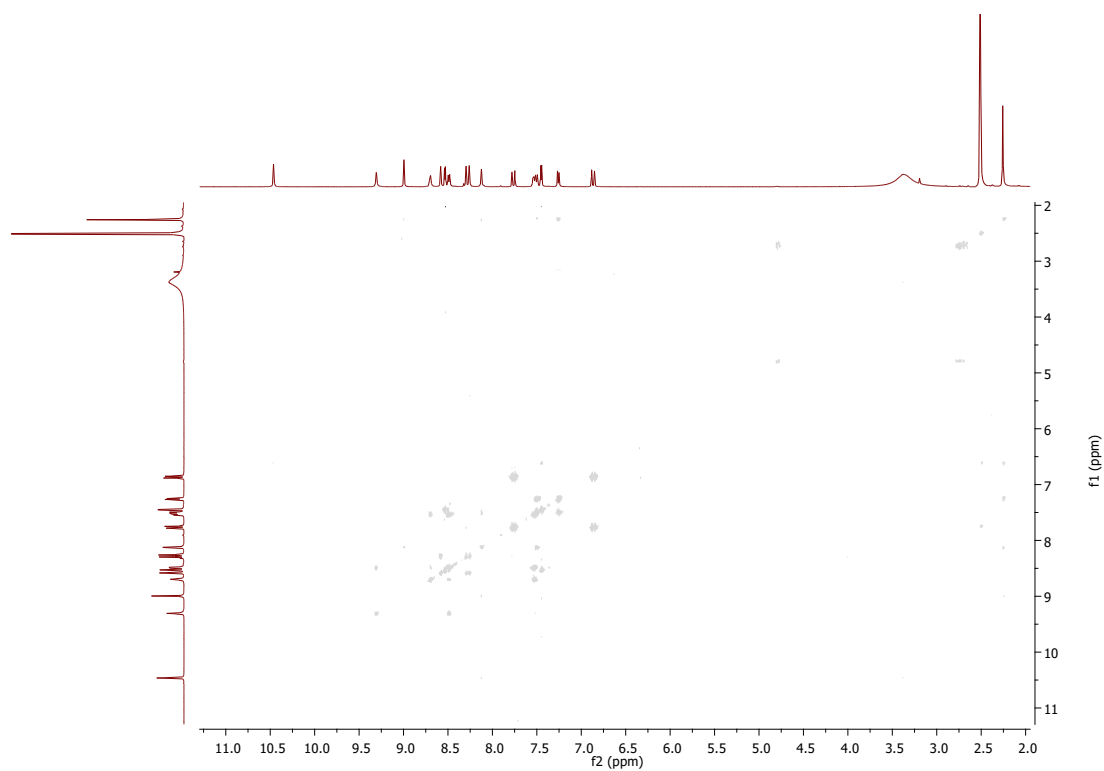


Fig. 9Sd. COSY of **11** in $\text{DMSO-}d_6$

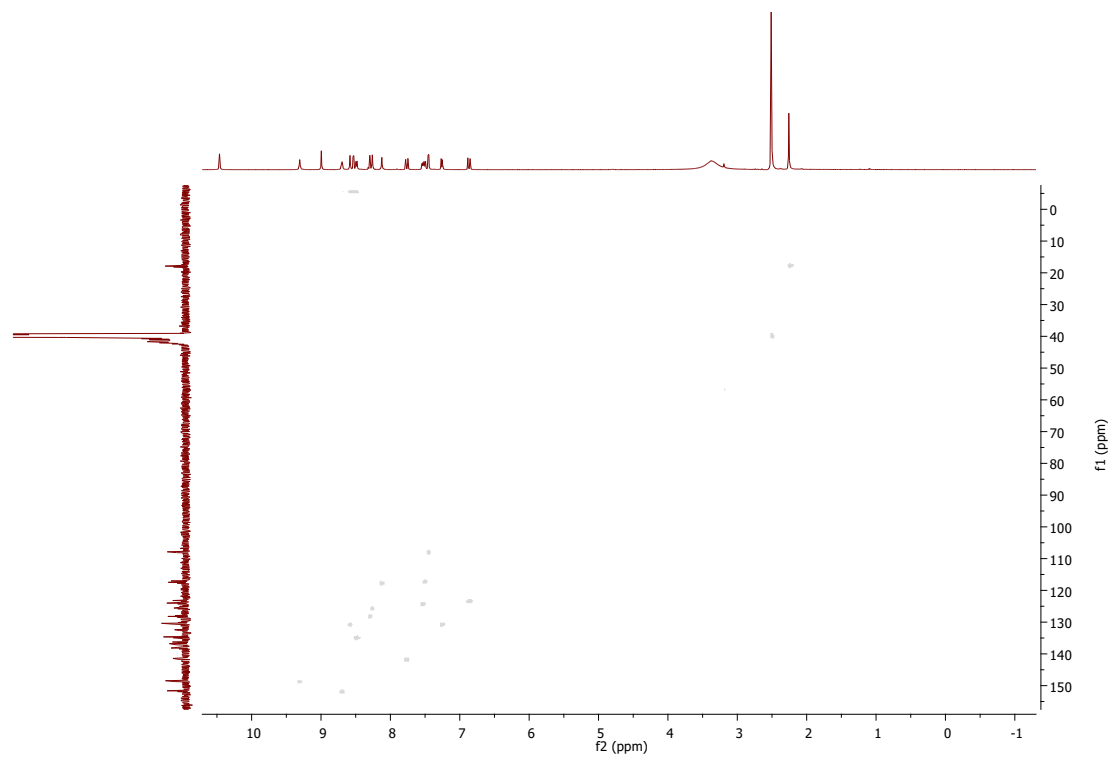


Fig. 9Se. HSQC of **11** in DMSO- d_6

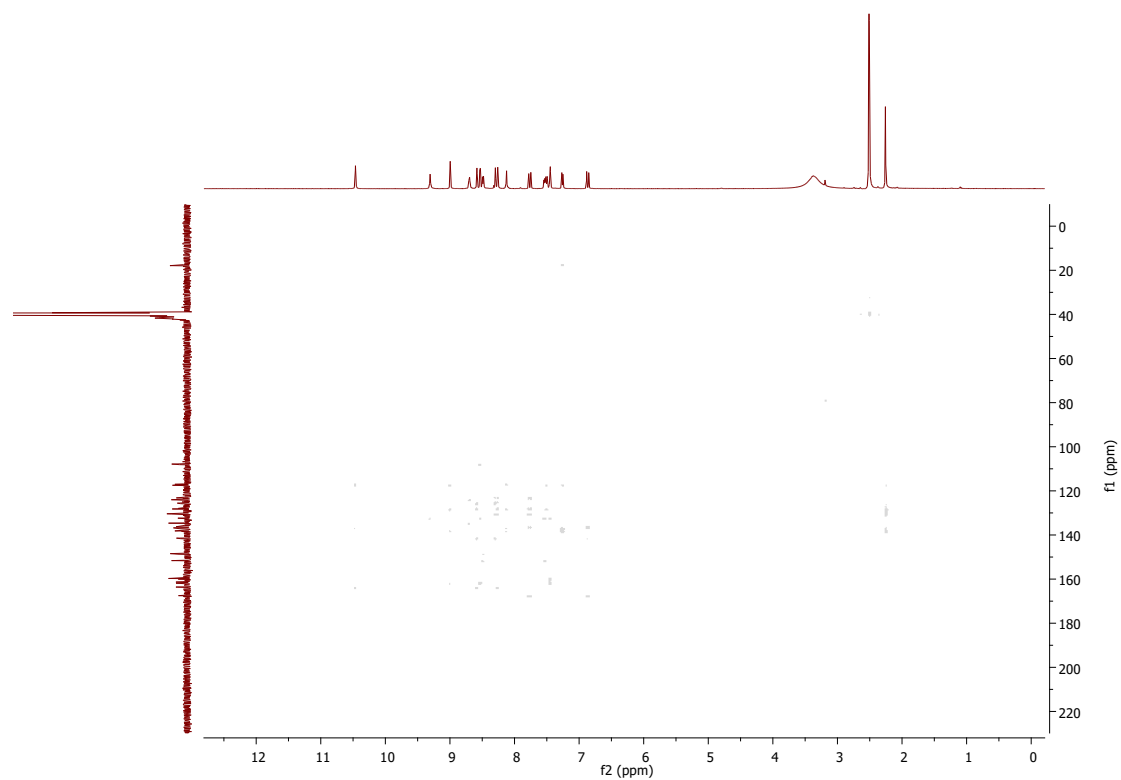


Fig. 9Sf. HMBC of **11** in DMSO- d_6

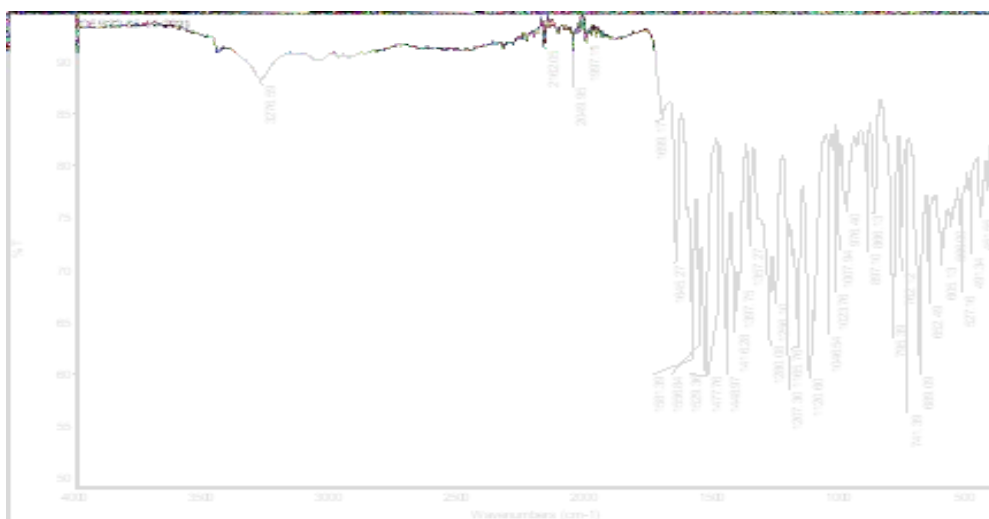


Fig. 9Sg. IR of **11**



Fig. 9Sh. HRMS of **11**

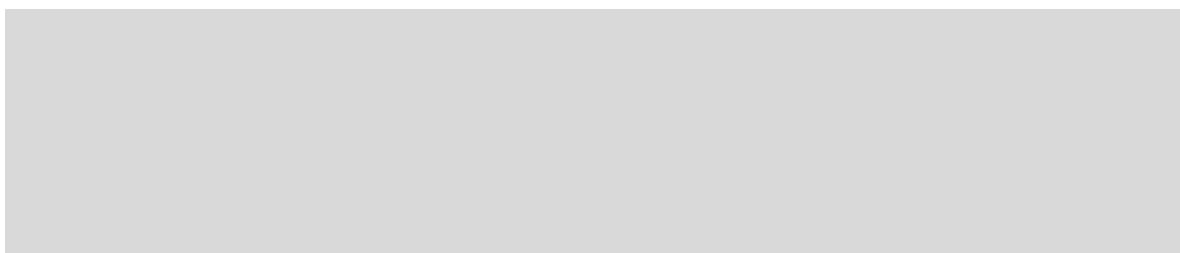
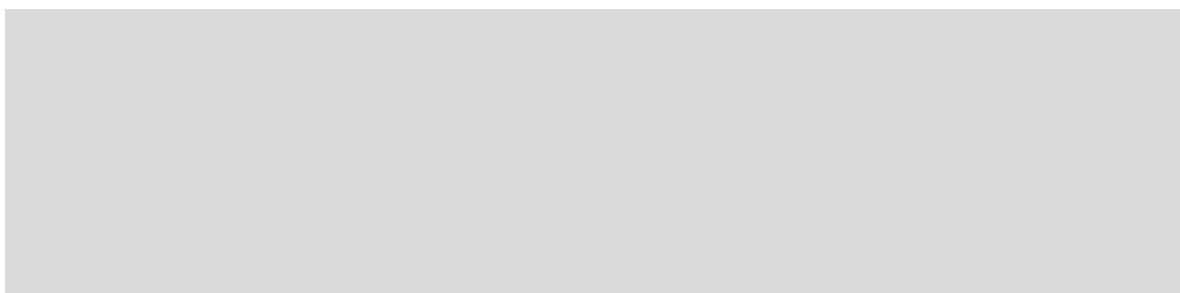


Fig. 9Si. LCMS of **11**

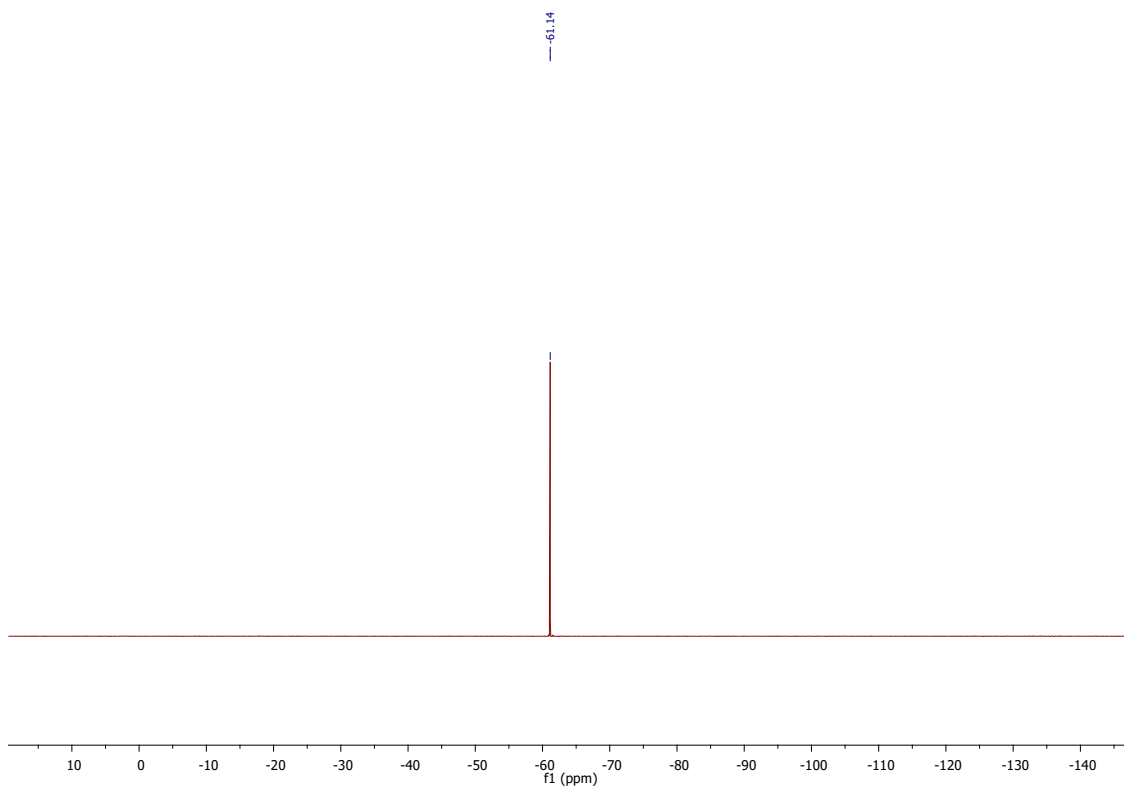


Fig. 10Sc. ^{19}F NMR of **12** in $\text{DMSO-}d_6$

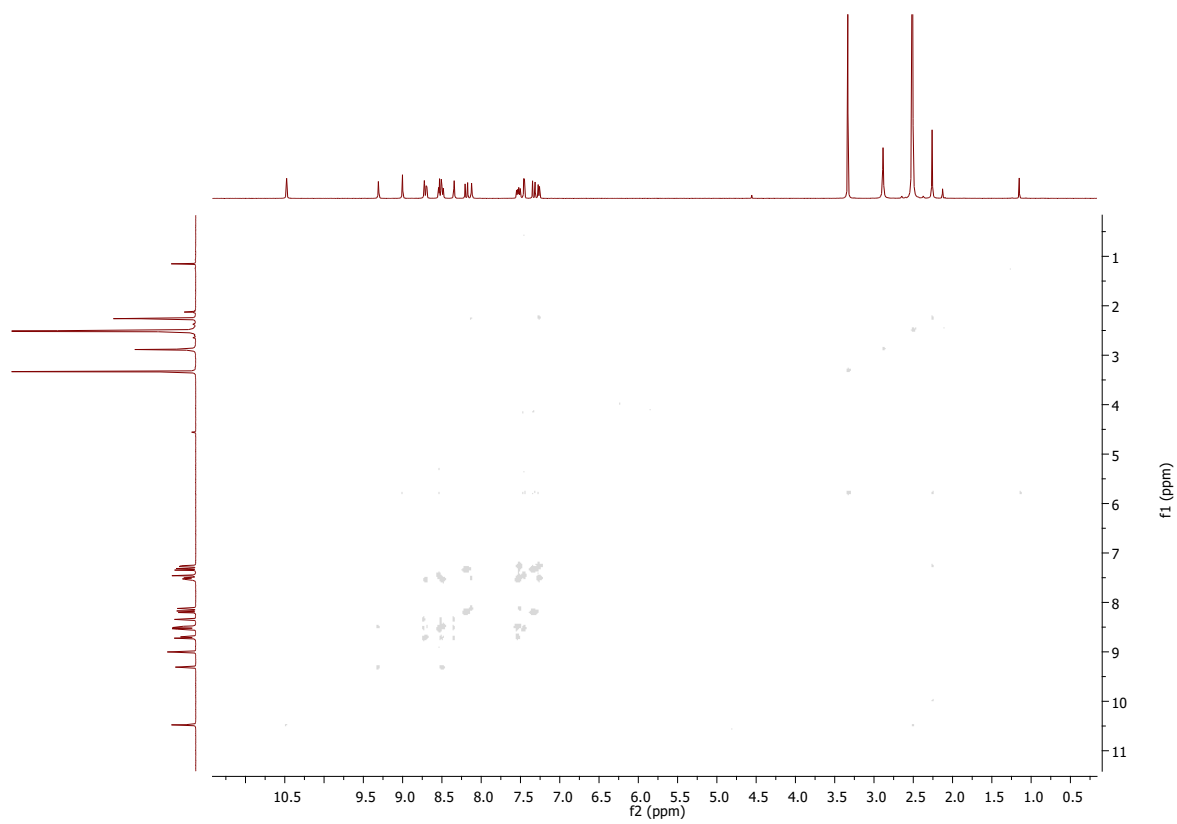


Fig. 10Sd. COSY of **12** in $\text{DMSO-}d_6$

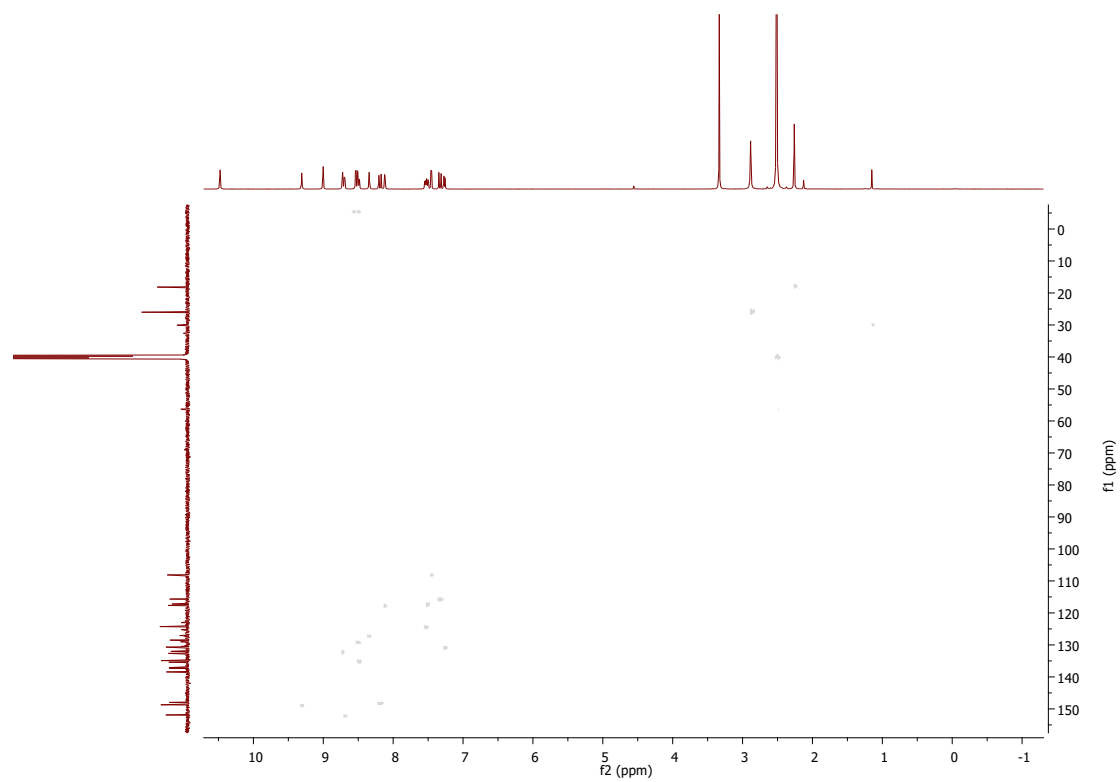


Fig. 10Se. HSQC of **12** in DMSO- d_6

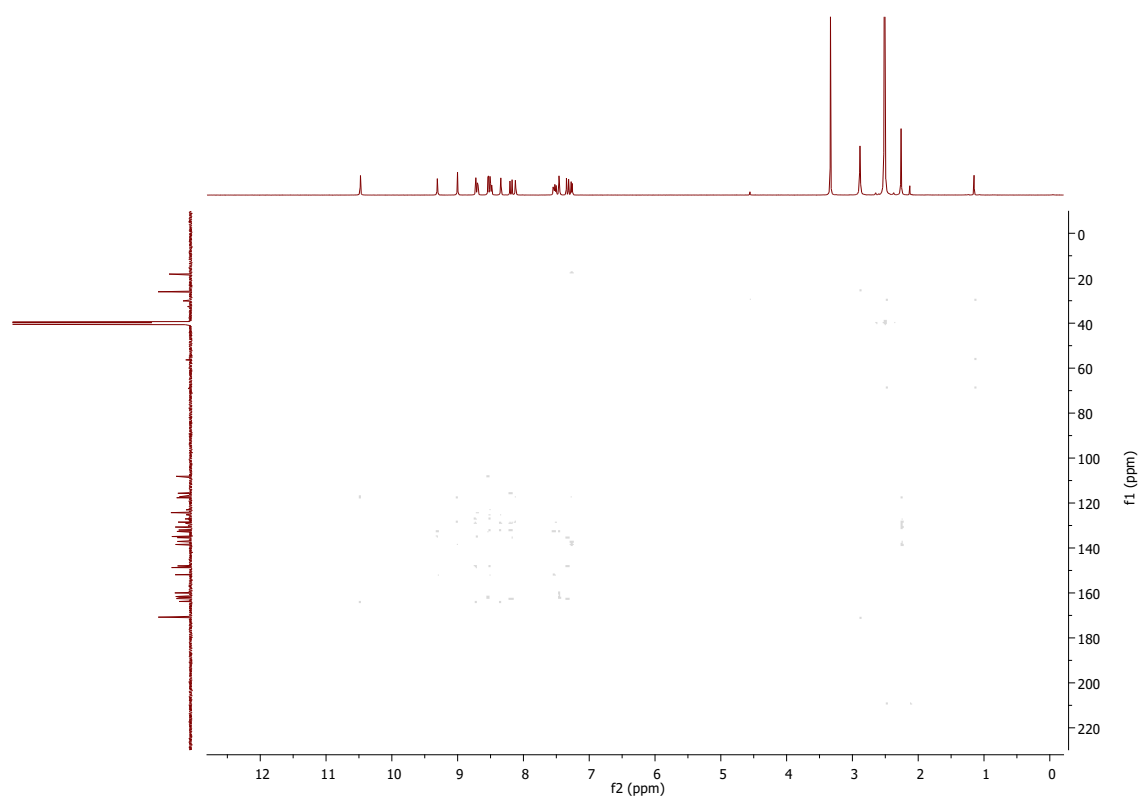


Fig. 10Sf. HMBC of **12** in DMSO- d_6

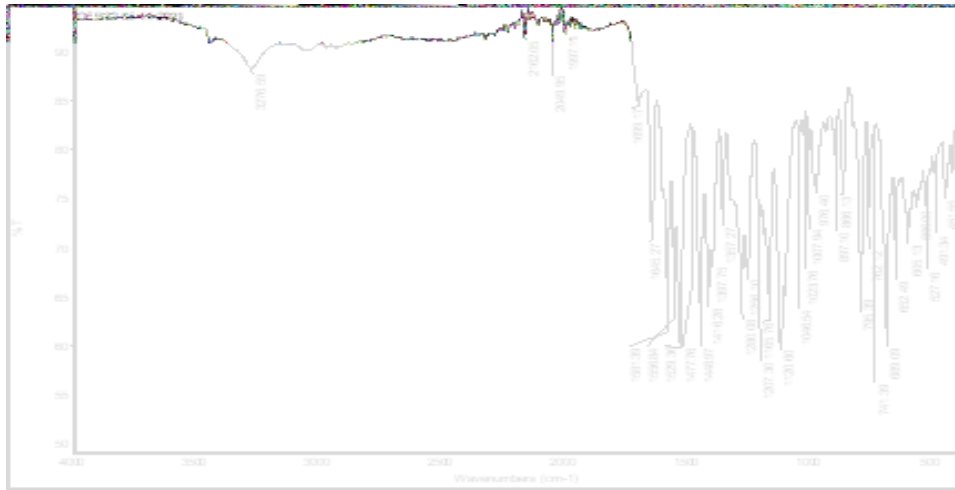


Fig. 10Sg. IR of **12**



Fig. 10Sh. HRMS of **12**

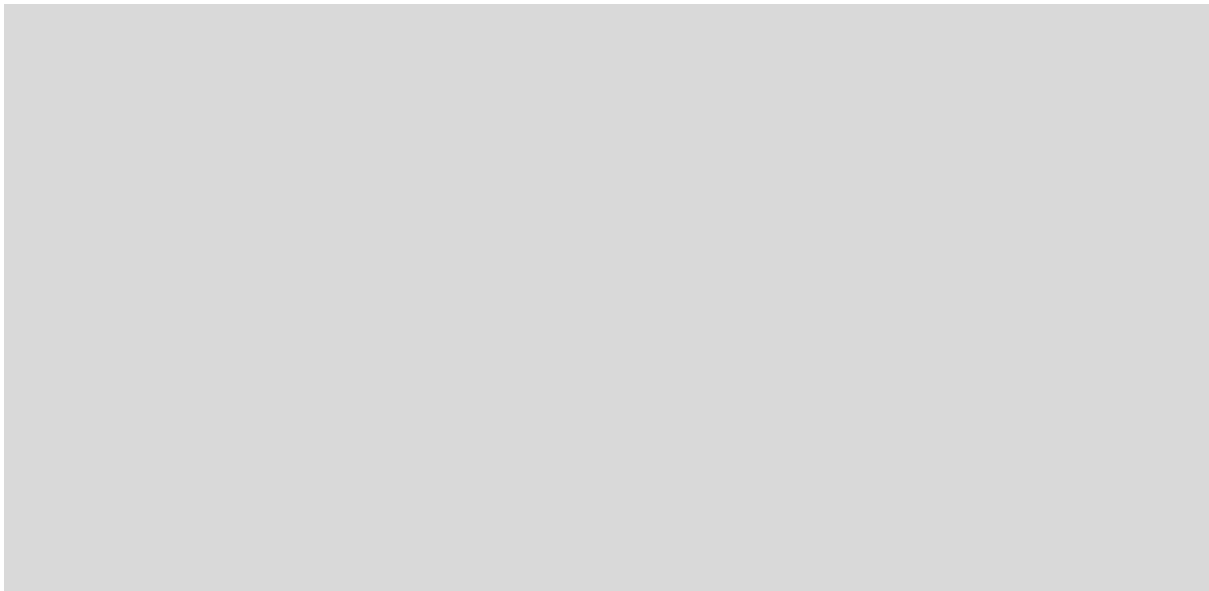


Fig. 10Si. LCMS of **12**

Complex B

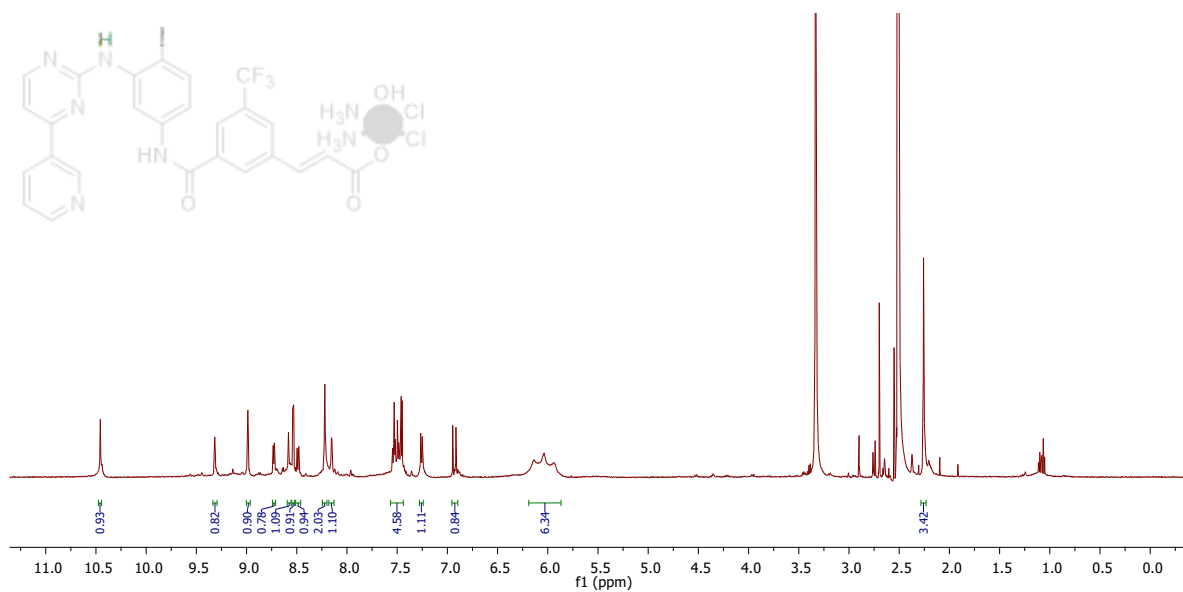


Fig. 11Sa. ^1H NMR of **B** in $\text{DMSO-}d_6$

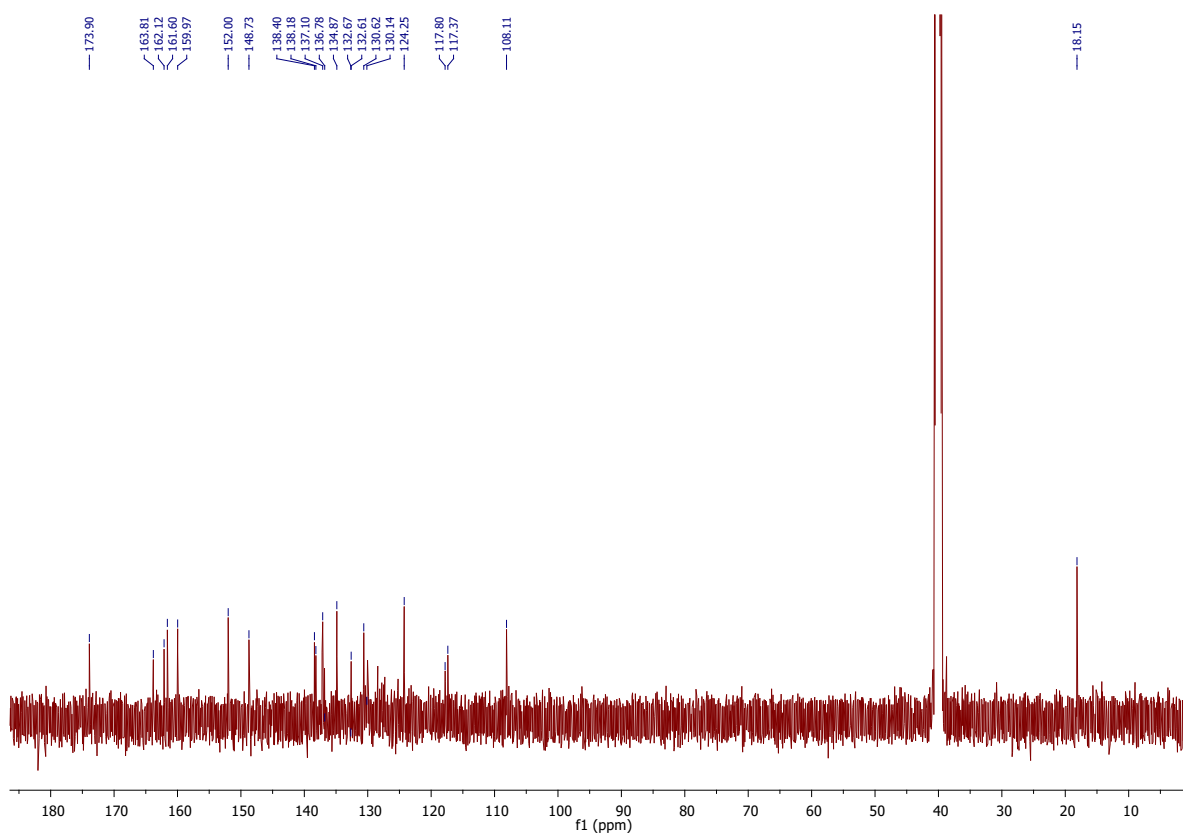


Fig. 11Sb. ^{13}C NMR of **B** in $\text{DMSO-}d_6$

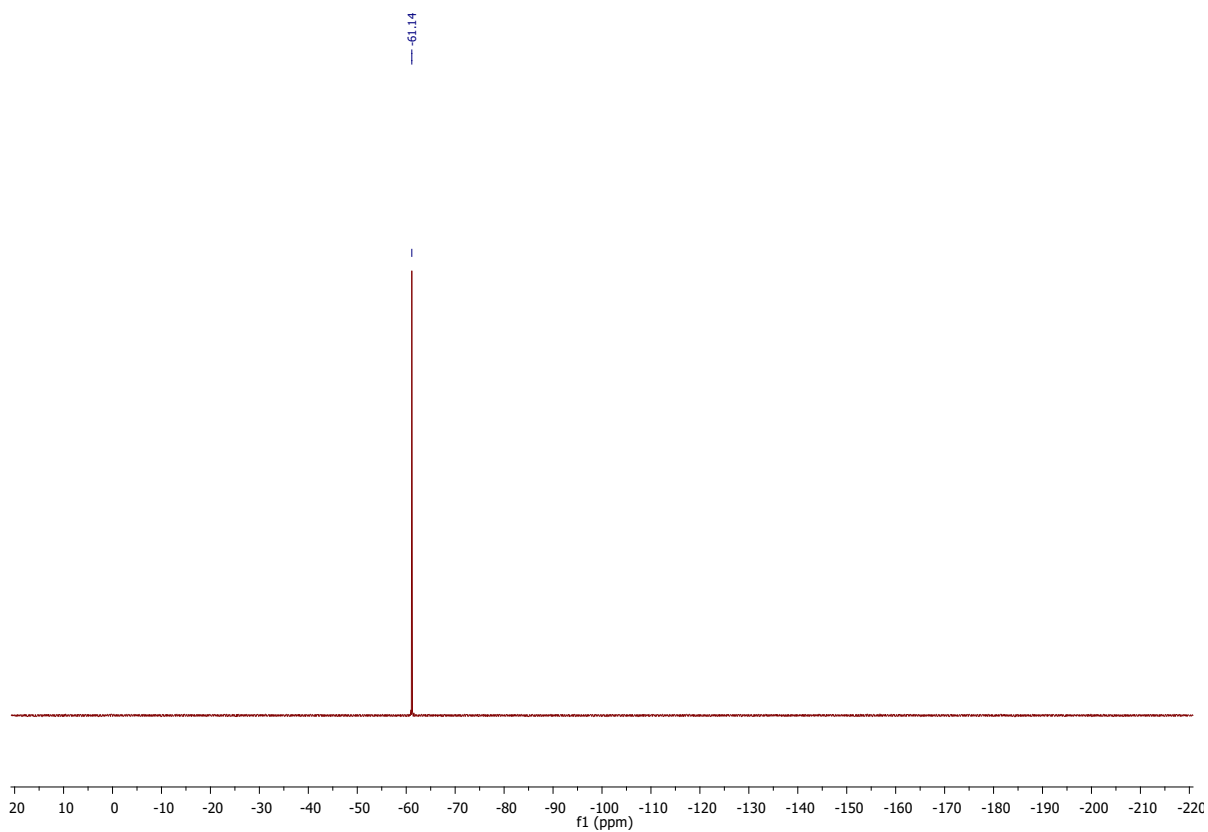


Fig. 11Sc. ^{19}F NMR of **B** in $\text{DMSO-}d_6$

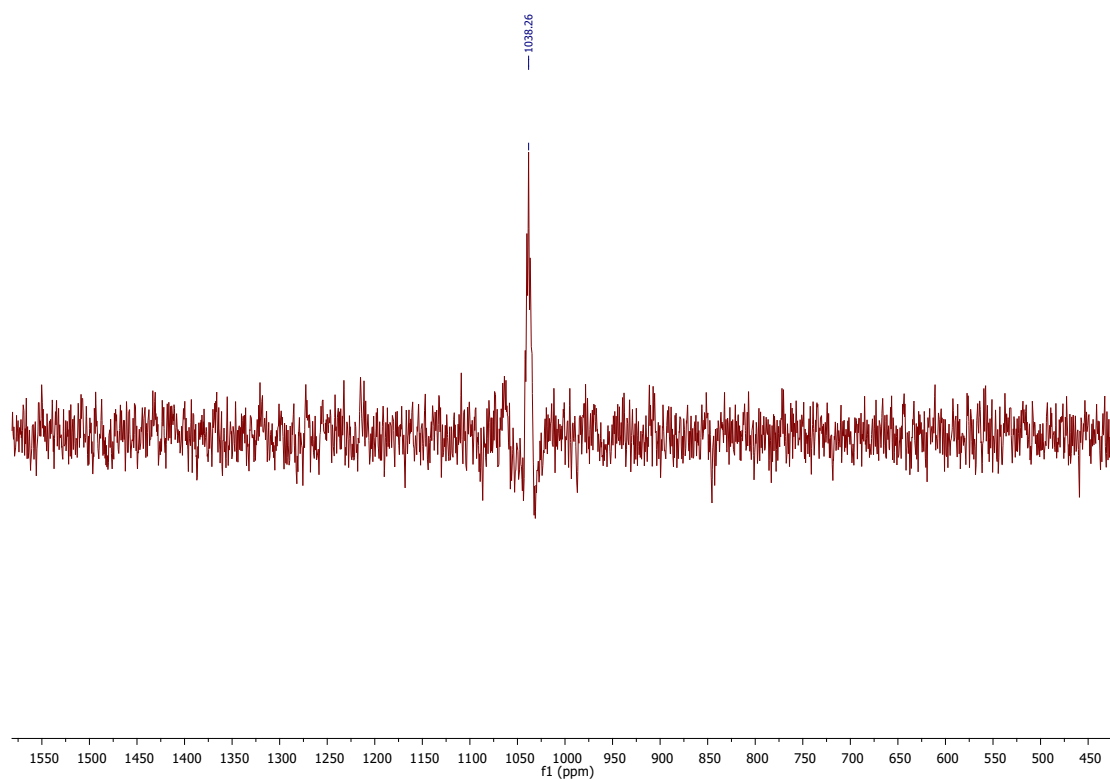


Fig. 11Sd. ^{195}Pt NMR of **B** in $\text{DMSO-}d_6$

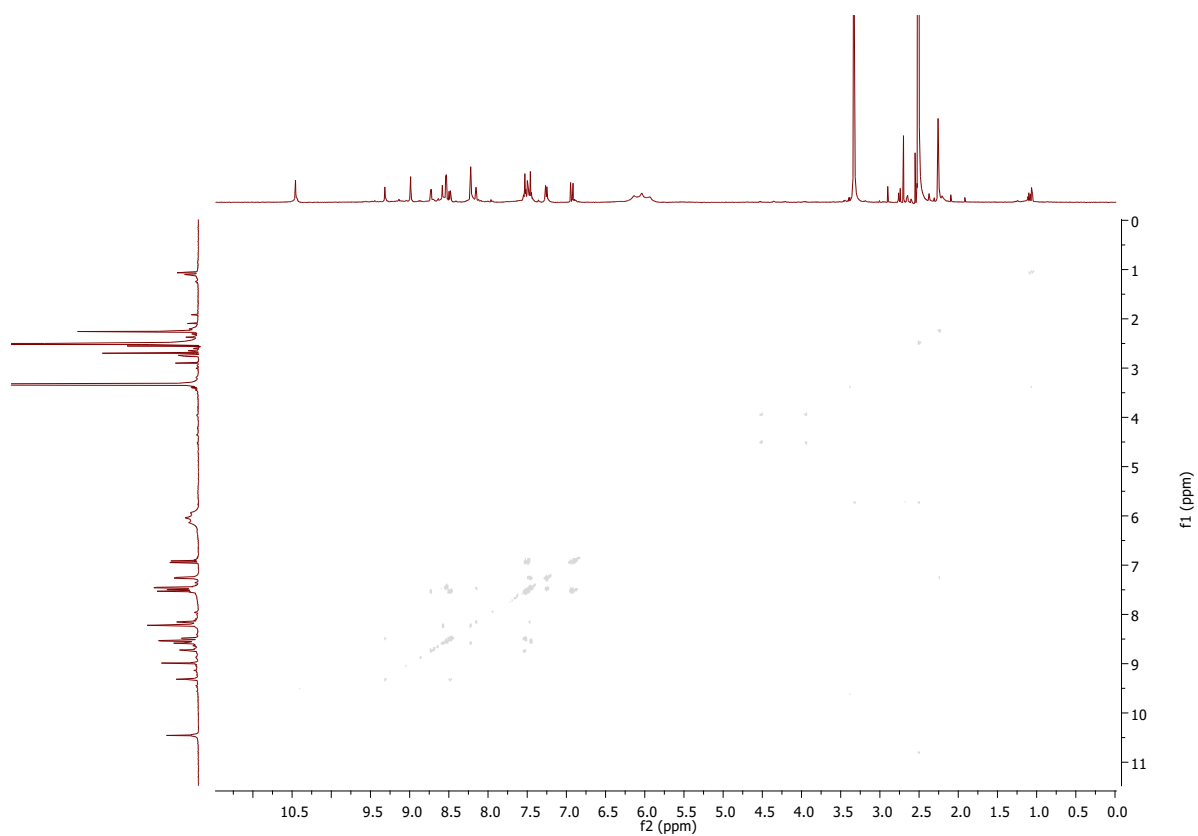


Fig. 11Se. COSY of **B** in DMSO- d_6

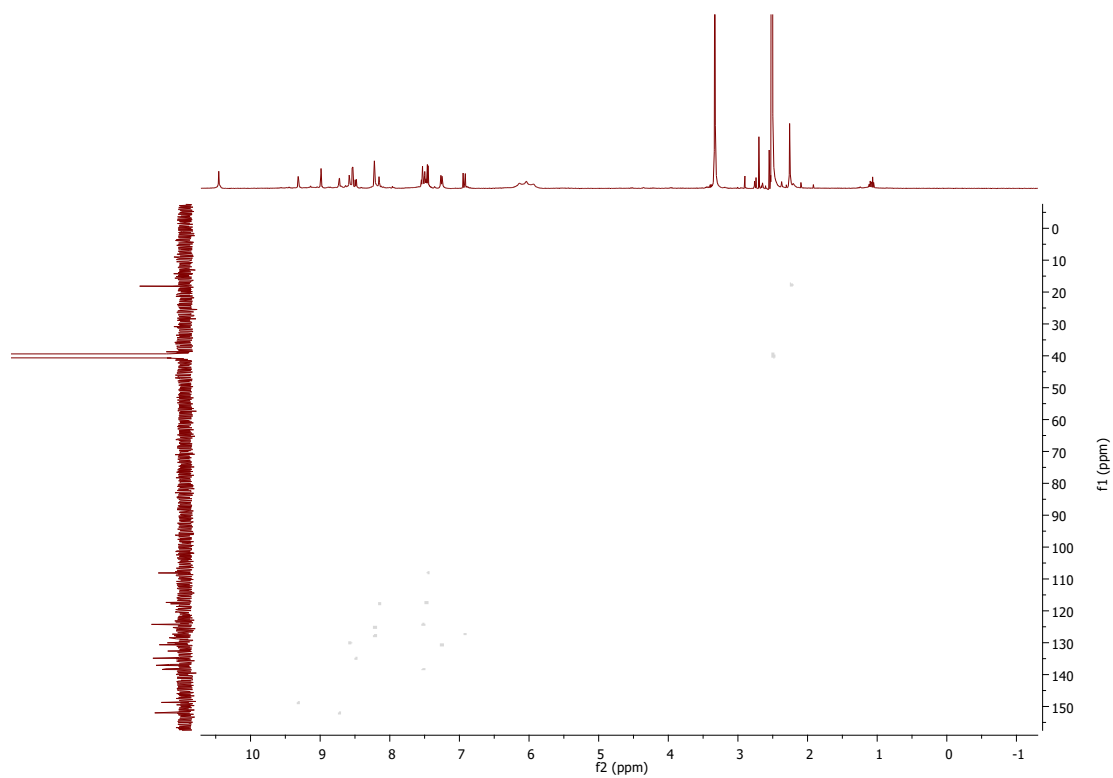


Fig. 11Sf. HSQC of **B** in DMSO- d_6

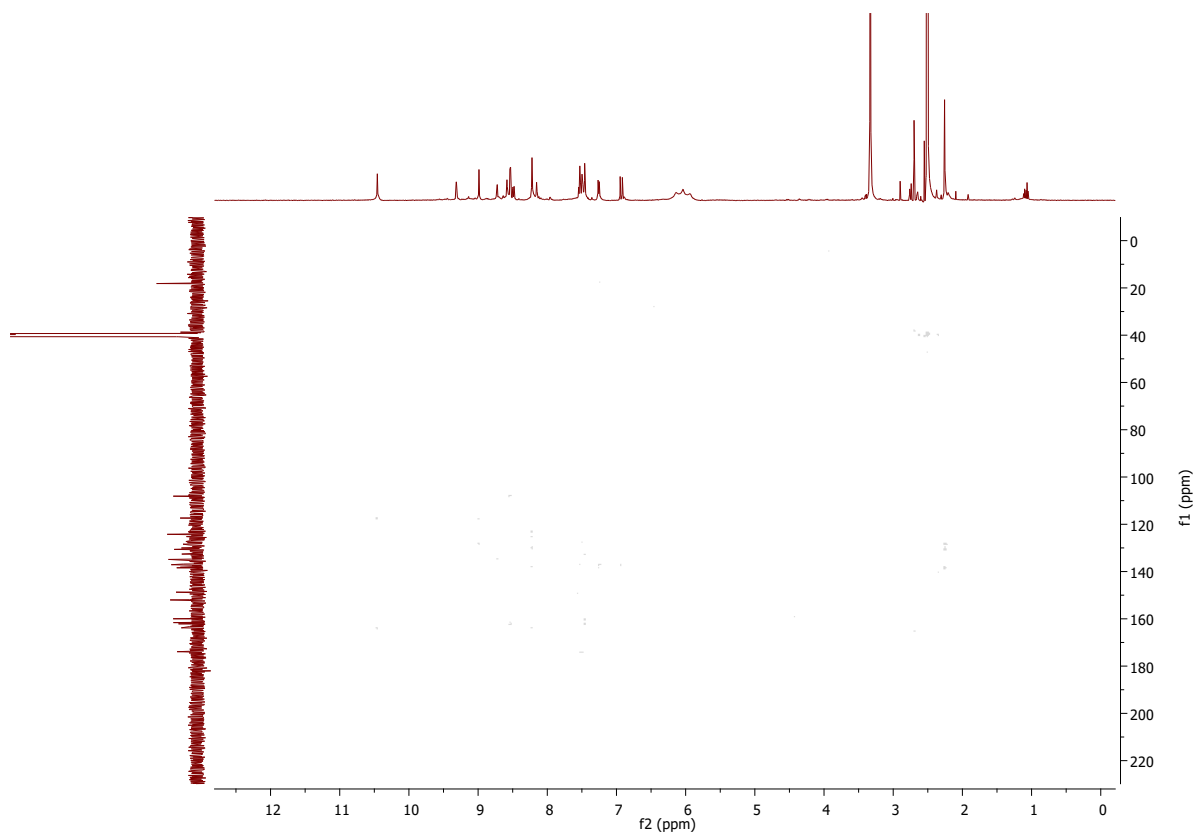


Fig. 11Sg. HMBC of **B** in DMSO- d_6

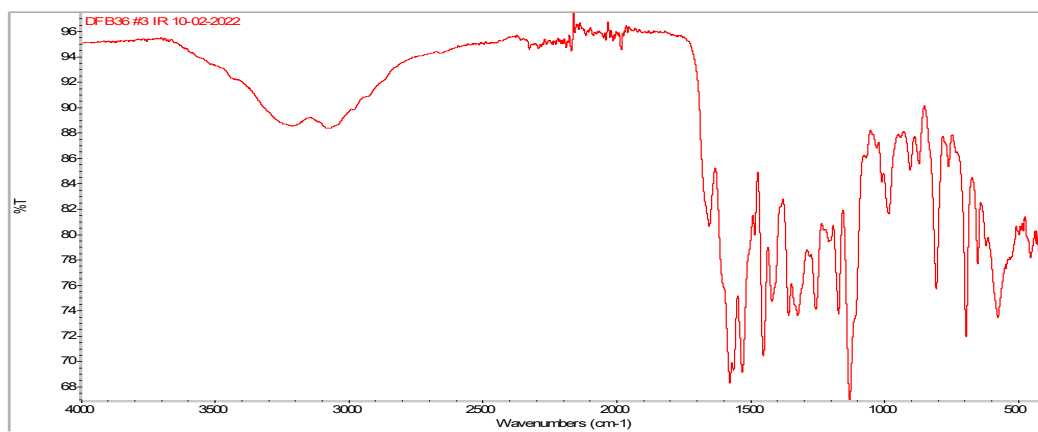


Fig. 11Sh. IR of **B**

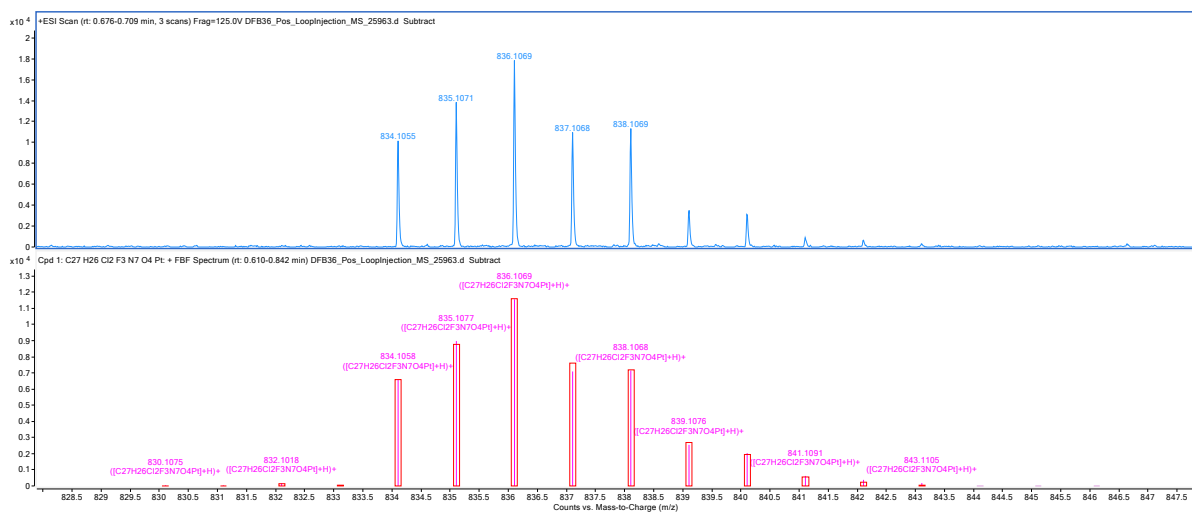


Fig. 11Si. HRMS of **B**

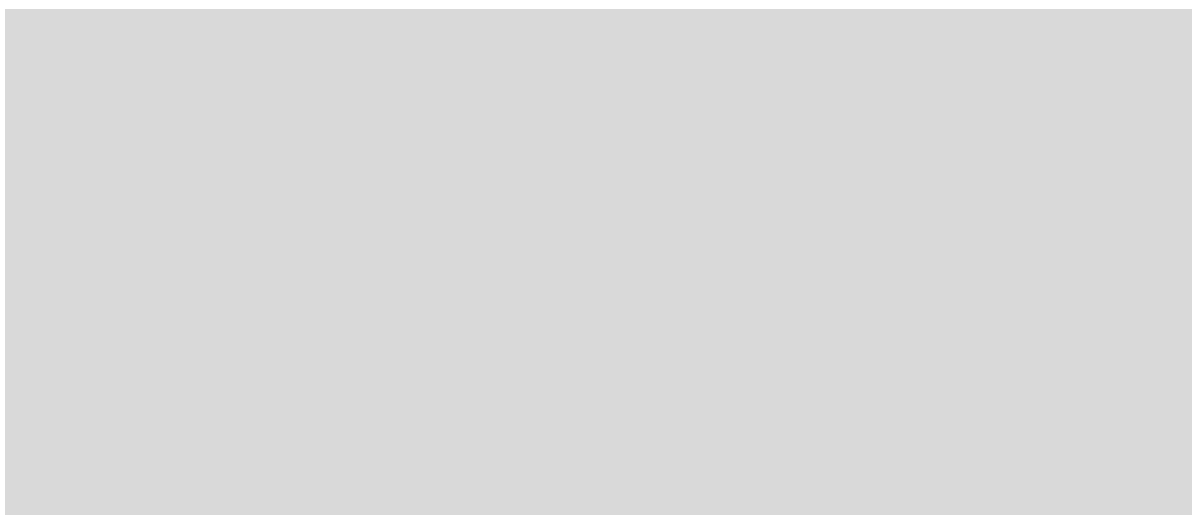


Fig. 12s. UV-VIS stability of complexes **A** and **B** in DMSO/PBS buffer (1/9). • t = 0; • t = 24 h; • t = 72 h.



Fig. 13Sa. Reduction behaviour of **A**. ^1H -NMR spectra at different intervals of **A** in the presence of 10 eq. of Ascorbic Acid in $\text{DMSO-}d_6$.



Fig. 13Sb. Reduction behaviour of **B**. ^1H -NMR spectra at different intervals of **B** in the presence of 10 eq. of Ascorbic Acid in $\text{DMSO-}d_6$.

Computational details

DFT Optimisation

Quantum mechanics (QM) simulations were performed to obtain optimised structures of Pt(IV)-imatinib and Pt(IV)-nilotinib using Gaussian 16 Rev C.016 at the wb97cf level of theory.^[1] Double- ξ LANL2DZ basis set consisting of 18 valence electrons associated with the effective core potentials (ECPs) of Hay and Wadt was employed for Pt atoms^[2], and the 6-31+G** basis set has been used for hydrogen, carbon, oxygen, nitrogen, and chlorine atoms.^[3] The solvent effect of water was taken into account using the polarizable continuum model (PCM).^[4] All optimised structures were characterised by positive frequency eigenvalues, indicating that true minima were located for each system.

Docking studies

The 1.90 Å and 1.60 Å x-ray crystal structures of PDGFR- α and c-KIT tyrosine kinase in complex with imatinib were retrieved from the Protein Data Bank (PDB ID codes 6JOL and 1T46). They were pre-processed and refined, including elimination of solvent molecules, addition of missing atoms, and assessment of appropriate protonation states at physiological pH, using the Protein Preparation Wizard employed in the Schrödinger Suite.^[5] c-KIT T670I mutated structure was prepared through Mutate module of the Schrödinger Suite, and appropriate positioning of the new residue and its closest neighbours was assured by their minimisation.

QM optimised structures of Pt(IV) prodrugs were used as inputs with minimal adjustments required to prepare the metal chelate structures for docking with Glide (assignment of zero-order bonds within the metal complex to obviate the need for specific force field parameters involving the metal ion). The coordination geometry of metal centre and complexation fragments was restrained during Glide optimisation and fitting to remain similar to the QM calculated geometry.

Molecular docking was performed with Glide in three steps; rigid docking to identify the best-fit orientation of the compounds into the binding site with single precision (SP) protocol, followed by extra precision (XP) protocol, and finally induced fit docking (IFD) allowing for receptor residues distanced up to 5 Å from the ligand heavy atoms to relax.^[6,7] The appropriate receptor grid was generated based upon the positioning of co-crystallised imatinib molecule within the original X-ray structures employing a grid box 25 Å each side. The larger grid box was necessary to ensure appropriate sampling of any atypical pockets close to the main drug-binding site considering larger sizes of the metal chelates compared to typical small molecules. Docking simulations of pre-bound imatinib were used to evaluate the accuracy of the chosen setup. Comparative docking study hence included original imatinib and nilotinib drugs, the Pt(IV) prodrugs, as well as their acidic form in case of the metal centre detachment, giving a total of 18 systems studied. Validation of the docking protocol was carried out by re-docking imatinib in both receptors with RMSD values of 0.79 and 0.74 Å in comparison to the co-crystallised poses (Figure 13S a/d), confirming the suitability of the approach used.

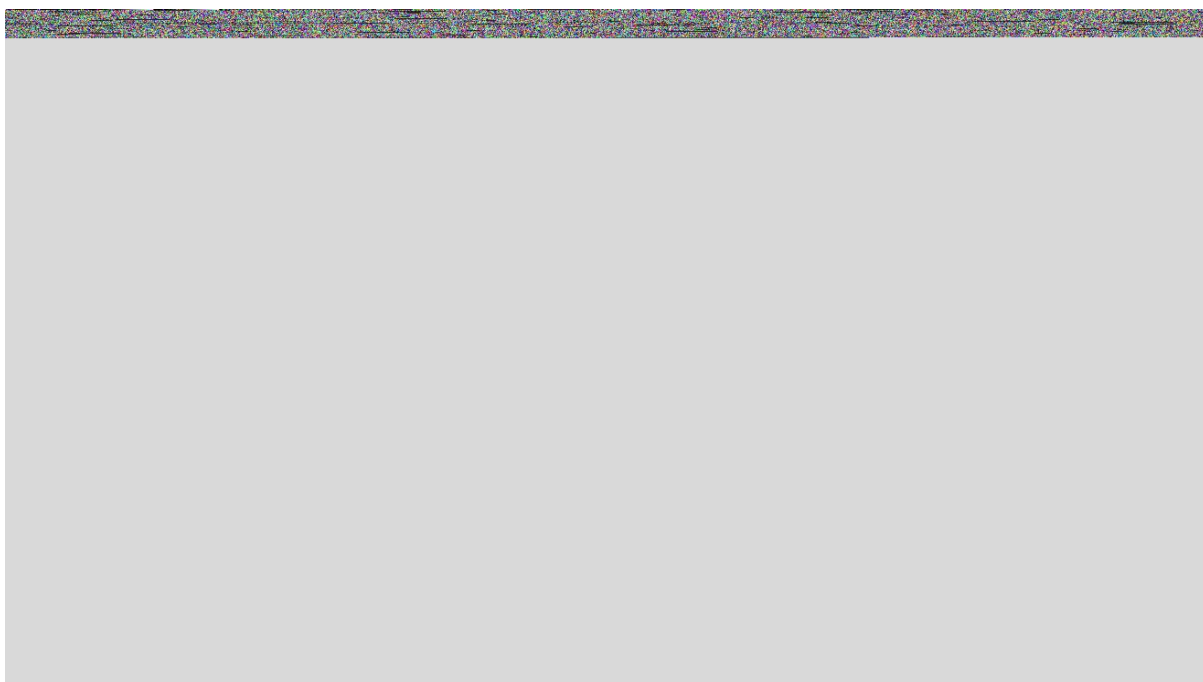


Fig. 14S. (a) Ribbon and surface representation of imatinib co-crystallised within PDGFR- α (PDB ID 6JOL). (b) Ribbon and surface representation of imatinib co-crystallised within c-kit tyrosine kinase (PDB ID 1T46). (c) Overlap of co-crystallised imatinib (grey) and imatinib docked in PDGFR- α using Glide (cyan). (d) Overlap of co-crystallised imatinib (grey) and imatinib docked in c-kit tyrosine kinase using Glide (cyan).



Fig. 15S. Docking scores (G_{score}) of imatinib, nilotinib, Pt(IV) complexes **A** and **B** and the A_ and B_ ligand-COOH structures in PDGFR- α , c-KIT, and mutated c-KIT T670I as obtained by Glide. Lighter shaded colours correspond to rigid docking scores, whereas docking scores from IFD flexible binding site protocol are shown as dimmed.

Contacts formed between the six ligands and PDGFR- α in the flexible docking with Glide

The binding poses of the six ligands within PDGFR- α as modelled by IFD in Glide are shown in Figure 3, and their two-dimensional interaction profiles are presented in Figure 15S. Several potential hydrogen bonds (HB) and other non-bonding interactions were observed to reoccur throughout the six studied systems. HB of the nitrogen from the terminal pyridine ring with the amino backbone group of CYS677 is maintained with all the ligands, as is the π - π stacking of pyrimidine moiety with PHE837. Except for the best scoring pose of Pt-nilotinib, HB between the amino group connecting pyrimidine and tri-substituted phenyl rings and THR674 is also seen in all the systems. Major differences in binding modes

arise from the remaining ligand fragments, namely amide connected phenyl rings with piperazine, imidazole, and Pt-complexed tails. In the case of both imatinib and nilotinib, amide functional group is the last fragment which interacts with the target, where NH acts as a hydrogen donor to GLU644, and carbonyl group of nilotinib forms an HB with ASP836. Neither of the two rings that extend towards out of the enclosed binding cavity contribute to non-covalent interactions with nearby residues. Acidic tails and metal centres of Pt-prodrug conjugates allow formation of hydrogen and halogen bonds well outside the binding pocket. Hydroxyl group of the Pt-imatinib metal complex established a HB with THR872, whereas that of the Pt-nilotinib metal complex formed a HB with ARG817. Complexation of Pt-nilotinib also benefited from two interactions between a chlorine and ARG817, one being a salt bridge and the other a halogen bond. Acidic Pt-prodrug forms with detached metal centre have each established a HB with the backbone amino groups of ARG817 in the case of Pt-imatinib-acid and that of LEU839 in the case of Pt-nilotinib-acid.

From the binding pose overlaps also shown in Figure 3, it can be concluded that the 4-pyridyl-pyrimidine core which is shared across all six ligands remains locked in the hydrophobic end of the binding pocket containing a series of non-polar amino acids (LEU599, VAL607, ALA625, VAL658, LEU825, PHE837) and two aromatic residues (TYR676 and PHE837) with consistent π - π bonding. Positively charged side-chain of LYS627 conveniently positioned in the centre of the cavity followed by hydrogen accepting carboxyl groups of GLU644 and ASP836 allows for efficient HB and π -cation network, securing the ligand binding. The entrance to the cavity is highly hydrophobic, surrounded by side chains of ILE647, LEU651, and LEU809. As the surface of the protein opens up, more points for a strong hydrogen and/or salt-based interaction arise, including SER643 and TYR872 with hydroxyl functional groups and very flexible nitrogen rich tails of LYS646 and ARG817. To reach these reactive residues, long ligands whose fragments can extend beyond the enclosed cavity, such as those containing flexible carbon chains functionalised with hydrogen deficient and/or negatively charged groups, as in the case of acidic form of the Pt-imatinib or Pt-nilotinib, are necessary.



Fig. 16S. Two-dimensional interaction diagrams for best scoring poses of imatinib, **A** and **A_ligand-COOH** (left panel top to bottom), and nilotinib, **B** and **B_ligand-COOH** (right panel top to bottom) after induced fit (IFD) docking in PDGFR- α with Glide. Legend for amino acid residues and interaction types is given on the right.

Contacts formed between the six ligands and c-KIT in the flexible docking with Glide

The binding poses of the six ligands within c-KIT as modelled by IFD in Glide are shown in Figure 4, and their two-dimensional interaction profiles are presented in Figure 16S. As the binding cavity shows similar features as those of PDGFR- α , allowing for dual inhibition of the two proteins, as shown in Figure 17S, the positioning and type of interactions established during the binding of the six ligands in the two targets are also similar. The 4-pyridyl-pyrimidine core sits comfortably in the hydrophobic cocoon enclosed by non-polar LEU595, VAL603, ALA621, VAL654, and LEU799, and two π -aromatic clouds of PHE811 and TYR672. Position of terminating pyridine is additionally ensured through HB with the amino backbone group of CYS673. Cationic end of LYS623 can be seen to form π -cation interactions with the central phenyl ring and nearby GLU640 and ASP810 are seen securing the surrounding amide and amine linkers of ligands through hydrogen bonds. Outside the binding cavity, ARG791 is the most successful in stabilising the position of metal complexed chains of Pt imatinib and nilotinib prodrugs. Position of the acidic chains after the metal centre detachment is less defined.

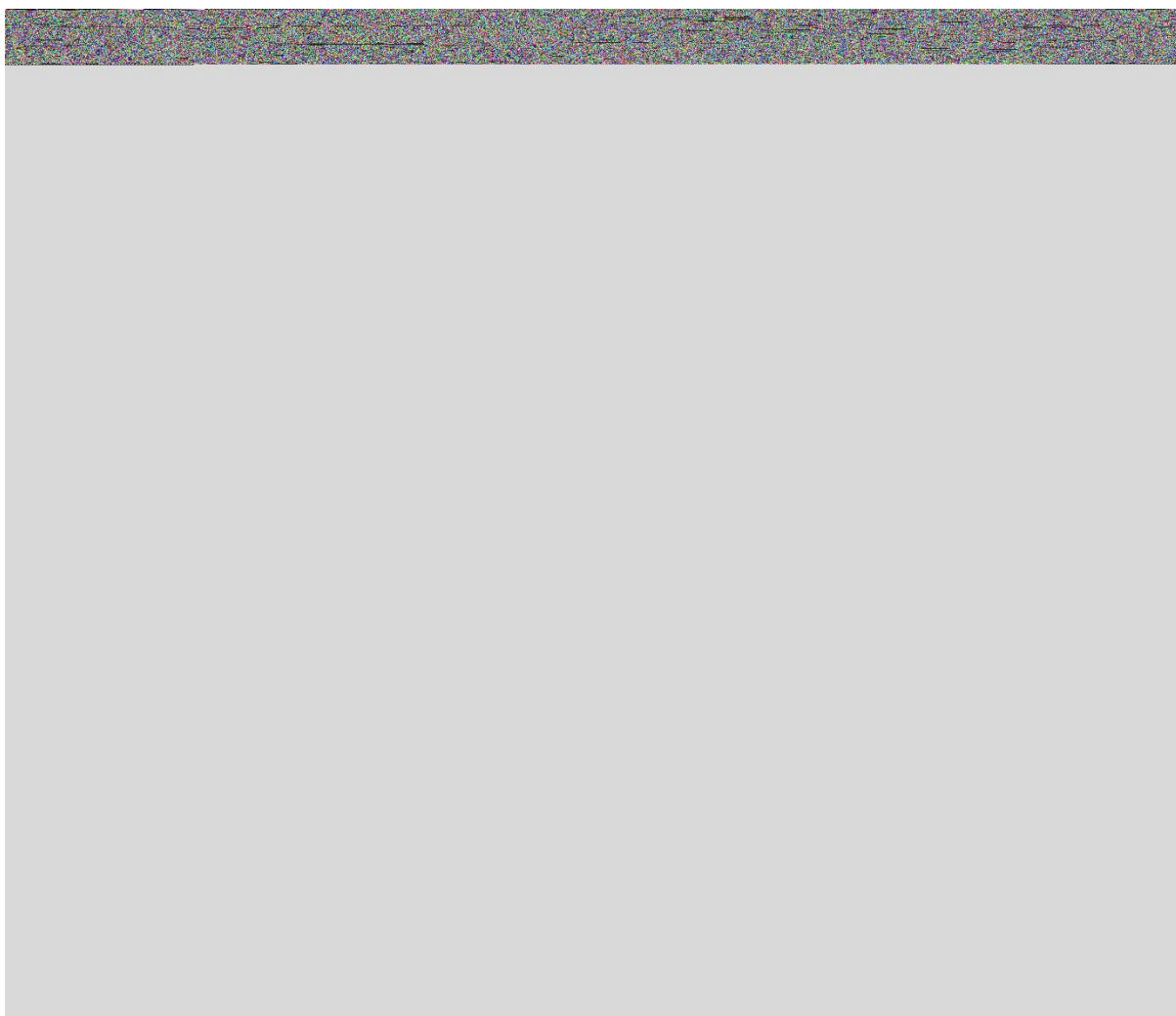


Fig. 17S. Two-dimensional interaction diagrams for best scoring poses of imatinib, **A**, and **5** (left panel top to bottom), and nilotinib, **B**, and **11** (right panel top to bottom) after induced fit (IFD) docking in c-KIT with Glide. Legend for amino acid residues and interaction types is given on the right.



Fig. 18S. Alignment of PDGFR- α and c-KIT proteins and enlarged area of their binding sites with imatinib.

Contacts formed between the six ligands and T670I mutated c-KIT in the flexible docking with Glide

IFD docked poses of the six ligands in c-KIT with T670I mutation are shown in Figure 18S and their two-dimensional interaction diagrams can be seen in Figure 19S. This crucial mutation of a polar residue in the centre of the binding pocket of c-KIT, THR670, which was seen to be an active hydrogen bond acceptor for a studied set of ligands, into a hydrophobic ILE with an ethyl side chain pointing into the binding pocket, is known to significantly hinder the inhibiting activity of imatinib and nilotinib. Loss of this HB interaction affects the ability of 4-pyridyl-pyrimidine core to bury itself deeply into the binding site, causing a reduced depth of entry of the whole ligand molecule into the binding cavity, as well as a less than ideal volume fit with a significant empty space, shown on the example of imatinib in 19S left. This, in turn, distances pyridine ring from CYS673 which was also captured as a consistent hydrogen donor for the six ligands. Instead, any interactions of the terminal 4-pyridyl-pyrimidine fragment are established through pyrimidine ring only, π - π stacking and HB with PHE811 and LYS623 for imatinib, and π -cation and HB interaction with LYS623 and ASP810 for nilotinib. In addition to a single HB formed between an amide NH and GLU640 (imatinib) or ASP810 (nilotinib), there are no other interactions between ligands and mutated receptor.

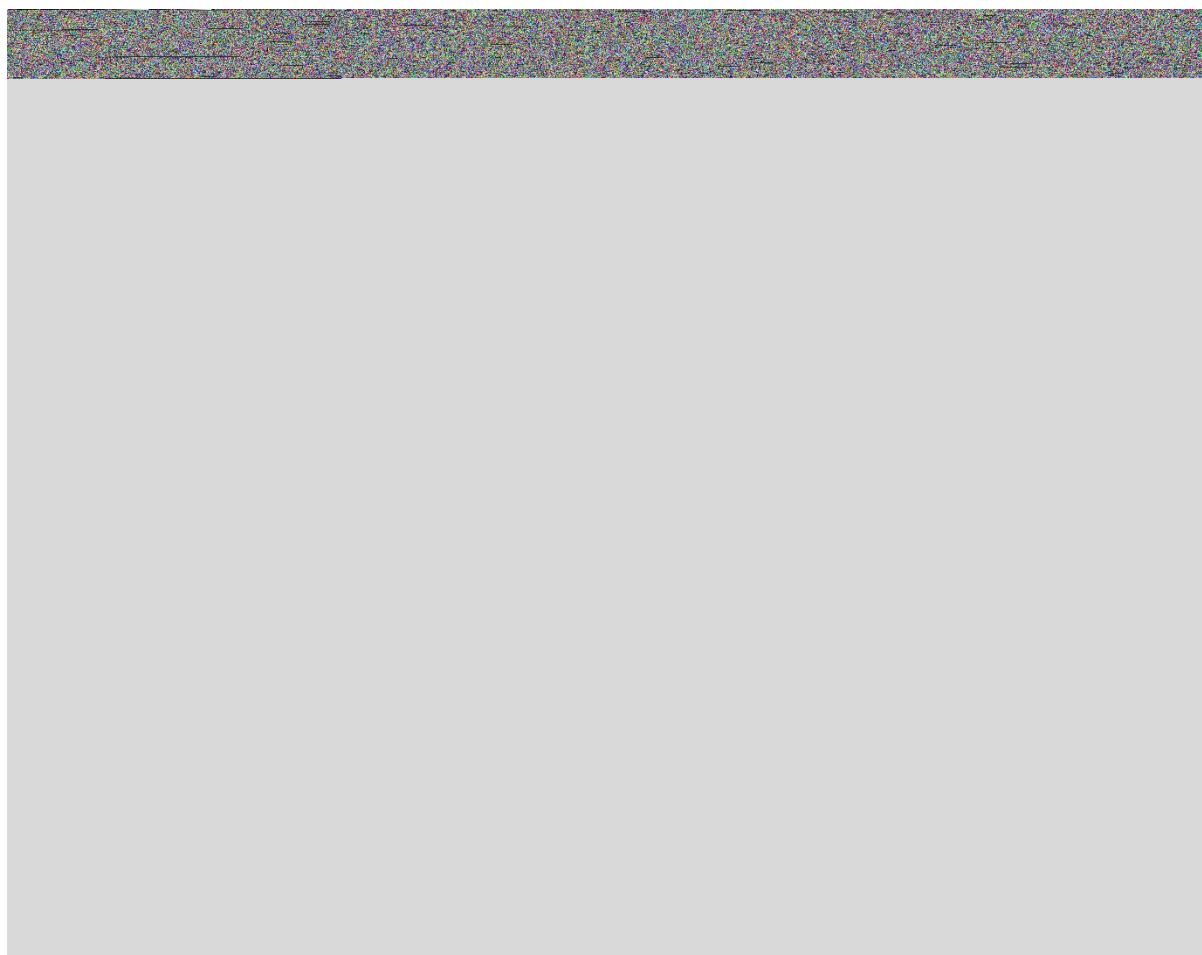


Fig. 19S. Best scoring poses of imatinib, **A** and **A_ligand-COOH** (left panel, top to bottom), and nilotinib, **B** and **B_ligand-COOH** (middle panel, top to bottom) after induced fit (IFD) in c-KIT with T-I mutation in position 670 docking with Glide. Alignment of ligand pairs is shown in the right panel (top to bottom), colouring matching the colouring in the ligand-receptor figures. For interaction colour scheme follow the caption of Figure 3.

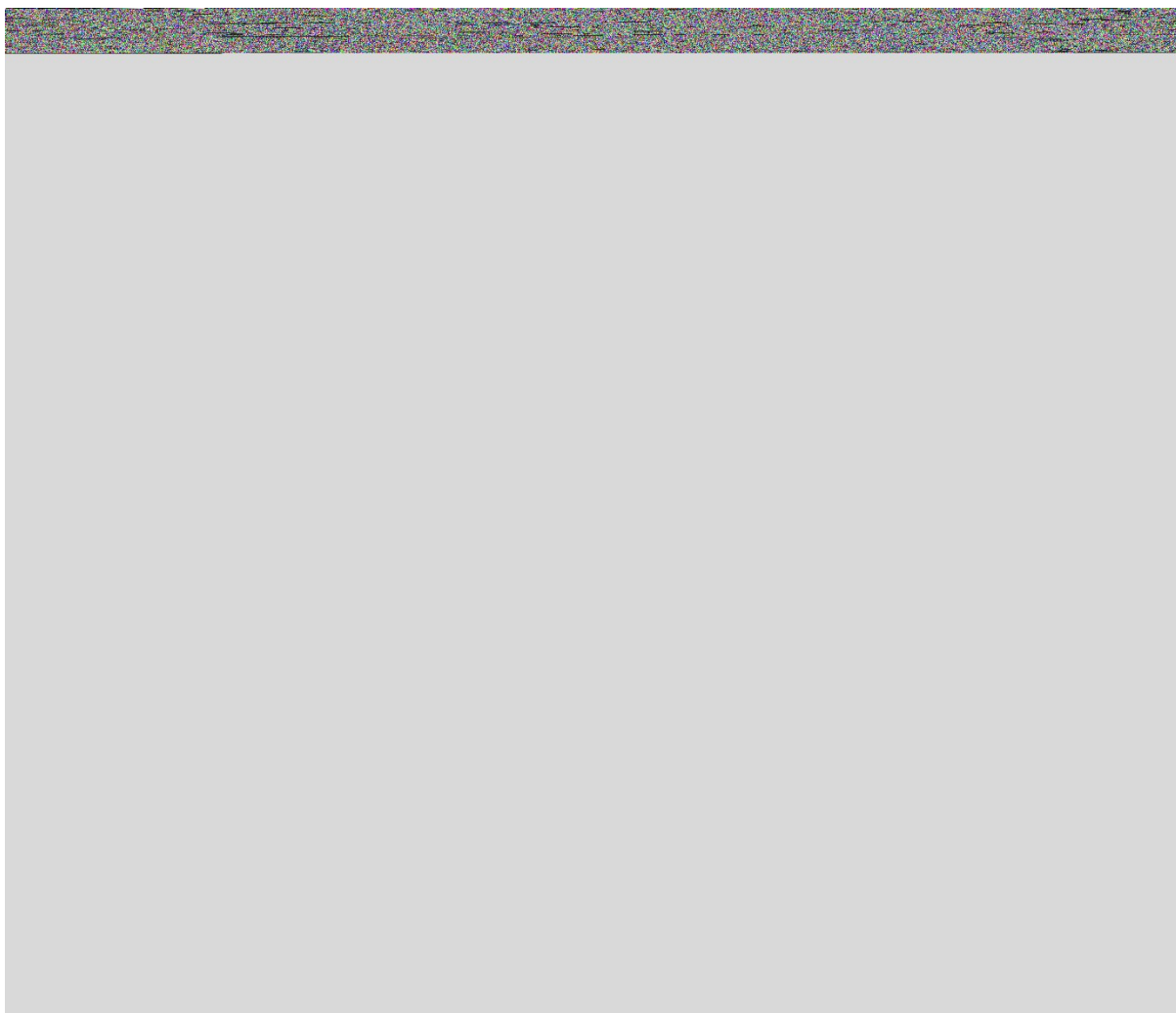


Fig. 20S. Two-dimensional interaction diagrams for best scoring poses of imatinib, **A** and **A_ligand-COOH** (left panel top to bottom), and nilotinib, **B** and **B_ligand-COOH** (right panel top to bottom) after induced fit (IFD) docking in T670I mutated c-KIT with Glide. Legend for amino acid residues and interaction types is given on the right.

Molecular Dynamics

Docking scores are very approximate, qualitative estimates of the binding affinity of the ligand for the protein and it has been shown they do not correlate with experimentally measured binding constants.^[8] This is mainly due to the protein conformational rigidity as well as solvation/desolvation effects which are not taken into the account. Additional caveat is the stability of the predicted pose in dynamical environment protein-ligand complexes find themselves in. Molecular dynamics (MD) simulations are an excellent approach to consider both the dynamics and the solvation.

The bottleneck of MD simulations, on the other hand, are force fields. The incompleteness of force field parameters has been a long-standing problem, especially for metal-related systems. For small organic molecules, generation of parameters has been well developed and automatized by a range of programmes such as ANTECHAMBER^[9] and CGenFF.^[10] To derive force field parameters for metal-containing systems, force constants can be directly derived from the Cartesian-based Hessian matrix after the QM calculation, as proposed in Seminario^[11] and Ayer methods.^[12] In this work, CHARMM36 force field was implemented for receptors, CGenFF platform was used to generate parameters of imatinib, nilotinib, and acid prodrug derivatives, and Seminario method as implemented in Visual Force Field Derivation Toolkit (VFFDT)^[13] was employed for derivation of force and angle constants for the metal centre and its chelating agents based on Hessian matrixes from Gaussian QM calculations. For solvent molecules, a CHARMM TIP3P water model was used.^[14]

To assess the stability of the docking poses obtained from Glide, MD simulations were performed in Gromacs.^[15,16] First, the ligand binding structures obtained through docking were solvated with approximately 14 000 water molecules at a physiological concentration of NaCl. Then, a simple energy minimisation was performed, followed by a short 10 ps equilibration in the NVT ensemble, and a longer 10 ns equilibration in the NPT ensemble with positional restraints on protein and ligand heavy atoms. After the system equilibration, 100 ns production MD runs were conducted under 310 K and 1 atm NPT conditions without any restraints. The Nose-Hoover thermostat^[17], with a relaxation time of 1 ps, and the Berendsen barostat^[18], with a relaxation time of 2 ps, were used. The cutoff radius of the Lennard-Jones (LJ) and electrostatic interactions were set to 1.2 nm, and the MD time step to 2 fs. To describe long-range electrostatic interactions, the particle mesh Ewald (PME) method was used.^[19] Root-mean-square deviation (RMSD), root-mean-square fluctuation (RMSF), and other interactions were analysed using internal Gromacs tools (gmx rms, rmsf, hbond etc) over full trajectories, taking configurations in every 50 ps.



Fig. 21S. Potential energy, E_{pot} (left), and temperature, T (right), time evolution over a 50 ns MD simulation of imatinib-PDGFR- α complex **A**.

Detailed analysis of MD production for imatinib and its derivatives complexed with PDGFR- α is showcased through a series of structural graphs in Figure 21S (SI). The average deviations observed in protein RMSD, 0.13, 0.12, and 0.12 nm and ligand RMSD, 0.11, 0.14, and 0.09 nm for PDGFR- α complexed with imatinib, **A** and **A_ligand-COOH**, respectively, indicate that complexes are very stable. The radius of gyration shows moderate modifications in the secondary structure of PDGFR- α , but also reflects the overall stability of the complexes, meaning that despite the structural changes caused by the compound binding, the protein remains folded, and no denaturation occurs negating any termination of the ligand inhibitory pathway. The flexibility patterns of the individual residues about their mean positions were studied through the RMSF analysis. The imatinib-PDGFR- α and **A** and **A_ligand-COOH** showed minimal fluctuations with an average RMSF of 0.11 nm in all cases. The complexes were relatively more stable near the interface domain with the HB network (ALA640-GLY680 and LEU809-ASP836), whereas the fluctuations of a higher magnitude were observed for the hydrophobic subdomain of the binding cavity and other residues within the same beta-sheet and belonging loops (LEU599-VAL624). A flexible coil (SER890-ASP902) exposed at the protein surface far from the binding site also showed more pronounced fluctuations.

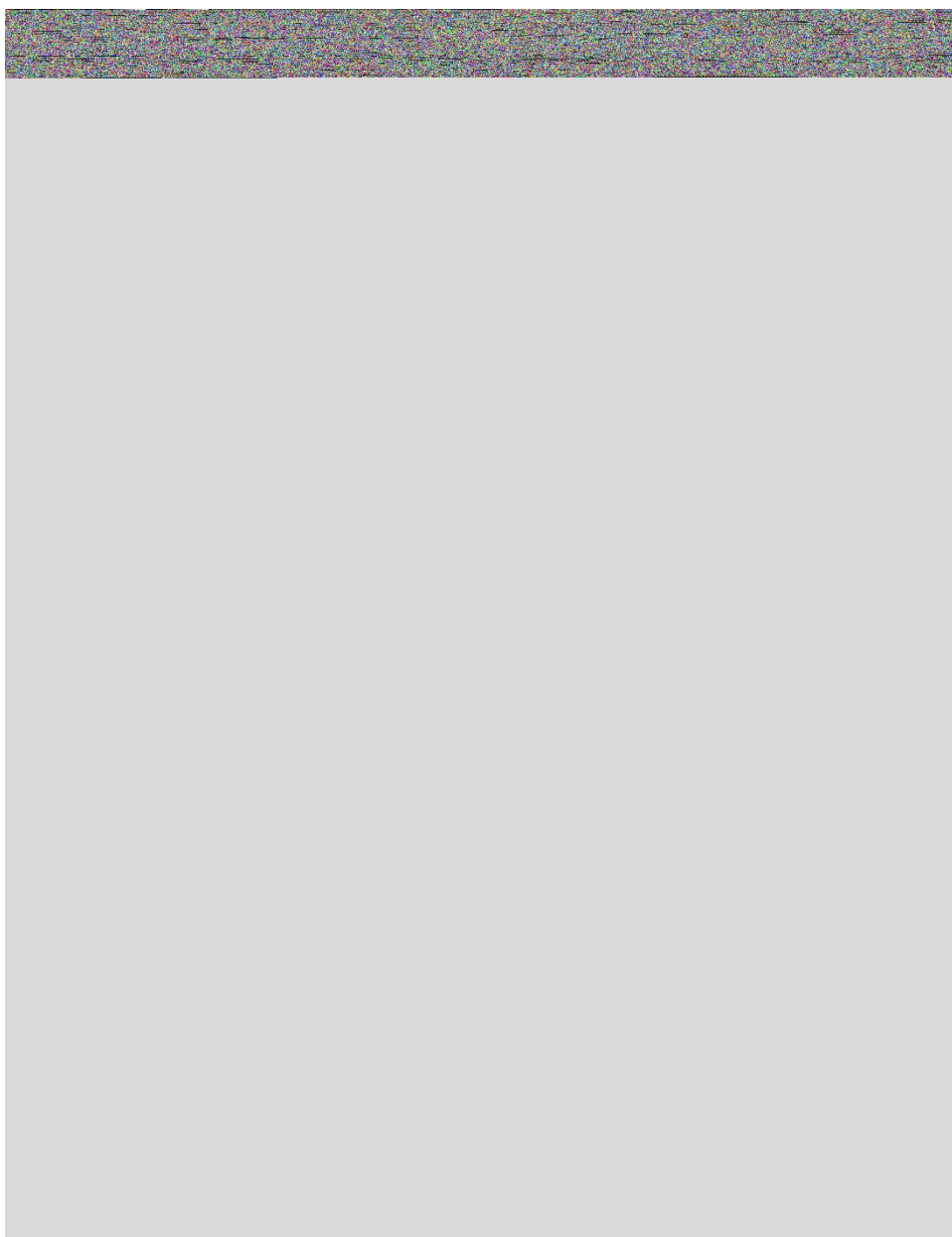


Fig. 22S. Analysis of MD trajectories after the 50 ns NPT production runs conducted on imatinib- (cyan), **A** (blue), and **A_ligand-COOH** with PDGFR- α (dark blue) complexes. Protein RMSD (nm), protein radius of gyration (R_g , nm), ligand RMSD (nm), and RMSF (nm) per residue are shown in the left panel (top to bottom). Hydrogen bond (HB) count and length (d_{HB} , nm) distribution are shown in the bottom right panel.

Principal component analysis was conducted in order to determine the relationship between statistically meaningful conformations sampled during the trajectory and recover a partial complex free energy profile correlated to the major global motions of the ligand. Through an eigenvalue rank plot it was discovered that the first two principal components (PC1 and PC2) are responsible for more than 85% of the total variance, and their correlation is projected in Figure 22S. Multiple energy clusters per system depict the structural transition between distinct active states, and by retrieving the two lowest energy structures it can be seen that different clusters appear due to the fluctuation in the position of the piperazine ring of imatinib and that of long tails with Pt-complex **A** or the corresponding ligand **A_ligand-COOH**.

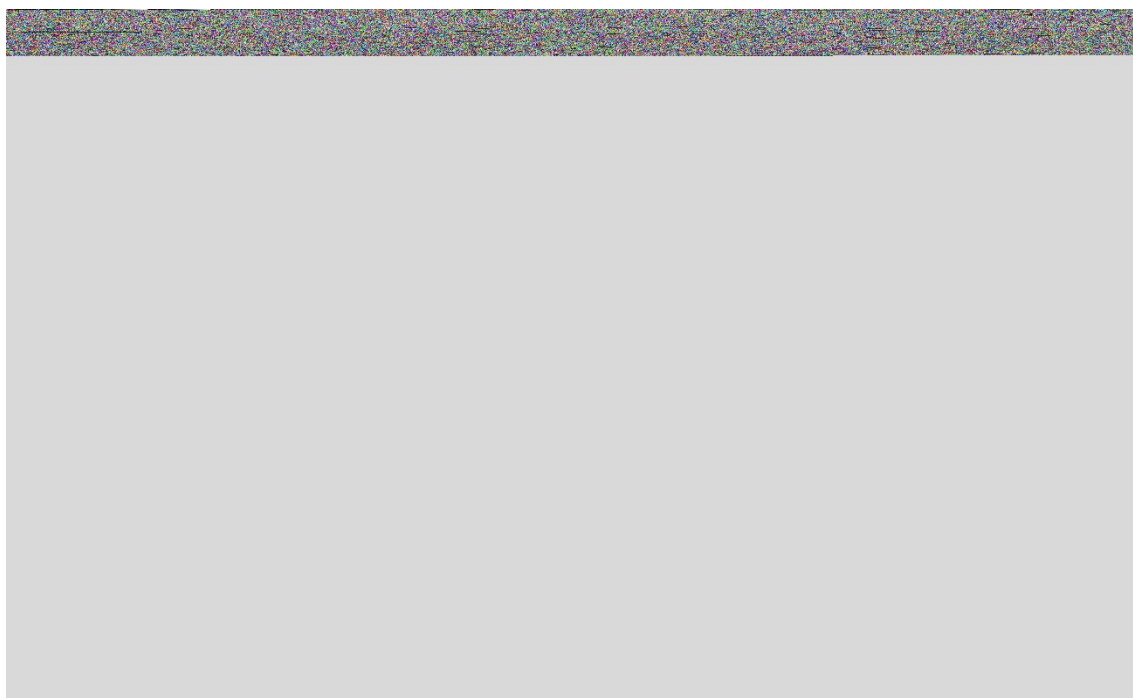


Fig. 23S. Principal component analysis of the 50 ns NPT production runs conducted on imatinib- (left), complex **A** (middle), and **A_ligand-COOH** -PDGFR- α (right) complexes. Projection of principle component 1 (PC1) on principal component 2 (PC2) with corresponding complex structures belonging to the energy minima.

To better understand which residues of the receptors are relevant for the binding process, trajectories were analysed by considering the statistical distribution in terms of contacts between ligands and single residues and the corresponding maps are shown in the top panel of Figure 22S. The contact frequency is defined as a fraction of the trajectory in which a certain contact is made, considering all contacts with atoms in the query residue, with contact defined within a cut-off distance of 4.0 Å.

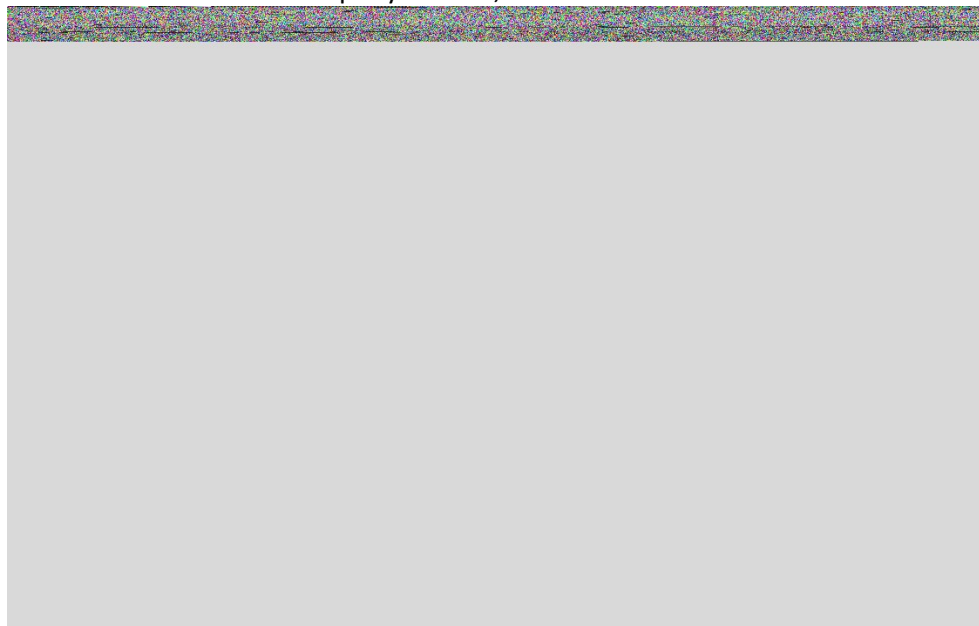


Fig. 24S. Analysis of contacts between the ligand and binding site residues and decomposed contribution of those residues to the free binding energy of imatinib (cyan), **A** (blue), and **A_ligand-COOH** (dark blue) within PDGFR- α .

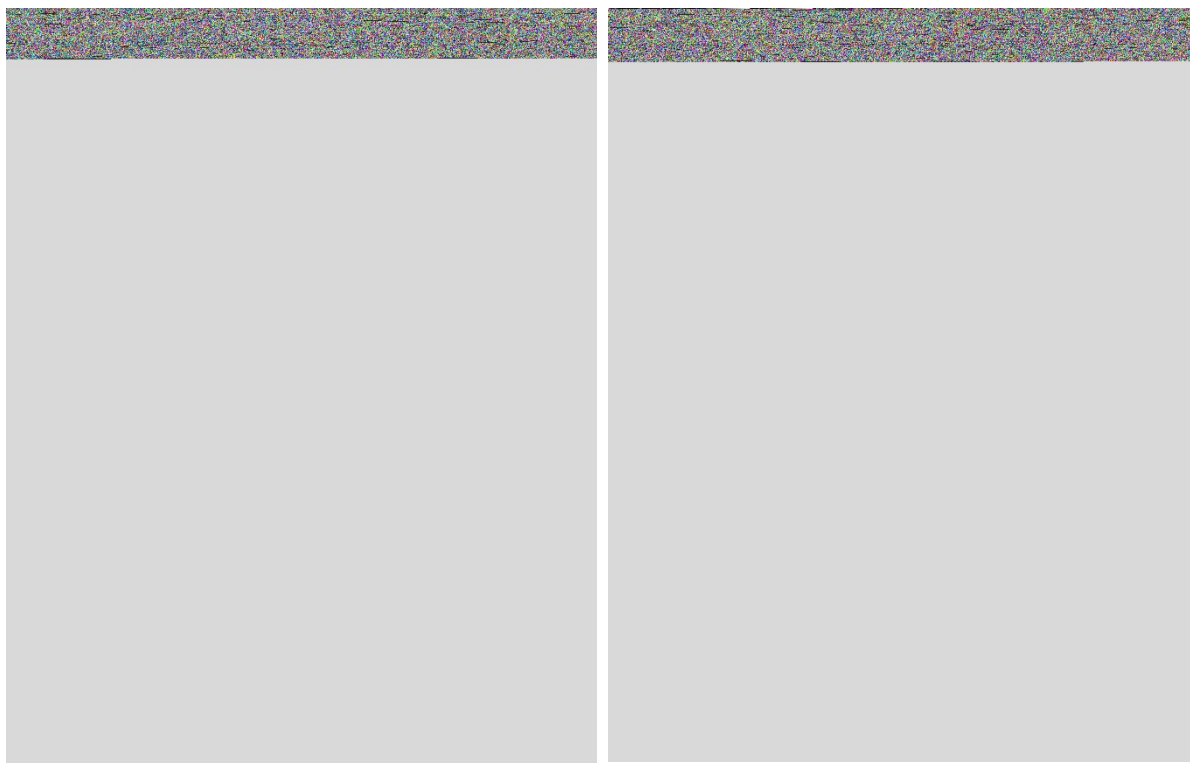


Fig. 25S. Analysis of MD trajectories after the 50 ns NPT production runs conducted on imatinib- (cyan), **A** (blue), and **A_ligand-COOH** (dark blue) complexes with c-KIT (left panel) and T670I mutated c-KIT (right panel).



Fig. 26S. Analysis of contacts between the ligand and binding site residues and decomposed contribution of those residues to the free binding energy of imatinib (cyan), **A** (blue), and **A_ligand-COOH** (dark blue) within c-KIT (left) and c-KIT with T670I mutation (right).

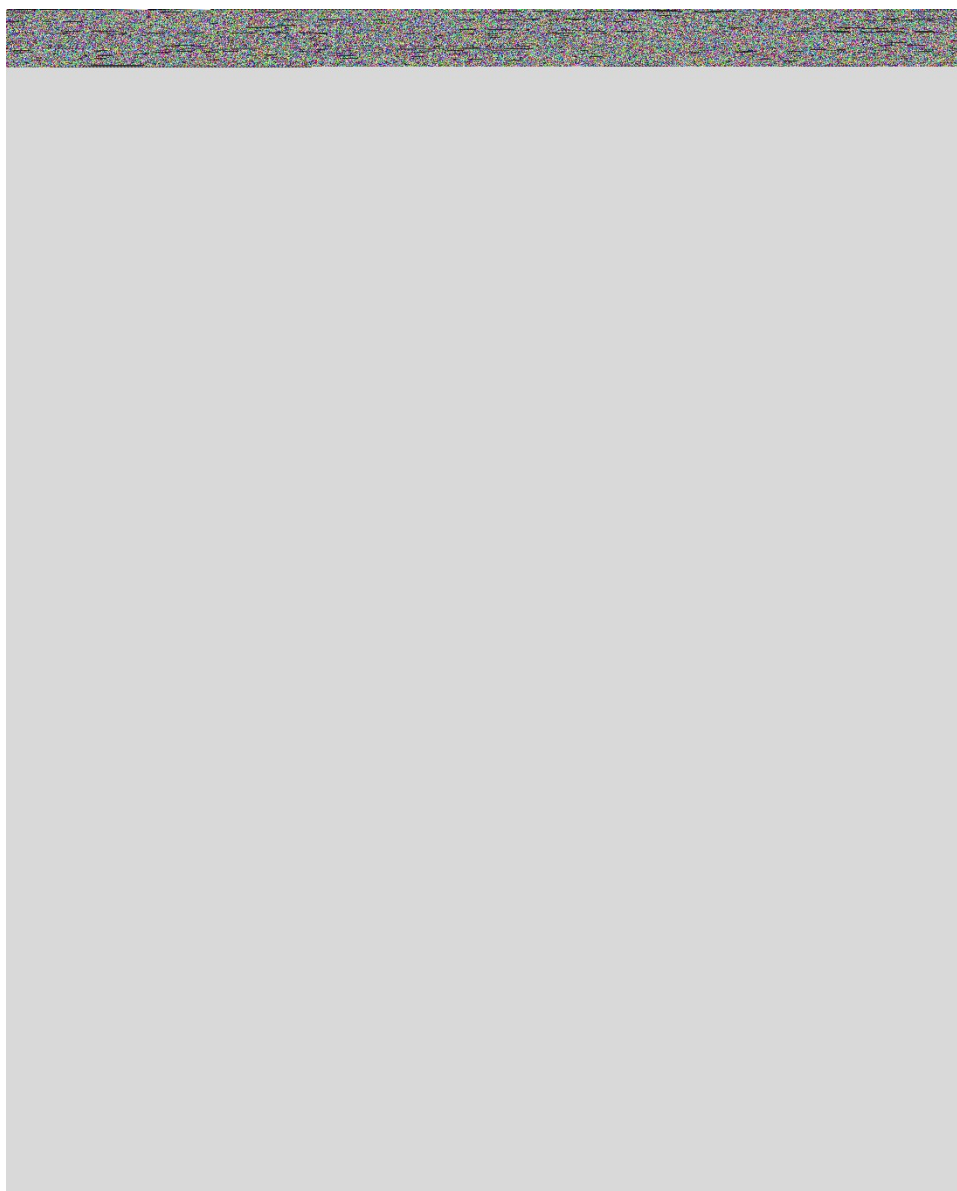


Fig. 27S. Analysis of MD trajectories after the 50 ns NPT production runs conducted on nilotinib- (pink), **B** (purple), and **B_ligand-COOH** PDGFR- α (dark purple) complexes. Protein RMSD, protein radius of gyration (R_g), ligand RMSD, and RMSF per residue are shown in the left panel. Hydrogen bond (HB) count and length (d_{HB}) distribution are shown in the right panel.

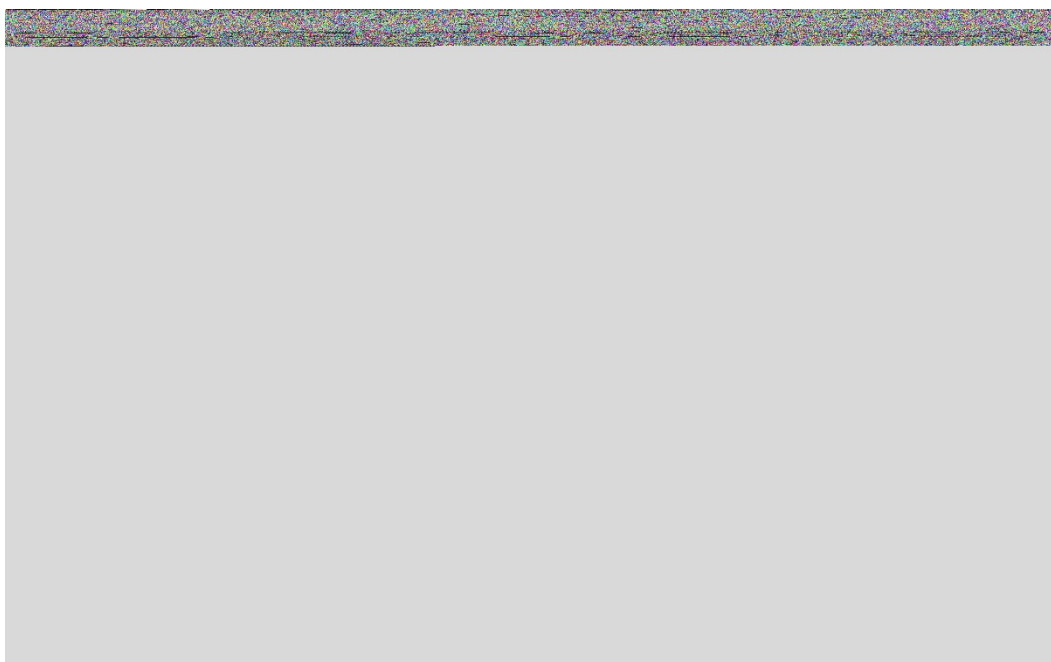


Fig. 28S. Analysis of contacts between the ligand and binding site residues and decomposed contribution of those residues to the free binding energy of nilotinib- (pink), **B** (purple), and **B_ligand-COOH** (dark purple) within PDGFR- α .



Fig. 29S. Analysis of MD trajectories after the 50 ns NPT production runs conducted on nilotinib- (pink), **B** (purple), and **B_ligand-COOH** (dark purple) complexes with c-KIT (left panel) and T670I mutated c-KIT (right panel).

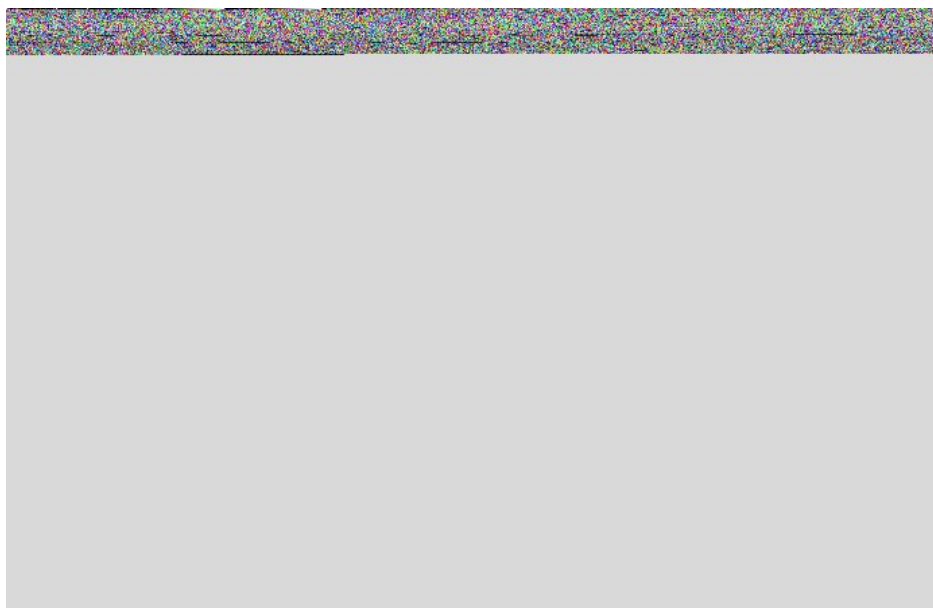


Fig. 30S. Analysis of contacts between the ligand and binding site residues and decomposed contribution of those residues to the free binding energy of nilotinib- (pink), **B** (purple), and **B_ligand-COOH** (dark purple) within c-KIT (up) and c-KIT with T670I mutation (down).

To calculate a quantitative approximation to the free binding energy, a MMPBSA approach [20,21, 22] which assesses individually solvation energies of free and complexed ligand as well as interaction energy of the ligand-receptor complex was used as implemented in gmx_MMPBSA tool.^[23,24]

Table 1S. Free binding energy (E_{bin}) and its components: van der Waals energy (ΔvdW), electrostatic energy (ΔE_{el}), polar solvation energy based on Poisson-Boltzmann approach (ΔEPB), non-polar solvation energy based on SASA approach (ΔnP), and dispersion energy (ΔE_{disp}) calculated using the MMPBSA method for imatinib, nilotinib, **A**, **B**, **5** and **11** interacting with PDGFR- α , c-KIT, and c-KIT mutated in position 670 (T-I). All energies are expressed in kJ/mol.

		imatinib	A	5	nilotinib	B	11
PDGFR- α	ΔvdW	-	-	-	-60.58±0.75	-66.91±1.31	-61.84±0.72
	ΔE_{el}	63.82±1.10	66.71±0.81	62.98±0.69	-8.49±0.09	-5.80±1.11	-14.36±0.29
	ΔEPB	-7.53±0.26	-6.79±1.20	-	12.12±0.12	14.36±0.64	19.51±0.12
	ΔnP	-	-	23.73±0.19	-44.31±0.22	-50.11±0.23	-44.24±0.18
	ΔE_{disp}	11.41±0.13	14.63±0.61	26.79±0.02	76.57±0.25	85.63±0.22	76.25±0.24
	E_{bin}	47.51±0.13	48.26±0.32	46.90±0.13	-	-	-
		80.11±0.12	85.31±0.06	79.88±0.14	24.69±1.10	22.84±2.08	24.68±1.23
c-KIT	ΔvdW	-	-	-	-60.38±0.66	-64.62±0.98	-62.40±1.05
	ΔE_{el}	63.96±0.90	66.63±1.19	65.08±0.52	-9.03±0.05	-8.29±0.87	-5.07±0.29
	ΔEPB	-7.44±0.09	-	-	12.38±0.10	13.52±0.43	11.83±0.34
	ΔnP	12.68±0.06	18.01±0.10	23.59±0.18	-44.65±0.08	-50.87±0.06	-45.63±0.05
	ΔE_{disp}	-	-	-	77.49±0.07	86.94±0.25	78.36±0.21
	E_{bin}	47.05±0.14	52.77±0.38	47.58±0.09	-24.20±1.11	-23.32±1.62	-22.92±1.50
		82.15±0.08	91.91±0.16	84.28±0.01	13.34±1.45	16.67±1.50	13.54±2.20
c-KIT T670I	ΔvdW	-	-	-	-45.70±1.03	-58.00±0.67	-43.96±1.13
	ΔE_{el}	59.87±0.38	55.25±1.17	46.81±0.89	-5.34±0.04	-6.93±0.91	-10.29±1.23
	ΔEPB	-4.64±0.22	-5.45±1.10	-	9.61±0.29	12.75±0.40	15.07±1.14
	ΔnP	10.05±0.07	13.78±0.55	19.71±0.57	-36.66±0.24	-44.10±0.46	-34.44±0.01
	ΔE_{disp}	-	-	-	64.74±0.28	79.62±0.12	60.08±0.28
	E_{bin}	43.67±0.20	42.72±0.48	38.33±0.37	-	-	-
		79.74±0.60	75.98±0.16	68.75±0.38	13.34±1.45	16.67±1.50	13.54±2.20

Biological Details

Experiments with Cultured Human Cancer Cells

All tested compounds were dissolved in DMSO just before the experiment, and a calculated amount of drug solution was added to the cell growth medium to a final solvent concentration of 0.5%, which had no detectable effects on cell viability. Cisplatin was dissolved in 0.9 % NaCl solution. MTT (3-(4,5-dimethylthiazol-2-yl)-2,5-diphenyltetrazolium bromide) and DTNB were obtained from Sigma Chemical Co, St. Louis, USA.

Cell Cultures

Human SH-SY5Y neuroblastoma carcinoma cells were obtained by ATCC (American Type Culture Collection, Rockville, MD, USA). The human ovarian cancer cell line 2008 were kindly provided by Prof. G. Marverti (Department of Biomedical Science of Modena University, Italy). Cell lines were maintained in the logarithmic phase at 37 °C in a 5% carbon dioxide atmosphere using RPMI-1640 medium (EuroClone) containing 10% fetal calf serum (EuroClone, Milan, Italy), antibiotics (50 units/mL penicillin and 50 µg/mL streptomycin) and 2 mM l-glutamine.

MTT Assay

The growth inhibitory effect on tumor cells was evaluated by means of the MTT assay. Briefly, 3–8 x 10³ cells/well, dependent upon the growth characteristics of the cell line, were seeded in 96-well microplates in growth medium (100 µL). After 24 h, the medium was removed and replaced with a fresh one containing the compound to be studied at the appropriate concentration. Triplicate cultures were established for each treatment. After 72 h, each well was treated with 10 µL of a 5 mg/mL MTT saline solution, and following 5 h of incubation, 100 µL of a sodium dodecyl sulfate (SDS) solution in HCl 0.01 M was added. After overnight incubation, cell growth inhibition was detected by measuring the absorbance of each well at 570 nm using a Bio-Rad 680 microplate reader. The mean absorbance for each drug dose was expressed as a percentage of the control untreated well absorbance and plotted vs. drug concentration. IC₅₀ values, the drug concentrations that reduce the mean absorbance at 570 nm to 50% of those in the untreated control wells, were calculated by the four-parameter logistic (4-PL) model. The evaluation was based on means from at least three independent experiments.

Inhibition of PDGFR α and c-KIT Kinase Activity

The inhibition of the kinase activity PDGFR- α and c-KIT was assessed through the KinomeScan assay service (DiscoverX) which is run in parallel with known inhibitors. An exhaustive description of the assay is given in ref.^[25]

References

1. J. Da Chai, M. Head-Gordon, *Phys. Chem. Chem. Phys.* 2008, **10**, 6615–6620.
2. P. J. Hay, W. R. Wadt, *J Chem Phys* 1985, **82**, 299–310.
3. M. J. Frisch, J. A. Pople, J. S. Binkley, *J Chem Phys* 1984, **80**, 3265–3269.
4. B. Mennucci, J. Tomasi, R. Cammi, J. R. Cheeseman, M. J. Frisch, F. J. Devlin, S. Gabriel, P. J. Stephens, *J. Phys. Chem. A* 2002, **106**, 6102–6113.
5. G. Madhavi Sastry, M. Adzhigirey, T. Day, R. Annabhimoju, W. Sherman, *J. Comput. Aided Mol. Des.* 2013, **27**, 221–234.
6. R. A. Friesner, J. L. Banks, R. B. Murphy, T. A. Halgren, J. J. Klicic, D. T. Mainz, M. P. Repasky, E. H. Knoll, M. Shelley, J. K. Perry, D. E. Shaw, P. Francis, P. S. Shenkin, *J. Med. Chem.* 2004, **47**, 1739–1749.
7. W. Sherman, H. S. Beard, R. Farid, *Chem. Biol. Drug. Des.* 2006, **67**, 83–84.
8. X.-Y. Meng, H.-X. Zhang, M. Mezei, M. Cui, *Curr. Comput. Aided Drug. Des.* 2011, **7**, 145–157.
9. J. Wang, W. Wang, P. A. Kollman, D. A. Case, *J. Mol. Graph. Model* 2006, **25**, 247–260.
10. K. Vanommeslaeghe, A. D. MacKerell, *J. Chem. Inf. Model* 2012, **52**, 3144–3154.
11. J. M. Seminario, *Int. J. Quantum Chem.* 1996, **60**, 1271–1277.

12. S. K. Burger, M. Lacasse, T. Verstraelen, J. Drewry, P. Gunning, P. W. Ayers, *J. Chem. Theory Comput.* 2012, **8**, 554–562.
13. S. Zheng, Q. Tang, J. He, S. Du, S. Xu, C. Wang, Y. Xu, F. Lin, *J. Chem. Inf. Model* 2016, **56**, 811–818.
14. S. Boonstra, P. R. Onck, E. Van Der Giessen, *J. Phys. Chem. B* 2016, **120**, 3692–3698.
15. H. J. C. Berendsen, D. Van Der Spoel, R. Van Drunen, *Comp. Phys. Comm.* 1995, **91**, 43 - 56
16. S. Páll, A. Zhmurov, P. Bauer, M. Abraham, M. Lundborg, A. Gray, B. Hess, E. Lindahl, *J. Chem. Phys.* 2020, **153**, 134110.
17. D. J. Evans, B. L. Holian, *J. Chem. Phys.* 1985, **83**, 4069–4074.
18. H. J. C. Berendsen, J. P. M. Postma, W. F. Van Gunsteren, A. Dinola, J. R. Haak, *J. Chem. Phys.* 1984, **81**, 3684–3690
19. U. Essmann, L. Perera, M. L. Berkowitz, T. Darden, H. Lee, L. G. Pedersen, *J. Chem. Phys.* 1995, **103**, 8577–8593.
20. J. Srinivasan, T. E. Cheatham, P. Cieplak, P. A. Kollman, D. A. Case, *J. Am. Chem. Soc.* 1998, **120**, 9401- 9409.
21. P. A. Kollman, I. Massova, C. Reyes, B. Kuhn, S. Huo, L. Chong, M. Lee, T. Lee, Y. Duan, W. Wang, O. Donini, P. Cieplak, J. Srinivasan, D. A. Case, T. E. Cheatham, *Acc. Chem. Res.* 2000, **33**, 889–897.
22. C. Wang, D. Greene, L. Xiao, R. Qi, R. Luo, *Front. Mol. Biosci.* 2018, **4**, 87.
23. B. R. Miller, T. D. McGee, J. M. Swails, N. Homeyer, H. Gohlke, A. E. Roitberg, *J. Chem. Theor. Comput.* 2012, **8**, 3314–3321.
24. M. S. Valdés-Tresanco, M. E. Valdés-Tresanco, P. A. Valiente, E. Moreno, *J. Chem. Theor. Comput.* 2021, **17**, 6281–6291.
25. Available online: https://www.discoverx.com/products-applications/kinase-solutions?gclid=EAlalQobChMI5-3mrL2V_gIVIM13Ch0RrAK8EAAYAiAAEgJEsPD_BwER.J.